The role of alveolar macrophages in biokinetics and biological effects of inhaled nanoparticles

Dissertation

zur Erlangung des Grades

des Doktors der Naturwissenschaften

der Naturwissenschaftlich-Technischen Fakultät

der Universität des Saarlandes

von

Johanna Koltermann-Jülly

Saarbrücken

2019

The role of alveolar macrophages in biokinetics and biological effects of inhaled nanoparticles

Dissertation

zur Erlangung des Grades

des Doktors der Naturwissenschaften

der Naturwissenschaftlich-Technischen Fakultät

der Universität des Saarlandes

von

Johanna Koltermann-Jülly

Saarbrücken

2019

Tag des Kolloquiums: 21. Januar 2020

Dekan:	Prof. Dr. Guido Kickelbick
Berichterstatter:	Prof. Dr. Claus-Michael Lehr
	Prof. Dr. Rolf W. Hartmann
	PD Dr. Robert Landsiedel
Vorsitz:	Prof. Dr. Marc Schneider
Akad. Mitarbeiter:	Dr. Jessica Hoppstädter

Die vorliegende Arbeit wurde unter der Leitung von Herrn PD Dr. Robert Landsiedel, Frau Dr. Lan Ma-Hock und Frau Dr. Sibylle Gröters in der Abteilung für Experimentelle Toxikologie und Ökologie in der BASF SE, Ludwigshafen am Rhein, und unter der Betreuung von Herrn Prof. Dr. Claus-Michael Lehr am Institut für Pharmazeutische Technologie der Universität des Saarlandes und am Helmholtz-Institut für Pharmazeutische Forschung Saarland angefertigt.

Table of contents

I. Summary

Some poorly-soluble nanoparticles (NPs) cause pulmonary inflammation upon inhalation. Histopathological effects of different NPs differ in types of initial inflammation as well as in long-term effects after chronic exposure. Surprisingly, also their lung clearance differs. Alveolar macrophages (AMs) are chiefly involved in pulmonary immune responses as well as in pulmonary clearance mechanisms. Thus, this dissertation project investigated on one hand whether AMs accelerate the biodissolution of e.g. $BaSO_4$ NPs. On the other, it aimed at identifying AM subpopulations in lungs of animals exposed to NPs such as TiO_2 or CeO_2, and to find a correlation between early AM polarization and long-term outcome. It could be shown that under acidic conditions, as present in AM lysosomes, and in synergy with the dynamic conditions, which prevail in the well perfused lungs, $BaSO_4$ NPs undergo accelerated biodissolution. Immunohistochemistry of lung specimen revealed a correlation of pro-inflammatory M1 and anti-inflammatory M2 AM relative numbers with acute inflammation after 5-day exposure to different NPs. A correlation with the quality of histopathological effects could not be found. Current data do not allow for the prediction of long-term outcome. An understanding of the contribution of AMs in the pathogenesis of pulmonary morphological changes might identify powerful, specific biomarkers, which potentially might allow for the prediction of the long-term outcome following NP exposure.

II. Zusammenfassung

Manche schwerlösliche Nanopartikel (NP) verursachen Lungenentzündungen nach Inhalation. Die histopathologischen Effekte verschiedener NP unterscheiden sich in der Art der initialen Entzündung und in den Langzeiteffekten nach chronischer Exposition. Überraschenderweise unterscheidet sich auch die pulmonale Clearance. Alveolarmakrophagen (AM) spielen sowohl in der pulmonalen Immunantwort als auch bei der Clearance eine vorrangige Rolle. Daher untersuchte diese Arbeit einerseits ob AM das Auflösungsverhalten von NP wie z.B. $BaSO_4$ beeinflussen. Andererseits wurden polarisierte AM in Lungen NP-exponierter Tiere identifiziert, um eine Korrelation mit Langzeiteffekten zu erkennen. Unter sauren Bedingungen, wie sie in Lysosomen vorherrschen, zusammen mit den dynamischen Bedingungen der gut perfundierten Lunge, lösten sich $BaSO_4$ NP deutlich schneller auf, als aufgrund ihres Löslichkeitsproduktes in Wasser erwartet. Immunohistochemische Untersuchungen von Lungengewebe ergaben eine Korrelation der relativen Zellzahl pro-inflammatorischer M1 und anti-inflammatorischer M2 AM mit akuter Entzündung nach 5-tägiger NP-Exposition, wie z.B. TiO_2 oder CeO_2. Es wurde keine Korrelation mit der Qualität der histopathologischen Effekte gefunden. Eine Prädiktion von Langzeiteffekten ist auf Basis der Daten nicht möglich. Das Verständnis der Mitwirkung von AM an der Entstehung krankhafter Lungenveränderungen könnte Biomarker identifizieren, die zu einer Vorhersage von Langzeiteffekten von NP befähigen.

III. List of abbreviations

AM	Alveolar macrophage
ArgI	Arginase I
BALF	Bronchoalveolar lavage fluid
$BaSO_4$	Barium sulfate
CD	Cluster of differentiation
CD206	Cluster of differentiation 206, mannose receptor
CeO_2	Cerium dioxide
DNA	Deoxyribonucleic acid
IFNγ	Interferon gamma
IL	Interleukin
iNOS	inducible nitric oxide synthase
LDH	Lactate dehydrogenase
M1	pro-inflammatory polarized macrophage
M2	anti-inflammatory polarized macrophage
mwCNT	Multi-walled carbon nanotubes
NF-κB	nuclear factor 'kappa-light-chain-enhancer' of activated B-cells
NP	Nanoparticle
PSF	Phagolysosomal simulant fluid
ROS	Reactive oxygen species
$SrCO_3$	Strontium carbonate
STIS	Short-term inhalation study
TiO_2	Titanium dioxide
TNFα	Tumor necrosis factor alpha
ZnO	Zinc oxide

1. Introduction

1.1 Introduction to the inhalation toxicology of poorly-soluble nanoparticles

Because of their unique physicochemical properties nanoparticles (NPs) can be found in various consumer applications, such as cosmetics, food, and textiles, industrial applications, such as nanoelectronics, catalysts, fillers, and coatings, and nanomedical applications, such as nanotherapeutics (Szakal et al., 2014; Vance et al., 2015). The variety of potential applications, for instance in nanomedicine, is still increasing (Webster, 2013; Lepeltier et al., 2015; Pelaz et al., 2017; Ovais et al., 2019). It is because of the extraordinary characteristics of NPs that concerns arose whether these materials might have unique toxicological attributes, which differ from those of their bulk counterparts (Ferin et al., 1992; Oberdörster et al., 2005; Nel et al., 2006). Indeed, their small size (particles with at least one dimension in the size range 1 - 100 nm), large surface to mass ratio, and exceptional surface reactivity lead to biological outcomes different from those of materials of the same chemical composition but with larger particle size (Oberdörster et al., 1994a; Oberdörster et al., 2005).

Based on the wide applications of NPs, all routes of exposure (oral, dermal, inhalation, injection) are relevant for human exposure (Kuhlbusch et al., 2018). The usage of NPs as food additives for instance leads to oral exposure. The utilization of NPs in sunscreens results in dermal exposure. Moreover, numerous NPs are currently under investigation as carriers or therapeutics for substance application by inhalation (Gunday Tureli et al., 2017; Rigo et al., 2017; Yasar et al., 2018). However, at the production sites of engineered NPs, NPs can be released in the ambient air. This results in exposure by inhalation of the worker during production, processing and handling of NPs at the workplace. Thus, inhalation represents the major route of occupational exposure and the greatest concern among other possible routes of exposure (Maynard and Kuempel, 2005; Borm et al., 2006). Because airborne NPs can easily reach the lower respiratory tract following inhalation and subsequently can deposit in the alveolar region, pulmonary effects are of particular interest for occupational safety (Oberdörster, 2000; Donaldson et al., 2002) and for this dissertation project. In general, the term ‘nanoparticles’ in this thesis refers to granular particles and does not include high aspect ratio materials (fibers) (WHO, 2000). The toxicity of granular particles differs partly from the toxicity induced by fibrous materials, but these differences are not the scope of the current dissertation project. The following paragraphs mainly focus on toxicological effects of granular particles. However, immunohistochemical investigations also include fibrous multi-walled carbon nanotubes (mwCNT).

When deposited in the alveolar region of the lungs, any particulate matter is rapidly engulfed by alveolar macrophages (AMs) (**Box 1**). Typically, particles $\geqslant$ 0.5 µm are subjected

Box 1 Anatomy of the respiratory tract and functions of alveolar macrophages

The respiratory system of mammalians is divided into the upper respiratory tract and the lower respiratory tract. The upper respiratory tract consists of the nose, the oropharynx and the larynx. The lower respiratory tract consists of the trachea, which divides at the bifurcation into two main bronchi, followed by the bronchial tree, and terminating in the alveolar sacs. The upper respiratory tract together with the tracheobronchial tree constitutes the conducting airways. They are lined amongst others with a ciliated pseudostratified columnar epithelium, which is covered by a mucus layer. In the distal part of the lower respiratory tract, the alveolar region, gas exchange takes place. The alveoli, more precisely the alveolar walls, are mainly formed by alveolar epithelial cells type I. The alveolar surface is lined with a thin layer of a lipid- and protein-rich fluid called surfactant. Here, at the alveolar surface, submersed in the lining fluid, resident alveolar macrophages (AMs) are located. AMs are large, mononuclear cells, which belong to the cellular arm of the innate immune system. They have a pivotal role in organ development and tissue homeostasis. As the first line of host defense, AMs are the key orchestrators of pulmonary immune responses. Following pathological stimuli, AMs become activated and exert their effector functions such as antimicrobial activities (e.g. respiratory burst). In addition, they have important roles in the resolution of inflammation and tissue repair. Apart from their diverse homeostatic and immunologic functions, AMs embody the main clearance mechanism of the alveolar region, which aims at disposing of any foreign particulate matter from the alveolar surface. As professional phagocytes AMs ensure the sterility of the alveolar surface by rapidly engulfing deposited particulate material, such as poorly-soluble NPs.

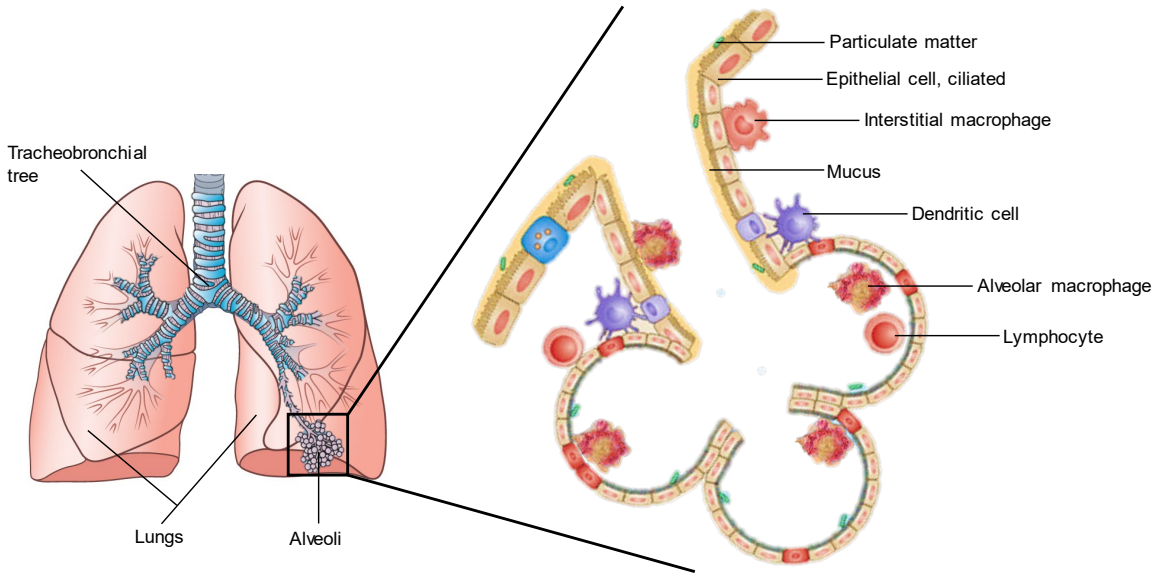

modified from (Hussell and Bell, 2014)

to phagocytosis, whereby the optimal particle size for rapid phagocytosis is 2-3 µm (Champion et al., 2008). Smaller particles (< 0.5 µm), including NPs, are internalized by AMs as well, however, less specifically and less efficiently than larger particles (Geiser et al., 2008; Geiser, 2010). AMs are professional phagocytes and the key orchestrators of pulmonary immune responses. They represent the first line of host immune defense at a location continuously exposed to the environment (Goldstein et al., 1974; Fels and Cohn, 1986). In addition, AMs embody the main clearance mechanism of particulate matter from the lower respiratory tract. When ingested by AMs, particulate matter can be removed from the lungs by migration of AMs to extrapulmonary targets (physical clearance) and/or it can be processed intracellularly (chemical clearance) (Bowden, 1984; Hussell and Bell, 2014) (**Box 2**).

Several decades ago, human epidemiological data and data from rat inhalation studies revealed that dust composed of poorly-soluble granular particles caused pulmonary inflammation following inhalation exposure (Davis et al., 1978; Pepelko et al., 1980; Green et al., 1983; Bowden, 1987). These findings were surprising because these dusts showed very little toxicity in previous studies via oral and dermal exposure. Because of the latter, they were initially described as poorly-soluble particles of low inherent toxicity (ACGIH, 2000; Oberdorster, 2002). However, observations of pulmonary inflammatory reactions and eventual lung tumor formation in rats (Heinrich et al., 1995; Muhle et al., 1995) challenged the assumption of the low toxicity of these particles.

Early examinations of inhalation toxicity studies suggested that following excessive engulfment of particulate matter, AMs seemed to gradually lose their mobility until they ultimately became immobile. Consequently, pulmonary clearance of particles gradually ceased, a phenomenon described as lung particle overload (Morrow, 1988). Importantly, the proposed overload mechanism is unspecific and applicable to poorly-soluble particles in general. Indeed, the lung overload concept seems to apply for a subset of microscale particles and NPs regarding pulmonary clearance (Oberdörster et al., 1994a; Keller et al., 2014; Borm et al., 2015). However, it does not explain observed differences in inflammatory potency, quality of inflammation, and long-term histopathological outcome (such as fibrosis or tumor formation) of different biopersistent NPs (as described in detail in section 1.3). Upon short-term exposure, many poorly-soluble NPs elicited acute pulmonary inflammation in rat lungs (Shvedova et al., 2008; Ma-Hock et al., 2009b; Keller et al., 2014; Morimoto et al., 2015). But sub-chronic (90-days) and long-term inhalation toxicity studies published till now revealed distinct differences in morphological changes of rat lungs caused by different NPs (Bermudez et al., 2004; Ma-Hock et al., 2009b; Schwotzer et al., 2017). With prolonged exposure effects may differ considerably. Pathological changes may persist or progress to fibrosis, or possibly lead to lung tumor formation (Heinrich et al., 1995; Muhle et al., 1995; Kasai et al., 2016; Ma-Hock et al., 2017).

Hence, attempts were made to refine Morrow's overload concept to explain why NPs caused more severe pulmonary effects than their microscale counterparts (Oberdörster et al., 1992a; Pauluhn, 2009a). Pauluhn hypothesized that the tendency of NPs to form agglomerates results in an increased "void-space volume" of the composite compared to solid particles, which in turn increases the displaced volume inside AM cells (Pauluhn, 2009a, 2011). Further, he stated that the increased particle displacement volume together with a lung overload concept most appropriately explain the biological effects of NPs (Pauluhn, 2012, 2014). Other investigators found that the deposited surface area of NPs seems to be the dose metric best correlating with the NP's biological effects (Oberdörster et al., 1992a; Oberdörster et al., 1994b; Lison et al., 1997; Tran et al., 2000; Brown et al., 2001; Duffin et al., 2002; Braakhuis et al., 2016). Because of the versatility of NPs, it remains questionable whether one generic dose metric will be identified as the solely appropriate metric, which will correlate with all NP induced, biological effects observed (Bevan et al., 2018).

Up to now, none of the postulated assumptions alone sufficiently explains all observed differences in the quality of effects elicited by different NPs. For instance, short-term inhalation exposure to Titanium dioxide (TiO_2) (5 day exposure) or Cerium dioxide (CeO_2) NPs (5 or 28 day exposure) caused an inflammatory response composed of polymorphonuclear neutrophils and AMs (Ma-Hock et al., 2009a; van Ravenzwaay et al., 2009; Keller et al., 2014). For TiO_2, effects regressed after an exposure-free period of 14 days. For CeO_2, however, the effects, as shown in a 28-day inhalation toxicity study, progressed to granulomatous inflammation after an exposure-free period of four weeks. In contrast, short-term as well as sub-chronic inhalation exposure to mwCNT provoked a multifocal granulomatous inflammation mainly composed of AMs immediately following exposure (Ma-Hock et al., 2009b). The effect was not reversible during a 24-day post-exposure period. Furthermore, a comparative study of the toxicological effects of TiO_2 NPs, TiO_2 microscale particles and Quartz microscale particles revealed that Quartz exerted the strongest toxicological effects, although the deposited surface area was considerably smaller than the one of the TiO_2 nano-/microparticles. This suggests a crucial role of a particle's composition for its toxicity (van Ravenzwaay et al., 2009). However, it was recognized that no single NP characteristic but characteristics such as chemical composition, size, shape, surface reactivity, surface structure, solubility, and aggregate formation together contribute to the mechanisms by which NPs interact with their local environment and provoke their specific biological effects (Nel et al., 2006; Donaldson et al., 2010a). Only considering the entirety of the physicochemical properties of a NP together with the conditions of the biological system in question will allow for the understanding of the toxic effects of NPs.

Although the term 'nanotoxicology' is frequently used in the literature (Donaldson et al., 2004; Oberdörster et al., 2005; Missaoui et al., 2018), there is no exclusive 'nanotoxicity' which might apply generally for NPs but not for their bulk counterparts (Donaldson and Poland, 2013;

ECETOC, 2013). Although toxicological properties of materials at nanoscale might differ from those of materials at microscale, they are not “nano-specific”, but resemble observations made already several decades ago in inhalation studies of e.g. ultrafine dusts, such as diesel soot or carbon black (McClellan et al., 1985; Mauderly et al., 1987; Heinrich et al., 1995; Nikula, 2000; Donaldson and Poland, 2013; Gebel et al., 2014; Stone et al., 2017).

In general, particle toxicity results from the material’s biokinetics (including the retained dose and it’s biopersistence) together with its physicochemical properties (such as surface reactivity) and the subsequent cellular effects. Importantly, AMs play a central role in integrating pulmonary clearance of particulates and pulmonary immunological reactions. Attracted by deposited particulate matter, AMs migrate to the deposition site and clear any material, e.g. NPs, from the alveolar surface by phagocytosis. The uptake of particulate matter by AMs, followed by their translocation to the mucociliary escalator, is the main clearance mechanism of the alveolar region (physical clearance). Moreover, on the inside of the phagolysosome, NPs might be subjected to degradation, such as biodissolution (chemical clearance). Consequently, AMs contribute through physical and chemical clearance processes to the biopersistence of NPs and ultimately to the pulmonary dose retained. NPs, in turn, might influence AMs or exert damage to the macrophage cell. During the described processes, beginning with phagocytosis and continuing with biochemical processes in the phagolysosomal compartment, NPs might activate the AM, which is followed by differentiation of the immune cell (Lucarelli et al., 2004). Or NPs might induce cellular injury, which triggers cellular stress responses (Fritsch-Decker et al., 2018). When exerting their immunological effector functions, activated AMs secrete various cytokines, reactive oxygen species, and reactive nitrogen intermediates triggering a pro-inflammatory reaction (Fels and Cohn, 1986; Hussell and Bell, 2014). Any modulating effect of the phagocytosed material on AM function can have an effect on the initiation and the course of the immunological response (Laskin, 2009; Alessandrini et al., 2017). Since AMs are chiefly involved in both the biokinetics and the (consequent) biological effects of inhaled NPs, the role of AMs on these two parameters is object of the present dissertation project.

1.2 Pulmonary biokinetics of inhaled, poorly-soluble nanoparticles

Upon inhalation, particle deposition in the respiratory tract occurs mainly by impaction, sedimentation, and diffusion. In general, air borne particulate matter with particle size smaller than 4 µm reach the alveolar region (ICRP, 1994). For particles greater than 1 µm, deposition in the respiratory tract is predominantly determined by inertial impaction on the walls (in rats) or bifurcations (in humans) of the airways (Brain and Valberg, 1979; Hofmann et al., 1996). For particles at nano-scale, deposition in the respiratory tract is not determined by aerodynamic characteristics but by Brownian diffusion, because sufficiently strong drag forces are absent. The random motion enables the deposition of NPs onto the surfaces of the entire respiratory system (Heyder, 1982; Heyder et al., 1986). However, mathematical modelling of particle deposition in the human respiratory tract demonstrates that deposition varies dependent on particle size. In the human respiratory tract, 20 nm NPs are deposited about 50% in the alveolar region, whereas in the nasopharyngeal and tracheobronchial regions about 15% of the inhaled particles deposit. In contrast, 1 nm NPs have their highest deposition in the nasopharyngeal region, where 90% of inhaled particles deposit. Only 10% of inhaled 1 nm NPs deposit in the tracheobronchial region and almost none deposit in the alveolar compartment (ICRP, 1994). Importantly, characterization of test atmospheres of inhalation studies revealed that NP aerosols consist mainly of NP agglomerates in the micrometer range and primary particles constitute only a minor fraction of the aerosol (Ma-Hock et al., 2007; Pauluhn, 2009b; van Ravenzwaay et al., 2009; Keller et al., 2014). These agglomerates behave like particles in the micrometer range in terms of aerodynamics and deposition (Pauluhn, 2009b; Morfeld et al., 2012). Examinations of histological lung sections of rats indicate that the NP agglomerates remain associated and that they do not disintegrate into their primary particles in the biological surrounding (Ma-Hock et al., 2009a; van Ravenzwaay et al., 2009; Creutzenberg et al., 2012a; Levy et al., 2012). Notably, the state of agglomeration or deagglomeration is relevant e.g. regarding particle clearance by AMs (Geiser, 2010) or translocation of NPs to secondary organs (Kermanizadeh et al., 2015). For instance, inhaled gold, iridium, and TiO_2 NPs were shown to be less efficiently phagocytized by rat AMs than their bulk counterparts (Takenaka et al., 2006; Semmler-Behnke et al., 2007; Geiser et al., 2008; Geiser, 2010). Biodistribution studies using gold NPs revealed size-dependent translocation of NPs to secondary organs following inhalation exposure of rats. When applied at similar aerosol concentrations (about 13 to 14 µg/m³) for 5 days, 13 nm-sized gold NPs translocated from lungs to liver, spleen, brain, testes, and blood, whereas 105 nm-sized gold NPs were detected only in blood. The authors concluded that the smaller gold NPs translocate at a faster rate than their larger counterparts (Han et al., 2015). In another rat inhalation study, animals were exposed for 15 days to gold NP aerosols with similar size distribution of NP agglomerates (45 nm) and particle number concentration (1×10^6 particles/cm³). Notably, the NP agglomerates were comprised of NPs

with different primary particle sizes, i.e. 7 nm and 20 nm. Size-related translocation, with the 7 nm NPs translocating more than the 20 nm NPs, from lungs to brain, aorta, esophagus, and kidneys was observed. These observations indicate translocation of NPs being size-dependent and suggest, in contrast to previous observations, disintegration of the 45 nm agglomerates in lungs (Balasubramanian et al., 2013). Importantly, translocation of poorly-soluble NPs to secondary organs is very low upon inhalation exposure (Kermanizadeh et al., 2015). There are several parameters, which influence the agglomeration status of NPs in inhalation studies, i.e. aerosol generation technique, aerosol concentration, and dispersion efficiency. These parameters primarily determine the deposition efficiency, site of deposition, and subsequent biokinetic fate of NPs (Laux et al., 2017).

Once deposited in the lower respiratory tract, NPs are subjected to various clearance mechanisms, which all aim at disposing of particulate matter from the lungs (**Box 2**). Importantly, it is not the initially deposited dose that is causal for the biological effects of NPs. The decisive parameter relevant for the dose-effect relationship is the retained dose (Oberdörster et al., 1994a). Retention describes a quantitative characteristic (measurable as organ burden [mg test material/ organ]) (Oberdörster et al., 1992b) and is thus a dosimetric parameter. The retained dose equals the amount of deposited material less the amount of cleared material at a certain timepoint. Hence, the eventually retained dose differs from the initially deposited dose over time. Importantly, it is the retained dose, which results in specific biological effects. Because different NPs become cleared at varying rates from the lungs, the in-depth knowledge of the clearance mechanisms (chemical, physical) most relevant for the material in question will enable the understanding of its behavior *in vivo.* Oberdörster et al. (1992b) suggested to describe this *in vivo* behavior with ‘biopersistence’. In contrast to retention, biopersistence describes a qualitative characteristic observable e.g. in histological tissue sections. Both, physical (translocation) and chemical (biodissolution) clearance processes contribute to the biopersistence of particulate matter in the lungs (Mercer, 1967).

In animal inhalation studies, lung burdens are frequently assessed at the end of exposure and subsequently to an exposure-free period. These quantitative data provide information about the retention of the test material. Using the information on lung burdens at different times, clearance kinetics can be calculated and presented as retention half-times. Knowledge of clearance rates is especially relevant to determine whether AM clearance capacity is overwhelmed resulting in volumetric particle overload (Morrow, 1988). In rats, the pulmonary retention half-time of poorly-soluble particles is about 70 days (Oberdörster, 1988; Bailey et al., 1989). Considerably greater half-times are an indication of lung (or rather macrophage) particle overload. Under overload conditions, when particle clearance by AMs is overwhelmed, NP contact with alveolar epithelial cells is prolonged. With this, the probability of NP uptake by epithelial cells, translocation of NPs through the air-blood-barrier, and NP

induced cell damage, which can trigger or amplify pro-inflammatory immune reactions, is increased (Elder and Oberdörster, 2006; Geiser and Kreyling, 2010). For example, inhalation exposure of rats to 0.5 mg/m³ CeO_2 NPs for 28 days resulted in an organ burden of 41 µg/lung one day after the end of exposure and 9 µg/lung 129 days after the end of exposure. The calculated clearance half-time was 40 days and rats showed minimal signs of pulmonary inflammation. Increasing aerosol concentration to 5 or 25 mg/m³ CeO_2 resulted in organ burdens of 520 µg/lung or 2620 µg/lung one day post-exposure, respectively, and 1800 µg/lung 129 days post-exposure in the 25 mg/m³ exposure group. Clearance half-times in the high dose group accounted for more than 200 days, suggesting lung overload conditions. Analysis of bronchoalveolar lavage fluid and histological examinations revealed a pronounced inflammatory reaction in rat lungs (Keller et al., 2014).

Thus, understanding pulmonary retention kinetics of inhaled NPs is an essential element of establishing dose-response relationship and identifying overload conditions.

Box 2 Pulmonary clearance mechanisms

The clearance mechanism, how particles are removed from the respiratory tract, depends on the region where they are deposited (nasopharyngeal, tracheobronchial or alveolar). In addition, particle removal can include chemical clearance, i.e. dissolution and absorption, or physical clearance, i.e. uptake by alveolar macrophages (AMs) and transport distal to the lungs. The latter is the most prevalent for poorly-soluble particulate matter in the lower respiratory tract.

Conducting airways

- The main clearance mechanism of particulate matter from the tracheobronchial tree is the mucociliary escalator. Ciliated cells of the epithelium of the trachea and the bronchi continuously propel the mucus layer, together with all trapped particulate matter, towards the pharynx. From here, the excretion via the gastrointestinal tract continues.
- Water-soluble substances readily dissolve in the mucus layer of the nasopharynx and tracheobronchial tree.

Alveolar region

- The main clearance mechanism of poorly soluble particles from the alveolar surface is the phagocytosis of particulate matter by AMs. AMs rapidly engulf any particulate matter, e.g. NPs, from the alveolar surface. Subsequently, AMs can migrate toward the bronchioli and bronchi, where they are transported via the mucociliary escalator to the pharynx. Alternatively, AMs can also migrate to the local lung-draining lymph nodes. Besides this physical clearance, AMs are also involved in chemical clearance (degradation of the incorporated material).
- NPs can be internalized to some extend by alveolar epithelial cells (Geiser et al., 2005).
- NPs can translocate through the alveolar epithelium into the interstitium (Ferin et al., 1992). Interstitial translocation occurs to a greater extend in primates and dogs than in rodents (Nikula et al., 1997; Oberdörster et al., 2005).
- NPs can enter the lymphatic network, for instance through crossing open intercellular junctions between endothelial cells (Lauweryns and Baert, 1977), and can accumulate in draining lymph nodes.
- NPs can translocate through the air-blood barrier into the blood stream, which renders them systemically available. NPs were found in liver, spleen, kidneys, heart, brain, reproductive organs, skeleton, and connective tissue after inhalation exposure (Oberdörster et al., 2002; Geiser et al., 2005; Geiser, 2010). However, systemic translocation of NPs subsequent to inhalation exposure occurs only at very low levels (Kreyling et al., 2002).

1.2.1 Theoretical considerations of biodissolution and transformation

NPs are produced on purpose with specific size, shape, composition and with or without surface functionalization. The by now available toxicological data suggest that it is not possible to link one single material characteristic to the behavior of a NP *in vivo.* Rather the sum of several material's characteristics affects its biokinetics and subsequent biological effects (Donaldson and Poland, 2013; Godwin et al., 2015; Landsiedel et al., 2017). The particle size and shape together with the surface chemistry (affecting e.g. surface charge) determine the agglomeration tendency, the hydrophobicity and importantly the protein binding capability of a NP. All physicochemical properties together distinctly influence the biokinetics of NPs (Landsiedel et al., 2012). In addition, the biokinetics of NPs are highly dependent on the conditions of the biological system (cell, tissue, organ) under investigation (Opanasopit et al., 2002; Nagayama et al., 2007; Aggarwal et al., 2009; Tenzer et al., 2013; Docter et al., 2015). Thus, intrinsic physicochemical material properties as well as system-dependent properties in the given biological system under investigation, should be considered together when assessing the potential hazards of NPs. Proposed frameworks for the testing and grouping of NPs take this into account (Arts et al., 2015; Collier et al., 2015; Oomen et al., 2015).

One parameter increasingly recognized as a fundamental parameter influencing inhalation toxicity of NPs is the material dissolution rate *in vivo* (Graham et al., 2017b), which should not be confused with the water solubility measured under static conditions (**Box 3**). Whereas first grouping strategies suggested water solubility as a grouping criterion, meanwhile it was recognized that the dissolution observed *in vivo*, the biodissolution, often differs from the water solubility measured in abiotic, static systems (Arts et al., 2015; Oberdörster and Kuhlbusch, 2018). Therefore, the rate of dissolution under simulated physiological conditions became one fundamental criterion to assess similarity between NPs in latest grouping frameworks (Gray et al., 2018; Oomen et al., 2018).

One factor responsible for the observed difference between water solubility and biodissolution is the contribution of AMs to chemical particle clearance *in vivo* (**Box 2**). Once NP agglomerates deposited in the alveolar region are phagocytized by AMs, the formed phagosome, containing the internalized cargo, fuses with lysosomes, containing various hydrolytic enzymes. Notably, the maturation of the phagolysosome is accompanied with its continuous acidification. When these intracellular organelles are fully mature, lysosomes harbor a milieu of pH 4.5. This condition might be decisive in the scope of chemical clearance, as particle dissolution can be influenced by varying pH. For instance, strontium carbonate ($SrCO_3$) has a very low water solubility but is readily soluble under acidic conditions. Similarly, the solubility of zinc oxide (ZnO) is known to be pH-dependent. At the end of a 90-day inhalation exposure period to ZnO NPs only 2 % of the deposited material were detectable

Box 3 Definitions for static solubility, non-equilibrium dissolution rate, biodissolution, and biotransformation (taken and modified from (Koltermann-Jülly et al., 2018)).

• Solubility	is measured in equilibrium saturated suspensions, with appropriate descriptor of mg/L ion, identical with the conventional solubility limit. Implicitly, it often means solubility in water at neutral pH and was proposed as a first screening method for soluble NPs (Arts et al., 2015), to be refined to the solubility in relevant medium as subsequent method (Arts et al., 2015; Avramescu et al., 2017). Plakhova et al. demonstrated that "% dissolved" is not an equivalent metric, and probably not appropriate (Plakhova et al., 2016).
• Dissolution rate	is measured at out-of-equilibrium conditions and below the saturation in the relevant medium, with appropriate descriptors in units of ion mass per solid mass per time (=%/h) or ion mass per solid particle surface per time (=ng/cm^2/h). It is considered an extrinsic property.
• Biodissolution	describes the chemical clearance process of ion liberation from a deposited solid in a given biological environment at the respective physiological conditions. Because of the continuous perfusion of organs, biodissolution describes rather a dynamic process out of equilibrium, although local (super)saturation conditions in certain microenvironments are possible.
• Biotransformation	describes the propensity of the non-dissolved remaining solids to "change what they are" in the relevant medium, regarding their physical shape, or size, chemical identity or crystallinity, and has no clearly defined descriptors. It is also considered as extrinsic property and has implications for hazard assessment, e.g. if the aspect ratio or crystalline phase changes.

in lungs, suggesting high biodissolution, although ZnO is poorly soluble in water (Creutzenberg et al., 2012b). No increased ZnO levels were found in other organs.

Another factor responsible for the difference between water solubility and dissolution rate *in vivo* is the different dynamics of the two systems under investigation. Water solubility is measured under static conditions, which allow for saturation of the receptor medium (water) and reaching equilibrium. After a while, a solubility limit is reached in the static system. Because the lungs are embedded in a dynamic system, continuously perfused with blood, pulmonary biodissolution is a dynamic process out of equilibrium. Further, the biodissolution

process is a gradual, time-dependent process. It reduces particle size, which in turn influences the dissolution kinetics (Pauluhn, 2014). Thus, using solubility as a surrogate for dissolution rate may underestimate the biodissolution.

An outstanding example of pulmonary biokinetics is the case of Barium sulfate ($BaSO_4$). $BaSO_4$ has a very low water solubility and is frequently used as a harmless radiocontrast agent for medical diagnostic purposes. In the past, $BaSO_4$ as bulk form was described as an inert dust (Einbrodt et al., 1972). Recent studies in rats, investigating $BaSO_4$ NPs, revealed that intratracheally instilled $^{131}BaSO_4$ had a pulmonary retention half-time of 9.6 days, which is around seven times faster than clearance via AMs and the mucociliary escalator. Histopathological analysis of exposed animals did not reveal any sign of pulmonary toxicity. Further, the instilled ^{131}Ba was found incorporated into bones and bone marrow of experimental animals (Konduru et al., 2014). Similarly, a 90-day inhalation study, exposing rats to a high aerosol concentration of 50 mg/m³ $BaSO_4$, revealed a pulmonary retention half-time of 56 days and no signs of lung overload and only slight pulmonary inflammation (Schwotzer et al., 2017). However, during a two-year rat inhalation study with 50 mg/m^3 $BaSO_4$ an increase of retained Ba in the lungs during the first year of exposure, subsequently reaching a steady-state during the second year of the study, was observed. Ba retention was accompanied by pulmonary inflammation (Ma-Hock et al., 2017). In addition, substantial Ba accumulation in bone and bone marrow was repeatedly observed after inhalation exposure to $BaSO_4$ (Konduru et al., 2014; Ma-Hock et al., 2017; Schwotzer et al., 2017). Notably, the applied analytical methods measured elemental Ba and did not differentiate ionic Ba^{2+} and particulate $BaSO_4$. When investigating the biokinetics of inhaled NPs, it has to be critically evaluated whether the element detected in secondary organs arrived there in the original particulate form or if biodissolution preceded the subsequent translocation of ions.

For NPs that undergo biodissolution, clearance mechanisms might be influenced due to binding to proteins or other biomolecules, or due to chemical or structural biotransformation. These bioprocessing events were found to be organ-specific and can prolong retention and modulate the overall biopersistence and eventually the biological effects of NPs (Graham et al., 2017a; Graham et al., 2017b; Graham et al., 2018; Oberdörster and Kuhlbusch, 2018). Biotransformation means physicochemical modifications of the parent solid during biodissolution, for example changes of particle size, particle shape, recrystallization, (re-)speciation (changing the chemical composition), and reprecipitation. Biotransformation in the form of recrystallization and respeciation was observed for zero-valent Ag- or Cu-particles in environmental media (Adeleye et al., 2014; Dale et al., 2015; Vencalek et al., 2016; Mitrano and Nowack, 2017; Gao and Lowry, 2018). Biotransformation in the form of reprecipitation was observed for amorphous SiO_2 NPs and CeO_2 NPs in the pulmonary microenvironment (Graham et al., 2017b). Cerium, for instance, forms secondary NPs via reprecipitation, i.e.

cerium phosphate particles, under lysosomal conditions (Berry et al., 1988; Li et al., 2014). Thus, biotransformation of NPs influences their biological effects and final toxicity.

1.2.2 Methodological considerations of biodissolution and biotransformation

It is more and more recognized that dissolution rates of poorly-soluble NPs might differ to a great extend from their determined water solubility and between different materials (Collier et al., 2015; Oberdörster and Kuhlbusch, 2018; Oomen et al., 2018). Oberdörster and Kuhlbusch (2018) realized that it might be too simplistic to group NPs just into groups of soluble and poorly-soluble materials. In addition, quantitative thresholds are still missing in most grouping frameworks for the testing of NPs proposed till now, as well as standardized (*in vitro*) methods, which are applicable to NPs (Steinhäuser and Sayre, 2017). Suitable methods should be specific, realistic and relevant to the assessment of pulmonary biodissolution of NPs. In addition, the ideal method will enable the evaluation of structural biotransformation of the remaining solid. However, establishing a standardized method representing biodissolution in the lungs is challenging, because the lungs have unique features that are difficult to replicate *in vitro* or in abiotic systems. For instance, lining and interstitial fluids are pH-balanced, complex mixtures of salts, lipids, serum proteins, and other biomolecules and it is not only difficult to simulate the composition but also the extremely small amount of lining fluid e.g. in the alveolar region, i.e. the thin layer of surfactant (Marques et al., 2011). Hence, simulated biological fluids need to be sufficiently complex to simulate oxidative, reductive and pH-driven dissolution pathways. For the purpose of simulating physiological conditions, several lung simulating fluids have been developed, such as Gamble's solution with pH 7.4, which simulates the interstitial fluid deep within the lungs (Colombo et al., 2008; Marques et al., 2011). Considering the main clearance mechanism of particulate matter from the alveolar surface, i.e. the phagocytosis by AMs, simulated biological fluids which mimic the acidic phagolysosomal conditions inside the cell are most appropriate for the assessment of pulmonary biodissolution. Therefore, media with pH 4.5, such as artificial lysosomal fluid or phagolysosomal simulant fluid (PSF) were developed (Stefaniak et al., 2005; Marques et al., 2011). Simulated biological fluids are expected to be a more potent tool in estimating the biodissolution and *in vivo* behavior of NPs.

Because the lungs are continuously and strongly perfused, grouping of NPs by static solubility values has been questioned (Klaessig, 2018). Dynamic systems may be better suited for evaluating the non-equilibrium biodissolution of deposited particles in the lungs, where ions that are liberated from the deposited particle's surface are continuously removed. To measure physiologically relevant dissolution rates, dynamic systems consisting of flow cells were used

to mimic the non-equilibrium physiological conditions of the lungs (Christensen et al., 1994; Nti, 2017). Different flow cells have been used to simulate biodissolution in the gastrointestinal tract (Bove et al., 2017). For mineral fibers, flow-through cell dissolution rates were found to correlate strongly with *in vivo* pulmonary clearance kinetics (Christensen et al., 1994; Guldberg et al., 1995). In flow-through cells, the material under investigation is trapped between two membranes with a pore size that excludes the translocation of the solid. Liberated ions pass through the membrane and are constantly removed from the system, following a flow, which is generated using a peristaltic pump. Thus, non-equilibrium conditions are achieved by flow-through dialysis. The dialysate is collected in discrete volumes and the target analyte can be quantified. Importantly, for NPs, appropriate separation membranes with sufficiently small pore sizes are required (Stefaniak et al., 2005).

In addition to biodissolution, dynamic systems are suitable to assess organ-specific transformation of the remaining solid under investigation when using an appropriate simulated biological fluid (Pompa et al., 2015; Bove et al., 2017; Graham et al., 2018). Subsequent to sample collection for dissolution analysis, remaining solid can be imaged through transmission electron microscopy (TEM) to investigate potential structural transformation processes (Graham et al., 2018).

Still, abiotic dissolution testing, mimicking physiological conditions, remains a simplistic approximation of the *in vivo* situation. The macrophage-assisted chemical clearance of pH-sensitive NPs might be underestimated (Kass, 1964; Geiser, 2010). To date, a vast amount of *in vitro* studies is being published investigating the cellular effects of NPs on pulmonary cells (Kroll et al., 2011; Nel et al., 2013; Vennemann et al., 2017; Wiemann et al., 2018). However, whether macrophage-based *in vitro* assays are applicable to assess the biokinetics of NPs needs further validation (Oberdörster and Kuhlbusch, 2018). The rat AM cell line NR8383 proved to be a suitable tool in the hazard assessment of NPs (Pulskamp et al., 2007; Wagner et al., 2007; Lison et al., 2008; Eidi et al., 2010; Scherbart et al., 2011; Bhattacharjee et al., 2012). The *in vitro* potency screening of NPs using NR8383 cells correlated well with results of short-term inhalation studies (STIS) regarding NP's inflammogenicity (Wiemann et al., 2016). Moreover, these cells, like other macrophages *in vivo*, are capable of producing reactive oxygen species such as H_2O_2 (Wiemann et al., 2016), which may contribute to bioprocessing of NPs. Hence, this dissertation project investigated whether biodissolution of NPs can be assessed *in vitro* by NR8383 AMs.

1.3 Pulmonary effects of inhaled, poorly-soluble nanoparticles

Data derived from early human epidemiological studies and rat inhalation studies, revealed that poorly-soluble granular dust caused pronounced pulmonary toxicity, in form of lung inflammation, although these materials caused very low toxicity in oral and dermal studies (Davis et al., 1978; Pepelko et al., 1980; Green et al., 1983; Bowden, 1987). Upon chronic exposure to granular dust, histopathological effects were reported to progress to fibrotic alterations of lung tissue and, in rats, chronic inflammation was repeatedly associated with lung tumor formation (Heinrich et al., 1995; Muhle et al., 1995). Similarly, *in vivo* studies in rodents indicated a hazard of inhaled, poorly-soluble NPs to cause pulmonary inflammation at sufficient dose. Prolonged exposure to NPs also seemed to facilitate potential progression of effects to fibrosis and/or lung tumor formation (Heinrich et al., 1995; Kasai et al., 2016; Landsiedel et al., 2017). Common observations made during long-term inhalation studies in rats, which investigated high aerosol concentrations of granular dusts, were ceasing particle clearance from the lungs and increasing lung burdens. To explain these observations, the lung particle overload concept, which is based on the overpowering of AM based particle clearance, was proposed (Morrow, 1988) (see section 1.1). Pulmonary clearance of deposited particulate matter begins to decrease when AM volume is increased by 6%, and it further decreases with more particles occupying increasing cellular volume as a result of excessive phagocytosis (Morrow, 1988). The overload concept for pulmonary particle clearance was described for micro-sized particles but seems to apply to biopersistent NPs and nanoparticle agglomerates, as well (Oberdörster et al., 1994a; Keller et al., 2014; Borm et al., 2015). Notably, the lung particle overload concept does not take the inherent toxicity of the investigated material into account (Morrow, 1988). Observed differences in inflammatory potency, quality of inflammation, and long-term histopathological outcome of different poorly-soluble NPs suggest, however, that this aspect should be considered.

Pulmonary exposure to biopersistent NPs at sufficient dose results in an inflammatory response of the lungs (Shvedova et al., 2008; Ma-Hock et al., 2009b; Keller et al., 2014; Morimoto et al., 2015). Notably, **intratracheal instillation and short-term inhalation studies** (STIS) indicate differences in early biological effects of poorly-soluble NPs (Takebayashi et al., 2019). STIS (5 day exposure) proved to be a valuable tool in the identification of hazard and potency (Ma-Hock et al., 2009a; Klein et al., 2012), prioritization (Landsiedel et al., 2008; Landsiedel et al., 2014), and grouping (Arts et al., 2015) of inhaled NPs. Cho et al. intratracheally instilled different metal oxide NPs (TiO_2, CeO_2, SiO_2, NiO, ZnO and CuO), carbon black, and amine-modified polystyrene beads to rat lungs. The doses were adjusted to the same surface area applied per animal (cm^2 NP/rat). 24 hours and four weeks post exposure they found that only CeO_2, NiO, ZnO and CuO elicited an inflammatory response and that the

reaction differed in types of infiltrating cells, inflammatory mediators, time course, and cytotoxicity. Distinct patterns of neutrophilic, lymphocytic, and/ or eosinophilic infiltrations, and for some materials, fibrotic changes of lung tissue or granulomatous inflammation were observed (Cho et al., 2010). Similarly, pulmonary toxicity of biopersistent NPs assessed by means of STIS differed from each other (Landsiedel et al., 2014). The inhalation exposure to 100 mg/m³ TiO_2 caused a pronounced inflammatory response as evidenced by highly increased parameters in BALF (e.g. dramatic increase in neutrophil cell counts, minimal increase in lymphocytes and monocytes). Histological lung sections of exposed animals revealed a minimal neutrophilic infiltration and minimal to moderate histiocytosis. The inflammation declined 14 days post-exposure. Lung burdens accounted 2.02 mg/lung at the end of exposure and 1.55 mg/lung two weeks post-exposure (van Ravenzwaay et al., 2009). Exposure to aerosol concentrations of 25 mg/m³ CeO_2 resulted in strong pulmonary inflammation based on highly increased parameters in BALF (e.g. pronounced increase in neutrophil, as well as increase of lymphocyte, eosinophil and monocyte cell counts), and minimal histiocytosis in lung tissue. 21 days post exposure BALF parameters partly regressed but inflammation persisted, as evidenced by histiocytosis in histological lung sections. Lung burdens were 0.53 mg/lung and 0.4 mg/lung one day and three weeks post-exposure, respectively. Notably, inflammation caused by 25 mg/m³ CeO_2 dust aerosol concentration, changed to granulomatous inflammation following 28-days exposure plus 34 days post-exposure. One day after the end of exposure lung burden accounted for 2.62 mg/lung and decreased to 1.8 mg/lung 129 days post-exposure. The calculated clearance half-time was more than 200 days, suggesting lung overload conditions (Keller et al., 2014). Short-term inhalation exposure to 32 mg/m³ mwCNT lead to granulomatous type of inflammation with minimal to mild histiocytosis in lungs of exposed animals immediately following exposure. In BALF, lymphocyte and neutrophil cell numbers were increased, demonstrating pulmonary inflammation. Histopathological findings were not reversible and granulomatous inflammation persisted during a 21-day post-exposure period (Ma-Hock et al., 2009b). In comparison, 100 mg/m³ non-nano quartz lead to a very strong inflammatory response with minimal to moderate histiocytosis in lungs of exposed animals one day post-exposure. BALF analysis resulted, similar to TiO_2, in increased neutrophil and slightly increased lymphocyte and monocyte numbers, but to a much greater extend when compared to TiO_2 NPs. 14 days post-exposure inflammatory parameters were not de- but increased and histological findings of a diffuse inflammatory response, composed of AMs, neutrophils and cell debris, progressed and increased in severity. Measured lung burden was 2.19 mg/lung and 1.76 mg/lung one day or two weeks post-exposure, respectively. The calculated clearance half-time of 92 days indicated slight lung overload conditions (van Ravenzwaay et al., 2009).

These differences in inflammatory potency of the investigated NPs became even more pronounced in **sub-chronic (90-day) inhalation studies** (Bermudez et al., 2004; Ma-Hock et al., 2009b; Schwotzer et al., 2017). Sub-chronic inhalation exposure to an aerosol concentration of 2 mg/m³ TiO_2 caused minimal to mild lesions comprised of particle-laden macrophage accumulations, aggregations in sub-pleural and in centriacinar regions (Bermudez et al., 2004). These lesions were associated with minimal hypertrophy and hyperplasia of alveolar type II cells. At 10 mg/m³ more severe epithelial proliferative changes were observed. However, most of these lesions regressed during a post-exposure period of 13 to 52 weeks. In comparison, sub-acute (28-day) and sub-chronic exposure to CeO_2 elicited pulmonary inflammation at very low dust aerosol concentrations down to 0.1 mg/m³. Notably, inflammatory findings changed to granulomatous type of inflammation and persisted with time post exposure (13 weeks) (Keller et al., 2014; Schwotzer et al., 2017). CeO_2 lung burdens were measured at termination of the 90-day exposure period and subsequent to a 90-day exposure free period and amounted to 1.3 mg/lung and 1.0 mg/lung, respectively. Under these overload conditions the clearance half-time was calculated to be 224 days (Schwotzer et al., 2017). Furthermore, biopersistent, high aspect ratio nanomaterials, such as mwCNT, showed very high inflammogenic potential following inhalation exposure (Ma-Hock et al., 2009b; Landsiedel et al., 2010). Sub-chronic exposure to 0.1, 0.5, or 2.5 mg/m³ mwCNT caused dose-dependently granulomatous inflammation, even at the lowest aerosol concentration. The granulomatous inflammation was composed of AMs and neutrophils and was located in the centriacinar region. In addition, intraseptal granuloma formation was observed. Deposition estimates of 1.2 mg deposited material/lung suggest that the highest dose tested caused pulmonary particle overload (Ma-Hock et al., 2009b). In another sub-chronic inhalation toxicity study, exposure of rats to 5 mg/m³ mwCNT, resulted in persistent pulmonary inflammation. Alveolar granulocytic infiltration, interstitial inflammation, and focal alveolar septal fibrosis were observed one year post-exposure (Pothmann et al., 2015; Régnier et al., 2017). High aerosol concentration of 60 mg/m³ non-nano quartz for 90 days lead i.a. to granuloma formation, histiocytosis, cellular debris, alveolar lipoproteinosis, increased septal cellularity, and focal interstitial fibrosis. Notably, the incidence and severity of these findings progressed during the course of the post-exposure period (52 weeks) (Reuzel et al., 1991). A second 90-day inhalation toxicity study exposing rats to 3 mg/m³ quartz found increased inflammatory parameters in BALF and increased numbers of neutrophils, histiocytosis, greatly thickened alveolar septa, and progressive inflammation in histological lung sections subsequently to exposure and at the end of the post-exposure period (32 weeks) (Johnston et al., 2000).

Finally, **long-term inhalation studies** uncovered distinct differences in long-term biological effects of these NPs. Inhalation exposure of rats for two years to 5 mg/m³ TiO_2 (Bayertitan T, rutile) resulted in slight fibrosis but no increased tumor incidence. The lung

burden was 2.7 mg/ lung, whereas the lung clearance was not determined (Muhle et al., 1995). Aerosol concentration of (on average) 10 mg/m³ TiO_2 NPs for two years, however, caused toxic effects on AMs, retardation of particle lung clearance (clearance half-time 368 days), high lung burden of 40 mg/ lung, bronchoalveolar hyperplasia, interstitial fibrosis, and increased lung tumor rates (Heinrich et al., 1995). A long-term rat inhalation toxicity study was also conducted with CeO_2. Animals were exposed to aerosol concentrations of 0.1, 0.3, 1, or 3 mg/m³ CeO_2. Lung inflammation based on increased BALF parameters, i.a. increased total cell number, neutrophils, eosinophils, lymphocytes, and macrophages, and on histopathological evaluation was observed for all doses tested. Lung burden after two-year exposure to 3 mg/m³ CeO_2 was 5.88 mg/lung. Histopathological evaluation lead i.a. to the diagnosis of interstitial fibrosis (Ma-Hock et al., 2017). During a long-term inhalation toxicity study performed by Kasai et al., rats were exposed for two years to fibrous, straight-type mwCNT (MWNT-7) at aerosol concentrations of 0.02, 0.2, or 2 mg/m³. Concentration-dependent toxic effects in the lungs such as epithelial hyperplasia, granulomatous changes and focal fibrosis of alveolar septa, and alterations in BALF parameters (increased numbers of neutrophils, eosinophils, lymphocytes, and macrophages) were found. Lung burdens accounted for 1.2 mg/ lung in female and 1.8 mg/ lung in male animals. The highest dose tested lead to increased lung tumor rates. In contrast to asbestos fibers, however, no development of pleural mesothelioma was observed (Kasai et al., 2016). A long-term inhalation toxicity study with quartz found that exposing rats to 1 mg/m³ quartz dust results in histological changes comprised of infiltration of neutrophils, multifocal lipoproteinosis, foamy macrophages, fibrosis, and increased lung tumor rates (Muhle et al., 1995). Thus, with prolonged exposure time, effects observed for NPs may persist or progress to fibrosis or possibly lead to lung tumor formation (Heinrich et al., 1995; Muhle et al., 1995; Kasai et al., 2016; Ma-Hock et al., 2017).

The above descriptions indicate that lung overload alone cannot account for the distinct biological effects of different biopersistent NPs. Further, it is now known that a material's hazard is not governed by a single physicochemical determinant but by a range of physicochemical properties of the material (see also section 1.2). Size, shape, chemical composition, surface area, solubility, crystalline structure and surface reactivity are material properties which were shown to impact the toxicity of NPs (Brunner et al., 2006; Duffin et al., 2007; Limbach et al., 2007; Wick et al., 2007; Yang et al., 2009; Landsiedel et al., 2010). Within a given biological microenvironment these material characteristics determine the toxic effects of NPs through different possible cellular mechanisms (Nel et al., 2006; Landsiedel et al., 2010):

- Direct interactions with cellular structures/ intracellular organelles (Yanamala et al., 2013; Lu et al., 2015), catalyzing formation of reactive species (see below), and release of toxic ions (Ivask et al., 2015).

- Potential to generate reactive oxygen species (ROS), either through catalyzing the formation of ROS at the particle's surface or through induction of (intra-)cellular stress, which leads to ROS generation. Either way, excessive amounts of ROS induce further cell damage in the form of lipid, protein and DNA damage (Sayes et al., 2006b; Kroll et al., 2011; Kroll et al., 2013; Sauer et al., 2014; Lu et al., 2015; Lujan and Sayes, 2017).
- Affecting cell viability, induction of cytotoxicity (Sayes et al., 2006a; Sayes et al., 2006b; Sauer et al., 2014; Lu et al., 2015).
- Induction of genotoxicity, primary or secondary (Donaldson et al., 2010b; Oesch and Landsiedel, 2012).
- Affecting gene expression profiles (Chen et al., 2006; Fujita et al., 2009).
- Induction of pro-inflammatory signaling (Sayes et al., 2006b; Schinwald et al., 2012; Xia et al., 2013; Sauer et al., 2014).

Thereby the apical toxic effect can result from a combination of various effects of particles on (different) cells. Due to their inherent surface reactivity, metal oxide NPs are potent inducers of oxidative stress (Limbach et al., 2007; Shvedova et al., 2008; Yang et al., 2009). Their ROS generating capacity is related to induction of DNA damage, inflammation, and cytotoxicity (Sayes et al., 2006b). For instance, although TiO_2 NPs initially were described as poorly soluble and of low toxicity, several studies suggest that TiO_2, might induce cellular oxidative stress, affecting intracellular redox signaling, and ultimately leading to the expression of pro-inflammatory mediators, including pro-inflammatory enzymes such as inducible nitric oxide synthase (iNOS) (Singh et al., 2007; Horie et al., 2010; Scherbart et al., 2011). Instillation experiments, applying 0.5, 5, or 50 mg/kg bw TiO_2 NPs to rats, revealed a dose-dependent induction of nitric oxide secretion by AMs (Liu et al., 2010). Similarly, it was shown that quartz particles are very potent in hydroxyl radical formation, and that AMs exposed to quartz particles suffer oxidative stress (Shi et al., 1988; Polimeni et al., 2008; Ghiazza et al., 2010). Because AMs represent the essential cell type of pulmonary defense and exert complex immunoregulatory functions, knowing the mechanisms induced by NPs at the cellular level will allow to understand the apical toxic effects that result in acute or chronic lung injury.

1.4 Effects of nanoparticles on alveolar macrophage polarization

Obviously, AMs hold a central role in pulmonary particle clearance and pulmonary immune responses (**Box 4**) (Mills et al., 2015). Thus, the inflammogenic potential of NPs in the lungs highly depends on its interactions with and impact on AMs. In general, particle uptake by phagocytes is largely influenced by opsonization of the particle with immunological proteins. For poorly soluble particles, and for some NPs, it was shown that phagocytic uptake is influenced by their physicochemical properties and, associated with this, their protein binding capacity (Kumar et al., 2016a). Depending on size, shape, surface, adsorbed proteins etc. interactions with specific plasma membrane receptors (phagocytic, immunogenic, signal transducing etc.) and uptake mechanisms by which macrophages internalize foreign material can substantially differ, which already influences the intracellular signaling cascade to be initiated (Beningo and Wang, 2002; Champion et al., 2008; Doshi and Mitragotri, 2010; Scherbart et al., 2011). All these early initiating events determine the downstream signaling cascades, including specific transcription factors and the downstream expression of effector molecules and proteins, which might be activated or suppressed (Savill et al., 1992; Platt and Gordon, 1998; Ma et al., 2012). Once internalized, NPs can disturb directly or indirectly intracellular homeostasis, for instance through interacting with or entering into intracellular organelles (Ahlinder et al., 2013) or induction of intracellular (oxidative) stress (generation of ROS), respectively (Asati et al., 2010; Ahamed et al., 2016). Furthermore, ROS can affect numerous intracellular signaling cascades. At low concentrations, ROS act as signaling molecules either directly by interacting with oxidation-sensitive transcription factors, or indirectly by inducing the phosphorylation of central transcription factors such as NF-κB (Asehnoune et al., 2004; Amma et al., 2005). This might further affect gene expression of enzymes for defense, or proteins for pro-inflammatory signaling (Weigert et al., 2018). At high concentrations, ROS damage lipids, proteins and DNA of macrophages and neighboring epithelial cells, ultimately leading to tissue destruction (Grosche et al., 2018; van der Vliet et al., 2018) (see also section 1.3).

Under physiological conditions, AMs handle metabolic tissue homeostasis; but when encountering pathological stimuli, danger signals arising from bacteria, NPs, or surrounding tissue damage, AMs become activated and exert their immunological effector functions, namely antimicrobial and antitumoral activities (Martinez et al., 2008; Wynn et al., 2013). However, their immunological repertoire comprises not only the induction of a pro-inflammatory immune response, but also the orchestration of resolution of inflammation and tissue repair (Laskin et al., 2011; Venosa et al., 2015). Data published during the past three decades suggest that these various activities are mediated by different subpopulations of macrophages, which exert these diverse roles and that their phenotype highly depends on the signals they

encounter in their local tissue microenvironment (de Waal Malefyt et al., 1993; Buttner et al., 1997; Hancock et al., 1998; Porcheray et al., 2005; Anthony et al., 2006; Edwards et al., 2006; Sindrilaru et al., 2011; Lu et al., 2018; Laskin et al., 2019). In a rather simplistic view, these macrophage subpopulations can be divided into two major distinct macrophage phenotypes, which have been categorized broadly as classically activated, pro-inflammatory M1 macrophages and alternatively activated, anti-inflammatory M2 macrophages (Mills, 2012; Gordon et al., 2014; Martinez and Gordon, 2014). As indicated above, the first response to pathogenic signals or toxicants is the release of mediators by activated AMs for eliminating foreign threats; here the cell acquires a M1 phenotype. This macrophage subpopulation is characterized by the expression and secretion of large quantities of pro-inflammatory cytokines (e.g. IL-6, TNFα, IL-1β, IL-8), high production of ROS and reactive nitrogen intermediates, with chemotactic and strong cytotoxic activities, respectively. Later in the immunological process, M2 macrophages appear at the inflamed and/or wounded site and secrete mediators that down-regulate the pro-inflammatory response and promote the resolution of inflammation, tissue remodeling, and wound repair. However, over-activation of M1 or M2 macrophages, characterized by prolonged or excessive release of respective mediators, can contribute to unrestrained tissue destruction, uncontrolled pulmonary inflammation, acceleration of disease progression, or development of fibrosis (Laskin, 2009; Mills et al., 2015).

Inhaled NPs are capable of activating AMs leading to the expression of pro-inflammatory mediators, recruitment of inflammatory cells and thereby mounting an inflammatory immune reaction (Blackford et al., 1994; Lucarelli et al., 2004; Rao et al., 2004; Ma et al., 2011; Scherbart et al., 2011; Barna et al., 2013; Chang et al., 2014; Rydman et al., 2014; Meng et al., 2015; Kumar et al., 2016b; Li et al., 2017a; Dong and Ma, 2018). Furthermore, an emerging data base demonstrates that NPs differentially influence macrophage polarization (Miao et al., 2017). It should be noted that, on one hand AMs could be polarized to M1 or M2 phenotype by the engulfed material itself. On the other, AMs could be polarized by extracellular signals they encountered in the pulmonary microenvironment, for example released by wounded epithelial cells. Ultimately, NPs can impact the local tissue M1/M2 balance, which can alter pulmonary immune system defense properties (Chang et al., 2014; Miao et al., 2017). TiO_2 NPs as well as quartz particles were repeatedly found to differently influence M1 and M2 specific protein expression, respectively (Blackford et al., 1994; Lucarelli et al., 2004; Rao et al., 2004; Scherbart et al., 2011; Chang et al., 2014; Kumar et al., 2016b). Also, there is first evidence that CeO_2 as well as mwCNT might affect macrophage polarization (Ma et al., 2011; Barna et al., 2013; Rydman et al., 2014; Meng et al., 2015; Li et al., 2017b; Dong and Ma, 2018). It seems that not only the dose but also the dose rate and the duration of exposure influence the dynamics and the herewith associated spatio-temporal changes of M1 and M2 polarization. For instance, Kumar et al. found a dose-dependent shift

from M2 to M1 polarization of macrophages after i.v. administration of TiO_2 in rats (Kumar et al., 2016b). Other authors found a time-dependent, sequential switch in the appearance of macrophage subpopulations (Ma et al., 2011; Venosa et al., 2016; Xiang et al., 2016; Dong and Ma, 2018). Intratracheal instillation of 0.15, 0.5, 1.3, 5 and 7 mg/kg bw CeO_2 NPs caused dose-dependently pulmonary inflammation in exposed rats. Pro-inflammatory mediators were increased one day post-instillation and decreased afterwards. M2 markers were found upregulated 28 days post-instillation. The authors concluded there might be a switch from pro-inflammatory M1 to pro-fibrogenic M2 macrophages (Ma et al., 2011). Similar results were found after oropharyngeal aspiration of mwCNT in mice. Administration of 1.86 mg/kg body weight mwCNT caused acute inflammation and fibrotic responses. Consistent with this, M1 macrophages were most prominent three days post exposure and declined thereafter, whereas M2 macrophages started to accumulate from this timepoint on (Dong and Ma, 2018). In a mouse model of lung fibrosis, the oropharyngeal instillation of crystalline silica particles resulted in an early upregulation of pro-inflammatory mediators beginning one day post-instillation, peaking at day three, and declining thereafter. At the same time, the authors observed a dramatic increase in M2 macrophages on day one, which progressively increased throughout the study period (day 28) (Xiang et al., 2016). Interestingly, there is first evidence that the crucial balance of M1 and M2 immune responses is not necessarily sequential (first M1, second M2 polarization) but there are various pathways, which are early stimulated in parallel, and which seem to be independent from each other; each differently affecting early macrophage polarization and leading to a different aspect of the observed pathophysiology (Re et al., 2014; Nikota et al., 2017; Fritsch-Decker et al., 2018).

Box 4 Alveolar macrophages – Origin, immunological functions, M1/M2 phenotypes and common M1/M2 markers

A long-held dogma that all tissue-resident macrophages are derived from local differentiation of blood circulating monocytes after extravasation (van Furth and Cohn, 1968) proved to be oversimplified. Lung resident alveolar macrophages (AMs) are derived from fetal monocytes of the fetal liver, which appear in the lungs from embryonic day 14 on. During development, the settled fetal lung monocyte population expands dramatically, thereby changing its expression profile of characteristic surface markers, until a mature phenotype defined as F4/80^{hi}CD11c^{hi}SiglecF^{hi}CD64^{hi}CD11b^{lo}Ly6C^{lo} AMs is reached (Guilliams et al., 2013). Thereafter the mature, tissue resident AM population is maintained by local cell proliferation, autonomously from immigrating blood monocytes (Guth et al., 2009; Guilliams et al., 2013; Hashimoto et al., 2013; Becher et al., 2014). The resident AM population turns over slowly, with a replacement rate of 40% per year in mice (Maus et al., 2006). AMs are found in the air space of the alveoli where they form 90-95% of the cellular content in the steady state. Their roles encompass contribution to tissue development, maintain tissue homeostasis, phagocytosis and degradation of dead cells, cell debris, and foreign entities such as pathogens, and orchestrating immune responses (AMs are capable of antigen-presentation) (Gordon and Read, 2002). On the inner alveolar surface, they occupy a unique niche constantly exposed to innocuous environmental antigens and challenged with potential threats. For this reason, a specialized, immunosuppressive microenvironment exists that prevents innate immune cell activation unless the threat is significant (Guth et al., 2009). Alveolar epithelial cells type I (AEC-I) play a significant role in limiting the activation of AMs, i.a. through expressing CD200 and MUC-1 (Snelgrove et al., 2008). Through constant inter-cellular communication (e.g. AMs express CD200R at their cellular membrane), AEC-I and AMs set the threshold and the quality of the immune response. AMs orchestrate the early pro-inflammatory immune response but also its subsequent resolution and promote tissue repair processes (Hussell and Bell, 2014). According to their versatile functions, AMs can be polarized into various activation states (M1, M2) (Martinez and Gordon, 2014). However, when over-activated, they can contribute to the progression of disease states such as fibrosis (Mills et al., 2015).

Pro-inflammatory immune responses are the host's physiological defense mechanism to constrain and destroy invading pathogens. For this purpose, activated AMs acquire a high antimicrobial activity, and proteolytic and catabolic capacity (Mackaness, 1964). AMs become activated when encountering pro-inflammatory activation signals such as LPS, TNFα, IFNγ, or GM-CSF. These mediators trigger the so-called classical pathway of activation (Ehrt et al., 2001), which results in an M1 phenotype.

Box 4 continued Alveolar macrophages – Origin, immunological functions, M1/M2 phenotypes and common M1/M2 markers

M1 polarized AMs up-regulate their phagocytic capacity, the synthesis and release of pro-inflammatory cytokines (i.a. IL-12, IL-23, TNFα, IL-6, and IL-1β), reactive oxygen species and reactive nitrogen intermediates. The latter being produced by the cytoplasmic enzyme nitric oxide synthase (iNOS). iNOS becomes induced upon pro-inflammatory signaling (e.g. by IFNγ) and metabolizes L-arginine to nitric oxide (NO) and citrulline. High amounts of NO are cytotoxic. Thus, iNOS is frequently used as a M1 macrophage marker (MacMicking et al., 1997; Mills, 2012; Davis et al., 2013).

An alternative form of macrophage activation is mediated by cytokines such as IL-4 and IL-13 and leads to a M2 polarization state (Stein et al., 1992). IL-4/IL-13 signaling suppresses the expression of pro-inflammatory cytokines and induces genes for immunoregulation and tissue remodeling (e.g. TGF-β) (McKenzie et al., 1999). In M2 polarized AMs the activity of a distinct phagocytic receptor repertoire is highly up-regulated, importantly expression of the mannose receptor (CD206 or MRC-1) becomes induced (Stein et al., 1992). Activation of CD206 is associated with up-regulation of anti-inflammatory cytokines (IL-10, IL-1RA) and expression of IL-1 decoy receptors (Taylor et al., 2005). CD206 is a phagocytic/endocytic receptor and responsible for the internalization of molecules released during an (inflammatory) immune reaction. Upon ligand binding, the receptor-ligand-complex gets internalized and pathogens or pro-inflammatory mediators undergo lysosomal degradation. Thus, CD206 is key in clearing pro-inflammatory signaling molecules and resolution of inflammation (Lee et al., 2002; Gazi and Martinez-Pomares, 2009; Martinez-Pomares, 2012; Kambara et al., 2015) and is frequently used as an M2 macrophage marker. In accordance with the immunosuppressive environment of the lungs, AMs show a M2 phenotype in the healthy lungs, expressing high amounts of CD206 (Hussell and Bell, 2014). Another common M2 marker is arginase I (ArgI). ArgI is a cytoplasmic enzyme of the arginine metabolism counteracting the effects of iNOS. Several studies point to the crucial role of the arginine metabolism in immune responses and the herewith associated regulation of iNOS and ArgI expression (Setoguchi et al., 1996; Hesse et al., 2001; Mills, 2001; Pesce et al., 2009). ArgI is suspected to be involved in cell proliferation, granuloma formation, fibrosis, and tissue repair (Mills et al., 1992; Hesse et al., 2001; Gordon, 2003; Mills, 2012; Mattila et al., 2013; Duque-Correa et al., 2014). However, several studies reported contradictory results on the role of ArgI in these processes (Setoguchi et al., 1996; Hesse et al., 2001; Wangoo et al., 2001; Pesce et al., 2009).

2. Working hypotheses, aims, and research strategy of the dissertation project

The present dissertation project focusses on the biokinetics and biological effects of NPs under simulated pulmonary conditions or in the lungs *in vivo*, respectively. Since the major route of occupational exposure during production or processing of NPs is the inhalation route.

Hypotheses

(1) Triggered by the observed unusual clearance for some poorly water-soluble NPs, such as $BaSO_4$, it was hypothesized that internalization of poorly water-soluble NPs by AMs can accelerate their biodissolution *in vivo*, leading to enhanced chemical clearance.
(2) Based on the key role of AMs in pulmonary pro- and anti-inflammatory immune responses, it was hypothesized that initial polarization of AMs correlates with short-term effects of NPs *in vivo* and that distinct early AM polarization is predictive for long-term outcome.

Aims

The aim of this dissertation project was to investigate to what extent AMs contribute to the biodissolution and biological effects of inhaled, biopersistent NPs. Both, the biopersistence as well as the pro-inflammogenic, cellular effects of NPs are driving its pulmonary toxicity.

Because AMs are chiefly involved in pulmonary particle clearance and pulmonary immune responses, the current body of work investigates on one hand whether the internalization by AMs accelerate biodissolution processes of poorly-soluble NPs, such as $BaSO_4$, and on the other whether distinct biological effects of NPs in the lungs correlate with different AM phenotypes and if AM phenotypes after short-term exposure are predictive for long-term effects. Based on short pulmonary clearance halt-times observed for $BaSO_4$, which could not be explained by physical clearance mechanisms, it was hypothesized that AMs facilitate accelerated biodissolution (chemical clearance) under physiological conditions. Referring to their effector and immunoregulatory functions, it was further hypothesized that AMs determine short-term and long-term effects of NPs *in vivo* and that distinct early AM polarization is predictive for the long-term outcome. Standardized abiotic test systems, which enable the simulation of physiological conditions, thereby avoiding animal studies, and which show good correlation with *in vivo* biokinetic data, will be valuable tools for these purposes. Furthermore, knowledge of the early contribution of M1 and M2 AMs to pathogenesis of early pulmonary inflammation and long-term outcome will enable efficient hazard assessment reducing the number of extensive long-term inhalation studies in animals.

Research strategy

In the first part of this dissertation project, biodissolution of NPs was assessed using different dissolution setups each mimicking various physiological conditions. The solubility and dissolution rate of NPs were evaluated as follows. (1) Static solubility of $BaSO_4$ was assessed in water and a relevant simulated biological fluid named phagolysosomal simulant fluid (PSF) at pH 4.5, to investigate to which extend intracellular phagolysosomal conditions and acidic pH affects solubility. (2) Quasi-dynamic dissolution of $BaSO_4$ was assessed in water and PSF with pH 4.5, to examine how dissolution changes when equilibrium is disturbed. (3) AM assisted dissolution was assessed *in vitro*, to simulate the complex macrophage-assisted dissolution *in vivo*. The rat AM cell line NR8383 was used. The experiments were performed (by the doctoral candidate) in collaboration at IBE R&D Institute for lung health gGmbH (Münster, Germany). (4) Dynamic dissolution rates of NPs were quantitatively assessed using flow-through or flow-by dissolution setups. Dissolution cells were flushed with acidic PSF (pH 4.5) for seven days. Further, measured dissolution rates were compared to *in vitro* and *in vivo* data, to ascertain to which extend measured abiotic dissolution rates are compatible with macrophage-assisted dissolution and *in vivo* biokinetic data. (5) In addition, and beyond the scope of this dissertation project, following the dissolution rate quantification, remaining solids were prepared on transmission electron microscopy (TEM) grids and assessed for possible biotransformation of (nano-)particles by TEM. In addition, lung tissue obtained from rats following twelve months inhalation exposure to an aerosol concentration of 50 mg/m³ of $BaSO_4$ was examined by high-resolution TEM to compare *in vivo* biotransformation processes with abiotic findings. Dynamic dissolution and biotransformation investigations were performed by collaborators at the material physics department of BASF SE (Ludwigshafen, Germany), University of Rochester medical center (Rochester, New York, USA), and National Institute of Occupational Safety and Health (Cincinnati, Ohio, USA). (6) Results obtained with the abiotic flow through setup and *in vitro* experiments were compared with each other and with results from published *in vivo* instillation/inhalation studies.

In the second part, this dissertation project examined the appearance of AM subpopulations in lung tissue following short-term (5-day) inhalation exposure to poorly-soluble NPs, and a subsequent exposure-free period, using an immunohistochemical approach. After establishing the immunohistochemical protocols, the expression of general (CD68) and specific (iNOS for M1 and CD206 and ArgI for M2) macrophage markers was detected by double immunolabelling of formalin-fixed, paraffin-embedded histological lung sections, which allowed to observe the appearance of AM subsets *in situ*. Next, occurrence of AM subsets was quantitatively analyzed. Quantification of M1 and M2 AMs was performed to examine whether the balance of M1 or M2 polarization correlates with the different qualities of histopathological outcomes of NPs. In addition, quantitative examination was conducted to ascertain whether

early macrophage polarization might be indicative for the progression of long-term effects of NPs (promoting inflammation, tissue injury, fibrosis or lung tumor formation).

To this end, highly industrial relevant NPs were selected, which are descriptive for the broad field of NP applications. Materials were chosen based on the availability of *in vivo* data and most materials are representatives of reference material- or benchmark material-inventories. Assessing similarity to known reference or benchmark materials can be a powerful approach to reduce the uncertainty related to the hazards of newly developed NPs and can be used to implement grouping and testing frameworks. The selected NPs and the comparative non-nano, bulk counterparts varied in chemical composition, size, shape, crystallinity, and coating; each being thoroughly characterized.

The test set for biodissolution experiments in the dynamic dissolution setup consisted of: ZnO NM-110, ZnO NM-111, $SrCO_3$, Levasil 50, Levasil 100, Levasil 200, Levasil 300, aminated SiO_2, phosphonated SiO_2, (unmodified) SiO_2 NM-203, Pigment Red 101, rod-shaped, spherical, or cubic Fe_2O_3, CuO, $Cu_2(OH)_2CO_3$, nano-scale Cu-Phthalocyanine (Pigment Blue 15), halogenated Cu-Phthalocyanine (Pigment Green 7), TiO_2 NM-104, TiO_2 NM-105, CeO_2 NM-211, CeO_2 NM-212, $BaSO_4$ IRMM381, and $BaSO_4$ NM-220.

The test set for biodissolution experiments using NR8383 AMs *in vitro* consisted of: $SrCO_3$, ZnO NM-110, and $BaSO_4$ NM-220. $SrCO_3$ and ZnO are pH sensitive materials with low solubility at neutral but high solubility at acidic pH. Inhalation toxicity studies revealed short pulmonary clearance half-times for ZnO. Based on the unexpected fast clearance kinetics of $BaSO_4$, it was hypothesized that macrophage-assisted biodissolution is the underlying mechanism of its short clearance half-times.

The test set for assessing AM activation state after NP inhalation exposure consisted of: TiO_2 NPs, CeO_2 NPs (NM-212), mwCNT, and micro-sized, non-nano quartz (DQ12). These materials were extensively tested in short-term (5-day exposure), sub-chronic (90-day exposure) and long-term (two-year exposure) inhalation studies. They are poorly soluble and highly biopersistent and their biological effects differ in terms of initial inflammatory response, reversibility of effects and long-term pathological outcome. Short-term inhalation studies are commonly used to identify hazard and potency of inhaled NPs and proved to be useful in prioritizing and grouping NPs. Previously published short-term inhalation studies performed with 100 mg/m³ TiO_2, 25 mg/m³ CeO_2, 32 mg/m³ mwCNT or 100 mg/m³ quartz were chosen for the present examinations. Thus, the current investigations were retrospectively performed using existing formalin-fixed, paraffin-embedded specimen.

3. Main findings

In this thesis, the main findings section (section 3) summarizes the most relevant results from three peer reviewed publications. Each publication is presented in the scientific output section (section 6).

The first two publications (sections 6.1 and 6.2) present research, which aimed at elucidating the dissolution kinetics of various NPs and potential biotransformation processes. Further, it was investigated whether results obtained with abiotic, dynamic dissolution setups are consistent with results of *in vitro* and/or *in vivo* studies. $BaSO_4$ was investigated in much detail because of its unexpected biokinetics observed in *in vivo* studies of varying exposure durations (instillation and five-day to two-year inhalation studies).

(1) Static solubility of $BaSO_4$ was assessed at static, equilibrium conditions (beaker) in acidic PSF and in water for seven and 28 days and two years. Measured Ba ion concentrations were slightly higher in acidic PSF than in pH neutral medium control. Approximately 0.1% dissolved $BaSO_4$ NPs was found in PSF at any time point, confirming the poor solubility of $BaSO_4$. The addition of EDTA, to mimic alkaline earth metal-transporting proteins, did not significantly increase solubility.

(2) Quasi-dynamic dissolution of $BaSO_4$ was assessed in water and PSF at pH 4.5. Dissolution of $BaSO_4$ at out-of-equilibrium conditions, was measured using a setup comprising two compartments, one inner donor (containing $BaSO_4$) and one outer receptor compartment. The medium in the receptor compartment was changed at constant time intervals, repeatedly disrupting equilibrium. The two compartments were separated from each other by a dialysis membrane. The measured ion concentration in the receptor medium remained roughly constant. The cumulative dissolution of 0.1% over 7 days and an overall dissolution rate of k = 0.01 ng/cm²/h remained on the same level as the static solubility system. This indicated that an equilibrium Ba concentration of about 1 to 2 mg/L in the pH 4.5 PSF medium was the limiting factor preventing further dissolution.

(3) NR8383 AM-assisted dissolution was assessed *in vitro*. NR8383 cells were exposed for 3, 6, 12, 24 and 48 hours to non-cytotoxic concentrations of $SrCO_3$, $BaSO_4$, or ZnO NPs. Incubation of NR8383 AMs with $SrCO_3$ significantly increased the concentration of dissolved ions in the cell culture medium compared to cell-free medium control at each time point tested. The macrophage-mediated increase in dissolved $SrCO_3$, whose solubility is known to be pH-dependent, developed progressively with longer incubation periods (up to 48 hours); due to the gradual acidification of macrophage's phagolysosomes (McNeil et al., 1983; Yamashiro et al., 1983). In comparison, the incubation of $SrCO_3$ in PSF (pH 4.5) led to a rapid dissolution of the total $SrCO_3$ mass. The high values remained fairly constant over time (3 to 48 h). In the

cell-free medium control, no significant dissolution of $SrCO_3$ was measured (Figure 1). After incubation of $BaSO_4$ with cell-free culture medium, NR8383 cells or acidic PSF for up to 48 hours very low amounts of dissolved material were found in cell culture medium for all time points investigated. At 24 and 48 hours dissolution was slightly increased following incubation with NR8383 cells or PSF. However, increased dissolution by NR8383 cells was hardly discernible from abiotic dissolution. One limiting factor might be the very low Ba concentration to be measured and/or the settings of the sensitivity of the analysis method used. The analytical uncertainty might mask subtle cellular effects. Next, macrophage-assisted dissolution was assessed for two ZnO NPs, uncoated ZnO NM-110 and surface-coated ZnO NM-111, which were shown to be readily soluble *in vivo*. While the solubility of both ZnO NPs was confirmed and shown to be increased in acidic PSF, phagolysosomal processes of AM cells *in vitro* had no major influence on the solubilization of Zn ions when compared to cell-free medium control. For all experiments, cytotoxicity was monitored by lactate dehydrogenase (LDH) activity measurement. LDH activity remained low till 24 h incubation but increased at the 48 h timepoint, although there were no visible signs of reduced cell viability or cell deterioration after 48 hours incubation seen (Figure 2). In summary, cultured AMs are able to accelerate the biodissolution of particulate matter, which was most obvious for $SrCO_3$. However, additional factors might contribute to the biodissolution processes *in vivo*, which cannot be simulated in static cell culture experiments *in vitro* as evidenced by the results for $BaSO_4$ and ZnO NPs. Certainly, sensitive methods are required when measuring trace concentrations of poorly soluble materials like $BaSO_4$.

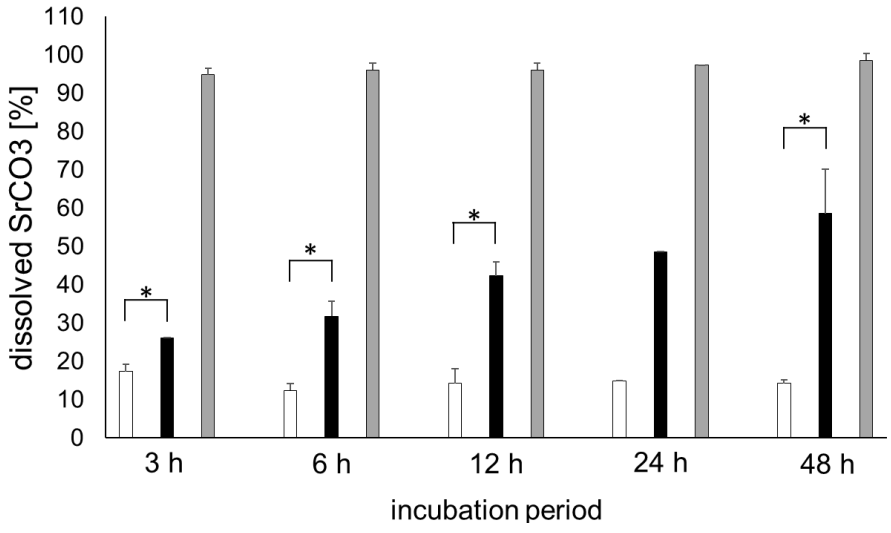

Figure 1: Dissolution of $SrCO_3$ subjected to neutral and acidic pH conditions over time. F-12K cell culture medium control without cells (white bars); NR8383 rat AM (black bars); PSF pH 4.5 (grey bars); n=3; * means $p \leq 0.05$. Taken from (Koltermann-Jülly et al., 2018).

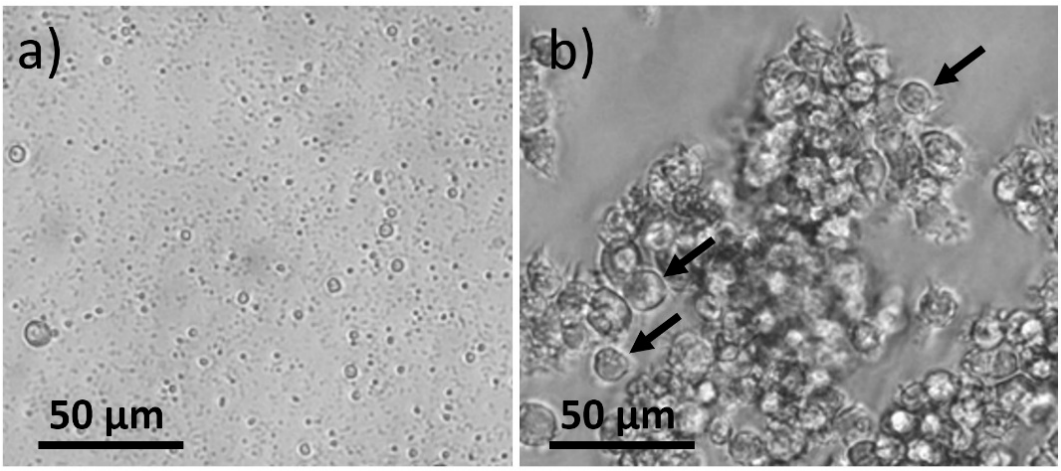

Figure 2: Exposure of NR8383 AMs to $SrCO_3$ NPs. Contrast-enhanced phase contrast micrograph showing **(a)** numerous $SrCO_3$ NP agglomerates settled onto the bottom of the culture vessel post centrifugation under cell-free conditions, and **(b)** NR8383 cells following 48 h incubation with $SrCO_3$ NPs. Note that cells appear healthy with smooth outer contours (arrows). The space between cells is devoid of visible particles. Taken from (Koltermann-Jülly et al., 2018).

(4) Dissolution rates of different (nano-)materials were quantitatively investigated by collaborators using dynamic dissolution setups flushed with PSF (pH 4.5). Notably, the dissolution rate *k* was given in units of ng/cm²/h, which takes the dissolved fraction of the material, the material's specific surface area, and the time elapsed into account. For all test items composed of TiO_2, CeO_2, and Fe_2O_3 dissolved ion concentration was below the detection limit of the analysis technique used. Additional measurements, using a more sensitive analysis technique, confirmed the poor solubility of the materials but revealed that although the dissolution rates did not differ between different (nano-)forms of the same substance, it differed between substances of different chemical composition. These results were published in an addendum to the original article. Test substances composed of SiO_2 showed low dissolution at simulated physiological conditions as expected from *in vivo* data. However, surface functionalization of SiO_2 particles was potent to accelerate the dissolution rate compared to untreated SiO_2 particles. The dissolution kinetics of different Cu-based materials varied considerably. One reason might be different technical grades used. ZnO NPs dissolved readily under acidic conditions as expected. Again, it was observed that coating of particles influenced the dissolution kinetics. Further, when normalizing to the initial surface area, the nano-form and the bulk-form of $BaSO_4$ had almost identical *k* values. This confirms the applicability of *k* as a surface-based metric to express dynamic dissolution kinetics. The maximum observed liberated Ba ion concentration in the dynamic flow-through setup was close to the pH 4.5 PSF solubility limit observed in the static and quasi-dynamic setups but the total dissolved fraction

after seven days was considerably higher in the flow-through system. The abiotic dissolution kinetic indicates 50% dissolution after five to six days ($t_{1/2}$ 5.9 days) at non-equilibrium, non-saturating conditions, which is close to the *in vivo* clearance half-time of 9.6 days after intratracheal instillation. In addition, more detailed investigations on $BaSO_4$ NPs revealed that the dissolution kinetics depend on the initial mass of $BaSO_4$ loaded into the flow-through dissolution cells. It was demonstrated that higher initial mass loading leads to system saturation thereby determining a solubility limit. When liberated Ba ion concentration in the local vicinity of the $BaSO_4$ particles reached this solubility limit, ions reprecipitated before the PSF flow removed them from the dissolution cell (see also below). This reprecipitation phenomenon was specific for $BaSO_4$ and could not be reproduced using another NPs (CuO). In summary, the biodissolution rate *k* obtained by abiotic, dynamic dissolution testing is consistent with *in vivo* clearance of NPs; although $BaSO_4$ is termed “insoluble” in static, aqueous systems, its relatively high *in vivo* biodissolution is correctly predicted by the dynamic dissolution method.

(5) Following the dissolution rate quantification for seven days, remaining solids were transferred to TEM grids and assessed for possible biotransformation of (nano-)particles by TEM. In addition, lung tissue from rats exposed to $BaSO_4$ NPs was examined by high-resolution TEM. These investigations were out of scope of the initial objectives of this dissertation project but were within the scope of the first two papers, which aimed at providing standardized methodology for the hazard assessment of NPs. For TiO_2, CeO_2, and Fe_2O_3 NPs no biotransformation was observed. According to the low dissolution, untreated SiO_2 particles decreased moderately. Further, for SiO_2 NPs different intermediate structures were observed, most probably due to the formation of aggregates. TEM analysis revealed that both Cu-based materials (nano-scale Cu-Phthalocyanine and halogenated Cu-Phthalocyanine) extensively formed aggregates during acidic treatment. Complete dissolution of ZnO NPs was confirmed by TEM analysis, as no particles could be found on TEM grids. Additional investigations demonstrated continuous decrease of radii of curvature of the particles until they were completely dissolved. On the contrary, for $BaSO_4$ NPs the radii of curvature increased after incubation at acidic conditions. This was observed under saturation conditions by TEM in the abiotic system as well as by high-resolution TEM inside AMs *in vivo*. Instead of shrinking the size, TEM scans of particles retrieved from flow-cells or rat lungs showed an increase in sphericity of the remaining solids at the expense of particles with smaller radii of curvature. Such chemical transformation is consistent with Ostwald ripening. Thus, the long-term biopersistence of $BaSO_4$ observed *in vivo* is dependent on both biodissolution as well as biotransformation processes.

(6) Results of abiotic, dynamic dissolution testing were compared with results of macrophage-assisted dissolution *in vitro* and with *in vivo* instillation/inhalation data. For all

(nano-)materials, the abiotic dissolution rates at out-of-equilibrium conditions were consistent with *in vivo* observations. Results were not enhanced by AM-assisted biodissolution experiments *in vitro* for up to 48 hours.

The third publication (section 6.3) presents research, which examined the appearance of polarized AM subpopulations in lung tissue following short-term (5-day) inhalation exposure to poorly-soluble NPs, and a subsequent exposure-free period, using an immunohistochemical approach. Immunohistochemical, double-staining protocols for the general AM marker CD68, and the M1 marker iNOS (CD68-iNOS double immunolabeling), and the M2 markers CD206 (CD68-CD206 double immunolabeling) and ArgI (CD68-ArgI double immunolabeling) were successfully established on formalin-fixed, paraffin-embedded histological lung sections. Expression of iNOS could be observed in lungs of treated animals, but not in control animals (Figure 3). In accordance with the immunosuppressive environment of the lungs, a high baseline expression of CD206 and ArgI were observed in control animals, which varied in the different NP-exposure groups (Figure 3). Quantitative analysis revealed that relative numbers of pro-inflammatory M1 AMs ($CD68^{+}iNOS^{+}$) were significantly increased in rat lungs, which were diagnosed with pulmonary inflammation, compared to control (Table 1). Furthermore, M1 AM relative numbers correlated with regression, persistence, or progression of inflammatory processes after a post-exposure period (Table 2). Relative numbers of CD206 expressing anti-inflammatory M2 AMs were generally downregulated during acute inflammation (Table 1) but recovered during the post-exposure period when inflammatory signs were declining (Table 2). However, between the four investigated (nano-)materials no substantially different expression pattern of M1 or M2 AMs after 5-day exposure or 14 or 21 days post-exposure, which might explain the different short-term and long-term histopathological outcomes, especially regarding granulomatous inflammation, could be determined. Thus, although the appearance of M1 and M2 macrophages correlated with acute pulmonary inflammation caused by (nano-)materials, it was neither indicative for the different qualities of histopathological outcomes upon short-term exposure nor predictive for long-term effects.

Figure 3: Micrographs of left lung sections of animals exposed to different (nano-)materials for 5 days. Effects on iNOS (M1), ArgI (M2) and CD206 (M2) expression shortly after the last exposure were visualized by immunohistochemistry. Binding of antibodies was visualized using a red chromogen for the AM marker CD68 and a brown chromogen for the M1 (iNOS) and M2 (ArgI and CD206) markers. Arrows indicate macrophages in insets. Scale bars in insets are 10 µm one scale line. Representative sections from each treatment group are shown. Controls were exposed to air only.

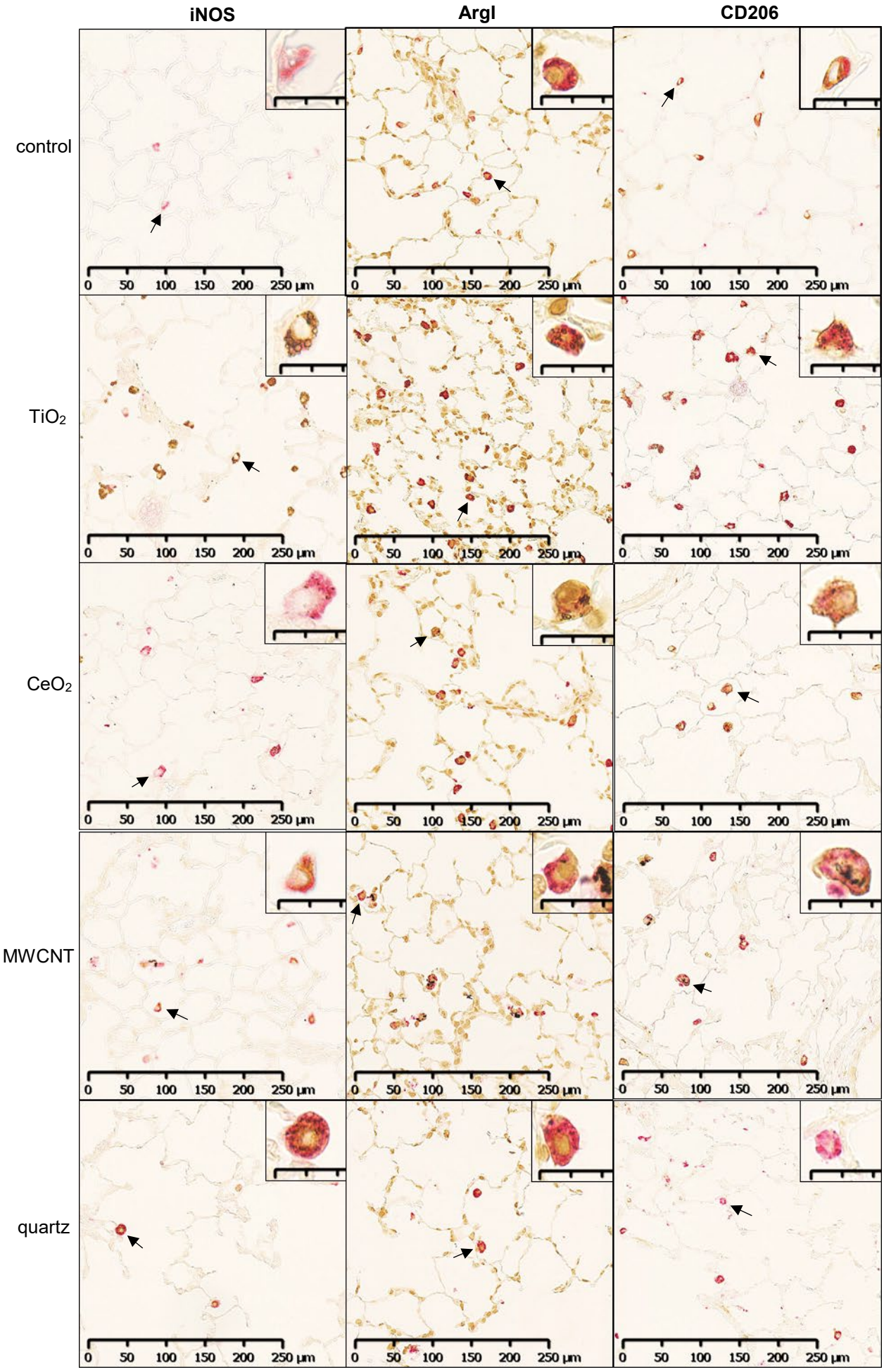
iNOS
Arg1
CD206
control
TiO2
CeO2
MWCNT
quartz
0 50 100 150 200 250 µm

Table 1 Percentages of CD68 and M1 (iNOS) or M2 (CD206 or Argl) marker double-positive alveolar macrophages (AMs). Animals were sacrificed after 5-day exposure to 100 mg/m³ TiO_2 (n=6), 100 mg/m³ quartz (n=6), 25 mg/m³ CeO_2 (n=5), or 32 mg/m³ mwCNT (n=3). Each animal was assessed for all three markers, i.e. three lung sections with one double-immunostaining each. In each lung section the marker-expression of one hundred AMs was assessed. Because mixed phenotype macrophages co-exist with M1 and M2 macrophages the overall percentage of cells per lung might exceed one hundred percent.

	M1 or M2 marker expressing AMs [%] ± SD		
	iNOS (M1)	**CD206** (M2)	**Argl** (M2)
control[a]	1.5 ± 0.8	77.2 ± 4.8	47.7 ± 5.4
TiO_2	79.3 ± 9.6**	65.2 ± 15.5	55.1 ± 6.8
quartz	44.9 ± 5.1**	55.5 ± 8.8**	26.0 ± 6.0**
control[b]	0.7 ± 0.2	91.5 ± 2.2	19.5 ± 5.5
CeO_2	8.0 ± 1.9**	83.2 ± 3.6**	33.0 ± 5.3**
mwCNT	42.0 ± 1.7**	71.7 ± 4.2**	21.7 ± 0.9

SD standard deviation

[a] control group of TiO_2 and quartz study

[b] mean of control groups of CeO_2 and mwCNT studies

* $p \leq 0.05$ treated vs. control group

** $p \leq 0.01$ treated vs. control group

Table 2 Percentages of CD68 and M1 (iNOS) or M2 (CD206 or ArgI) marker double-positive alveolar macrophages (AMs). Animals were sacrificed 14 (TiO_2, quartz) or 21 (mwCNT) days post exposure. Animals were exposed for 5 days to 100 mg/m³ TiO_2 (n=6), 100 mg/m³ quartz (n=6), or 32 mg/m³ mwCNT (n=3). Each animal was assessed for all three markers, i.e. three lung sections with one double-immunostaining each. In each lung section the marker-expression of one hundred AMs was assessed. Because mixed phenotype macrophages co-exist with M1 and M2 macrophages the overall percentage of cells per lung might exceed one hundred percent.

	M1 or M2 marker expressing AMs [%] ± SD		
	iNOS (M1)	**CD206** (M2)	**ArgI** (M2)
control[a]	2.0 ± 2.5	82.0 ± 6.4	37.0 ± 2.3
TiO_2	73.4 ± 8.3**	80.7 ± 4.2	47.2 ± 7.7*
quartz	59.1 ± 10.6**	66.7 ± 6.4**	41.0 ± 5.1
control[b]	2.0 ± 0.8	93.7 ± 2.5	24.2 ± 7.6
mwCNT	44.7 ± 4.9**	78.5 ± 0.5*	38.8 ± 2.0

SD standard deviation
[a] control group of TiO_2 and quartz study
[b] control group of mwCNT study
* $p \leq 0.05$ treated vs. control group
** $p \leq 0.01$ treated vs. control group

4. Summary, conclusion and outlook

This dissertation project investigated the role of AMs in biodissolution and biological effects of inhaled, biopersistent NPs.

Summary

In vitro experiments using NR8383 cells revealed that AMs can accelerate the biodissolution of pH-sensitive materials, such as $SrCO_3$. However, the unusual biokinetics initially observed for $BaSO_4$ could neither be explained by the *in vitro* experimental setup nor by abiotic, static experimental designs. By simulating the acidic lysosomal conditions of AMs in an abiotic, dynamic dissolution system, where liberated ions were continuously removed from the vicinity of the solids by a constant flow, short *in vivo* clearance half-times of $BaSO_4$ could be replicated. In additional experiments of collaborators, biodissolution testing at out-of-equilibrium conditions was extended to a set of different benchmark and industrial relevant NPs. Simulated biodissolution rates of different NPs measured with flow-through or flow-by dissolution systems achieved a high degree of consistency with *in vivo* pulmonary clearance kinetics of rats. Further investigations of the remaining solids, subsequent to dissolution testing, using electron microscopy, revealed different biotransformation processes for different NPs. For $BaSO_4$, biotransformation in the form of recrystallization could be observed. Remarkably, increase in particle size of $BaSO_4$ NPs was consistent with Ostwald ripening, which could be observed for particles of flow-cells as well as on the inside of AMs *in vivo*.

To determine the polarization state of AMs, histological lung sections of rats exposed for five days to biopersistent NPs were immunohistochemically investigated. Quantitative analysis revealed that relative cell numbers of pro-inflammatory M1 and anti-inflammatory M2 AMs correlated with BALF analysis and histopathological findings of acute pulmonary inflammation. The initial inflammatory response correlated with a strong upregulation of $CD68^+iNOS^+$ M1 and a downregulation of $CD68^+CD206^+$ M2 AMs. Following an exposure-free period, sequential changes in M1 or M2 AM relative cell numbers correlated with regression, persistence or progression of the acute inflammatory immune response. This suggests a role of M1/ M2 AMs in the pathogenesis of pulmonary inflammation. Regarding the regression of inflammation this is of special importance for the hazard assessment of NPs. It remains to be determined to what extent these findings can be generalized to other biopersistent NPs. In fact, AM polarization was not indicative or predictive for the different quality of histopathological findings observed for different (nano-)materials after short-term or long-term exposure, respectively.

Conclusion

In conclusion, I ascertained during this dissertation project, together with collaborators, that AM-assisted biodissolution *in vitro* is acknowledged as a potential method for specific mechanistic investigations but cannot represent the numerous characteristics and features of a complex organ such lungs. Results of abiotic, dynamic dissolution testing at simulated physiological conditions were consistent for all NPs and non-nano materials tested with *in vivo* biokinetics. Importantly, the non-equilibrium conditions of flow-cells are essential to simulate *in vivo* biodissolution, as results of static or quasi-dynamic systems were not consistent with *in vivo* data. Further, simulation of physiological conditions requires the use of relevant biological/ physiological fluids. Obviously, for (nano-)materials with very low biodissolution pulmonary clearance is mainly mediated by physical clearance mechanisms, i.e. macrophage-mediated transport via the mucociliary escalator. For (nano-)materials with high biodissolution *in vivo* clearance is dominated by chemical clearance. Importantly, biokinetics can be modulated by biotransformation processes, such as reprecipitation, which in turn might alter toxicological effects.

Triggered by the observed unusual clearance for some poorly water-soluble NPs, such as $BaSO_4$, it was hypothesized that internalization of poorly water-soluble NPs by AMs accelerates their biodissolution *in vivo,* leading to enhanced chemical clearance. Consequently, chemical clearance together with physical clearance would be the underlying mechanisms of the unusual biokinetics. Using a dynamic dissolution system, the hypothesis could be verified, as measured dissolution rates correlated with *in vivo* clearance.

Based on the key role of AMs in pulmonary pro- and anti-inflammatory immune responses, it was hypothesized that initial polarization of AMs correlates with short-term effects of NPs *in vivo* and that distinct early AM polarization is predictive for long-term outcome. I recognized at the end of the present dissertation project that the current data does not allow for the prediction of histopathological long-term effects. However, following short-term exposure to different NPs, acute pulmonary inflammation was accompanied by increased pro-inflammatory M1 relative cell numbers and decreased anti-inflammatory M2 relative cell numbers.

Outlook

Beyond the scope of this dissertation project a new grouping hypothesis by means of the similarity of biodissolution rates (quantitative data obtained with abiotic, dynamic flow-through dissolution setup at simulated physiological conditions) and biotransformation (qualitative data obtained with TEM analysis of the remaining solids) was proposed (Koltermann-Jülly et al., 2018). The mechanistic understanding of biodissolution processes and possible biotransformation of NPs will enable the development of standardized abiotic test systems, which enable the simulation of physiological conditions (by means of appropriate simulated biological fluids) and which show good correlation with *in vivo* biokinetic data.

An in-depth understanding of the underlying processes of nanomaterial-induced morphological changes and the role of M1 and M2 AMs in their pathophysiology is needed. Investigations on involved signaling pathways will add to this understanding. A distinct induction of AM polarization might indicate different underlying initiating events, which in turn might explain the various histopathological outcomes after long-term exposure to different inhaled NPs. Interestingly, first evidence points out that the crucial balance of M1 and M2 immune responses is not necessarily sequential (first M1, second M2 polarization) but there are various pathways, which are early stimulated in parallel, and which seem to be independent from each other; each differently affecting early macrophage polarization and leading to a different aspect of the observed pathophysiology (Re et al., 2014; Nikota et al., 2017; Fritsch-Decker et al., 2018). Additionally, in humans it was observed that AMs can express M1 and M2 markers simultaneously, which confirms that M1 and M2 signatures of activated AMs do not necessarily exclude each other, but coexist (Bazzan et al., 2017). Unraveling these pathways will add to our understanding of the pathogenesis of morphological changes observed and the exact contribution of AM subsets. In addition, specific biomarkers might be identified, which potentially will allow for the prediction of the quality of long-term histopathological outcome following NP exposure. This will also promote further development of scientifically sound adverse outcome pathways, which could path the way to predictive *in vitro* testing strategies, for inhalation hazard of NPs.

5. References

ACGIH. 2000. 2000 TLVs and BEIs. Based on the Documentations of the Threshold Limit Values and Biological Exposure Indices. In: A. C. o. G. I. Hygienists ed. Cincinnati, OH.

Adeleye, A. S., Conway, J. R., Perez, T., Rutten, P. and Keller, A. A. 2014. Influence of Extracellular Polymeric Substances on the Long-Term Fate, Dissolution, and Speciation of Copper-Based Nanoparticles. Environmental Science & Technology 48:12561-12568.

Aggarwal, P., Hall, J. B., McLeland, C. B., Dobrovolskaia, M. A. and McNeil, S. E. 2009. Nanoparticle interaction with plasma proteins as it relates to particle biodistribution, biocompatibility and therapeutic efficacy. Adv Drug Deliv Rev 61:428-437.

Ahamed, M., Akhtar, M. J., Alhadlaq, H. A. and Alshamsan, A. 2016. Copper ferrite nanoparticle-induced cytotoxicity and oxidative stress in human breast cancer MCF-7 cells. Colloids Surf B Biointerfaces 142:46-54.

Ahlinder, L., Ekstrand-Hammarstrom, B., Geladi, P. and Osterlund, L. 2013. Large uptake of titania and iron oxide nanoparticles in the nucleus of lung epithelial cells as measured by Raman imaging and multivariate classification. Biophysical journal 105:310-319.

Alessandrini, F., Vennemann, A., Gschwendtner, S., Neumann, A. U., Rothballer, M., Seher, T., ...Schmidt-Weber, C. B. 2017. Pro-Inflammatory versus Immunomodulatory Effects of Silver Nanoparticles in the Lung: The Critical Role of Dose, Size and Surface Modification. Nanomaterials (Basel) 7.

Amma, H., Naruse, K., Ishiguro, N. and Sokabe, M. 2005. Involvement of reactive oxygen species in cyclic stretch-induced NF-kappaB activation in human fibroblast cells. Br J Pharmacol 145:364-373.

Anthony, R. M., Urban, J. F., Jr., Alem, F., Hamed, H. A., Rozo, C. T., Boucher, J. L., ...Gause, W. C. 2006. Memory T(H)2 cells induce alternatively activated macrophages to mediate protection against nematode parasites. Nat Med 12:955-960.

Arts, J. H., Hadi, M., Irfan, M. A., Keene, A. M., Kreiling, R., Lyon, D., ...Landsiedel, R. 2015. A decision-making framework for the grouping and testing of nanomaterials (DF4nanoGrouping). Regul Toxicol Pharmacol 71:S1-27.

Asati, A., Santra, S., Kaittanis, C. and Perez, J. M. 2010. Surface-charge-dependent cell localization and cytotoxicity of cerium oxide nanoparticles. ACS Nano 4:5321-5331.

Asehnoune, K., Strassheim, D., Mitra, S., Kim, J. Y. and Abraham, E. 2004. Involvement of reactive oxygen species in Toll-like receptor 4-dependent activation of NF-kappa B. J Immunol 172:2522-2529.

Avramescu, M. L., Rasmussen, P. E., Chenier, M. and Gardner, H. D. 2017. Influence of pH, particle size and crystal form on dissolution behaviour of engineered nanomaterials. Environ Sci Pollut Res Int 24:1553-1564.

Bailey, M. R., Kreyling, W. G., Andre, S., Batchelor, A., Collier, C. G., Drosselmeyer, E., ...Talbot, R. J. 1989. An interspecies comparison of the lung clearance of inhaled monodisperse cobalt oxide particles—Part I: Objectives and summary of results. Journal of Aerosol Science 20:169-188.

Balasubramanian, S. K., Poh, K.-W., Ong, C.-N., Kreyling, W. G., Ong, W.-Y. and Yu, L. E. 2013. The effect of primary particle size on biodistribution of inhaled gold nano-agglomerates. Biomaterials 34:5439-5452.

Barna, B. P., Huizar, I., Malur, A., McPeek, M., Marshall, I., Jacob, M., ...Thomassen, M. J. 2013. Carbon nanotube-induced pulmonary granulomatous disease: Twist1 and alveolar macrophage M1 activation. Int J Mol Sci 14:23858-23871.

Bazzan, E., Turato, G., Tinè, M., Radu, C. M., Balestro, E., Rigobello, C., ...Cosio, M. G. 2017. Dual polarization of human alveolar macrophages progressively increases with smoking and COPD severity. Respiratory Research 18:40.

Becher, B., Schlitzer, A., Chen, J., Mair, F., Sumatoh, H. R., Teng, K. W. W., ...Newell, E. W. 2014. High-dimensional analysis of the murine myeloid cell system. Nature Immunology 15:1181.

Beningo, K. A. and Wang, Y. L. 2002. Fc-receptor-mediated phagocytosis is regulated by mechanical properties of the target. J Cell Sci 115:849-856.

Bermudez, E., Mangum, J. B., Wong, B. A., Asgharian, B., Hext, P. M., Warheit, D. B. and Everitt, J. I. 2004. Pulmonary responses of mice, rats, and hamsters to subchronic inhalation of ultrafine titanium dioxide particles. Toxicol Sci 77:347-357.

Berry, J. P., Meignan, M., Escaig, F. and Galle, P. 1988. Inhaled soluble aerosols insolubilised by lysosomes of alveolar cells. Application to some toxic compounds; electron microprobe and ion microprobe studies. Toxicology 52:127-139.

Bevan, R. J., Kreiling, R., Levy, L. S. and Warheit, D. B. 2018. Toxicity testing of poorly soluble particles, lung overload and lung cancer. Regul Toxicol Pharmacol 100:80-91.

Bhattacharjee, S., Ershov, D., Fytianos, K., van der Gucht, J., Alink, G. M., Rietjens, I. M., ...Zuilhof, H. 2012. Cytotoxicity and cellular uptake of tri-block copolymer nanoparticles with different size and surface characteristics. Part Fibre Toxicol 9:11.

Blackford, J. A., Jr., Antonini, J. M., Castranova, V. and Dey, R. D. 1994. Intratracheal instillation of silica up-regulates inducible nitric oxide synthase gene expression and increases nitric oxide production in alveolar macrophages and neutrophils. Am J Respir Cell Mol Biol 11:426-431.

Borm, P., Cassee, F. R. and Oberdörster, G. 2015. Lung particle overload: old school -new insights? Part Fibre Toxicol 12:10.

Borm, P. J., Robbins, D., Haubold, S., Kuhlbusch, T., Fissan, H., Donaldson, K., ...Oberdorster, E. 2006. The potential risks of nanomaterials: a review carried out for ECETOC. Part Fibre Toxicol 3:11.

Bove, P., Malvindi, M. A., Kote, S. S., Bertorelli, R., Summa, M. and Sabella, S. 2017. Dissolution test for risk assessment of nanoparticles: a pilot study. Nanoscale 9:6315-6326.

Bowden, D. H. 1984. The Alveolar Macrophage. Environmental Health Perspectives 55:327-341.

Bowden, D. H. 1987. Macrophages, dust, and pulmonary diseases. Exp Lung Res 12:89-107.

Braakhuis, H. M., Cassee, F. R., Fokkens, P. H., de la Fonteyne, L. J., Oomen, A. G., Krystek, P., ...Park, M. V. 2016. Identification of the appropriate dose metric for pulmonary inflammation of silver nanoparticles in an inhalation toxicity study. Nanotoxicology 10:63-73.

Brain, J. D. and Valberg, P. A. 1979. Deposition of aerosol in the respiratory tract. The American review of respiratory disease 120:1325-1373.

Brown, D. M., Wilson, M. R., MacNee, W., Stone, V. and Donaldson, K. 2001. Size-dependent proinflammatory effects of ultrafine polystyrene particles: a role for surface area and oxidative stress in the enhanced activity of ultrafines. Toxicol Appl Pharmacol 175:191-199.

Brunner, T. J., Wick, P., Manser, P., Spohn, P., Grass, R. N., Limbach, L. K., ...Stark, W. J. 2006. In vitro cytotoxicity of oxide nanoparticles: comparison to asbestos, silica, and the effect of particle solubility. Environ Sci Technol 40:4374-4381.

Buttner, C., Skupin, A., Reimann, T., Rieber, E. P., Unteregger, G., Geyer, P. and Frank, K. H. 1997. Local production of interleukin-4 during radiation-induced pneumonitis and pulmonary fibrosis in rats: macrophages as a prominent source of interleukin-4. Am J Respir Cell Mol Biol 17:315-325.

Champion, J. A., Walker, A. and Mitragotri, S. 2008. Role of particle size in phagocytosis of polymeric microspheres. Pharmaceutical research 25:1815-1821.

Chang, X., Fu, Y., Zhang, Y., Tang, M. and Wang, B. 2014. Effects of Th1 and Th2 cells balance in pulmonary injury induced by nano titanium dioxide. Environ Toxicol Pharmacol 37:275-283.

Chen, H. W., Su, S. F., Chien, C. T., Lin, W. H., Yu, S. L., Chou, C. C., ...Yang, P. C. 2006. Titanium dioxide nanoparticles induce emphysema-like lung injury in mice. FASEB J 20:2393-2395.

Cho, W. S., Duffin, R., Poland, C. A., Howie, S. E., MacNee, W., Bradley, M., ...Donaldson, K. 2010. Metal oxide nanoparticles induce unique inflammatory footprints in the lung: important implications for nanoparticle testing. Environ Health Perspect 118:1699-1706.

Christensen, V. R., Lund Jensen, S., Guldberg, M. and Kamstrup, O. 1994. Effect of chemical composition of man-made vitreous fibers on the rate of dissolution in vitro at different pHs. Environ Health Perspect 102 (Suppl 5):83-86.

Collier, Z. A., Kennedy, A. J., Poda, A. R., Cuddy, M. F., Moser, R. D., MacCuspie, R. I., ...Steevens, J. A. 2015. Tiered guidance for risk-informed environmental health and safety testing of nanotechnologies. Journal of Nanoparticle Research 17:155.

Colombo, C., Monhemius, A. J. and Plant, J. A. 2008. Platinum, palladium and rhodium release from vehicle exhaust catalysts and road dust exposed to simulated lung fluids. Ecotoxicology and Environmental Safety 71:722-730.

Creutzenberg, O., Bellmann, B., Korolewitz, R., Koch, W., Mangelsdorf, I., Tillmann, T. and Schaudien, D. 2012a. Change in agglomeration status and toxicokinetic fate of various nanoparticles in vivo following lung exposure in rats. Inhal Toxicol 24:821-830.

Creutzenberg, O. H., Ziemann, C. and Hansen, T. 2012b. Subacute and subchronic inhalation toxicity and dermal absorption of the nanoscaled zinc oxide Z-COTE HP1 in the rat. Toxicologist 126 (1):142–143.

Dale, A. L., Lowry, G. V. and Casman, E. A. 2015. Stream Dynamics and Chemical Transformations Control the Environmental Fate of Silver and Zinc Oxide Nanoparticles in a Watershed-Scale Model. Environmental Science & Technology 49:7285-7293.

Davis, J. M., Beckett, S. T., Bolton, R. E., Collings, P. and Middleton, A. P. 1978. Mass and number of fibres in the pathogenesis of asbestos-related lung disease in rats. British journal of cancer 37:673-688.

Davis, M. J., Tsang, T. M., Qiu, Y., Dayrit, J. K., Freij, J. B., Huffnagle, G. B. and Olszewski, M. A. 2013. Macrophage M1/M2 polarization dynamically adapts to changes in cytokine microenvironments in Cryptococcus neoformans infection. MBio 4:1-10.

de Waal Malefyt, R., Figdor, C. G., Huijbens, R., Mohan-Peterson, S., Bennett, B., Culpepper, J., ...de Vries, J. E. 1993. Effects of IL-13 on phenotype, cytokine production, and cytotoxic function of human monocytes. Comparison with IL-4 and modulation by IFN-gamma or IL-10. J Immunol 151:6370-6381.

Docter, D., Westmeier, D., Markiewicz, M., Stolte, S., Knauer, S. K. and Stauber, R. H. 2015. The nanoparticle biomolecule corona: lessons learned – challenge accepted? Chemical Society Reviews 44:6094-6121.

Donaldson, K., Brown, D., Clouter, A., Duffin, R., MacNee, W., Renwick, L., ...Stone, V. 2002. The pulmonary toxicology of ultrafine particles. Journal of aerosol medicine : the official journal of the International Society for Aerosols in Medicine 15:213-220.

Donaldson, K., Murphy, F. A., Duffin, R. and Poland, C. A. 2010a. Asbestos, carbon nanotubes and the pleural mesothelium: a review of the hypothesis regarding the role of long fibre retention in the parietal pleura, inflammation and mesothelioma. Particle and Fibre Toxicology 7:5.

Donaldson, K. and Poland, C. A. 2013. Nanotoxicity: challenging the myth of nano-specific toxicity. Current Opinion in Biotechnology 24:724-734.

Donaldson, K., Poland, C. A. and Schins, R. P. 2010b. Possible genotoxic mechanisms of nanoparticles: criteria for improved test strategies. Nanotoxicology 4:414-420.

Donaldson, K., Stone, V., Tran, C. L., Kreyling, W. and Borm, P. J. A. 2004. Nanotoxicology. Occupational and Environmental Medicine 61:727-728.

Dong, J. and Ma, Q. 2018. Macrophage polarization and activation at the interface of multi-walled carbon nanotube-induced pulmonary inflammation and fibrosis. Nanotoxicology 12:153-168.

Doshi, N. and Mitragotri, S. 2010. Macrophages recognize size and shape of their targets. PLoS One 5:e10051.

Duffin, R., Tran, L., Brown, D., Stone, V. and Donaldson, K. 2007. Proinflammogenic effects of low-toxicity and metal nanoparticles in vivo and in vitro: highlighting the role of particle surface area and surface reactivity. Inhal Toxicol 19:849-856.

Duffin, R., Tran, L., Clouter, A., Brown, D., MacNee, W., Stone, V. and Donaldson, K. 2002. The Importance of Surface Area and Specific Reactivity in the Acute Pulmonary Inflammatory Response to Particles.

Duque-Correa, M. A., Kuhl, A. A., Rodriguez, P. C., Zedler, U., Schommer-Leitner, S., Rao, M., ...Reece, S. T. 2014. Macrophage arginase-1 controls bacterial growth and pathology in hypoxic tuberculosis granulomas. Proc Natl Acad Sci U S A 111:E4024-4032.

ECETOC. 2013. European Centre for Ecotoxicology and Toxicology of Chemicals. Poorly Soluble Particles/ Lung Overload. Technical Report No. 122.

Edwards, J. P., Zhang, X., Frauwirth, K. A. and Mosser, D. M. 2006. Biochemical and functional characterization of three activated macrophage populations. J Leukoc Biol 80:1298-1307.

Ehrt, S., Schnappinger, D., Bekiranov, S., Drenkow, J., Shi, S., Gingeras, T. R., ...Nathan, C. 2001. Reprogramming of the macrophage transcriptome in response to interferon-gamma and Mycobacterium tuberculosis: signaling roles of nitric oxide synthase-2 and phagocyte oxidase. J Exp Med 194:1123-1140.

Eidi, H., Joubert, O., Attik, G., Duval, R. E., Bottin, M. C., Hamouia, A., ...Rihn, B. H. 2010. Cytotoxicity assessment of heparin nanoparticles in NR8383 macrophages. Int J Pharm 396:156-165.

Einbrodt, H. J., Wobker, F. and Klippel, H.-G. 1972. Tierexperimentelle Untersuchungen über Ablagerung und Verteilung von BaSO4 im Rattenorganismus nach Inhalation. Int Arch Arbeitsmed 30:237-244.

Elder, A. and Oberdörster, G. 2006. Translocation and effects of ultrafine particles outside of the lung. Clin Occup Environ Med 5:785-796.

Fels, A. O. and Cohn, Z. A. 1986. The alveolar macrophage. J Appl Physiol (1985) 60:353-369.

Ferin, J., Oberdörster, G. and Penney, D. P. 1992. Pulmonary retention of ultrafine and fine particles in rats. Am J Respir Cell Mol Biol 6:535-542.

Fritsch-Decker, S., Marquardt, C., Stoeger, T., Diabate, S. and Weiss, C. 2018. Revisiting the stress paradigm for silica nanoparticles: decoupling of the anti-oxidative defense, pro-inflammatory response and cytotoxicity. Arch Toxicol 92:2163-2174.

Fujita, K., Horie, M., Kato, H., Endoh, S., Suzuki, M., Nakamura, A., ...Nakanishi, J. 2009. Effects of ultrafine TiO2 particles on gene expression profile in human keratinocytes without illumination: involvement of extracellular matrix and cell adhesion. Toxicol Lett 191:109-117.

Gao, X. and Lowry, G. V. 2018. Progress towards standardized and validated characterizations for measuring physicochemical properties of manufactured nanomaterials relevant to nano health and safety risks. NanoImpact 9:14-30.

Gazi, U. and Martinez-Pomares, L. 2009. Influence of the mannose receptor in host immune responses. Immunobiology 214:554-561.

Gebel, T., Foth, H., Damm, G., Freyberger, A., Kramer, P. J. r., Lilienblum, W., ...Hengstler, J. G. 2014. Manufactured nanomaterials: categorization and approaches to hazard assessment. Archives of Toxicology 88:2191-2211.

Geiser, M. 2010. Update on macrophage clearance of inhaled micro- and nanoparticles. J Aerosol Med Pulm Drug Deliv 23:207-217.

Geiser, M., Casaulta, M., Kupferschmid, B., Schulz, H., Semmler-Behnke, M. and Kreyling, W. 2008. The role of macrophages in the clearance of inhaled ultrafine titanium dioxide particles. Am J Respir Cell Mol Biol 38:371-376.

Geiser, M. and Kreyling, W. G. 2010. Deposition and biokinetics of inhaled nanoparticles. Particle and fibre toxicology 7:2-2.

Geiser, M., Rothen-Rutishauser, B., Kapp, N., Schurch, S., Kreyling, W., Schulz, H., ...Gehr, P. 2005. Ultrafine particles cross cellular membranes by nonphagocytic mechanisms in lungs and in cultured cells. Environ Health Perspect 113:1555-1560.

Ghiazza, M., Polimeni, M., Fenoglio, I., Gazzano, E., Ghigo, D. and Fubini, B. 2010. Does vitreous silica contradict the toxicity of the crystalline silica paradigm? Chem Res Toxicol 23:620-629.

Godwin, H., Nameth, C., Avery, D., Bergeson, L. L., Bernard, D., Beryt, E., ...Nel, A. E. 2015. Nanomaterial Categorization for Assessing Risk Potential To Facilitate Regulatory Decision-Making. ACS Nano 9:3409-3417.

Goldstein, E., Lippert, W. and Warshauer, D. 1974. Pulmonary alveolar macrophage. Defender against bacterial infection of the lung. J Clin Invest 54:519-528.

Gordon, S. 2003. Alternative activation of macrophages. Nat Rev Immunol 3:23-35.

Gordon, S., Plüddemann, A. and Martinez Estrada, F. 2014. Macrophage heterogeneity in tissues: Phenotypic diversity and functions. Immunological Reviews 262:36-55.

Gordon, S. B. and Read, R. C. 2002. Macrophage defences against respiratory tract infections: The immunology of childhood respiratory infections. British Medical Bulletin 61:45-61.

Graham, U., Fernback, J., Wang, C., Dozier, A., Drummy, L., Mahalingam, K., ...Brain, J. 2017a. Calcium co-Localization with in vivo Cerium Phosphate Nanoparticle Formation after Intratracheal Instillation Dosing with CeCl3 or CeO2 NPs.

Graham, U. M., Jacobs, G., Yokel, R. A., Davis, B. H., Dozier, A. K., Birch, M. E., ...DeLouise, L. 2017b. From Dose to Response: In Vivo Nanoparticle Processing and Potential Toxicity. Adv Exp Med Biol 947:71-100.

Graham, U. M., Yokel, R. A., Dozier, A. K., Drummy, L., Mahalingam, K., Tseng, M. T., ...Fernback, J. 2018. Analytical High-resolution Electron Microscopy Reveals Organ-specific Nanoceria Bioprocessing. Toxicologic Pathology 46:47-61.

Gray, E. P., Browning, C. L., Wang, M., Gion, K. D., Chao, E. Y., Koski, K. J., ...Hurt, R. H. 2018. Biodissolution and cellular response to MoO3 nanoribbons and a new framework for early hazard screening for 2D materials. Environmental Science: Nano 5:2545-2559.

Green, F. H., Boyd, R. L., Danner-Rabovsky, J., Fisher, M. J., Moorman, W. J., Ong, T. M., ...et al. 1983. Inhalation studies of diesel exhaust and coal dust in rats. Scand J Work Environ Health 9:181-188.

Grosche, J., Meißner, J. and Eble, J. A. 2018. More than a syllable in fib-ROS-is: The role of ROS on the fibrotic extracellular matrix and on cellular contacts. Molecular Aspects of Medicine 63:30-46.

Guilliams, M., De Kleer, I., Henri, S., Post, S., Vanhoutte, L., De Prijck, S., ...Lambrecht, B. N. 2013. Alveolar macrophages develop from fetal monocytes that differentiate into long-lived cells in the first week of life via GM-CSF. J Exp Med 210:1977-1992.

Guldberg, M., Christensen, V. R., Krois, W. and Sebastian, K. 1995. Method for determining in-vitro dissolution rates of man-made vitreous fibres. Glastech Ber Glass Sci Technol 68:181-187.

Gunday Tureli, N., Torge, A., Juntke, J., Schwarz, B. C., Schneider-Daum, N., Tureli, A. E., ...Schneider, M. 2017. Ciprofloxacin-loaded PLGA nanoparticles against cystic fibrosis P. aeruginosa lung infections. Eur J Pharm Biopharm 117:363-371.

Guth, A. M., Janssen, W. J., Bosio, C. M., Crouch, E. C., Henson, P. M. and Dow, S. W. 2009. Lung environment determines unique phenotype of alveolar macrophages. Am J Physiol Lung Cell Mol Physiol 296:L936-946.

Han, S. G., Lee, J. S., Ahn, K., Kim, Y. S., Kim, J. K., Lee, J. H., ...Yu, I. J. 2015. Size-dependent clearance of gold nanoparticles from lungs of Sprague-Dawley rats after short-term inhalation exposure. Arch Toxicol 89:1083-1094.

Hancock, A., Armstrong, L., Gama, R. and Millar, A. 1998. Production of interleukin 13 by alveolar macrophages from normal and fibrotic lung. Am J Respir Cell Mol Biol 18:60-65.

Hashimoto, D., Chow, A., Noizat, C., Teo, P., Beasley, M. B., Leboeuf, M., ...Merad, M. 2013. Tissue-resident macrophages self-maintain locally throughout adult life with minimal contribution from circulating monocytes. Immunity 38:792-804.

Heinrich, U., Fuhst, R., Rittinghausen, S., Creutzenberg, O., Bellmann, B., Koch, W. and Levsen, K. 1995. Chronic inhalation exposure of wistar rats and two different strains of mice to diesel engine exhaust, carbon black, and titanium dioxide. Inhal Toxicol 7:533-556.

Hesse, M., Modolell, M., La Flamme, A. C., Schito, M., Fuentes, J. M., Cheever, A. W., ...Wynn, T. A. 2001. Differential Regulation of Nitric Oxide Synthase-2 and Arginase-1 by Type 1/Type 2 Cytokines In Vivo: Granulomatous Pathology Is Shaped by the Pattern of L-Arginine Metabolism. The Journal of Immunology 167:6533-6544.

Heyder, J. 1982. Particle transport onto human airway surfaces. Eur J Respir Dis Suppl 119:29-50.

Heyder, J., Gebhart, J., Rudolf, G., Schiller, C. F. and Stahlhofen, W. 1986. Deposition of particles in the human respiratory tract in the size range 0.005–15 μm. Journal of Aerosol Science 17:811-825.

Hofmann, W., Bálásházy, I., Heistracher, T. and Koblinger, L. 1996. The Significance of Particle Deposition Patterns in Bronchial Airway Bifurcations for Extrapolation Modeling. Aerosol Science and Technology 25:305-327.

Horie, M., Nishio, K., Fujita, K., Kato, H., Endoh, S., Suzuki, M., ...Yoshida, Y. 2010. Cellular responses by stable and uniform ultrafine titanium dioxide particles in culture-medium dispersions when secondary particle size was 100 nm or less. Toxicol In Vitro 24:1629-1638.

Hussell, T. and Bell, T. J. 2014. Alveolar macrophages: plasticity in a tissue-specific context. Nat Rev Immunol 14:81-93.

ICRP. 1994. Human Respiratory Tract Model for Radiological Protection. International Commission on Radiological Protection - Publication 66 Ann 24:1-3.

Ivask, A., Titma, T., Visnapuu, M., Vija, H., Kakinen, A., Sihtmae, M., ...Kahru, A. 2015. Toxicity of 11 Metal Oxide Nanoparticles to Three Mammalian Cell Types In Vitro. Current topics in medicinal chemistry 15:1914-1929.

Johnston, C. J., Driscoll, K. E., Finkelstein, J. N., Baggs, R., O'Reilly, M. A., Carter, J., ...Oberdörster, G. 2000. Pulmonary Chemokine and Mutagenic Responses in Rats after Subchronic Inhalation of Amorphous and Crystalline Silica. Toxicological Sciences 56:405-413.

Kambara, K., Ohashi, W., Tomita, K., Takashina, M., Fujisaka, S., Hayashi, R., ...Hattori, Y. 2015. In vivo depletion of CD206+ M2 macrophages exaggerates lung injury in endotoxemic mice. Am J Pathol 185:162-171.

Kasai, T., Umeda, Y., Ohnishi, M., Mine, T., Kondo, H., Takeuchi, T., ...Fukushima, S. 2016. Lung carcinogenicity of inhaled multi-walled carbon nanotube in rats. Part Fibre Toxicol 13:53.

Kass, E. H. 1964. THE ROLE OF T H E ALVEOLAR MACROPHAGE IN THE CLEARANCE OF BACTERIA FROM THE LUNG * (From the Channing Laboratory , Mallory Institute of Pathology , Thorndike Memorial Laboratory , and Second and Fourth (Harvard) Medical Semices , Boston City Hospital. Methods.

Keller, J., Wohlleben, W., Ma-Hock, L., Strauss, V., Gröters, S., Kuttler, K., ...Landsiedel, R. 2014. Time course of lung retention and toxicity of inhaled particles: short-term exposure to nano-Ceria. Arch Toxicol 88:2033-2059.

Kermanizadeh, A., Balharry, D., Wallin, H., Loft, S. and Moller, P. 2015. Nanomaterial translocation--the biokinetics, tissue accumulation, toxicity and fate of materials in secondary organs--a review. Crit Rev Toxicol 45:837-872.

Klaessig, F. C. 2018. Dissolution as a paradigm in regulating nanomaterials. Environmental Science: Nano 5:1070-1077.

Klein, C. L., Wiench, K., Wiemann, M., Ma-Hock, L., van Ravenzwaay, B. and Landsiedel, R. 2012. Hazard identification of inhaled nanomaterials: making use of short-term inhalation studies. Arch Toxicol 86:1137-1151.

Koltermann-Jülly, J., Keller, J. G., Vennemann, A., Werle, K., Müller, P., Ma-Hock, L., ...Wohlleben, W. 2018. Abiotic dissolution rates of 24 (nano)forms of 6 substances compared to macrophage-assisted dissolution and in vivo pulmonary clearance: Grouping by biodissolution and transformation. NanoImpact 12:29-41.

Konduru, N., Keller, J., Ma-Hock, L., Gröters, S., Landsiedel, R., Donaghey, T. C., ...Molina, R. M. 2014. Biokinetics and effects of barium sulfate nanoparticles. Particle and fibre toxicology 11:55-55.

Kreyling, W. G., Semmler, M., Erbe, F., Mayer, P., Takenaka, S., Schulz, H., ...Ziesenis, A. 2002. Translocation of ultrafine insoluble iridium particles from lung epithelium to extrapulmonary organs is size dependent but very low. J Toxicol Environ Health A 65:1513-1530.

Kroll, A., Dierker, C., Rommel, C., Hahn, D., Wohlleben, W., Schulze-Isfort, C., ...Schnekenburger, J. 2011. Cytotoxicity screening of 23 engineered nanomaterials using a test matrix of ten cell lines and three different assays. Part Fibre Toxicol 8:9.

Kroll, A., Gietl, J. K., Wiesmuller, G. A., Gunsel, A., Wohlleben, W., Schnekenburger, J. and Klemm, O. 2013. In vitro toxicology of ambient particulate matter: correlation of cellular effects with particle size and components. Environ Toxicol 28:76-86.

Kuhlbusch, T. A. J., Wijnhoven, S. W. P. and Haase, A. 2018. Nanomaterial exposures for worker, consumer and the general public. NanoImpact 10:11-25.

Kumar, A., Bicer, E. M., Morgan, A. B., Pfeffer, P. E., Monopoli, M., Dawson, K. A., ...Mudway, I. S. 2016a. Enrichment of immunoregulatory proteins in the biomolecular corona of nanoparticles within human respiratory tract lining fluid. Nanomedicine: Nanotechnology, Biology and Medicine 12:1033-1043.

Kumar, S., Meena, R. and Paulraj, R. 2016b. Role of Macrophage (M1 and M2) in Titanium-Dioxide Nanoparticle-Induced Oxidative Stress and Inflammatory Response in Rat. Appl Biochem Biotechnol 180:1257-1275.

Landsiedel, R., Fabian, E., Ma-Hock, L., Wohlleben, W., Wiench, K., Oesch, F. and Van Ravenzwaay, B. 2012. Toxico-/biokinetics of nanomaterials. Archives of Toxicology 86:1021-1060.

Landsiedel, R., Ma-Hock, L., Hofmann, T., Wiemann, M., Strauss, V., Treumann, S., ...van Ravenzwaay, B. 2014. Application of short-term inhalation studies to assess the inhalation toxicity of nanomaterials. Part Fibre Toxicol 11:16.

Landsiedel, R., Ma-Hock, L., Kroll, A., Hahn, D., Schnekenburger, J., Wiench, K. and Wohlleben, W. 2010. Testing metal-oxide nanomaterials for human safety. Adv Mater 22:2601-2627.

Landsiedel, R., Sauer, U. G. and De Jong, W. H. 2017. Chapter 8: Risk Assessment and Risk Management. Adverse Effects of Engineered Nanomaterials - Exposure, Toxicology, and Impact on Human Health. Academic Press, 189–222.

Landsiedel, R., Wiench, K. and Wohlleben, W. 2008. Geeignete Methoden zur Prüfung der Sicherheit von Nanomaterialien. Chemie Ingenieur Technik 80(11):1641-1651.

Laskin, D. L. 2009. Macrophages and inflammatory mediators in chemical toxicity: a battle of forces. Chem Res Toxicol 22:1376-1385.

Laskin, D. L., Malaviya, R. and Laskin, J. D. 2019. Role of Macrophages in Acute Lung Injury and Chronic Fibrosis Induced by Pulmonary Toxicants. Toxicol Sci 168:287-301.

Laskin, D. L., Sunil, V. R., Gardner, C. R. and Laskin, J. D. 2011. Macrophages and tissue injury: agents of defense or destruction? Annu Rev Pharmacol Toxicol 51:267-288.

Lauweryns, J. M. and Baert, J. H. 1977. Alveolar clearance and the role of the pulmonary lymphatics. The American review of respiratory disease 115:625-625.

Laux, P., Riebeling, C., Booth, A. M., Brain, J. D., Brunner, J., Cerrillo, C., ...Luch, A. 2017. Biokinetics of Nanomaterials: The Role of Biopersistence. NanoImpact 6:69-80.

Lee, S. J., Evers, S., Roeder, D., Parlow, A. F., Risteli, J., Risteli, L., ...Nussenzweig, M. C. 2002. Mannose receptor-mediated regulation of serum glycoprotein homeostasis. Science 295:1898-1901.

Lepeltier, E. A., Nuhn, L., Lehr, C. M. and Zentel, R. 2015. Not just for tumor targeting: unmet medical needs and opportunities for nanomedicine. Nanomedicine (Lond) 10:3147-3166.

Levy, L., Chaudhuri, I. S., Krueger, N. and McCunney, R. J. 2012. Does Carbon Black Disaggregate in Lung Fluid? A Critical Assessment. Chemical Research in Toxicology 25:2001-2006.

Li, B., Hu, Y., Zhao, Y., Cheng, M., Qin, H., Cheng, T., ...Zhang, X. 2017a. Curcumin Attenuates Titanium Particle-Induced Inflammation by Regulating Macrophage Polarization In Vitro and In Vivo. Front Immunol 8:55.

Li, K., Shen, Q., Xie, Y., You, M., Huang, L. and Zheng, X. 2017b. Incorporation of cerium oxide into hydroxyapatite coating regulates osteogenic activity of mesenchymal stem cell and macrophage polarization. J Biomater Appl 31:1062-1076.

Li, R., Ji, Z., Chang, C. H., Dunphy, D. R., Cai, X., Meng, H., ...Xia, T. 2014. Surface Interactions with Compartmentalized Cellular Phosphates Explain Rare Earth Oxide Nanoparticle Hazard and Provide Opportunities for Safer Design. ACS Nano 8:1771-1783.

Limbach, L. K., Wick, P., Manser, P., Grass, R. N., Bruinink, A. and Stark, W. J. 2007. Exposure of engineered nanoparticles to human lung epithelial cells: influence of chemical composition and catalytic activity on oxidative stress. Environ Sci Technol 41:4158-4163.

Lison, D., Lardot, C., Huaux, F., Zanetti, G. and Fubini, B. 1997. Influence of particle surface area on the toxicity of insoluble manganese dioxide dusts. Arch Toxicol 71:725-729.

Lison, D., Thomassen, L. C., Rabolli, V., Gonzalez, L., Napierska, D., Seo, J. W., ...Martens, J. A. 2008. Nominal and effective dosimetry of silica nanoparticles in cytotoxicity assays. Toxicol Sci 104:155-162.

Liu, R., Zhang, X., Pu, Y., Yin, L., Li, Y., Zhang, X., ...Zhang, J. 2010. Small-sized titanium dioxide nanoparticles mediate immune toxicity in rat pulmonary alveolar macrophages in vivo. J Nanosci Nanotechnol 10:5161-5169.

Lu, H. L., Huang, X. Y., Luo, Y. F., Tan, W. P., Chen, P. F. and Guo, Y. B. 2018. Activation of M1 macrophages plays a critical role in the initiation of acute lung injury. Bioscience reports 38.

Lu, S., Zhang, W., Zhang, R., Liu, P., Wang, Q., Shang, Y., ...Wang, Q. 2015. Comparison of cellular toxicity caused by ambient ultrafine particles and engineered metal oxide nanoparticles. Part Fibre Toxicol 12:5.

Lucarelli, M., Gatti, A. M., Savarino, G., Quattroni, P., Martinelli, L., Monari, E. and Boraschi, D. 2004. Innate defence functions of macrophages can be biased by nano-sized ceramic and metallic particles. Eur Cytokine Netw 15:339-346.

Lujan, H. and Sayes, C. M. 2017. Cytotoxicological pathways induced after nanoparticle exposure: studies of oxidative stress at the 'nano-bio' interface. Toxicol Res (Camb) 6:580-594.

Ma-Hock, L., Burkhardt, S., Strauss, V., Gamer, A. O., Wiench, K., van Ravenzwaay, B. and Landsiedel, R. 2009a. Development of a short-term inhalation test in the rat using nano-titanium dioxide as a model substance. Inhal Toxicol 21:102-118.

Ma-Hock, L., Gamer, A. O., Landsiedel, R., Leibold, E., Frechen, T., Sens, B., ...van Ravenzwaay, B. 2007. Generation and Characterization of Test Atmospheres with Nanomaterials. Inhalation Toxicology 19:833-848.

Ma-Hock, L., Gröters, S., Strauss, V., Keller, J., Wiench, K., van Ravenzwaay, B. and Landsiedel, R. 2017. Long-term inhalation study with CeO2- and BaSO4 nanomaterials – study design, in-life findings, and lung burden. Eurotox 2017.

Ma-Hock, L., Treumann, S., Strauss, V., Brill, S., Luizi, F., Mertler, M., ...Landsiedel, R. 2009b. Inhalation toxicity of multiwall carbon nanotubes in rats exposed for 3 months. Toxicol Sci 112:468-481.

Ma, Zhao, Mercer, Barger, Rao, Meighan, ...Ma. 2011. Cerium oxide nanoparticle-induced pulmonary inflammation and alveolar macrophage functional change in rats. Nanotoxicology 5:312-325.

Ma, J., Becker, C., Lowell, C. A. and Underhill, D. M. 2012. Dectin-1-triggered recruitment of light chain 3 protein to phagosomes facilitates major histocompatibility complex class II presentation of fungal-derived antigens. The Journal of biological chemistry 287:34149-34156.

Mackaness, G. B. 1964. The Immunological Basis of Acquired Cellular Resistance. J Exp Med 120:105-120.

MacMicking, J., Xie, Q. W. and Nathan, C. 1997. Nitric oxide and macrophage function. Annu Rev Immunol 15:323-350.

Marques, M. R. C., Loebenberg, R. and Almukainzi, M. 2011. Simulated biological fluids with possible application in dissolution testing. Dissolution Technologies:15-28.

Martinez-Pomares, L. 2012. The mannose receptor. J Leukoc Biol 92:1177-1186.

Martinez, F. O. and Gordon, S. 2014. The M1 and M2 paradigm of macrophage activation: time for reassessment. F1000Prime Rep 6:13.

Martinez, F. O., Sica, A., Mantovani, A. and Locati, M. 2008. Macrophage activation and polarization. Front Biosci 13:453-461.

Mattila, J. T., Ojo, O. O., Kepka-Lenhart, D., Marino, S., Kim, J. H., Eum, S. Y., ...Flynn, J. L. 2013. Microenvironments in tuberculous granulomas are delineated by distinct populations of macrophage subsets and expression of nitric oxide synthase and arginase isoforms. J Immunol 191:773-784.

Mauderly, J. L., Jones, R. K., Griffith, W. C., Henderson, R. F. and McClellan, R. O. 1987. Diesel exhaust is a pulmonary carcinogen in rats exposed chronically by inhalation. Toxicological Sciences 9:208-221.

Maus, U. A., Janzen, S., Wall, G., Srivastava, M., Blackwell, T. S., Christman, J. W., ...Lohmeyer, J. 2006. Resident alveolar macrophages are replaced by recruited

monocytes in response to endotoxin-induced lung inflammation. Am J Respir Cell Mol Biol 35:227-235.

Maynard, A. D. and Kuempel, E. D. 2005. Airborne Nanostructured Particles and Occupational Health. Journal of Nanoparticle Research 7:587-614.

McClellan, R. O., Mauderly, J. L., Jones, R. K. and Cuddihy, R. G. 1985. Health effects of diesel exhaust. A contemporary air pollution issue. Postgrad Med 78:199-201, 204-197.

McKenzie, G. J., Fallon, P. G., Emson, C. L., Grencis, R. K. and McKenzie, A. N. 1999. Simultaneous disruption of interleukin (IL)-4 and IL-13 defines individual roles in T helper cell type 2-mediated responses. J Exp Med 189:1565-1572.

McNeil, P. L., Tanasugarn, L., Meigs, J. B. and Taylor, D. L. 1983. Acidification of phagosomes is initiated before lysosomal enzyme activity is detected. The Journal of cell biology 97:692-702.

Meng, J., Li, X., Wang, C., Guo, H., Liu, J. and Xu, H. 2015. Carbon nanotubes activate macrophages into a M1/M2 mixed status: recruiting naive macrophages and supporting angiogenesis. ACS Appl Mater Interfaces 7:3180-3188.

Mercer, T. T. 1967. On the role of particle size in the dissolution of lung burdens. Health Phys 13:1211-1221.

Miao, X., Leng, X. and Zhang, Q. 2017. The Current State of Nanoparticle-Induced Macrophage Polarization and Reprogramming Research. Int J Mol Sci 18.

Mills, C. D. 2001. Macrophage arginine metabolism to ornithine/urea or nitric oxide/citrulline: a life or death issue. Crit Rev Immunol 21:399-425.

Mills, C. D. 2012. M1 and M2 Macrophages: Oracles of Health and Disease. Critical reviews in immunology 32:463-488.

Mills, C. D., Lenz, L. L. and Ley, K. 2015. Macrophages at the fork in the road to health or disease. Front Immunol 6:59.

Mills, C. D., Shearer, J., Evans, R. and Caldwell, M. D. 1992. Macrophage arginine metabolism and the inhibition or stimulation of cancer. Journal of immunology (Baltimore, Md : 1950) 149:2709-2714.

Missaoui, W. N., Arnold, R. D. and Cummings, B. S. 2018. Toxicological status of nanoparticles: What we know and what we don't know. Chemico-Biological Interactions 295:1-12.

Mitrano, D. M. and Nowack, B. 2017. The need for a life-cycle based aging paradigm for nanomaterials: importance of real-world test systems to identify realistic particle transformations. Nanotechnology 28:072001.

Morfeld, P., Treumann, S., Ma-Hock, L., Bruch, J. and Landsiedel, R. 2012. Deposition behavior of inhaled nanostructured TiO2 in rats: fractions of particle diameter below 100 nm

(nanoscale) and the slicing bias of transmission electron microscopy. Inhalation Toxicology 24:939-951.

Morimoto, Y., Izumi, H., Yoshiura, Y., Tomonaga, T., Oyabu, T., Myojo, T., ...Sasaki, T. 2015. Pulmonary toxicity of well-dispersed cerium oxide nanoparticles following intratracheal instillation and inhalation. J Nanopart Res 17:442.

Morrow, P. E. 1988. Possible mechanisms to explain dust overloading of the lungs. Fundamental and applied toxicology : official journal of the Society of Toxicology 10:369-384.

Muhle, H., Kittel, B., Ernst, H., Mohr, U. and Mermelstein, R. 1995. Neoplastic lung lesions in rat after chronic exposure to crystalline silica. Scand J Work Environ Health 21 Suppl 2:27-29.

Nagayama, S., Ogawara, K., Fukuoka, Y., Higaki, K. and Kimura, T. 2007. Time-dependent changes in opsonin amount associated on nanoparticles alter their hepatic uptake characteristics. Int J Pharm 342:215-221.

Nel, A., Xia, T., Mädler, L. and Li, N. 2006. Toxic potential of materials at the nanolevel. Science (New York, NY) 311:622-627.

Nel, A., Xia, T., Meng, H., Wang, X., Lin, S., Ji, Z. and Zhang, H. 2013. Nanomaterial toxicity testing in the 21st century: use of a predictive toxicological approach and high-throughput screening. Acc Chem Res 46:607-621.

Nikota, J., Banville, A., Goodwin, L. R., Wu, D., Williams, A., Yauk, C. L., ...Halappanavar, S. 2017. Stat-6 signaling pathway and not Interleukin-1 mediates multi-walled carbon nanotube-induced lung fibrosis in mice: insights from an adverse outcome pathway framework. Part Fibre Toxicol 14:37.

Nikula, K. J. 2000. Rat lung tumors induced by exposure to selected poorly soluble nonfibrous particles. Inhalation Toxicology 12:97-119.

Nikula, K. J., Avila, K. J., Griffith, W. C. and Mauderly, J. L. 1997. Lung tissue responses and sites of particle retention differ between rats and cynomolgus monkeys exposed chronically to diesel exhaust and coal dust. Fundamental and applied toxicology : official journal of the Society of Toxicology 37:37-53.

Nti. 2017. PD ISO/TR 19057:2017 - Nanotechnologies. Use and application of acellular in vitro tests and methodologies to assess nanomaterial biodurability. Nanotechnologies Use and application of acellular in vitro tests and methodologies to assess nanomaterial biodurability.

Oberdorster, G. 2002. Toxicokinetics and effects of fibrous and nonfibrous particles. Inhal Toxicol 14:29-56.

Oberdörster, G. 1988. Lung Clearance of Inhaled Insoluble and Soluble Particles. Journal of Aerosol Medicine 1:289-330.

Oberdörster, G. 2000. Toxicology of ultrafine particles: in vivo studies. Philosophical Transactions of the Royal Society of London Series A: Mathematical, Physical and Engineering Sciences 358:2719-2740.

Oberdörster, G., Ferin, J., Gelein, R., Soderholm, S. C. and Finkelstein, J. 1992a. Role of the alveolar macrophage in lung injury: studies with ultrafine particles. Environ Health Perspect 97:193-199.

Oberdörster, G., Ferin, J. and Lehnert, B. E. 1994a. Correlation between particle size, in vivo particle persistence, and lung injury. Environmental health perspectives 102 Suppl 5:173-179.

Oberdörster, G., Ferin, J. and Morrow, P. E. 1992b. Volumetric loading of alveolar macrophages (AM): a possible basis for diminished AM-mediated particle clearance. Experimental lung research 18:87-104.

Oberdörster, G., Ferin, J., Soderholm, S., Gelein, R., Cox, C., Baggs, R. and Morrow, P. E. 1994b. Increased Pulmonary Toxicity of Inhaled Ultrafine Particles: Due to Lung Overload Alone? The Annals of Occupational Hygiene 38:295-302.

Oberdörster, G. and Kuhlbusch, T. A. J. 2018. In vivo effects: Methodologies and biokinetics of inhaled nanomaterials. NanoImpact 10:38-60.

Oberdörster, G., Oberdörster, E. and Oberdörster, J. 2005. Nanotoxicology: an emerging discipline evolving from studies of ultrafine particles. Environ Health Perspect 113:823-839.

Oberdörster, G., Sharp, Z., Atudorei, V., Elder, A., Gelein, R., Lunts, A., ...Cox, C. 2002. Extrapulmonary translocation of ultrafine carbon particles following whole-body inhalation exposure of rats. J Toxicol Environ Health A 65:1531-1543.

Oesch, F. and Landsiedel, R. 2012. Genotoxicity investigations on nanomaterials. Arch Toxicol 86:985-994.

Oomen, A. G., Bleeker, E. A. J., Bos, P. M. J., van Broekhuizen, F., Gottardo, S., Groenewold, M., ...Landsiedel, R. 2015. Grouping and Read-Across Approaches for Risk Assessment of Nanomaterials. International journal of environmental research and public health 12:13415-13434.

Oomen, A. G., Steinhäuser, K. G., Bleeker, E. A. J., van Broekhuizen, F., Sips, A., Dekkers, S., ...Sayre, P. G. 2018. Risk assessment frameworks for nanomaterials: Scope, link to regulations, applicability, and outline for future directions in view of needed increase in efficiency. NanoImpact 9:1-13.

Opanasopit, P., Nishikawa, M. and Hashida, M. 2002. Factors affecting drug and gene delivery: effects of interaction with blood components. Crit Rev Ther Drug Carrier Syst 19:191-233.

Ovais, M., Guo, M. and Chen, C. 2019. Tailoring Nanomaterials for Targeting Tumor-Associated Macrophages. Advanced materials (Deerfield Beach, Fla):e1808303.

Pauluhn, J. 2009a. Comparative pulmonary response to inhaled nanostructures: considerations on test design and endpoints. Inhalation Toxicology 21:40-54.

Pauluhn, J. 2009b. Pulmonary toxicity and fate of agglomerated 10 and 40 nm aluminum oxyhydroxides following 4-week inhalation exposure of rats: toxic effects are determined by agglomerated, not primary particle size. Toxicol Sci 109:152-167.

Pauluhn, J. 2011. Poorly soluble particulates: Searching for a unifying denominator of nanoparticles and fine particles for DNEL estimation. Toxicology 279:176-188.

Pauluhn, J. 2012. Subchronic inhalation toxicity of iron oxide (magnetite, Fe(3) O(4)) in rats: pulmonary toxicity is determined by the particle kinetics typical of poorly soluble particles. J Appl Toxicol 32:488-504.

Pauluhn, J. 2014. Derivation of occupational exposure levels (OELs) of low-toxicity isometric biopersistent particles: How can the kinetic lung overload paradigm be used for improved inhalation toxicity study design and OEL-derivation? Part Fibre Toxicol 11:72.

Pelaz, B., Alexiou, C., Alvarez-Puebla, R. A., Alves, F., Andrews, A. M., Ashraf, S., ...Parak, W. J. 2017. Diverse Applications of Nanomedicine. ACS Nano 11:2313-2381.

Pepelko, W. E., Mattox, J. K., Yang, Y. Y. and Moore, W., Jr. 1980. Pulmonary function and pathology in cats exposed 28 days to diesel exhaust. J Environ Pathol Toxicol 4:449-457.

Pesce, J. T., Ramalingam, T. R., Mentink-Kane, M. M., Wilson, M. S., El Kasmi, K. C., Smith, A. M., ...Wynn, T. A. 2009. Arginase-1-expressing macrophages suppress Th2 cytokine-driven inflammation and fibrosis. PLoS Pathog 5:e1000371.

Plakhova, T. V., Romanchuk, A. Y., Yakunin, S. N., Dumas, T., Demir, S., Wang, S., ...Kalmykov, S. N. 2016. Solubility of Nanocrystalline Cerium Dioxide: Experimental Data and Thermodynamic Modeling. The Journal of Physical Chemistry C 120:22615-22626.

Platt, N. and Gordon, S. 1998. Scavenger receptors: diverse activities and promiscuous binding of polyanionic ligands. Chemistry & biology 5:R193-203.

Polimeni, M., Gazzano, E., Ghiazza, M., Fenoglio, I., Bosia, A., Fubini, B. and Ghigo, D. 2008. Quartz inhibits glucose 6-phosphate dehydrogenase in murine alveolar macrophages. Chem Res Toxicol 21:888-894.

Pompa, P. P., Sabella, S. and Cingolani, R. 2015. Device and method for determining the dissolution kinetics of colloidal nanoparticles. Google Patents.

Porcheray, F., Viaud, S., Rimaniol, A. C., Leone, C., Samah, B., Dereuddre-Bosquet, N., ...Gras, G. 2005. Macrophage activation switching: an asset for the resolution of inflammation. Clin Exp Immunol 142:481-489.

Pothmann, D., Simar, S., Schuler, D., Dony, E., Gaering, S., Le Net, J. L., ...Regnier, J. F. 2015. Lung inflammation and lack of genotoxicity in the comet and micronucleus assays of industrial multiwalled carbon nanotubes Graphistrength((c)) C100 after a 90-day nose-only inhalation exposure of rats. Part Fibre Toxicol 12:21.

Pulskamp, K., Diabate, S. and Krug, H. F. 2007. Carbon nanotubes show no sign of acute toxicity but induce intracellular reactive oxygen species in dependence on contaminants. Toxicol Lett 168:58-74.

Rao, K. M., Porter, D. W., Meighan, T. and Castranova, V. 2004. The sources of inflammatory mediators in the lung after silica exposure. Environ Health Perspect 112:1679-1686.

Re, S. L., Giordano, G., Yakoub, Y., Devosse, R., Uwambayinema, F., Couillin, I., ...Huaux, F. 2014. Uncoupling between inflammatory and fibrotic responses to silica: evidence from MyD88 knockout mice. PLoS One 9:e99383.

Régnier, J.-F., Pothmann-Krings, D., Simar, S., Dony, E., Net, J.-L. L. and Beausoleil, J. 2017. Graphistrength© C100 MultiWalled Carbon Nanotubes (MWCNT): thirteen-week inhalation toxicity study in rats with 13- and 52-week recovery periods combined with comet and micronucleus assays. Journal of Physics: Conference Series 838:012030.

Reuzel, P. G. J., Bruijntjes, J. P., Feron, V. J. and Woutersen, R. A. 1991. Subchronic inhalation toxicity of amorphous silicas and quartz dust in rats. Food and Chemical Toxicology 29:341-354.

Rigo, L. A., Carvalho-Wodarz, C. S., Pohlmann, A. R., Guterres, S. S., Schneider-Daum, N., Lehr, C. M. and Beck, R. C. R. 2017. Nanoencapsulation of a glucocorticoid improves barrier function and anti-inflammatory effect on monolayers of pulmonary epithelial cell lines. Eur J Pharm Biopharm 119:1-10.

Rydman, E. M., Ilves, M., Koivisto, A. J., Kinaret, P. A., Fortino, V., Savinko, T. S., ...Alenius, H. 2014. Inhalation of rod-like carbon nanotubes causes unconventional allergic airway inflammation. Part Fibre Toxicol 11:48.

Sauer, U. G., Vogel, S., Aumann, A., Hess, A., Kolle, S. N., Ma-Hock, L., ...Landsiedel, R. 2014. Applicability of rat precision-cut lung slices in evaluating nanomaterial cytotoxicity, apoptosis, oxidative stress, and inflammation. Toxicol Appl Pharmacol 276:1-20.

Savill, J., Hogg, N., Ren, Y. and Haslett, C. 1992. Thrombospondin cooperates with CD36 and the vitronectin receptor in macrophage recognition of neutrophils undergoing apoptosis. J Clin Invest 90:1513-1522.

Sayes, C. M., Liang, F., Hudson, J. L., Mendez, J., Guo, W., Beach, J. M., ...Colvin, V. L. 2006a. Functionalization density dependence of single-walled carbon nanotubes cytotoxicity in vitro. Toxicol Lett 161:135-142.

Sayes, C. M., Wahi, R., Kurian, P. A., Liu, Y., West, J. L., Ausman, K. D., ...Colvin, V. L. 2006b. Correlating nanoscale titania structure with toxicity: a cytotoxicity and inflammatory response study with human dermal fibroblasts and human lung epithelial cells. Toxicol Sci 92:174-185.

Scherbart, A. M., Langer, J., Bushmelev, A., van Berlo, D., Haberzettl, P., van Schooten, F.-J., ...Albrecht, C. 2011. Contrasting macrophage activation by fine and ultrafine titanium

dioxide particles is associated with different uptake mechanisms. Particle and Fibre Toxicology 8:31-31.

Schinwald, A., Murphy, F. A., Jones, A., MacNee, W. and Donaldson, K. 2012. Graphene-based nanoplatelets: a new risk to the respiratory system as a consequence of their unusual aerodynamic properties. ACS Nano 6:736-746.

Schwotzer, D., Ernst, H., Schaudien, D., Kock, H., Pohlmann, G., Dasenbrock, C. and Creutzenberg, O. 2017. Effects from a 90-day inhalation toxicity study with cerium oxide and barium sulfate nanoparticles in rats. Part Fibre Toxicol 14:23.

Semmler-Behnke, M., Takenaka, S., Fertsch, S., Wenk, A., Seitz, J., Mayer, P., ...Kreyling, W. G. 2007. Efficient elimination of inhaled nanoparticles from the alveolar region: evidence for interstitial uptake and subsequent reentrainment onto airways epithelium. Environ Health Perspect 115:728-733.

Setoguchi, K., Takeya, M., Akaike, T., Suga, M., Hattori, R., Maeda, H., ...Takahashi, K. 1996. Expression of inducible nitric oxide synthase and its involvement in pulmonary granulomatous inflammation in rats. Am J Pathol 149:2005-2022.

Shi, X. L., Dalal, N. S. and Vallyathan, V. 1988. ESR evidence for the hydroxyl radical formation in aqueous suspension of quartz particles and its possible significance to lipid peroxidation in silicosis. J Toxicol Environ Health 25:237-245.

Shvedova, A. A., Kisin, E., Murray, A. R., Johnson, V. J., Gorelik, O., Arepalli, S., ...Kagan, V. E. 2008. Inhalation vs. aspiration of single-walled carbon nanotubes in C57BL/6 mice: inflammation, fibrosis, oxidative stress, and mutagenesis. Am J Physiol Lung Cell Mol Physiol 295:L552-565.

Sindrilaru, A., Peters, T., Wieschalka, S., Baican, C., Baican, A., Peter, H., ...Scharffetter-Kochanek, K. 2011. An unrestrained proinflammatory M1 macrophage population induced by iron impairs wound healing in humans and mice. J Clin Invest 121:985-997.

Singh, S., Shi, T., Duffin, R., Albrecht, C., van Berlo, D., Hohr, D., ...Schins, R. P. 2007. Endocytosis, oxidative stress and IL-8 expression in human lung epithelial cells upon treatment with fine and ultrafine TiO2: role of the specific surface area and of surface methylation of the particles. Toxicol Appl Pharmacol 222:141-151.

Snelgrove, R. J., Goulding, J., Didierlaurent, A. M., Lyonga, D., Vekaria, S., Edwards, L., ...Hussell, T. 2008. A critical function for CD200 in lung immune homeostasis and the severity of influenza infection. Nat Immunol 9:1074-1083.

Stefaniak, A. B., Guilmette, R. A., Day, G. A., Hoover, M. D., Breysse, P. N. and Scripsick, R. C. 2005. Characterization of phagolysosomal simulant fluid for study of beryllium aerosol particle dissolution. Toxicol In Vitro 19:123-134.

Stein, M., Keshav, S., Harris, N. and Gordon, S. 1992. Interleukin 4 potently enhances murine macrophage mannose receptor activity: a marker of alternative immunologic macrophage activation. J Exp Med 176:287-292.

Steinhäuser, K. G. and Sayre, P. G. 2017. Reliability of methods and data for regulatory assessment of nanomaterial risks. NanoImpact 7:66-74.

Stone, V., Miller, M. R., Clift, M. J. D., Elder, A., Mills, N. L., Moller, P., ...Cassee, F. R. 2017. Nanomaterials Versus Ambient Ultrafine Particles: An Opportunity to Exchange Toxicology Knowledge. Environ Health Perspect 125:106002.

Szakal, C., Roberts, S. M., Westerhoff, P., Bartholomaeus, A., Buck, N., Illuminato, I., ...Rogers, M. 2014. Measurement of Nanomaterials in Foods: Integrative Consideration of Challenges and Future Prospects. ACS Nano 8:3128-3135.

Takebayashi, T., Landsiedel, R. and Gamo, M. 2019. In Vivo Inhalation Toxicity Screening Methods for Manufactured Nanomaterials. Series: Current Topics in Environmental Health and Preventive Medicine. 1st ed. Springer. ISBN 978-981-13-8432-5

Takenaka, S., Karg, E., Kreyling, W. G., Lentner, B., Moller, W., Behnke-Semmler, M., ...Schulz, H. 2006. Distribution pattern of inhaled ultrafine gold particles in the rat lung. Inhal Toxicol 18:733-740.

Taylor, P. R., Martinez-Pomares, L., Stacey, M., Lin, H. H., Brown, G. D. and Gordon, S. 2005. Macrophage receptors and immune recognition. Annu Rev Immunol 23:901-944.

Tenzer, S., Docter, D., Kuharev, J., Musyanovych, A., Fetz, V., Hecht, R., ...Stauber, R. H. 2013. Rapid formation of plasma protein corona critically affects nanoparticle pathophysiology. Nat Nanotechnol 8:772-781.

Tran, C. L., Buchanan, D., Cullen, R. T., Searl, A., Jones, A. D. and Donaldson, K. 2000. Inhalation of Poorly Soluble Particles. II. Influence of Particle Surface Area on Inflammation and Clearance. Inhalation Toxicology 12:1113-1126.

van der Vliet, A., Janssen-Heininger, Y. M. W. and Anathy, V. 2018. Oxidative stress in chronic lung disease: From mitochondrial dysfunction to dysregulated redox signaling. Molecular Aspects of Medicine 63:59-69.

van Furth, R. and Cohn, Z. A. 1968. The origin and kinetics of mononuclear phagocytes. The Journal of Experimental Medicine 128:415-435.

van Ravenzwaay, B., Landsiedel, R., Fabian, E., Burkhardt, S., Strauss, V. and Ma-Hock, L. 2009. Comparing fate and effects of three particles of different surface properties: nano-TiO2, pigmentary TiO2 and quartz. Toxicol Lett 186:152-159.

Vance, M. E., Kuiken, T., Vejerano, E. P., McGinnis, S. P., Hochella, M. F., Jr., Rejeski, D. and Hull, M. S. 2015. Nanotechnology in the real world: Redeveloping the nanomaterial consumer products inventory. Beilstein Journal of Nanotechnology 6:1769-1780.

Vencalek, B. E., Laughton, S. N., Spielman-Sun, E., Rodrigues, S. M., Unrine, J. M., Lowry, G. V. and Gregory, K. B. 2016. In Situ Measurement of CuO and Cu(OH)2 Nanoparticle Dissolution Rates in Quiescent Freshwater Mesocosms. Environmental Science & Technology Letters 3:375-380.

Vennemann, A., Alessandrini, F. and Wiemann, M. 2017. Differential Effects of Surface-Functionalized Zirconium Oxide Nanoparticles on Alveolar Macrophages, Rat Lung, and a Mouse Allergy Model. Nanomaterials (Basel) 7.

Venosa, A., Malaviya, R., Choi, H., Gow, A. J., Laskin, J. D. and Laskin, D. L. 2016. Characterization of Distinct Macrophage Subpopulations during Nitrogen Mustard-Induced Lung Injury and Fibrosis. Am J Respir Cell Mol Biol 54:436-446.

Venosa, A., Malaviya, R., Gow, A. J., Hall, L., Laskin, J. D. and Laskin, D. L. 2015. Protective role of spleen-derived macrophages in lung inflammation, injury, and fibrosis induced by nitrogen mustard. Am J Physiol Lung Cell Mol Physiol 309:L1487-1498.

Wagner, A. J., Bleckmann, C. A., Murdock, R. C., Schrand, A. M., Schlager, J. J. and Hussain, S. M. 2007. Cellular interaction of different forms of aluminum nanoparticles in rat alveolar macrophages. J Phys Chem B 111:7353-7359.

Wangoo, A., Sparer, T., Brown, I. N., Snewin, V. A., Janssen, R., Thole, J., ...Young, D. B. 2001. Contribution of Th1 and Th2 cells to protection and pathology in experimental models of granulomatous lung disease. J Immunol 166:3432-3439.

Webster, T. J. 2013. Interview: Nanomedicine: past, present and future. Nanomedicine 8:525-529.

Weigert, A., von Knethen, A., Fuhrmann, D., Dehne, N. and Brüne, B. 2018. Redox-signals and macrophage biology. Molecular Aspects of Medicine 63:70-87.

WHO. 2000. World Health Organization. Air quality guidelines for Europe. second edition.

Wick, P., Manser, P., Limbach, L. K., Dettlaff-Weglikowska, U., Krumeich, F., Roth, S., ...Bruinink, A. 2007. The degree and kind of agglomeration affect carbon nanotube cytotoxicity. Toxicol Lett 168:121-131.

Wiemann, M., Sauer, U. G., Vennemann, A., Bäcker, S., Keller, J.-G., Ma-Hock, L., ...Landsiedel, R. 2018. In Vitro and In Vivo Short-Term Pulmonary Toxicity of Differently Sized Colloidal Amorphous SiO2. Nanomaterials 8:160.

Wiemann, M., Vennemann, A., Sauer, U. G., Wiench, K., Ma-Hock, L. and Landsiedel, R. 2016. An in vitro alveolar macrophage assay for predicting the short-term inhalation toxicity of nanomaterials. J Nanobiotechnology 14:16.

Wynn, T. A., Chawla, A. and Pollard, J. W. 2013. Macrophage biology in development, homeostasis and disease. Nature 496:445-455.

Xia, T., Hamilton, R. F., Bonner, J. C., Crandall, E. D., Elder, A., Fazlollahi, F., ...Holian, A. 2013. Interlaboratory evaluation of in vitro cytotoxicity and inflammatory responses to engineered nanomaterials: the NIEHS Nano GO Consortium. Environ Health Perspect 121:683-690.

Xiang, G. A., Zhang, Y. D., Su, C. C., Ma, Y. Q., Li, Y. M., Zhou, X., ...Ji, W. J. 2016. Dynamic changes of mononuclear phagocytes in circulating, pulmonary alveolar and

interstitial compartments in a mouse model of experimental silicosis. Inhal Toxicol 28:393-402.

Yamashiro, D. J., Fluss, S. R. and Maxfield, F. R. 1983. Acidification of endocytic vesicles by an ATP-dependent proton pump. The Journal of cell biology 97:929-934.

Yanamala, N., Kagan, V. E. and Shvedova, A. A. 2013. Molecular modeling in structural nano-toxicology: interactions of nano-particles with nano-machinery of cells. Advanced drug delivery reviews 65:2070-2077.

Yang, H., Liu, C., Yang, D., Zhang, H. and Xi, Z. 2009. Comparative study of cytotoxicity, oxidative stress and genotoxicity induced by four typical nanomaterials: the role of particle size, shape and composition. J Appl Toxicol 29:69-78.

Yasar, H., Ho, D. K., De Rossi, C., Herrmann, J., Gordon, S., Loretz, B. and Lehr, C. M. 2018. Starch-Chitosan Polyplexes: A Versatile Carrier System for Anti-Infectives and Gene Delivery. Polymers 10.

6. Scientific output

6.1 Paper 1: „Abiotic dissolution rates of 24 (nano)forms of 6 substances compared to macrophage-assisted dissolution and in vivo pulmonary clearance: Grouping by biodissolution and transformation“

The following section contains the publication:

Abiotic dissolution rates of 24 (nano)forms of 6 substances compared to macrophage-assisted dissolution and in vivo pulmonary clearance: Grouping by biodissolution and transformation

Johanna Koltermann-Jülly[1], Johannes G. Keller[1], Antje Vennemann, Kai Werle, Philipp Müller, Lan Ma-Hock, Robert Landsiedel, Martin Wiemann, Wendel Wohlleben

NanoImpact. Volume 12, 2018, Pages 29-41

[1] *Equal contribution.*

ISSN 2452-0748

https://doi.org/10.1016/j.impact.2018.08.005

NanoImpact 12 (2018) 29–41

Contents lists available at ScienceDirect

NanoImpact

journal homepage: www.elsevier.com/locate/nanoimpact

Abiotic dissolution rates of 24 (nano)forms of 6 substances compared to macrophage-assisted dissolution and in vivo pulmonary clearance: Grouping by biodissolution and transformation

Johanna Koltermann-Jülly[a,c,1], Johannes G. Keller[a,b,1], Antje Vennemann[d], Kai Werle[b], Philipp Müller[b], Lan Ma-Hock[a], Robert Landsiedel[a], Martin Wiemann[d,*], Wendel Wohlleben[a,b,**]

[a] BASF SE, Dept. of Experimental Toxicology and Ecology, 67056 Ludwigshafen, Germany
[b] BASF SE, Dept. of Material Physics, 67056 Ludwigshafen, Germany
[c] Biopharmaceutics and Pharmaceutical Technology, Saarland University, 66123 Saarbrücken, Germany
[d] IBE R&D Institute for Lung Health gGmbH, 48149 Münster, Germany

ARTICLE INFO

Keywords:
Dissolution
Transformation
Grouping
Read-across
Alveolar macrophages

ABSTRACT

Numerous recent reviews have highlighted the urgent need for methods to determine the biodissolution of nanomaterials in relevant lung fluids, and to validate the results against the bioprocessing *in vivo*. Moreover, it is largely unknown to what extent (nano)forms of a substance that differ in size, shape, or coating also differ in biodissolution. Here we apply a previously optimized abiotic flow-through method to 24 (nano)forms of 6 substances and compare the results with alveolar macrophage-assisted biodissolution of a subset of these nanomaterials *in vitro* and short-term inhalation results *in vivo*. As a main result we found that the results obtained with the flow-through method for the lung were consistent to the results of *in vivo* studies and were not improved by measuring alveolar macrophage-assisted biodissolution for up to 48 h. Based on selected benchmark materials we propose four groups of materials according to quantitative biodissolution rates (1 ng/cm^2/h to 100 ng/cm^2/h cutoffs) and qualitative transformation parameters, as detected by TEM analysis. These groups were also reflected by different lung clearance rates, as previously determined in short term inhalation studies. Biodissolution was similar within substance (nano)forms of Fe_2O_3, SiO_2, CeO_2, ZnO, though slightly varied upon surface area/coating. But the difference of biodissolution between the substances was in some cases > 1000-fold. Among the Cu-containing materials, the behavior of the two CuPhthalocyanin nanoforms was similar with each other, but completely different than the dissolution and transformation of Cu salts. Different production routes and/or surface coatings significantly modulated biodissolution, whereas effects of shape or size were limited. In summary, we refined a protocol for the abiotic determination of biodissolution along with an integrated assessment of nanomaterial transformation. The protocol is suggested as tier 2 methodology for grouping and read-across purposes.

1. Introduction

Engineered nanomaterials (ENM) are produced in numerous grades, which are each optimized for specific applications and differ in properties such as composition, size, shape, surface treatments. Especially fillers and pigments represent established materials that are produced in megaton quantities in many different (nano)forms (Wohlleben et al., 2017a; Ministère de l'Environnement, 2015). For a given material composition, the properties size, shape, and surface chemistry describe the "nanoform" for regulatory purposes (ECHA, 2017a), but none of these properties is sufficient to predict the extent to which human or environmental hazards differ from the non-nanoform of the same composition (Godwin et al., 2015; Landsiedel et al., 2017; Donaldson and Poland, 2013). Assessing similarity to known benchmark materials

* Correspondence to: M. Wiemann, IBE R&D Institute for Lung Health gGmbH, 48149 Münster, Germany.
** Correspondence to: W. Wohlleben, BASF SE, Dept. of Material Physics and Dept. of Experimental Toxicology and Ecology, 67056 Ludwigshafen, Germany.
E-mail addresses: johanna.koltermann-juelly@basf.com (J. Koltermann-Jülly), johannes-georg.keller@basf.com (J.G. Keller), vennemann@ibe-ms.de (A. Vennemann), kai.werle@basf.com (K. Werle), lan.ma-hock@basf.com (L. Ma-Hock), robert.landsiedel@basf.com (R. Landsiedel), martin.wiemann@ibe-ms.de (M. Wiemann), wendel.wohlleben@basf.com (W. Wohlleben).
[1] Equal contribution.

https://doi.org/10.1016/j.impact.2018.08.005
Received 26 April 2018; Received in revised form 6 August 2018; Accepted 22 August 2018
Available online 25 August 2018

can be a powerful approach to reduce the uncertainty related to the risks of innovative (nano)materials, and to revisit the safety of established materials. Especially the rate of dissolution under simulated physiological conditions (biodissolution) is an important criterion to assess similarity between (nano)forms of the same substance in several frameworks of grouping and read-across (Collier et al., 2015; Nel et al., 2013; Kuempel et al., 2012; Braakhuis et al., 2014; Oomen et al., 2017; Arts et al., 2015, 2016). However, Steinhäuser and Sayre have stressed that most frameworks do not propose a specific method, often confound solubility with the dissolution rate or transformation, and rarely propose quantitative group limits (Steinhäuser and Sayre, 2017). One has to differentiate:

- "solubility" is measured in equilibrium saturated suspensions, with appropriate descriptors of mg/L ion, identical with the conventional solubility limit. Implicitly, it often means solubility in water at neutral pH and was proposed as Tier 1 screening for soluble ENM, (Arts et al., 2015) to be refined to the solubility in relevant medium as Tier 2 method (Arts et al., 2015; Avramescu et al., 2016). Plakhova et al. demonstrated that "% dissolved" is not an equivalent metric, and probably not appropriate (Plakhova et al., 2016).
- "dissolution rate" is measured out of equilibrium conditions and below the saturation in the relevant medium, with appropriate descriptors in units of ion mass per solid mass per time (=%/h) or ion mass per solid particle surface per time (=ng/cm^2/h). It is considered an extrinsic property.
- "transformation" describes the propensity of the non-dissolved remaining solids to "change what they are" in the relevant medium, regarding their physical shape, or size, or chemical identity, and has no clearly defined descriptors. It is also considered as extrinsic property and has implications for hazard assessment, e.g. if the aspect ratio or crystalline phase changes.

Accordingly, a recent review by Oberdörster and Kuhlbusch found that "because the *in vivo* dissolution rates of ENM can differ widely, it is too simplistic to group ENM just into soluble and poorly soluble materials." (Oberdörster and Kuhlbusch, 2018), and the appropriate differentiation of (nano)materials by static solubility values has been questioned (Klaessig, 2018). To measure instead dissolution rates, flow cells (Nti, 2017) mimic the non-equilibrium physiological conditions, where ions can be transported away from the lungs. Variants of flow cells have been used recently for environmental dissolution (Kent and Vikesland, 2016) and for oral dissolution of nanomaterials (Bove et al., 2017a). For mineral fibers, flow-through cell dissolution rates correlate strongly with *in vivo* pulmonary clearance (Guldberg et al., 1995; IARC, 2002). Simulant media need to be sufficiently complex to offer oxidative, reductive and pH-driven dissolution pathways (Wang et al., 2016). Specifically for pulmonary biodissolution, phagolysosomal simulant media with a low pH value (4.5) are appropriate because alveolar macrophages (AMs) collect and engulf the vast majority of inhaled ENM from the alveolar surface, and rapidly transfer them into acidic phagolysosomes (Stefaniak et al., 2005; Marques et al., 2011).

Here we apply the abiotic flow-through method with a phagolysosomal simulant to a wide range of (nano)materials with different substance, size, shape, coating. Following the dissolution rate quantification we prepare the remaining solids on transmission electron microscopy (TEM) grids and assess the transformation of nanoparticles by electron microscopy.

However, abiotic dissolution at phagolysosomal conditions remains a simplistic approximation and may underestimate the more complex macrophage-assisted physical (mobility) and chemical (dissolution) clearance (Kass, 1964; Geiser, 2010). Oberdörster and Kuhlbusch concluded that "Results from [Alveolar Macrophage] *in vitro* assays with microparticles show good agreement with *in vivo* kinetics; yet further studies using MNs/ENM of different solubilities are required to validate this *in vitro* AM assay for nanomaterials." (Oberdörster and Kuhlbusch, 2018) Here we hypothesize that AMs might accelerate dissolution, especially of pH sensitive nanomaterials, and explore to which extent the dissolution rates are compatible between abiotic and macrophage-assisted dissolution, using $BaSO_4$, ZnO and $SrCO_3$ as test cases. ZnO was proposed earlier as benchmark material, because it is poorly soluble in water, but becomes soluble under phagolysosomal conditions (Arts et al., 2015; Avramescu et al., 2016). Further, it is known that $SrCO_3$ is poorly soluble in water but readily soluble under acidic conditions. In contrast to an earlier approach based on human and dog AMs (Kreyling et al., 1979) whose isolation demands human volunteers or animal experiments, we used an AM cell line (NR8383) from rat lung lavage cells (Helmke et al., 1987, 1989). It was shown, that NR8383 cells maintain their typical AM-like size, appearance, and phagocytic properties over many passages. In addition, they maintain their immunological properties, thus reacting to test material exposure by the formation and release of different pro-inflammatory and fibrogenic cytokines and chemokines, including TNF-α, IL-1, TGF-β and PDFG (Helmke et al., 1987, 1989; Koslowski et al., 2003; Albrecht et al., 2007; Scherbart et al., 2011; Bhattacharjee et al., 2012). Furthermore, the cells are capable of producing H_20_2 e.g. via the NADPH oxidase reaction process (also known as "respiratory burst") which is an inherent part of the macrophages' armament and may contribute to the processing or dissolution of ENM.

NR8383 cells have been used for the *in vitro* testing of a variety of ENM including functionalized amorphous silicates, indium tin oxide, alumina, ultrafine titania, (multi-walled) carbon nanotubes (mwCNTs), various copolymers and also heparin nanoparticles (Scherbart et al., 2011; Bhattacharjee et al., 2012; Lison et al., 2008, 2009; Pulskamp et al., 2007; Wagner et al., 2007; Eidi et al., 2010, 2012; Bhattacharjee et al., 2013). Most specifically, the *in vitro* potency screening by NR8383 cells correlates excellently with *in vivo* inflammatory short-term inhalation study (STIS) results for the purposes of Tier 2 grouping of ENM in the DF4nanoGrouping framework (Arts et al., 2015; Wiemann et al., 2016), such that cell-assisted biodissolution with NR8383 macrophages would seamlessly integrate in a grouping framework, if necessary.

2. Materials and methods

2.1. Materials

To obtain results which are representative for the broad field of ENM applications, six substances with 24 different (nano)forms were selected with prioritization by availability of *in vivo* studies (cited for each material in the following) and industrial relevance (Ministère de l'Environnement, 2015). The (nano)forms vary in size, crystallinity/shape and coating. Both, CeO_2 NM-211 and CeO_2 NM-212 were provided by the JRC repository of the Organization for Economic Co-operation and Development (OECD) sponsorship program, they differ in size and form (Keller et al., 2014; Molina et al., 2014). The test set also includes two kinds of $BaSO_4$ whereas the nanosized $BaSO_4$ NM-220 was provided by the OECD sponsorship program (via Fraunhofer Institute) and the non-nano-sized $BaSO_4$ IRMM381 is a reference material, provided by the Institute for Reference Materials and Measurement (IRMM, Geel, with kind permission by Solvay) (Babick et al., 2016; Wohlleben et al., 2017b). Seven different silica materials were investigated. Four different sizes of untreated, colloidal silica: Levasil 50, Levasil 100, Levasil 200 and Levasil 300 were all commercially acquired from Akzo Nobel N. V. (Wiemann et al., 2018). Based on Levasil 200, we synthesized two nanoforms with surface coatings: SiO_2_aminated and SiO_2_phosphonated (Landsiedel et al., 2014). The powdered silica NM-203 was provided by the JRC repository of the OECD sponsorship program. In addition, the test set includes three different kinds of Iron Oxides (Pigment Red 101), the rod shaped Fe_2O_3_nano_A and the spherical Fe_2O_3_nano_B were both provided by BASF SE and the cubic Fe_2O_3_larger (borderline non-nano) was provided by Rockwood

Holdings Inc. (Hofmann et al., 2016). Two UV-active TiO_2 materials were compared: TiO_2 NM-104 with an Al_2O_3 coating and TiO_2 NM-105, both supplied by the JRC repository of the OECD sponsorship program and extensively tested by inhalation (Landsiedel et al., 2010). Both ZnO materials NM-110 and NM-111 are supplied by the JRC repository of the OECD sponsorship program and differ in their coating. ZnO NM-111 has a hydrophobic silicone coating, and is a benchmark "biosoluble" material in the DF4nanogrouping framework (Arts et al., 2016; Landsiedel et al., 2010). Furthermore, the test set consists of four copper-containing materials: The powdered nanoform CuO, provided by PlasmaChem GmbH (Gosens et al., 2016), and the suspension-micronized nanoform $Cu_2(OH)_2CO_3$, were previously studied for environmental transformations (Pantano et al., 2018), and we added two nanoforms of metal-organic pigments Cu_Phthalocyanine_nano (Pigment Blue 15) and Cu_Phthalocyanine_halogen (Pigment Green 7), which were provided by BASF SE (Arts et al., 2016). Hydrophilic $SrCO_3$ was donated by Solvay and was characterized previously in the course of the NanoCare project (Kroll et al., 2011).

2.2. Abiotic flow-through testing of dissolution and transformation

The setup (Fig. 1) implements a "continuous flow system" described in ISO 19057:2017 (Nti, 2017). It is essentially a replication of the established flow-through testing of the dissolution kinetics of mineral fibers (Guldberg et al., 1995; IARC, 2002), was described for this purpose (Wohlleben et al., 2017c), and was used here with minor adaptations to match the specifics of ENM: The ENM mass of 1 mg was weighed onto a membrane (cellulose triacetate, Sartorius Stedim Biotech GmbH, Goettingen, Germany): 47 mm diameter, 5 kDa pore size, topped by another membrane, and enclosed in flow-through cells. Standard conditions are 1 mg initial solid mass in the flow-through cell, and 2 mL/h flow. The phagolysosomal simulant fluid (PSF), an acidic buffer simulating the phagolysosomal compartment of macrophages (Stefaniak et al., 2005; Wohlleben et al., 2017c), which was previously validated for the purpose of inhaled beryllium dissolution by NIST laboratories (Stefaniak et al., 2005), was employed at 37 ± 0.5 °C. The PSF composition is reproduced in the supplementary information (SI). In contrast to the larger volume flow cells used by Bove et al. for oral dissolution testing (Bove et al., 2017a), in our setup the ENM are in direct contact with the ultrafiltration membrane. In contrast to the flow cells used by Kent et al., our cells hold industrially produced ENM, not lab-grown arrays of same chemical composition (Kent and Vikesland, 2016). The core idea of separating ions from remaining solids is shared by all three setups.

The programmable sampler drew 4–10 mL of the eluate once per day for seven days. For shorter sampling times at the beginning of the dissolution, the samples were drawn for only 2–3 h instead of 5 h. The rest of the eluate was collected in a container. The ion concentrations of the eluates from different time points were determined by inductively coupled plasma-optical emission spectrometry (ICP-OES Agilent 5100 and Varian 725 ES) with a limit of detection of 0.1 mg/L, alternatively by inductively coupled plasma-mass spectrometry (ICP-MS Perkin Elmer Nexion 2000b) with a limit of detection of 0.1 ppb. Prior to taking the measurement, the instrument was optimized in accordance with the manufacturer's specification. Duplicate measurements are taken and averaged. We measured with 10 s integration time, and the dilution factors were between 1 and 10. External calibration used concentrations of 0/1/5 mg/L with matrix-matched standards. The nebulizer (Meinhard 1 mL) had a flow of 0.7 L/min at a pump rate of 15 rpm. For ICP-MS duplicate measurements were taken and averaged. The eluate was diluted with a factor between 100 to 1000 and the external calibration used concentrations of 0.1/1/10 ppb. The nebulizer had a flow of 0.92 L/min at a pump rate of 35 rpm.

After the experiment, the remaining solids were rinsed off the membrane as shown in the photo-protocol in Fig. SI_S3 documenting specifically developed accessories. The resulting suspension was then pelleted onto a TEM grid held at the bottom of a centrifuge vial within 30 min, then dried, so that the remaining solids morphology can be inspected without interference from drying artifacts of PSF salts, which are removed by this preparation. The remaining solids were analyzed by TEM with a Tecnai G2-F20ST or Tecnai Osiris Microscope (FEI Company, Hillsboro, USA) at an acceleration voltage of 200 keV under bright-field conditions. For the automated image analysis the pre-validated NanoDefine SEM/TEM software packages were used (Ullmann and Müller, 2017; Mielke et al., 2016; Muller et al., 2015).

We multiplied the measured ion concentration of each eluate with the eluted volume to obtain a mass of dissolved ions, and corrected for the molar mass m of the pristine ENM and of the detectable metal ion, to obtain the mass of ENM solids $M_{dissolved}(t)$ that were dissolved during the sampling interval Δt_i. Interim calculations are detailed in the SI. Cumulated from all samplings with concentration c_i, flow V_i and sampling interval Δt_i, the dissolved mass at the final time T is

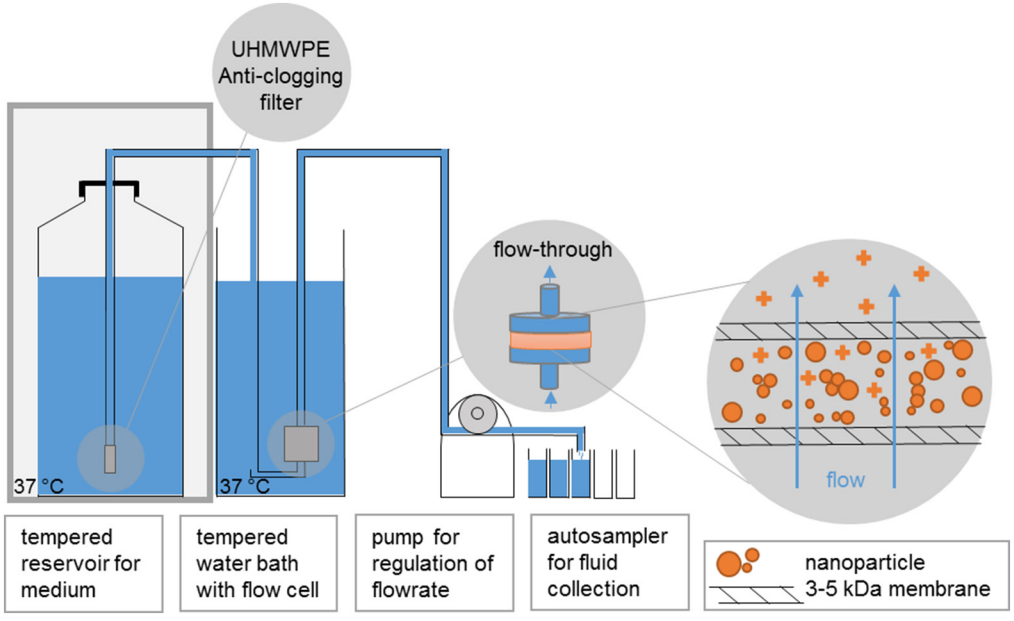

Fig. 1. Dissolution setup. The reservoir for the physiological fluid is controlled at 37 °C, as well as the flow-through cells. The peristaltic pump regulates the flow-rate of up to 8 cells in parallel, with a programmable autosampler for fluid collection. The flow-through cell is equipped with 5 kDa membranes to hold back particles and only allow the flow of ions. The meniscus of the reservoir is elevated approx. 0.5 m above the cells such that the hydrostatic pressure balances the pressure drop by the 5 kDa membrane.

$$M_{dissolved}(T) = \frac{m(ENM)}{m(metal\_ion)} * \sum_{i=0}^{T} c_i(ion) * V_i * \Delta t_i. \quad (1)$$

The dissolution rate k is then obtained via $M_{solids}(T) = M_0 - M_{dissolved}(T)$ with the relation:

$$k = \ln\{M_0/M_{solids}(T)\}/(SSA(T) * T) \quad (2)$$

This calculation is consistent with the first order modeling of ISO 19057:2017 (Nti, 2017), but gives k in units of ng/cm^2/h as recommended by Oberdörster and Kuhlbusch (2018). SSA(T) is the specific surface area at time T, equal to BET at time zero; k can be converted to a halftime $t_{1/2}$ by Eq_SI_1. The alternative metric "% dissolved" is given by $M_{dissolved}(T)/M_0$.

2.3. Preparation of nanoparticle suspensions for in vitro testing

$BaSO_4$ NM-220, $SrCO_3$, ZnO NM-110, or ZnO NM-111 ENM were suspended in double distilled H_2O at a concentration of 1 mg/mL. Suspensions were ultrasonicated on ice for 10 × 10 s using a 3 mm probe adjusted to 50 W (Vibra Cell™, Sonics & Materials, USA). To remove larger aggregates (typical for the spray dried $BaSO_4$ ENM) which cannot be engulfed by macrophages, the $BaSO_4$ and $SrCO_3$ suspensions were filtered through a depth-type filter with 2.7 µm pore size (Whatman™ GD/X 25 syringe filter with 2.7 µm GF/D Glass Microfiber Membrane). The filtrate was dried and the particle content was measured gravimetrically, resulting in a concentration of 500 µg/mL. Aqueous suspensions of $SrCO_3$ and $BaSO_4$ were then adjusted to 90 µg/mL. Suspensions of ZnO NM-110 and ZnO NM-111 were diluted to 11.25 µg/mL. All aqueous suspensions were then mixed with an equal volume of double-concentrated (2×) F-12K cell culture medium prepared from powder medium (Sigma-Aldrich GmbH, Munich, Germany), supplemented with glutamine (4 mM) and penicillin (200 U), streptomycin (200 mg/ml), and 10% (v/v) fetal bovine serum (FBS) (PAN Biotech GmbH, Aidenbach, Germany), or with double-concentrated phagolysosomal simulant fluid (PSF) adjusted to pH 4.5 with 1 M NaOH. The final suspension, as used for dissolution experiments, therefore contained all F-12K components and supplements, 5% FBS and 45 µg/mL ($SrCO_3$, $BaSO_4$) or 5.6 µg/mL (ZnO) of the ENM, respectively. Equal concentrations of ENM were prepared in PSF. All ENM suspensions were prepared shortly before use and vortexed immediately before *in vitro* application. Based on previous cytotoxicity data for $BaSO_4$ and ZnO (Wiemann et al., 2016) the concentrations were maximized up to values where cytotoxic effects were absent or minimal. For $SrCO_3$, a no adverse effect level larger than 90 µg/mL was found under the same conditions. This strategy was chosen to increase the yield of dissolved ions and also to avoid early cell death.

2.4. Preparation of the NR8383 test system

The rat AM cell line NR8383 (Helmke et al., 1987, 1989) was purchased from ATCC (Manassas, VA, USA) and used for *in vitro* experiments. Cells were grown in F-12K medium (Sigma-Aldrich GmbH, Munich, Germany) supplemented with 15% FBS, glutamin, and penicillin (100 U), streptomycin (100 µg/ml) under standard cell culture conditions (37 °C, 5% CO_2) as described (Wiemann et al., 2016). For dissolution tests, the macrophages were detached from the substrate by mechanical agitation, fully dispersed by pipetting, seeded into 96-well flat-bottom plates (Primaria™, Corning, NY, USA) at a density of 3×10^5 live cells per well, and pre-incubated in F-12K supplemented with 5% FBS for 24 h. Then the medium was completely replaced by ENM suspensions (see above). Cell-free experiments were conducted side-by-side, i.e. on the same plates, using F-12K medium with 5% FBS and PSF as dispersants. For each single experiment 8 identical wells were run in parallel. To accelerate sedimentation of particles and unify the onset of exposure of cells to ENM, plates were centrifuged at 100 ×g (37 °C) for 10 min and incubated under cell culture conditions for 3 h, 6 h, 12 h, 24 h, and 48 h with $SrCO_3$ or $BaSO_4$, or 24 h to ZnO NM-110 or NM-111, respectively. Phase contrast micrographs were taken to monitor gravitational settling, uptake of larger particles or cell lysis using a Zeiss Axiovert C40 microscope equipped with an Axiocam C3 camera.

Following incubation with ENM, cells were completely lysed by adding 20 µl of a concentrated mixture of Triton X-100 and proteinase K (final concentration: 0.1% and 0.1 mg/mL, respectively) for 45 min, as controlled by phase contrast microscopy. Non-lysed ENM were separated by ultrafiltration. Therefore lysates were pooled, loaded onto 100 kDa filter devices (Amicon 100k ultra-0.5, Merck KGaA, Darmstadt, Germany) and centrifuged at 14,000 ×g for 15 min. Filtrates were then forced through a 3 kDa filter (Amicon 3k ultra-0.5, Merck KGaA, Darmstadt, Germany) by centrifugation (14,000 ×g, 20 min) and used for chemical analysis.

The ionic Ba, Sr, or Zn concentration was assessed by ICP-MS (ICP-MS 8800, Agilent Technologies, Santa Clara, CA, US) and corrected for the molar mass of the pristine ENM and the detectable metal ion, to obtain the mass of dissolved ENM solids. Results are shown as mean ± standard deviation (SD). To test for statistical significance, test values were compared to control values using Welch's unequal variances *t*-test. Test results with $p \leq 0.05$ were assessed as significant (*). All experiments were performed in triplicates.

2.5. Determination of cytotoxicity

Cytotoxic effects of ENM were monitored by measuring the lactate dehydrogenase (LDH) activity in the cell culture supernatant as an indicator for membrane damage and/or cell necrosis. Measurements were carried out as described (Wiemann et al., 2016) using the Roche Cytotoxicity Kit (Roche, Germany). In brief, cell culture supernatants were centrifuged (10 min, 200g) to remove larger particles and cell debris. A volume of 50 µL was incubated with LDH reaction mix (Roche Cytotoxicity Kit; Roche, Germany) and evaluated as described by the manufacturer. Optical density (OD) was measured at 490 and 620 nm in a plate photometer (Tecan 200Pro, Tecan, Germany). Measurements were routinely corrected for cell free-adsorption (to erase effects of particles on the optical signal) and normalized to the positive control value (set to 100%) obtained from NR8383 cells lysed with 0.1% Triton X-100 (Sigma, Aldrich, Germany). Particles investigated in this study had no influence on the LDH signals.

3. Results

3.1. Abiotic dissolution and transformation

The dissolution kinetics of 24 ENM was investigated in pH 4.5 PSF (Fig. 2A–E). For some materials, e.g. both nanoforms of CeO_2, the ion concentration in the eluate remains below the limit of detection (LoD) at any sampling time. In this case a virtual value was calculated from the number of consecutive measurements multiplied by LoD, however no plot was generated for this data. With ICP-OES as analysis technique, dissolution remained below LoD for all nanoforms of CeO_2 and Fe_2O_3. With ICP-MS as analysis technique that is sufficiently sensitive on the ppb ion level that is to be expected, (Plakhova et al., 2016) quantitative values could be generated also by the flow cells, but would not change the assignment to the group of materials with low dissolution rate. The dissolution of the barely soluble material $BaSO_4$ NM-220 (Fig. 2B) has been identified elsewhere as a combination of dissolution and Ostwald ripening, highlighted by an unexpected growth of particle size (reproduced in Fig. SI_S6) (Keller et al., 2018). Here we compare the non-nanoform by the same supplier $BaSO_4$_IRMM381, and find that by matching the initial surface area of the two forms (testing $BaSO_4$ NM-220 at M_0 = 0.17 mg), both the nanoform and the non-nanoform have nearly identical k_{app} and M_{ion}/T (Table 1). In this manner, the maximum ion concentration is different but remains for both below the

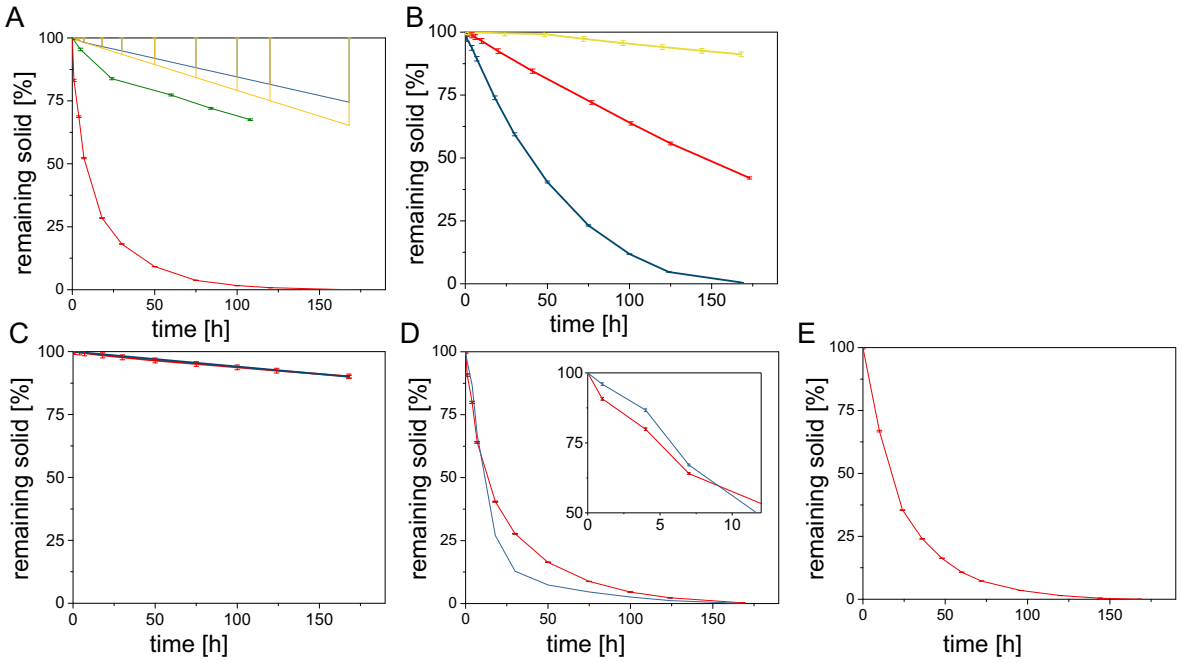

Fig. 2. Dissolution kinetics. A: Cu (red CuO, blue CuPhtalo_nano, yellow CuPhtalo_halogen, green $Cu_2(OH)_2CO_3$); B: $BaSO_4$ (red NM-220 1.05 mg, blue NM-220 0.17 mg, yellow IRMM381), C: SiO_2 (red NM-203, blue SiO_2_amino), D: ZnO (red NM-110, blue NM-111), with inset enlarging the initial effects. E: $SrCO_3$. The error bars displayed here equal the duplicate uncertainty of the ICP-OES measurements.

pH 4.5 solubility limit, such that reprecipitation and Ostwald ripening are suppressed. The matching of dissolution rates from nano- and non-nanoform confirms the validity of the surface-based k metric.

For all six forms of SiO_2 (Table 1 and Fig. 2C) the dissolution is rather limited in the acidic PSF medium, as expected. However, we do observe a higher dissolution for SiO_2 NM-203, which is produced by a different process (precipitation, then drying) than the colloidal nanoforms of SiO_2 (SiO_2_untreated_50 to SiO_2_untreated_300). Knowing that soluble forms of SiOx tend to polymerize, we stored the elution samples from NM-203 alternatingly with or without addition of 10% of 1 M HCl, but the resulting kinetics superimposed completely, confirming sufficient stability of dissolved Si-species before detection. Additionally, we measured another SiO_2 powder (NM-200) and found similar dissolution rates. While there is a trend to release more ions from smaller particles (in the SiO_2_untreated_50 to SiO_2_untreated_300 family (Wiemann et al., 2018)), the surface increase is larger so that the nominal dissolution rate k is lower for the smaller forms. Considering that especially in acidic medium SiO_2 tends to undergo polymerization and gel formation, a lower initial concentration of solids might help to demonstrate a stronger relationship with size, but would underscore the detection limit of our ICP-MS. Interestingly, surface functionalization (SiO2_amino_200, SiO2_phosphonate_200) can increase dissolution threefold compared to the core particle (SiO2_untreated_200).

The four Cu-containing nanoforms show a very diverse dissolution as seen in Fig. 2A. CuO dissolves completely after 7 days under standard conditions, whereas $Cu_2(OH)_2CO_3$ dissolves moderately (32% after 7 days) and both Cu_Phthalocyanin nanoforms shed only negligible amounts of ions. The difference is evident by the comparison of daily Cu release of 456 µg from CuO compared to 0.66 µg from Cu_Phthalocyanin_nano (Pigment Blue 15). These traces of Cu from Pigment Blue 15 are not necessarily attributed to particle dissolution but rather to remaining Cu from the complexation synthesis of the technical materials.

Very interestingly, Fig. 2D demonstrates a small retardation (from day 2 to 5) of the dissolution kinetic for the ZnO nanoform with coating, ZnO NM-111. However, after this retardation, attributed to the dissolution of the coating, the overall dissolution of ZnO NM-111 is accelerated (Table 2).

Transformation is frequently observed for zero-valent Ag- or Cu-particles with numerous studies showing re-crystallization, re-speciation (changing the chemical composition) especially in environmental media (Gao and Lowry, 2018; Vencalek et al., 2016; Dale et al., 2015; Mitrano and Nowack, 2017; Mitrano et al., 2015). Here we apply a standardized protocol of aging and sample preparation (Fig. SI_S3), with representative results shown in Fig. 3. Comparing the first pair of images (Fig. 3a), the TEM results support the complete dissolution of ZnO NM-110 incurred from the addition of all ions in the eluates, observations made for with the dissolution setup, as no particles could be found. In contrast, Fe_2O_3_nano_B (Fig. 3b) showed no significant difference between the pristine material and the material after a week of exposure to PSF. Cu_Phthalocyanin_nano tended to form aggregates, as no smaller particles remained (Fig. 3c). TEM images of SiO_2_untreated nanoparticles (Fig. 3d) revealed a moderate shrinkage. Furthermore, the homogeneous electron density of the particles transformed into an electron dense core and a less electron dense surface layer, which may be interpreted as gel-like and is not unexpected for SiO_2 under acidic conditions (Iler, 1979).

In addition to the representative cases (potential benchmark materials) in Fig. 3, more ENM have been analyzed with TEM of initial solids vs. remaining solids (Fig. 4). For Cu_Phthalocyanin_halogenated we observed the same behavior as for Cu_Phthalocyanin_nano, because the remaining particles were strongly aggregated. When comparing the TEM image of the pristine particles of $Cu_2(OH)_2CO_3$ with the TEM after the treatment with PSF, we observed that pristine particles had disappeared, while very few secondary particles were visible which consisted mainly of Si, but were devoid of Cu. SiO_2 NM-203 was found to dissolve faster than colloidal silica of roughly the same constituent particle size (SiO_2_untreated_200), and forms different intermediate structures (Fig. 4c). This may be due to the aggregate structure with negative radii of curvature (necks between primary particles) (Iler, 1979). As CuO and ZnO underwent complete dissolution within 7 days, an “infinite dilution” approach was employed to study transformation processes: we repeatedly dipped the grids into PSF and successively imaged the same spot of a TEM grid. The results on ZnO nicely demonstrate how its dissolution behavior is completely different from

Table 1
Nanoform physical-chemical descriptors of the 24 test materials.

	Minimum external dimension (TEM or AUC[a])	Shape (TEM)	Specific surface area (BET)	Composition/crystallinity/ impurities (XRD, ICP-MS, XPS)	Surface modification
	[nm]	Descriptive	[m^2/g]	[%]	Descriptive
$BaSO_4$ NM-220	32	Spheroidal	41	Purity > 93.8%; Na, Ca, Sr, F, Cl, organic compounds	None
$BaSO_4$ IRMM381	253	Spheroidal	2.5	Ba 58.8% O 27.4% S 13.7%	None
CeO_2 NM-211	4–15	Spheroidal	66	Purity > 95%	None
CeO_2 NM-212	40	Mixed spheroidal + platelets	27	Purity > 99.5%, 0.7% organic contaminations	None
$Cu_2(OH)_2CO_3$	34[a]	Platelets	19	Cu 57%	None
Cu_Phthalo_halogen	14	Platelets	61	Cu 5%	None
Cu_Phthalo_nano	17	Spheroidal	58	Cu 10.4%	None
CuO	40	Spheroidal	34	Purity > 99%, Al, Si 0.1–1%	None
Fe_2O_3_larger	48 ± 27	Spheroidal	12	Predominantly Fe_2O_3, hematite; traces of magnetite (cubic) Fe_3O_4	None
Fe_2O_3_nano_A	15–130 × 4–21	Rod shaped	107	Fe_2O_3, hematite	None
Fe_2O_3_nano_B	37	Spheroidal	30	Fe_2O_3, hematite	None
SiO_2 NM-203	20	Spheroidal	200–226	Purity > 99%, Al 0.43%	None
SiO_2_aminated	15[a]	Spheroidal	200	SiO_2 amorphous	covalent surface functionalization with low-molar-mass silane having a pos. charged amino end group
SiO_2_phosphonated	15[a]	Spheroidal	200	SiO_2 amorphous	covalent surface functionalization with low-molar-mass silane having a neg. charged phosphonate end group
SiO_2_untreated_50	55[a]	Spheroidal	50	SiO_2 amorphous	None
SiO_2_untreated_100	30[a]	Spheroidal	100	SiO_2 amorphous	None
SiO_2_untreated_200	15[a]	Spheroidal	200	SiO_2 amorphous	None
SiO_2_untreated_300	9[a]	Spheroidal	300	SiO_2 amorphous	None
$SrCO_3$	13–19	Rod shaped	33	Sr: 21.1%; C 27.1%; O: 51.3%	None
TiO_2 NM-104	21	Spheroidal	57	TiO_2 rutile	Al_2O_3 coating + 2% Polydimethylsiloxan
TiO_2 NM-105	25	Spheroidal	51	TiO_2 mix rutile/anatase	None
ZnO NM-110	42	Mixed spheroidal and rod shaped	12	ZnO > 99%	None
ZnO NM-111	34	Mixed spheroidal and rod shaped	14	ZnO > 97%	Triethoxycaprylsilane silicone coating

[a] Following the NanoDefine e-tool (http://www.nanodefine.eu/index.php/nanodefiner-e-tool), materials that are originally produced as colloidal suspensions were characterized by Analytical Ultracentrifugation (AUC) (Mehn et al., 2018), and powders by Transmission Electron Microscopy (TEM).

$BaSO_4$ NM-220 (Keller et al., 2018), as ZnO reduces the radii of curvature until complete disappearance (Fig. SI_S4). No dissolution was quantified with our ICP-OES limit of detection for TiO_2 NM-104, CeO_2 NM-212 or Fe_2O_3_nano_A. The absence of major dissolution or transformation was also confirmed through the analyzation of the crystal structure through selected area electron diffraction (SAD, Fig. SI_S7). The SAD graph showed unique Cerianite (CeO_2) signals and thus confirmed that transformation remained limited, although especially Ce^{III}-rich surface layers may have undergone transformations. In contrast to the case of $BaSO_4$ NM-220 (Fig. SI_S6 reproduced from (Keller et al., 2018)) no Ostwald ripening has occurred for $BaSO_4$ non-nano (Fig. SI_S7).

3.2. Uptake of nanomaterials by NR8383 cells and cell-assisted dissolution

In the next step we explored in as much macrophage-assisted dissolution differs from the abiotic flow-through dissolution. In contrast to former experiments with AMs (Kreyling et al., 1979), we used cultivated NR8383 rat AMs to avoid animal consumption necessary for the use of primary cells. NR8383 cells are actively moving phagocytic cells which gather particles from the bottom of the cell culture vessels. The cells can be transiently cultivated under low serum-conditions. However, as NR8383 cells are not firmly attached to the substrate, a change of medium may lead to cell loss, such that their incubation with $SrCO_3$ and $BaSO_4$ in wells of a 96 well plate was limited to 1–2 days. To increase the yield of dissolved ions under these conditions, a comparatively high concentration of 45 µg/mL was used which, in case of $BaSO_4$, were found to be non-toxic under the conditions of the macrophage assay ((Wiemann et al., 2016), see Supplement Table SI 1 for $SrCO_3$). Exposure of the cells to the particle was accelerated by brief centrifugation of ENM onto the bottom of the 96-well plate (Fig. 5a). This procedure had no obvious influence on cell shape or motility but circumvented the phase of gravitational settling and, therefore, provided a common starting point for the time-lapse study of particle dissolution. Under these conditions AMs had entirely engulfed microscopically visible $SrCO_3$ agglomerates from the bottom of the wells after ≥3 h and this situation persisted until the end of incubation (Fig. 5b).

To measure the total amount of intra- and extracellular Sr ions by ICP-MS analysis, cells within each well were completely lysed with Triton X-100 and proteinase K after 3, 6, 12, 24 and 48 h and the homogenates were separated from any particulate constituents by passing through a 3 kDa filter unit. Incubation of $SrCO_3$ with NR8383 cells significantly increased the concentration of dissolved material in the medium compared to cell-free control at any point in time. For example, after 24 h concentrations of 21.87 ± 0 mg/kg (49% of total mass) and 6.71 ± 0 mg/kg (15% of total mass, n = 3) were measured for the macrophage-mediated dissolution and the cell-free medium control, respectively. Of note, the macrophage-mediated increase in dissolved $SrCO_3$ developed progressively up to 48 h, indicating ongoing cellular activity. In contrast, the incubation of $SrCO_3$ ENM in acidic PSF for 24 h led to a rapid dissolution of 97% of the total $SrCO_3$ mass (43.79 ± 0 mg/kg) and these high values remained fairly constant over time (Fig. 6, Table SI S1a). To analyze cytotoxic effects during $SrCO_3$ incubation, the activity of LDH was monitored in the cell culture

Table 2
Cumulative evaluation of biodissolution of ENM in flow cells with pH 4.5 media at 2 mL/h flow-through. For many materials, the ion concentration remained below the limit of detection (LoD), but could be improved by using dedicated ICP-MS instruments. **Significant dissolution** is marked bold.

	M_0	Max. ion concentration	Dissolved per 7 days	k	M_{ion}/T
Unit	[mg]	[mg/L]	[%]	[ng/cm^2/h]	[µg/day]
$BaSO_4$ NM-220 (nano)	1.05	**1.3**	**58**	**10**	**51**
$BaSO_4$ NM-220 (nano)	0.17	**0.8**	**100**	**45**	**18**
$BaSO_4$ IRMM381 (non-nano)	1.78	**0.49**	**9**	**53**	**16**
CeO_2 NM-211	1.1	< 0.1 (LoD)	< 3	< 0.28 (LoD)	< 3.9 (LoD)
CeO_2 NM-212	1.02	< 0.1 (LoD)	< 3	< 0.73 (LoD)	< 3.6 (LoD)
$Cu_2(OH)_2CO_3$	1.07	**3.0**	**32**	**172**	**24**
Cu_Phthalo_halogen	1	< 0.1 (LoD)	< 35 (LoD)	< 3.7 (LoD)	< 2.4 (LoD)
Cu_Phthalo_nano	0.98	**0.05**	**0.4**	**0.531**	**0.66**
CuO	1.56	**37**	**100**	**283**	**456**
Fe_2O_3_larger	1.09	< 0.1 (LoD)	< 3 (LoD)	< 1.56 (LoD)	< 3.7 (LoD)
Fe_2O_3_nano_A	1.07	< 0.1 (LoD)	< 3 (LoD)	< 0.17 (LoD)	< 3.2 (LoD)
Fe_2O_3_nano_B	0.99	< 0.1 (LoD)	< 3 (LoD)	< 0.65 (LoD)	< 3.6 (LoD)
SiO_2 NM-203	1.12	**0.3**	**8**	**0.23**	**11**
SiO_2 NM-200	1.01	**0.45**	**11**	**0.383**	**7.76**
SiO_2_amino_200	1.06	**0.28**	**7**	**0.216**	**4.83**
SiO_2_phosphonate_200	1.01	**0.18**	**8**	**0.275**	**5.76**
SiO_2_untreated_50	1.17	**0.03**	**0.5**	**0.088**	**1.6**
SiO_2_untreated_100	1.08	**0.04**	**0.9**	**0.066**	**1.7**
SiO_2_untreated_200	1.0	**0.05**	**1.2**	**0.044**	**2.1**
SiO_2_untreated_300	1.05	**0.06**	**1.4**	**0.034**	**2.6**
$SrCO_3$	1.08	**12.7**	**100**	**108**	**240**
TiO_2 NM-104	1.09	< 0.1 (LoD)	< 0.03 (LoD)	< 0.031 (LoD)	< 2.4 (LoD)
TiO_2 NM-105	1.04	< 0.01 (LoD)	< 0.1 (LoD)	< 0.013 (LoD)	< 0.1 (LoD)
ZnO NM-110	1.12	**18**	**100**	**204**	**217**
ZnO NM-111	1.12	**17**	**100**	**177**	**150**

supernatants. LDH activity was low after 3 h and 24 h (9.8 ± 6.5% of Triton X-100 control), but increased to 81.0 ± 38.1% of positive control at 48 h. At this point in time light microscopic inspection revealed cells with many pseudopodia and smooth surface, devoid of any signs of cell deterioration (Fig. 5b). In summary, $SrCO_3$, whose solubility is known to be pH-dependent, showed an enhanced and progressive dissolution upon uptake and digestion by live macrophages *in vitro*.

In the next step we analyzed whether the dissolution of $BaSO_4$, a material with a low solubility at neutral pH, might be also enhanced after uptake by macrophages. Following the same procedure as described for $SrCO_3$, 45 µg/mL $BaSO_4$ ENM suspension was applied to NR8383 AMs. Phase contrast micrographs confirmed the settling of $BaSO_4$ to the bottom of the wells after centrifugation (Fig. 7a). No $BaSO_4$ agglomerates remained visible between the cells at all timepoints ≥ 3 h (Fig. 7b). ICP-MS analysis of the filtrated cell homogenates and respective controls revealed that, after 24 h incubation of $BaSO_4$ with NR8383 cells, 1.88 ± 0.38 mg/kg material had dissolved, compared to 1.33 ± 0.37 mg/kg in the cell-free medium control, which corresponds to 4.18% and 2.95% of applied material, respectively. Exposure of $BaSO_4$ ENM to acidic PSF for 24 h led to dissolved material fractions of 2.4 ± 0.08 mg/kg, which corresponds to a dissolution of 5.34% (Figs. 8 and SI S1b). In accord with the well-known poor solubility of $BaSO_4$, we found low amounts of dissolved material in F-12K medium for all time points investigated, namely 2.98% of applied material in average. Although very subtle, NR8383 AM increased the dissolved material portion up to 6.13% at the 48 h timepoint. Similarly, PSF accelerated the dissolution up to 5.34% after 48 h.

The release of LDH 3, 6, 12, and 24 h post administration was very moderate (9.53 ± 4.05% of positive control) but raised to 48.86 ± 10.22% of positive control values after 48 h. Again, the microscopic inspection of $BaSO_4$-treated cells showed no signs of cell deterioration.

We finally assessed the macrophage-assisted dissolution of uncoated ZnO (NM-110) and surface-coated ZnO (NM-111). Both materials show a high solubility under *in vivo* conditions, i.e. at near neutral pH. NR8383 cells were exposed to only 5.6 µg/mL ZnO NM-110 and ZnO NM-111. At this concentration, cytotoxic effects of both ENM were moderate after 24 h (ZnO NM-110: 33.59%; ZnO NM-111: 33.69%) and were not influenced by stimulation with lipopolysaccharide (data not shown). ZnO agglomerates of either quality were not visible on the bottom of the cell culture vessel between the cells (not shown) after 24 h. At this timepoint 2.86 ± 0.1 mg/kg (51% dissolution) and 2.7 ± 0.12 mg/kg ZnO NM-110 (48% dissolution) were detected in the supernatant in the presence and absence of NR8383 cells, respectively. Compared to the medium control a significantly higher amount of ZnO NM-110 ($p = 0.005$) was dissolved in PSF (3.78 ± 0.06 mg/kg, 67% dissolution). Likewise, concentrations of ZnO NM-111 amounted to 2.2 ± 0.06 mg/kg in the NR8383 sample (39%), 2.2 ± 0.38 mg/kg in the medium control (39%), and 2.86 ± 0.35 mg/kg in PSF (51%). Due to these results we abstained from measuring after 48 h.

In summary, while the high solubility of both ZnO ENM was confirmed and shown to be increased in acidic PSF, phagolysosomal processes of live macrophages had no major influence on the solubilization of Zn ions (Fig. SI S1c and d).

4. Discussion

4.1. Discussion of macrophage-assisted mechanisms

As previously shown for the dissolution of poorly soluble, radiolabeled $^{57}Co_3O_4$ by primary alveolar macrophages (AMs) from humans and dogs (Kreyling et al., 1979), we found that also cultured AMs can accelerate the biodissolution of particulate matter. This was most obvious for $SrCO_3$, which is known to be soluble only under acidic conditions. Whereas $SrCO_3$ was readily soluble in PSF after 3 h incubation, only a minor fraction was dissolved after 3 h incubation with NR8383 macrophages. However, with longer incubation periods the dissolved fraction increased continuously. This might be due to the gradual acidification of the macrophage's phagolysosomes. In contrast, no significant dissolution occurred in the control experiment of medium without macrophages.

$BaSO_4$ was tested in comparable static (beaker) super-saturation condition in acidic PSF and in pH neutral medium. In this static

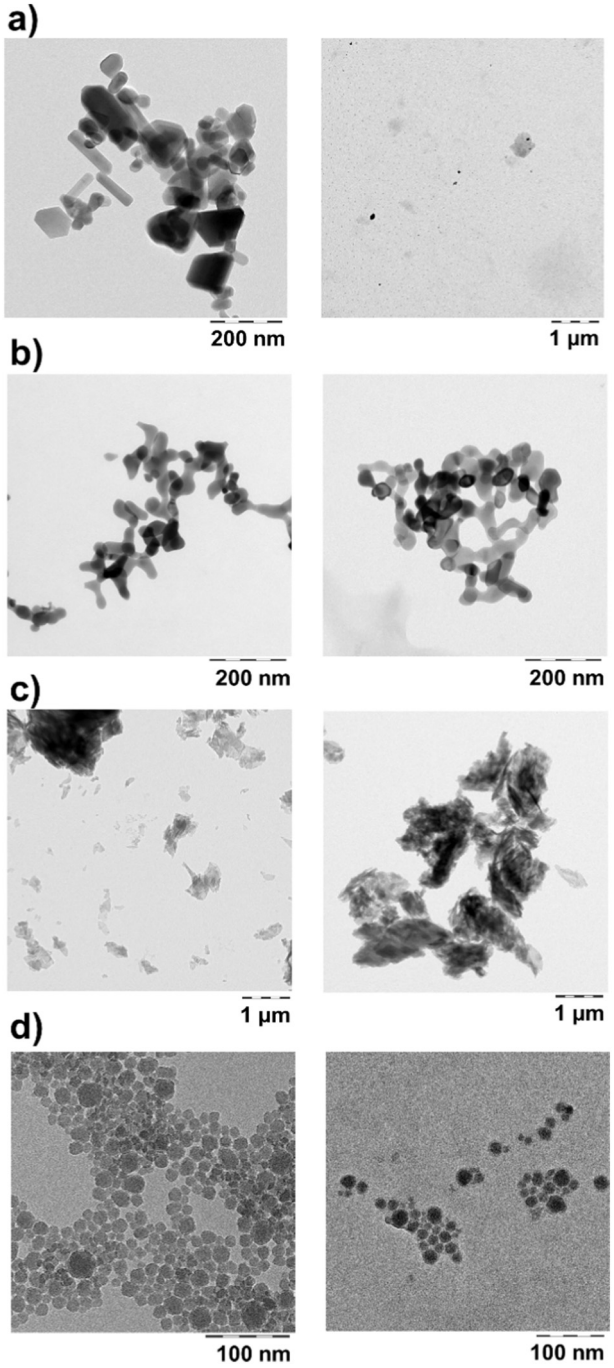

Fig. 3. Electron microscopic analysis of representative cases of ENM transformation. Comparison between TEM images of the pristine state (left column) and after the recovery from the flow-through cell after 7 days of treatment (right column). a) ZnO NM-110 (complete dissolution), b) Fe_2O_3_nano_B (no dissolution, no transformation), c) Cu_Phtalo_nano (no dissolution, aggregating transformation), d) SiO_2_untreated_200 (low dissolution, reprecipitation transformation).

experiment, Ba ion concentration was slightly higher in acidic PSF than in pH neutral medium control. Interestingly, the total dissolved fraction was considerably higher in the flow-through system (Keller et al., 2018). However, a trend of acceleration was hardly discernible after incubation with NR8383 cells. Because of the trace concentrations of Ba to be measured the analytical uncertainty might mask subtle cellular effects. In addition, the incubation time was limited to 48 h (to prevent a change of medium), and this is a major difference to the study of Kreyling and co-workers on the *in vitro* dissolution of $^{57}Co_3O_4$, who exposed AMs for 14 days and measured dissolved Co ions by gamma counting.

To compare the dissolution efficiency of AMs *in vivo*, we approximate the deposited dose per AM for an inhalation exposure of rats to 50 mg/m^3 $BaSO_4$ for 5 days, resulting in a lung burden of 1055.7 µg/lung. After a post-exposure period of 21 days the lung burden decreased to 239.7 µg/lung (difference 816 µg) (Landsiedel et al., 2014). The average AM cell count of female Wistar rats is approximately 1×10^7 (Rehn et al., 1992). Assuming a stable AM number throughout the post-exposure period, each macrophage engulfed/cleared 3.9×10^{-6} µg $BaSO_4$ per day, partially by dissolution. In the present study, 3×10^5 NR8383 cells were exposed to 9 µg $BaSO_4$ (45 µg/mL). After 24 h each macrophage dissolved 1.3×10^{-6} µg $BaSO_4$. Hence, the *in vivo* dissolution was augmented approximately by a factor of 3 compared to the *in vitro* situation. The *in vivo* clearance of particulate matter from the alveolar surface is primarily triggered by AMs, as particles are known to be phagocytosed within a few hours. Besides AM-associated mucociliary clearance, dissolution may contribute significantly to the clearance *in vivo*, which is obviously dependent on additional factors like surfactant turnover, lymphatic flow, and lung perfusion. This complex process cannot be mimicked *in vitro*. We conclude that for materials with a low solubility limit, an increase of biological complexity e.g. using macrophages of the testing method, compared to the abiotic dissolution system, is not beneficial.

This is also true for the ZnO ENM investigated. The dynamic *in vivo* situation which leads to a fast ZnO clearance from rat lungs could not be simulated in the static cell culture approach. It should be noted, that LDH activity was increased after 48 h incubation with $SrCO_3$ and $BaSO_4$ possibly pointing at beginning cytotoxicity although there were no visible signs of reduced viability or deteriorated cells. Apart from Sr, Ba, or Zn ions high LDH activity or membrane leakage may be caused by the comparatively high cell density under static culture conditions. Moreover, the AM approach suffers from unknown effective doses. Even if dissolution in phagolysosome occurs, reprecipitation and low-dose effects may occur, as shown for Ni-containing particles (Latvala et al., 2016). The dose uncertainties are especially relevant for materials that are partially soluble in the medium (ZnO) and/or well dispersed nanoparticles (such as colloidal silica) whose gravitational settling cannot be monitored by light microscopy (Wiemann et al., 2018). Complete transformation (by dissolution) during the *in vitro* incubation was confirmed for CuO and ZnO using advanced characterization with a synchrotron X-ray source (Ivask et al., 2017).

4.2. Discussion of abiotic dissolution vs. macrophage-assisted dissolution vs. in vivo pulmonary clearance

For the three cases of direct abiotic-vs-*in vitro* comparison, $BaSO_4$ NM-220, $SrCO_3$ and ZnO NM-111, the differentiation of dissolution rates from abiotic flow-through testing was consistent with differentiation by the *in vitro* AM method, and quantitative rates were within a factor 2.4, 1.8 and 1.5, respectively (Table 3). Time-resolved *in vivo* clearance kinetics are available for CeO_2 NM-212 and $BaSO_4$ NM-220 (from radio-activated intratracheal instillation), and are plotted against the dissolution rates of flow-through testing (Fig. 9) (Keller et al., 2014; Konduru et al., 2014). For all other materials, the percentage of remaining solid after 7 days in abiotic flow-through testing is compared in Table 3 to the remaining lung burden after 21 days of recovery *in vivo*, because only this value is available from the standardized STIS inhalation results. Thus our comparison in Table 3 targets consistency, not quantitative predictivity, and avoids modeling that would require several assumptions, such as mono-exponential decay, spherical shape etc. Assuming first-order kinetics (mono-exponential decay), the dissolution rate can be converted to half-times by Eq. SI_1, with the results given in Table 3. Assuming monodisperse size and spherical shape, Eqs. SI_4 to SI_5b reproduce the modeling of shrinking spheres from ISO

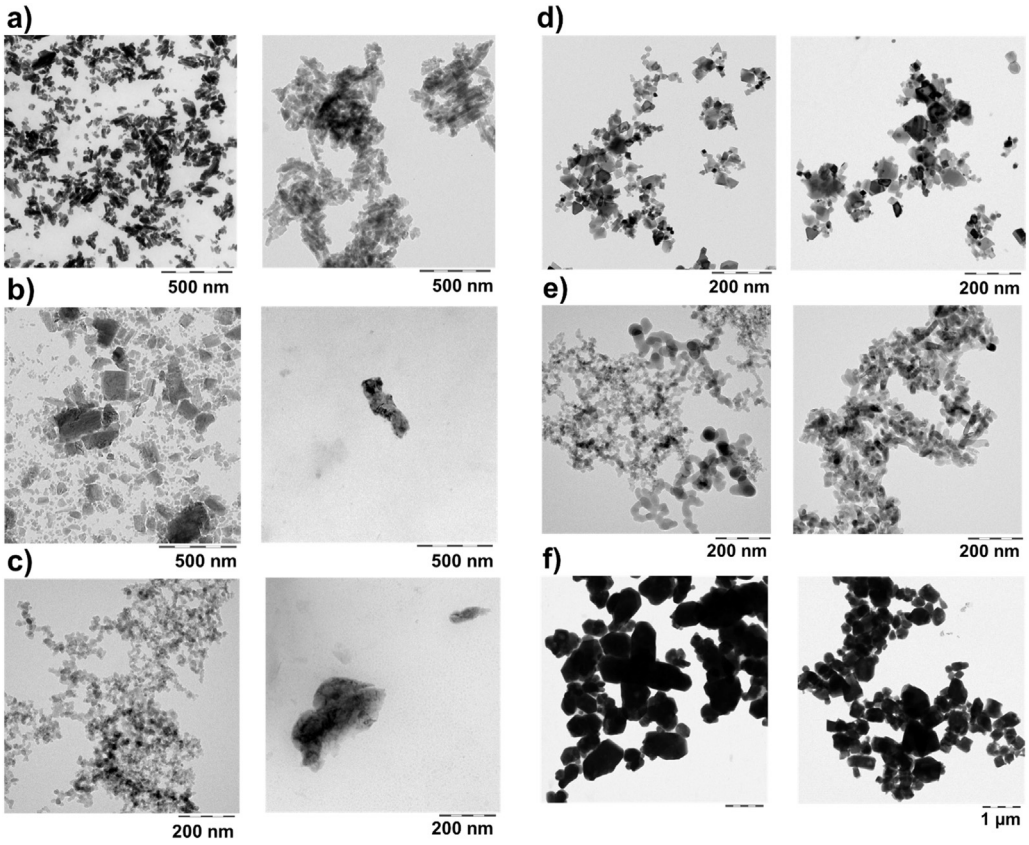

Fig. 4. Transformation analysis of additional materials: TEM images of the pristine materials (left) and after 7 days dissolution under standard conditions in PSF (right). a) CuPhthalocyanin_halogenated, b) $Cu(OH)_2CO_3$, c) SiO_2 NM-203, d) CeO_2 NM-212, e) TiO_2 NM-104, f) non-nano $BaSO_4$_IRMM381. By additional EDX, the structure in b) was found to contain mainly Si, not Cu, and is thus not assigned to the test material.

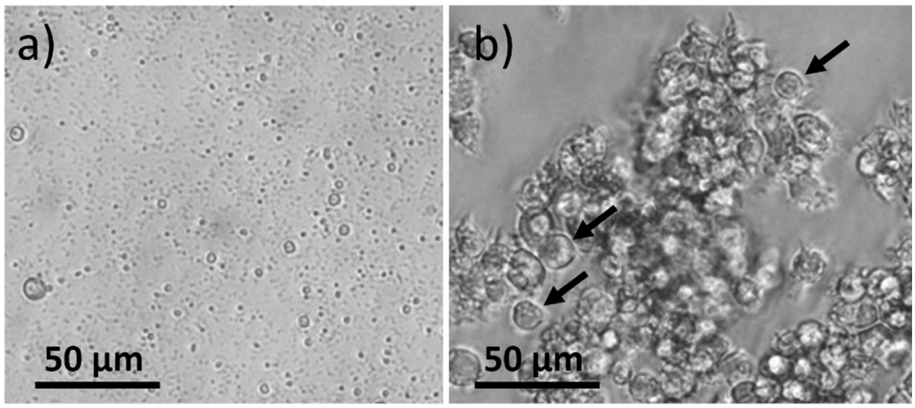

Fig. 5. Exposure of NR8383 alveolar macrophages to $SrCO_3$ ENM. Contrast-enhanced phase contrast micrograph showing (a) numerous $SrCO_3$ ENM agglomerates settled onto the bottom of the culture vessel post centrifugation under cell-free conditions, and (b) NR8383 cells after a 48 h incubation period with $SrCO_3$ ENM. Note that cells appear healthy with smooth outer contours (arrows). The space between cells is devoid of visible particles.

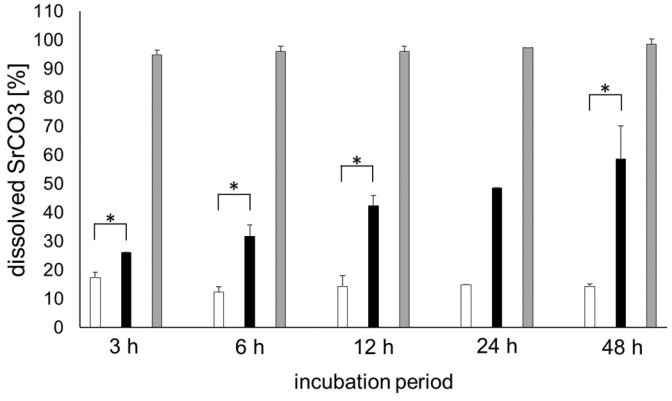

Fig. 6. Dissolution of $SrCO_3$ subjected to neutral and acidic pH conditions over time. F-12K cell culture medium control without cells (white bars); NR8383 rat AM (black bars); PSF pH 4.5 (grey bars); n = 3; * means $p \leq 0.05$.

TR19057:2017. With polydispersity, however, the time course of mass and surface area may result in multiphase kinetics, such as observed for ZnO (Fig. 2D); the *in situ* TEM (Fig. SI_4) confirms that this material is initially polydisperse in size and shape, and deviates even stronger from spherical shape during dissolution and transformation.

The measured reduction of lung burden was available for CuO (Gosens et al., 2016), ZnO NM-111 and TiO_2 NM-105 (Landsiedel et al., 2010), CeO_2 NM-212, NM-211 (Keller et al., 2014), SiO_2_untreated, and SiO_2_amino (Landsiedel et al., 2014). Most of these studies were also summarized as case studies of the DF4nanogrouping framework (Arts et al., 2016).

For all materials, the abiotic dissolution is consistent with *in vivo* observations, considering that both physical clearance and chemical dissolution contribute. For TiO_2 NM-105 and both nanoforms of SiO_2, dissolution means a marginal contribution to clearance, indicating that *in vivo* clearance is dominated by macrophage-mediated transport. However, for $BaSO_4$ NM-220, CuO, ZnO NM-110 and ZnO NM-111 lung

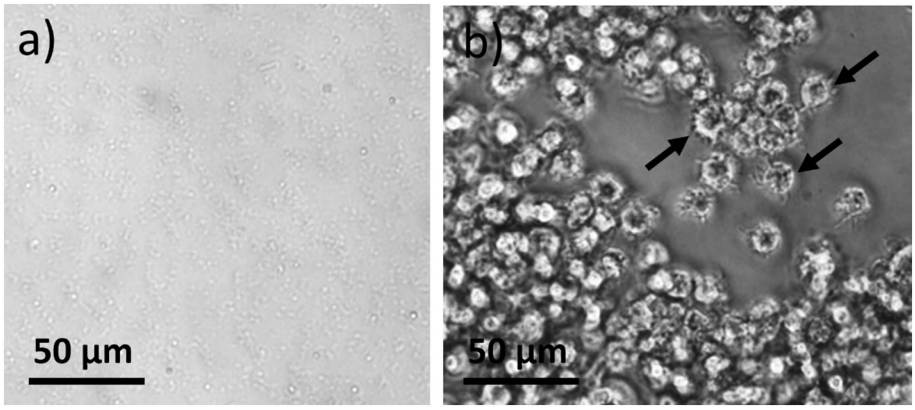

Fig. 7. Exposure of NR8383 alveolar macrophages to $BaSO_4$ ENM. Contrast-enhanced phase contrast micrographs showing (a) numerous $BaSO_4$ ENM agglomerates settled onto the bottom of the culture vessel post centrifugation under cell-free conditions and (b) NR8383 cells after a 48 h incubation period with $BaSO_4$ ENM. Note that cells have numerous pseudopodia (arrows). The space between cells is devoid of particles.

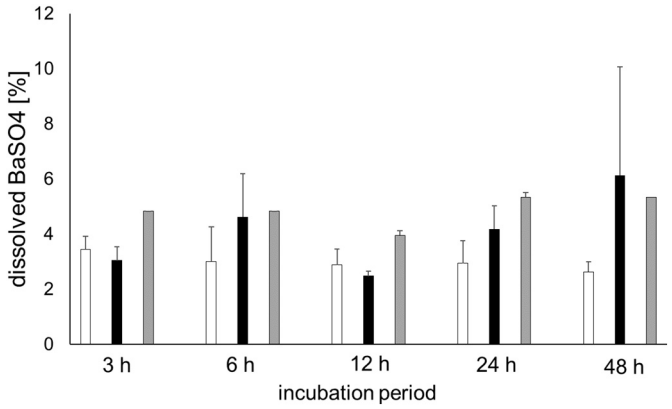

Fig. 8. Dissolution of $BaSO_4$ subjected to neutral and acidic pH conditions over time. F-12K cell culture medium control without cells (white bars); NR8383 rat AM (black bars); PSF pH 4.5 (grey bars); n = 3.

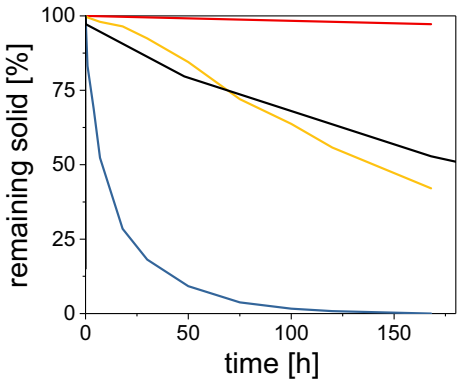

Fig. 9. Comparison of *in vivo* clearance vs. abiotic flow-through dissolution in PSF on $BaSO_4$ NM-220, CuO and CeO_2 NM-212. Red: CeO_2 NM-212 *in vivo* (Molina et al., 2014), yellow: $BaSO_4$ NM-220 abiotic flow-through, black: $BaSO_4$ NM-220 *in vivo* (Konduru et al., 2014), blue: CuO abiotic flow-through. After 504 h, the *in vivo* remaining CuO solids are zero or maximally 15% (LoD *in vivo*), consistent with the abiotic results (Gosens et al., 2016). Throughout the abiotic test from 0 h to 168 h, the dissolved CeO_2 is < 3% (LoD abiotic), consistent with the *in vivo* result.

clearance is dominated by dissolution. The dynamic dissolution flow-through system is the method of choice to predict the contribution of dissolution for *in vivo* clearance. Materials that were identified as of low dissolution rate in this system (e.g. TiO_2 NM-105) will be removed *in vivo* from the lungs mainly by AM-assisted mucociliary clearance. The physical clearance as well as the mobility of particles within the rat lungs may also be influenced by agglomeration *in situ*, whose mechanisms are beyond the scope of this discussion. For a read-across on low dissolution ENM (see group ranges proposed below), extrinsic properties such as dispersion stability, heteroagglomeration, affinity need to be considered to appropriately frame the mobility in the body. E.g., affinity to phospholipids is higher for SiO_2_amino than for SiO_2_untreated (Wohlleben et al., 2016), and may contribute to the slightly lower clearance despite faster dissolution rates. Chemical transformation has been observed also *in vivo* (Graham et al., 2017a,b), and specifically for the case of $BaSO_4$ we showed that the Ostwald ripening is consistently observed in the flow-through setup and *in vivo* (Keller et al., 2018). In principle, the remaining solids that we recover by the centrifugation procedure could be administered to cell cultures to test the response to the transformed material, as was done for static transformation in stomach/intestine simulants (DeLoid et al., 2017). However, our system cannot currently predict reprecipitation after systemic circulation, as has been observed on some ceria species (Graham et al., 2014).

It should be noted that the recommended conditions of (M_0 = 1 mg,

Table 3
Comparison of 7-day abiotic dissolution (standard conditions) with 1-day alveolar macrophage-assisted dissolution and 28-day clearance *in vivo* STIS.

	Dissolution rate macrophage-assisted (24 h) [ng/cm²/h]	Dissolution rate Abiotic flow-through, pH 4.5 [ng/cm²/h]	Half-time calculated from k [days]	Dissolution rate Abiotic flow-through, pH 4.5 [% per 7 days]	*In vivo* pulmonary clearance in STIS recovery [% per 21 days]
$BaSO_4$ NM-220	4.2	10	7	58%	52%
CeO_2 NM-211		< 0.28 (LoD)	> 156	< 3% (LoD)	7%
CeO_2 NM-212		< 0.73 (LoD)	> 146	< 3% (LoD)	5%
CuO		283	0.7	100%	> 85% (LoD)
SiO_2_amino		0.216	66	7%	34%
SiO_2_untreated		0.044	328	1.2%	39%
TiO_2 NM-105		< 0.013 (LoD)	> 4356	< 0.1% (LoD)	26%
ZnO NM-111	117	177	1.2	100%	93%
$SrCO_3$	61	108	1.9	100%	

LoD: level of detection. STIS: short term inhalation study.

V = 2 mL/h) are appropriate for many materials, but no universal optimum. As a quality control, it is recommended to check that measurement at two different SA/V leads to the same grouping. If SA/V was lower, then for several materials in our test set (e.g. the Cu-Phthalocyanins, the SiO_2 materials), the ion concentration in the eluate drops below the limit of detection of ICP-OES as a method that is highly established and robust against the high matrix concentrations of physiological buffers. ICP-MS and more optimization would allow to measure at lower SA/V. In contrast, for higher SA/V more materials may be limited by saturation. The specific SA/V conditions are selected to reproduce on the critical test case of $BaSO_4$ the *in vivo* transformation and dissolution behavior (Fig. 9) (Keller et al., 2018).

Flow-through systems are described by ISO 19057:2017 as "seen to be the best method of measuring durability *in vitro*" (Nti, 2017). Recently, flow-systems have been used to study gastro-intestinal dissolution of nanomaterials (without the exact same flow cells) (Bove et al., 2017a,b), and with the same flow cells (De Jong et al., 2018), and to study environmental dissolution (Pantano et al., 2018). To capture reactions of highly instable ENM-medium combinations on a time scale of minutes, it appears possible to eliminate fraction collection, and instead to hyphenate flow-cells directly to an ICP-MS; however, we adapted sampling times to physiological time scales (hours to days), guided by earlier evidence on other oxide materials. More specifically, flow-through systems have previously been used to study the pulmonary biodissolution of respirable man-made vitreous fibers (MMVF) (Nti, 2017). A large collection of abiotic dissolution rates and associated *in vivo* lung clearance rates has been made available for natural and man-made mineral fibers in a WHO report (IARC, 2002) which lists, among others, the following biodissolution rates of MMVF:

- MMVF34 "biosoluble stone wool" with a lung clearance half-life time of 6 days and k = 620 ng/cm^2/h (at pH 4.5) and k = 59 ng/cm^2/h (at pH 7.4);
- MMVF11 glass wool with a lung clearance half-life time of 9 days and k = 25 ng/cm^2/h (at pH 4.5) and k = 100 ng/cm^2/h (at pH 7.4);
- MMVF32 E-glass-wool with half-life time of 79 days and k = 9 ng/cm^2/h (at pH 4.5) and k = 7 ng/cm^2/h (at pH 7.4);
- crocidolite and amosite asbestos with half-life time of > 400 days and k < 1 ng/cm^2/h (at both pH).

It is interesting to note that many of the nanomaterials have dissolution rates (k values) at the lower end of the range spanned by the partially amorphous, partially crystalline aluminosilicates (stone wool, glass wool, asbestos). This is plausible considering the chemical composition. On the other hand, the BET surface of ENM is > 100× larger than that of typical glass or mineral fibers (which range around 0.2 m^2/g, due to several micrometer diameter) and this favors a low biopersistence of ENM, because half-times are given by the inverse of k and lung-deposited specific surface area (Eq. SI_1).

4.3. Discussion grouping and read-across

The results of the abiotic flow-through dissolution can be essential to substantiate a grouping hypothesis via the similarity of dissolution rates: The degree of biodissolution is similar for families of Fe_2O_3 (nano)forms, SiO_2 nanoforms, CeO_2 nanoforms, ZnO nanoforms, thus primarily determined by the substance, but shows significant modulation by production routes and surface coatings. In contrast, the modulation by shape or size is limited. Nanoforms although different in shape (Fe_2O_3), size (CeO_2, Fe_2O_3) or coatings (SiO_2, ZnO) can be grouped for pulmonary persistence, if their dissolution is sufficiently similar.

On the contrary, a dissimilarity of dissolution may be used to differentiate between ENM which are seemingly similar due to toxic components: Thus the four Cu-containing materials fall into different groups as CuO and $Cu_2(OH)_2CO_3$ exhibit a significant or complete dissolution after 7 days, whereas both Cu-Phthalocyanine ENM do not show significant solubility. Accordingly, the *in vivo* potency (mediated by Cu ions) was high for CuO (Gosens et al., 2016) but low for Cu-Phthalocyanine (Arts et al., 2016). Similarly, a differential lung toxicity was observed for a set of NiO nanoparticles after intratracheal instillation. Also in this case there was a strong correlation of inflammation parameters with solubility in artificial lysosomal fluid (Shinohara et al., 2017).

Especially coatings or functionalization modulated the dissolution rate within an order of magnitude in our dataset. Stronger modulation is expected only for closed shells, such as oxide coatings on more soluble core particles. For those materials with a very low equilibrium solubility limit under lysosomal conditions, the local dose of the ENM is another important parameter affecting the dissolution rate. This was the case for $BaSO_4$, but not for the other materials. Accordingly, also *in vitro* the dissolution rate can depend on initial mass, and this needs to be considered in screening and grouping strategies, e.g. for implementation of the DF4nanoGrouping framework:

- **Tier 1 Solubility**: The method for Tier 1 should be stirring of the suspension in a beaker, followed by ultrafiltration and ICP-OES (or -MS) analysis, as established by (Avramescu et al., 2016) for their enhancement of the DF4nanoGrouping framework. A cutoff between soluble and non-soluble ENM should be defined as absolute concentration, e.g. 100 mg/L, as by the DF4nanoGrouping framework.
  - If already at Tier 1 the intended use and the critical route of exposure are known, then it is an option to perform the same test in the most relevant biological medium.
  - For environmental hazard assessment purposes, the same method with simple media ranging from pH 4 to pH 9, and a cutoff at 9 mg/L (at 10 mg/mL initial solids) is discussed in the OECD task group on dissolution (Rasmussen et al., 2018).
- **Tier 2 Dissolution**: For a more detailed measurement and a refinement in Tier 2 a flow-through dissolution setup is recommended. Dissolution rates are thus tested out of equilibrium using relevant media that are derived from the intended exposure scenario of the ENM, such as pH 4.5 PSF for mimicking the dissolution within alveolar macrophages. The flow-through setup (consisting of an ultrafiltration cell, subsequent ICP-MS analysis of the eluate, and TEM analysis of the remaining solids) has been standardized and benchmarked against inhalation results with the following parameters: 1 mg of ENM initial solids, relevant medium (for inhalation concern: PSF at pH 4.5) and a continuous flow-rate of 2 mL/h for 7 consecutive days. However, the dose of ENM, the medium and the flow-rate used for the flow-through dissolution can be adapted to the requirements of other exposure scenarios, such as investigation of the dissolution in the gastrointestinal tract, requiring independent validation.
- **Tier 2 Transformation**: The analysis of changes during dissolution can be integrated into this strategy by our medium-removing TEM sample preparation after completion of the flow-through dissolution test. In a companion paper, we show that also complex transformations of a borderline soluble material ($BaSO_4$) are assessed correctly (Keller et al., 2018). The results presented here for 21 additional materials furthermore support the plausibility of transformation detection. No quantitative evaluation of crystallinity or composition can be proposed yet, but changes of the constituent particle size are quantified by automated image analysis (N > 300, e.g. using the NanoDefine tools).

Contrary to the hypothesis that AMs *in vitro* dissolution provides a more realistic model than the abiotic simulation of the AM lysosome alone, we found that macrophage-assisted dissolution *in vitro* is applicable only for a limited exposure period (1–2 days) and, therefore, may liberate comparatively low amounts of ions from ENM. Since the

method, as performed here, provided no further predictive value, we suggest that the Tier 2 "assessment of ENM similarity" can stick to abiotic flow-through dissolution at standardized conditions (initial mass of 1 mg, flow 2 mL/h) for grouping and read-across purposes. This experimental setup is in line with standards for evaluating biodissolution of mineral fibers. However, mechanistic investigations in Tier 3 may still require *in vivo* and cell-assisted studies.

The results of this study allow us to propose quantitative ranges to assign the tested nanomaterials in four distinct groups for the purpose of grouping of inhalation hazards.

1. The first group are non-persistent materials showing a high dissolution rate **k > 100 ng/cm²/h** and no remaining original particles in TEM, including CuO, $Cu(OH)_2CO_3$, $SrCO_3$, ZnO NM-110 and coated ZnO NM-111. This cutoff corresponds to an abiotic dissolution ranging from 30% to 100% after 7 days. Materials in this group are cleared completely (down to LoD) during a STIS inhalation recovery period.
2. The second group are non-persistent materials showing a **k ranging from 1 ng/cm²/h to 100 ng/cm²/h** and also **significant transformation** or reprecipitation. The range corresponds to a significant dissolution above 10% per 7 days. This group comprises both (nano) forms nano-$BaSO_4$ NM-220 and non-nano $BaSO_4$ IRMM381. Chemical clearance (dissolution) dominates, but physical clearance (transport) and reprecipitation contribute to the processes in a relatively complex interplay.
3. The third group of nanomaterials shows a very low dissolution (**k < 1 ng/cm²/h or below LoD**) but a **significant transformation** during the test period. This corresponds to an abiotic dissolution ≪30% (or even no apparent dissolution). Examples are both nanoforms of Cu-Phthalocyanine and all tested silica materials, where differences may be related to the silica production process. For these materials the physical clearance from the lung (transport) is accompanied by aggregation and/or reprecipitation.
4. The fourth group contains all biopersistent materials that show very low or no dissolution (**k < 1 ng/cm²/h or below LoD**) and no significant transformation. All tested (nano)forms of Fe_2O_3 (A, B, larger) as well as both CeO_2 (NM-211, NM-212) and both TiO_2 NM-104 and NM-105 belong to this group. Physical clearance (transport) dominates the pulmonary clearance.

Alternatively, group ranges might be defined by k values given in ng/cm²/h, or by the more pragmatic "% dissolution per 7 days" which requires no BET measurement of the specific surface area of the ENM for evaluation of the flow-through raw data. The consideration of the specific surface area in case of the "k metric" is the major difference between the two metrics, and allows us to motivate the decadic group ranges with a rich body of mineral fiber literature (see discussion above). The k metric also favors the read-across between nanoform and non-nanoform, because it eliminates the dissimilarity of the specific surface and focuses on differences beyond size and surface area.

5. Conclusions

In this work, the flow-through dissolution system was used to investigate the out of equilibrium dissolution behavior of a broad set of ENM and compared to alveolar macrophage-assisted dissolution as well as the *in vivo* clearance in rats. A high degree of consistency of the abiotic dissolution and the *in vivo* clearance has been achieved for CeO_2 NM-212, two forms of colloidal SiO_2, TiO_2 NM-105, CuO, nano $BaSO_4$ NM-220 and ZnO NM-111. This method and benchmark materials can be used to implement grouping frameworks such as those of ECHA (2017b) or ECETOC (Arts et al., 2015): For Tier 1 testing the investigation of the dissolution under static conditions is sufficient as proposed by (Avramescu et al., 2016). However, for Tier 2 testing the abiotic flow-through setup in relevant media is required, as proposed in this work on the example of pulmonary biodissolution. Cultured alveolar macrophage-assisted dissolution is acknowledged as a potential method for very specific Tier 3 investigations but needs to be further explored to achieve sufficiently long exposure periods.

The flow-through dissolution setup and protocol used in this work combines an integrated quantification of dissolution by ICP-MS/-OES and detection of transformation through TEM. Using our 24 case studies, we proposed four groups based on decadic ranges of quantitative dissolution rates and on a qualitative analysis of transformation. The representatives of the four groups (benchmark materials) are ZnO NM-110 (complete dissolution), $BaSO_4$ NM-220 (slow dissolution, reprecipitation transformation), SiO_2 NM-203 (very low dissolution, reprecipitation/aggregation transformation), TiO_2 NM-105 or Fe_2O_3_nano_B (very low dissolution, very low transformation). Finally, the method can be employed for testing of dissolution and transformation in environmental media.

Acknowledgement

We thank Thorsten Wieczorek for excellent laboratory support on TEM imaging. We gratefully acknowledge helpful discussions with Alison Elder, Uschi Graham and Günter Oberdörster.

Funding

This work was part of the project nanoGRAVUR supported by German Federal Ministry of Education and Research (BMBF), grant numbers 03XP0002B and 03XP0002J.

Appendix A. Supplementary data

Supplementary data to this article can be found online at https://doi.org/10.1016/j.impact.2018.08.005.

References

Albrecht, C., et al., 2007. Surface-dependent quartz uptake by macrophages: potential role in pulmonary inflammation and lung clearance. Inhal. Toxicol. 19 (Suppl. 1), 39–48.
Arts, J.H.E., et al., 2015. A decision-making framework for the grouping and testing of nanomaterials (DF4nanoGrouping). Regul. Toxicol. Pharmacol. 71 (2), S1–S27.
Arts, J.H.E., et al., 2016. Case studies putting the decision-making framework for the grouping and testing of nanomaterials (DF4nanoGrouping) into practice. Regul. Toxicol. Pharmacol. 76, 234–261.
Avramescu, M.-L., et al., 2016. Influence of pH, particle size and crystal form on dissolution behaviour of engineered nanomaterials. Environ. Sci. Pollut. Res. 1–12.
Babick, F., et al., 2016. How reliably can a material be classified as a nanomaterial? Available particle-sizing techniques at work. J. Nanopart. Res. 18 (6), 1–40.
Bhattacharjee, S., et al., 2012. Cytotoxicity and cellular uptake of tri-block copolymer nanoparticles with different size and surface characteristics. Part. Fibre Toxicol. 9, 11.
Bhattacharjee, S., et al., 2013. Cytotoxicity of surface-functionalized silicon and germanium nanoparticles: the dominant role of surface charges. Nanoscale 5 (11), 4870–4883.
Bove, P., et al., 2017a. Dissolution test for risk assessment of nanoparticles: a pilot study. Nanoscale 9 (19), 6315–6326.
Bove, P., Malvindi, M.A., Sabella, S., 2017b. In Vitro Human Digestion Test to Monitor the Dissolution of Silver Nanoparticles. vol. 838. pp. 012003.
Braakhuis, H.M., et al., 2014. Physicochemical characteristics of nanomaterials that affect pulmonary inflammation. Part. Fibre Toxicol. 11.
Collier, Z.A., et al., 2015. Tiered guidance for risk-informed environmental health and safety testing of nanotechnologies. J. Nanopart. Res. 17 (3), 155.
Dale, A.L., Lowry, G.V., Casman, E.A., 2015. Stream dynamics and chemical transformations control the environmental fate of silver and zinc oxide nanoparticles in a watershed-scale model. Environ. Sci. Technol. 49 (12), 7285–7293.
De Jong, Wim H., De Rijk, Eveline, Bonetto, Alessandro, Wohlleben, Wendel, Stone, Vicki, Brunelli, Andrea, Badetti, Elena, Marcomini, Antonio, Gosens, Ilse, Cassee, Flemming R., 2018. Toxicity of copper oxide and basic copper carbonate nanoparticles after short-term oral exposure in rats. Nanotoxicology (revised June 2018).
DeLoid, G.M., et al., 2017. An integrated methodology for assessing the impact of food matrix and gastrointestinal effects on the biokinetics and cellular toxicity of ingested engineered nanomaterials. Part. Fibre Toxicol. 14 (1), 40.
Donaldson, K., Poland, C.A., 2013. Nanotoxicity: challenging the myth of nano-specific toxicity. Curr. Opin. Biotechnol. 24, 724–734.
ECHA, 2017a. How to Prepare Registration Dossiers that Cover Nanoforms: Best

Practices.
ECHA, 2017b. Appendix R.6-1 for Nanomaterials Applicable to the Guidance on QSARs and Grouping of Chemicals.
Eidi, H., et al., 2010. Cytotoxicity assessment of heparin nanoparticles in NR8383 macrophages. Int. J. Pharm. 396 (1–2), 156–165.
Eidi, H., et al., 2012. Drug delivery by polymeric nanoparticles induces autophagy in macrophages. Int. J. Pharm. 422 (1–2), 495–503.
Gao, X., Lowry, G.V., 2018. Progress towards standardized and validated characterizations for measuring physicochemical properties of manufactured nanomaterials relevant to nano health and safety risks. NanoImpact 9 (Supplement C), 14–30.
Geiser, M., 2010. Update on macrophage clearance of inhaled micro- and nanoparticles. J. Aerosol Med. Pulm. Drug Deliv. 23 (4), 207–217.
Godwin, H., et al., 2015. Nanomaterial categorization for assessing risk potential to facilitate regulatory decision-making. ACS Nano 9 (4), 3409–3417.
Gosens, I., et al., 2016. Organ burden and pulmonary toxicity of nano-sized copper (II) oxide particles after short-term inhalation exposure. Nanotoxicology 10 (8), 1084–1095.
Graham, U.M., et al., 2014. In vivo processing of ceria nanoparticles inside liver: impact on free-radical scavenging activity and oxidative stress. ChemPlusChem 79 (8), 1083–1088.
Graham, U., et al., 2017a. Calcium Co-localization With In Vivo Cerium Phosphate Nanoparticle Formation After Intratracheal Instillation Dosing With CeCl3 or CeO2 NPs. vol. 23. pp. 1344–1345.
Graham, U.M., et al., 2017b. From dose to response: in vivo nanoparticle processing and potential toxicity. In: Tran, L., Bañares, M.A., Rallo, R. (Eds.), Modelling the Toxicity of Nanoparticles. Springer International Publishing, Cham, pp. 71–100.
Guldberg, M., et al., 1995. Method for determining in-vitro dissolution rates of man-made vitreous fibres. Glas. Sci. Technol. 68 (6), 181–187.
Helmke, R.J., et al., 1987. From growth factor dependence to growth factor responsiveness: the genesis of an alveolar macrophage cell line. In Vitro Cell. Dev. Biol. 23 (8), 567–574.
Helmke, R.J., German, V.F., Mangos, J.A., 1989. A continuous alveolar macrophage cell line: comparisons with freshly derived alveolar macrophages. In Vitro Cell. Dev. Biol. 25 (1), 44–48.
Hofmann, T., et al., 2016. Comparative short-term inhalation toxicity of five organic diketopyrrolopyrrole pigments and two inorganic iron-oxide-based pigments. Inhal. Toxicol. 28 (10), 463–479.
IARC, I.A.F.R.O.C, 2002. Man-made Vitreous Fibres. World Health Organization, pp. 1–433.
Iler, R.K., 1979. The Chemistry of Silica Solubility, Polymerization, Colloid and Surface Properties, and Biochemistry of Silica. Wiley.
Ivask, A., et al., 2017. Complete transformation of ZnO and CuO nanoparticles in culture medium and lymphocyte cells during toxicity testing. Nanotoxicology 1–16.
Kass, E.H., 1964. The Role of the Alveolar Macrophage in the Clearance of Bacteria From the Lung * (From the Channing Laboratory, Mallory Institute of Pathology, Thorndike Memorial Laboratory, and Second and Fourth (Harvard) Medical Semices, Boston City Hospital. Methods).
Keller, J., et al., 2014. Time course of lung retention and toxicity of inhaled particles: short-term exposure to nano-Ceria. Arch. Toxicol. 88 (11), 2033–2059.
Keller, J., Graham, U., Koltermann-Jülly, J., Gelein, R., Ma-Hock, L., Landsiedel, R., Wiemann, M., Oberdörster, G., Elder, A., Wohlleben, W., 2018. Predicting dissolution and transformation of inhaled nanoparticles in the lung using abiotic flow cells: the case of barium sulfate. (to be submitted).
Kent, R.D., Vikesland, P.J., 2016. Dissolution and persistence of copper-based nanomaterials in undersaturated solutions with respect to cupric solid phases. Environ. Sci. Technol. 50 (13), 6772–6781.
Klaessig, F., 2018. Dissolution as a Paradigm in Regulating Nanomaterials. Environ. Sci. Nano 5, 1070–1077. https://doi.org/10.1039/C7EN01130J.
Konduru, N., et al., 2014. Biokinetics and effects of barium sulfate nanoparticles. Part. Fibre Toxicol. 11 (1), 55.
Koslowski, R., et al., 2003. Evidence for the involvement of TGF-beta and PDGF in the regulation of prolyl 4-hydroxylase and lysyloxidase in cultured rat lung fibroblasts. Exp. Toxicol. Pathol. 55 (4), 257–264.
Kreyling, W., et al., 1979. In vitro dissolution of uniform cobalt oxide particles by human and canine alveolar macrophages. Am. J. Respir. Cell Mol. Biol. 2, 413–422.
Kroll, A., et al., 2011. Cytotoxicity screening of 23 engineered nanomaterials using a test matrix of ten cell lines and three different assays. Part. Fibre Toxicol. 8 (1), 1.
Kuempel, E., et al., 2012. Development of risk-based nanomaterial groups for occupational exposure control. J. Nanopart. Res. 14, 1029.
Landsiedel, R., et al., 2010. Testing metal-oxide nanomaterials for human safety. Adv. Mater. 22 (24), 2601–2627.
Landsiedel, R., et al., 2014. Application of short-term inhalation studies to assess the inhalation toxicity of nanomaterials. Part. Fibre Toxicol. 11 (1), 16.
Landsiedel, R., Sauer, U.G., de Jong, W.H., 2017. Chapter 8: risk assessment and risk management. In: Adverse Effects of Engineered Nanomaterials, Second edition. Exposure, Toxicology, and Impact on Human Health Academic Press, pp. 189–222.
Latvala, S., et al., 2016. Nickel release, ROS generation and toxicity of Ni and NiO micro- and nanoparticles. PLoS One 11 (7), e0159684.
Lison, D., et al., 2008. Nominal and effective dosimetry of silica nanoparticles in cytotoxicity assays. Toxicol. Sci. 104 (1), 155–162.
Lison, D., et al., 2009. Sintered indium-tin-oxide (ITO) particles: a new pneumotoxic entity. Toxicol. Sci. 108 (2), 472–481.
Marques, M., Loebenberg, R., Almukainzi, M., 2011. Simulated biological fluids with possible application in dissolution testing. Dissolut. Technol. 8.
Mehn, D., et al., 2018. Identification of nanomaterials: a validation report of two laboratories using analytical ultracentrifugation with fixed and ramped speed options. NanoImpact 10, 87–96.
Mielke, J., et al., 2016. Evaluation of electron microscopy techniques for the purpose of classification of nanomaterials. In: European Microscopy Congress 2016: Proceedings. Wiley Online Library.
Ministère de l'Environnement, d.l.É.e.d.l.M, 2015. Éléments issus des déclarations des substances à l'état nanoparticulaire: Exercice 2015.
Mitrano, D.M., Nowack, B., 2017. The need for a life-cycle based aging paradigm for nanomaterials: importance of real-world test systems to identify realistic particle transformations. Nanotechnology 28 (7), 072001.
Mitrano, D.M., et al., 2015. Review of nanomaterial aging and transformations through the life cycle of nano-enhanced products. Environ. Int. 77 (0), 132–147.
Molina, R.M., et al., 2014. Bioavailability, distribution and clearance of tracheally instilled, gavaged or injected cerium dioxide nanoparticles and ionic cerium. Environ. Sci. Nano 1 (6), 561–573.
Muller, P., et al., 2015. Assessment of different electron microscopy techniques for particle size quantification of potential nanomaterials. Microsc. Microanal. 21 (Supplement S3), 2403–2404.
Nel, A.E., et al., 2013. A multi-stakeholder perspective on the use of alternative test strategies for nanomaterial safety assessment. ACS Nano 7.
Nti, 2017. PD ISO/TR 19057:2017 - nanotechnologies. Use and application of acellular in vitro tests and methodologies to assess nanomaterial biodurability. Nanotechnologies. Use and Application of Acellular In Vitro Tests and Methodologies to Assess Nanomaterial Biodurability.
Oberdörster, G., Kuhlbusch, T.A.J., 2018. In vivo effects: methodologies and biokinetics of inhaled nanomaterials. NanoImpact 10 (Supplement C), 38–60.
Oomen, A.G., et al., July 2017. Risk assessment frameworks for nanomaterials: scope, link to regulations, applicability, and outline for future directions in view of needed increase in efficiency. NanoImpact 2018 (9), 1–13.
Pantano, D., et al., 2018. Transformations of nanoenabled copper formulations govern release, antifungal effectiveness, and sustainability throughout the wood protection lifecycle. Environ. Sci. Technol. 52 (3), 1128–1138.
Plakhova, T.V., et al., 2016. Solubility of nanocrystalline cerium dioxide: experimental data and thermodynamic modeling. J. Phys. Chem. C 120 (39), 22615–22626.
Pulskamp, K., Diabate, S., Krug, H.F., 2007. Carbon nanotubes show no sign of acute toxicity but induce intracellular reactive oxygen species in dependence on contaminants. Toxicol. Lett. 168 (1), 58–74.
Rasmussen, K., et al., 2018. Physico-chemical properties of manufactured nanomaterials - characterisation and relevant methods. An outlook based on the OECD Testing Programme. Regul. Toxicol. Pharmacol. 92 (Supplement C), 8–28.
Rehn, B., et al., 1992. Recovery of rat alveolar macrophages by bronchoalveolar lavage under normal and activated conditions. Environ. Health Perspect. 97, 11–16.
Scherbart, A.M., et al., 2011. Contrasting macrophage activation by fine and ultrafine titanium dioxide particles is associated with different uptake mechanisms. Part. Fibre Toxicol. 8 (1), 31.
Shinohara, N., et al., 2017. Kinetics and dissolution of intratracheally administered nickel oxide nanomaterials in rats. Part. Fibre Toxicol. 14 (1), 48.
Stefaniak, A.B., et al., 2005. Characterization of phagolysosomal simulant fluid for study of beryllium aerosol particle dissolution. Toxicol. in Vitro 19 (1), 123–134.
Steinhäuser, K.G., Sayre, P.G., 2017. Reliability of methods and data for regulatory assessment of nanomaterial risks. NanoImpact 7 (Supplement C), 66–74.
Ullmann, C., Müller, P., 2017. SOP, Applicability Range and Method Performance Description for DLS & MiniTEM.
Vencalek, B.E., et al., 2016. In situ measurement of CuO and Cu(OH)2 nanoparticle dissolution rates in quiescent freshwater mesocosms. Environ. Sci. Technol. Lett. 3 (10), 375–380.
Wagner, A.J., et al., 2007. Cellular interaction of different forms of aluminum nanoparticles in rat alveolar macrophages. J. Phys. Chem. B 111 (25), 7353–7359.
Wang, Z., et al., 2016. Biological and environmental interactions of emerging two-dimensional nanomaterials. Chem. Soc. Rev. 45 (6), 1750–1780.
Wiemann, M., et al., 2016. An in vitro alveolar macrophage assay for predicting the short-term inhalation toxicity of nanomaterials. J. Nanobiotechnol. 14 (1), 1–27.
Wiemann, M., et al., 2018. In vitro and in vivo short-term pulmonary toxicity of differently sized colloidal amorphous SiO2. Nanomaterials 8 (3), 160.
Wohlleben, W., et al., 2016. Influence of agglomeration and specific lung lining lipid/protein interaction on short-term inhalation toxicity. Nanotoxicology 1–11.
Wohlleben, W., et al., 2017a. Nanoenabled products: categories, manufacture, and applications: protocols and industrial innovations. In: Mansfield, E. (Ed.), Metrology and Standardization for Nanotechnology: Protocols and Industrial Innovations. John Wiley & Sons, pp. 411–464.
Wohlleben, W., et al., 2017b. Reliable nanomaterial classification of powders using the volume-specific surface area method. J. Nanopart. Res. 19 (2), 61.
Wohlleben, W., et al., 2017c. Composition, respirable fraction and dissolution rate of 24 stone wool MMVF with their binder. Part. Fibre Toxicol. 14 (1), 29.

6.1.1 Authors contributions

Abiotic dissolution rates of 24 (nano)forms of 6 substances compared to macrophage-assisted dissolution and in vivo pulmonary clearance: Grouping by biodissolution and transformation

Johanna Koltermann-Jülly[1], Johannes G. Keller[1], Antje Vennemann, Kai Werle, Philipp Müller,
Lan Ma-Hock, Robert Landsiedel, Martin Wiemann, Wendel Wohlleben

[1] *Equal contribution.*

NanoImpact. Volume 12, 2018, Pages 29-41

Authors contributions

JKJ, AV, MW conceived and performed the NR8383 macrophage-assisted dissolution testing in vitro, analyzed the data, and evaluated the results.
JGK, KW performed the abiotic flow-through testing of dissolution.
PM supervised and evaluated electron microscopy for transformation analysis.
WW conceived and, together with LMH, MW and RL, supervised the project and contributed to the interpretation of results.
All authors contributed to the writing of the manuscript.

We hereby confirm the accuracy of the above information (all authors).

Koltermann-Jülly, Johanna	
Name	*Date, Signature*
Keller, Johannes Georg	
Name	*Date, Signature*
Vennemann, Dr. Antje	
Name	*Date, Signature*
Werle, Kai	
Name	*Date, Signature*
Müller, Dr. Philipp	
Name	*Date, Signature*
Ma-Hock, Dr. Lan	
Name	*Date, Signature*
Landsiedel, PD Dr. Robert	
Name	*Date, Signature*
Wiemann, Prof. Dr. Martin	
Name	*Date, Signature*
Wohlleben, Dr. Wendel	
Name	*Date, Signature*

6.1.2 Addendum

To the original article

Abiotic dissolution rates of 24 (nano)forms of 6 substances compared to macrophage-assisted dissolution and in vivo pulmonary clearance: Grouping by biodissolution and transformation

Johanna Koltermann-Jülly[1], Johannes G. Keller[1], Antje Vennemann, Kai Werle, Philipp Müller,
Lan Ma-Hock, Robert Landsiedel, Martin Wiemann, Wendel Wohlleben

[1] *Equal contribution.*

NanoImpact. Volume 12, 2018, Pages 29-41

an addendum was published in

NanoImpact. Volume 14, 2019, 100154

https://doi.org/10.1016/j.impact.2019.100154

6.2 Paper 2: „Predicting dissolution and transformation of inhaled nanoparticles in the lung using abiotic flow cells: The case of barium sulfate“

The following section contains the publication:

Predicting dissolution and transformation of inhaled nanoparticles in the lung using abiotic flow cells: The case of barium sulfate

Johannes G. Keller[1], Uschi Graham[1], **Johanna Koltermann-Jülly**, Robert Gelein, Lan Ma-Hock, Robert Landsiedel, Martin Wiemann, Günter Oberdörster, Alison Elder, Wendel Wohlleben

[1] *Equal contribution.*

Scientific Reports, 2019, submitted manuscript

Predicting dissolution and transformation of inhaled nanoparticles in the lung using abiotic flow cells: The case of barium sulfate

Johannes G. Keller[1,2]†, Uschi Graham[3]†, Johanna Koltermann-Jülly[1,4], Robert Gelein[6], Lan Ma-Hock[1], Robert Landsiedel[1], Martin Wiemann[5], Günter Oberdörster[6], Alison Elder[6]*, Wendel Wohlleben[1]*

† equal contribution

* Correspondence: alison_elder@urmc.rochester.edu; wendel.wohlleben@basf.com

Affiliations:

[1] BASF SE, Dept. Experimental Toxicology and Ecology, and Dept. Material Physics, 67056 Ludwigshafen, Germany; johanna.koltermann-juelly@basf.com, johannes-georg.keller@basf.com, lan.ma-hock@basf.com, robert.landsiedel@basf.com, wendel.wohlleben@basf.com

[2] Institute of Pharmacy, Faculty of Biology, Chemistry & Pharmacy, Freie Universität Berlin, 14195 Berlin, Germany

[3] National Institute of Occupational Safety and Health, Cincinnati, Ohio, 45226, USA; graham@topasol.com

[4] Biopharmaceutics and Pharmaceutical Technology, Saarland University, 66123 Saarbrücken, Germany

[5] IBE R&D Institute for Lung Health gGmbH, Mendelstr. 11, 48149 Münster, Germany; martin.wiemann@ibe-ms.de

[6] University of Rochester Medical Center, Rochester, New York, USA; alison_elder@urmc.rochester.edu, gunter_oberdorster@urmc.rochester.edu, robert_gelein@urmc.rochester.edu

Abstract

Barium sulfate ($BaSO_4$) was considered to be poorly-soluble and toxicologically inert, but $BaSO_4$ NM-220 showed a surprisingly short retention after intratracheal instillation in rat lungs, and incorporation of Ba within the bones. Here we show that static abiotic dissolution cannot rationalize this result, whereas two dynamic abiotic dissolution systems (one flow-through and one flow-by) indicated 50 % dissolution after 5 to 6 days at non-saturating conditions regardless of flow orientation, which is close to the *in vivo* half-time of 9.6 days. Non-equilibrium conditions were thus essential to simulate *in vivo* biodissolution. Instead of shrinking from 32 nm to 23 nm (to match the mass loss to ions), TEM scans of particles retrieved from flow-cells showed an increase to 40 nm. Such transformation suggested either material transport through interfacial contact or Ostwald ripening at saturating conditions and was also observed *in vivo* inside macrophages by high-resolution TEM following 12 months inhalation exposure. The abiotic flow cells thus adequately predicted the overall pulmonary biopersistence of the particles that was mediated by non-equilibrium dissolution and recrystallization. The present methodology for dissolution and transformation fills a high priority gap in nanomaterial hazard assessment and is proposed for the implementation of grouping and read-across by dissolution rates.

Keywords: inhaled engineered nanomaterial, in vivo processing, nanomaterial dissolution,

transformation, in vivo clearance

Introduction

Knowledge about pulmonary retention kinetics of inhaled particles is an essential element of hazard assessment and of understanding the mechanisms by which adverse health outcomes may occur. Barium sulfate was generally assumed to be poorly-soluble and toxicologically inert unless delivered at high concentrations over an extended period [1,2]. However, Konduru and colleagues reported that intratracheally instilled $^{131}BaSO_4$ NM-220 exhibited a lung retention half-time of only 9.6 days in rats and that ^{131}Ba was incorporated into the bones, suggesting nanoparticle dissolution and/or translocation to extrapulmonary sites [3]. A subsequent 90-day inhalation study in rats with a high concentration of aerosolized $BaSO_4$ NM-220 (50 mg/m^3) [4] revealed no signs of lung overload and a retention half-time of 56 days, which is close to the normal range for the rat lung [4]. A two-year rat inhalation study with $BaSO_4$ NM-220 (50 mg/m^3), however, demonstrated an increase of retained Ba in the lung during the first year of exposure, after which a steady-state was achieved [5]. Since significant Ba accumulation in bone and bone marrow was also observed and, given that the measurements of Ba distribution [1-3] provide no information about its physicochemical characteristics, the complex *in vivo* dissolution and/or transformation of $BaSO_4$ secondary to inhalation exposure require more detailed investigation.

Particle clearance from the lung involves absorptive (dissolution) and non-absorptive (physical) mechanisms. For poorly-soluble particles, physical clearance mechanisms – involving macrophage engulfment, transport, and mucociliary propulsion towards the oropharynx – dominate the pattern of overall clearance. Kreyling [6] demonstrated a retention half-time of 70 days in the rat for poorly-soluble particles [7]. For metal nanoparticles that undergo *in vivo* dissolution, clearance may not be immediate due to biotransformation and binding events (proteins or other biomolecules) that prolong retention [8-10]. Thus, the collective *in vivo* observations with lung-deposited $BaSO_4$ suggest that it is more biosoluble than assumed and, therefore, *in vivo* dissolution and processing must be considered.

The evaluation of particle solubility is a key element of many integrated testing strategies [10-12] and of frameworks for categorizing broad classes of materials, such as engineered nanomaterials (ENMs), in

terms of their physicochemical properties [13-19]. Methods to assess the equilibrium (or quasi-dynamic) solubility of ENMs that are suspended in water or physiological buffers – as was done with $BaSO_4$ and supported the conclusion regarding its low solubility – are relatively well developed [20,21]. The OECD draft guideline under current discussion involves suspending particles in a medium, incubation, removal of remaining solids by centrifugation or ultrafiltration, and measurement of the analyte in solution [22]. These approaches could be adequately predictive of particle dissolution in a closed system, e.g., a cell culture well for *in vitro* exposure studies [21]. There are several drawbacks with these approaches, however, when the model in question is an *in vivo* one. First, the lung is not a static (equilibrium) system, as the ions that are liberated from the particles via dissolution are continuously removed from the compartment where deposition originally occurred, or they become bound to biomolecules or may form secondary nanoparticles via reprecipitation. Secondly, if the closed system reaches the solubility limit in the selected medium, the dissolution rate is easily underestimated and particles with some solubility may appear as very poorly-soluble. Thirdly, commonly-used methods generally lack a means for evaluating the structural transformation of remaining solids, i.e., physicochemical modifications that could impact clearance and particle disposition. Lastly, any abiotic system does not fully reflect disposition in lung because the lining and interstitial fluids throughout the respiratory tract are pH-balanced, complex mixtures of salts, serum proteins, and other biomolecules. Most importantly, phagocytosis by macrophages or other cell types introduces particles to the lysosomal microenvironment with an acidic pH. Thus, a dynamic (non-equilibrium) system may be better suited to an evaluation of the *in vivo* bioprocessing of deposited particles in the lung, particularly if both the intraphagolysosomal and lung surface microenvironments are considered.

Indeed, dynamic systems were developed and validated to estimate the biopersistence of mineral fibers [23-25]. In these systems, dissolved ions pass through a membrane with a pore size that excludes the parent particles. The ions on the other side of the membrane are continually removed from the system using flow-through or flow-by macrodialysis, thus achieving non-equilibrium conditions over the time course – hours to days – of the study. The dialysate is collected in discrete volumes, after

which the target analyte is quantitated in the collected fractions and the waste that was not sampled. Adaptation to ENMs mainly requires the choice of appropriate separation membranes. Stefaniak and colleagues employed a membrane to separate the suspended particles from a larger volume of particle-free receptor medium, thus gaining size exclusion in addition to the flow-mediated concentration gradient that provided short-term disruption of equilibrium conditions [21]. Another quasi-dynamic system with relatively large volume was explored and a setup patented for oral exposure purposes [26], demonstrating that dynamic setups can also be employed to study the structural transformations of remaining solids [27]. Transformation of nanoparticles by *in vivo* processing has been directly observed for the relatively biosoluble amorphous SiO_2 in the pulmonary compartment [9]. Transition metal oxides, specifically CeO_2, have also demonstrated the potential to recrystallize in lysosomal conditions [28] or in extracellular medium [9], and bioprocessing was observed to be organ-specific [29]. Such modulations of biopersistence by local physiological conditions could, thus, contribute significantly to the unusual biokinetics of nanoscale $BaSO_4$ [4,5,30].

We hypothesize that both the shedding of ions and *in vivo* biotransformation of remaining solids contribute to the biokinetics of nanoparticles. We describe here methodology to evaluate the abiotic dissolution of $BaSO_4$, thought to be a poorly-soluble ENM, and explore the extent of agreement that can be reached in comparison to *in vivo* results.

Materials

Previous *in vivo* studies on $BaSO_4$ NM-220 have already been conducted [3,4] and their physicochemical properties published in multiple reports [31-33]. $BaSO_4$ NM-220 is a benchmark material of the OECD sponsorship program. **Table 1** lists physicochemical properties of NM-220 as relevant for ECHA nanoforms [34].

Table 1 Physicochemical properties of $BaSO_4$ NM-220

Property	**$BaSO_4$ NM-220**
Composition / crystallinity / impurities (XRD*)	purity > 93.8 %; Na, Ca, Sr, F, Cl, organic compounds
Minimum external dimension (TEM)**	32 nm
Shape (TEM)**	Spheroidal
Specific surface area (BET*)**	41 m^2/g
Surface modification	None
Contact angle (water)	<10° (hydrophilic)

*X-ray diffraction (XRD); **Transmission electron microscopy (TEM); ***Brunauer-Emmett-Teller method (BET)

Methods

Static solubility or quasi-dynamic abiotic dissolution

Details for testing the solubility of $BaSO_4$ in phagolysosomal simulant fluid (PSF) under static conditions are provided in the ***Supplementary Information***. In short, $BaSO_4$ was suspended in 200 mL PSF (composition described in [21]) at a concentration of 10 mg/mL, then incubated for 7 or 28 days at 37 °C with stirring. The remaining particulate matter was separated from the ions in solution using ultracentrifugation at 67,000 ×g for 2 h, and the Ba concentration in the supernatant fraction was analyzed by inductively-coupled plasma mass spectrometry (ICP-MS). Particle dissolution under quasi-dynamic conditions was performed by suspending $BaSO_4$ in PSF (10 mg/mL) and injecting the suspension into a 2 mL dialysis cassette with a cut-off at 7 kDa (***Supplementary Information***). The dialysis cassette was placed horizontally in a glass vessel filled with 200 mL PSF as receptor medium at

37 °C with stirring. The receptor medium was exchanged daily and analyzed by ICP-MS. The methodological limit of detection for Ba was 0.1 mg/L.

Flow-by abiotic dissolution

The setup implements a Continuous Flow System (CFS) according to ISO TR 19057. A dynamic flow-by macrodialysis system [23,24] has been employed to estimate the *in vivo* dissolution of ENMs [35]. Here (**Figure 1**), $BaSO_4$ (~1 mg/mL) was suspended in dissolution buffer before being injected into the upper chamber of a dialysis cell fitted with a 3.5 kDa cellulose ester symmetric membrane (Spectra/Pore®, Gardena, CA; effective pore size ~1.4 nm). The Ba-free dissolution buffers simulated extracellular lung lining fluid (pH maintained at 7.4 by bubbling 5% carbon dioxide into the buffer reservoir) or intraphagolysosomal fluid (pH adjusted to 4.5 with HCl). The latter of the two buffers is termed EU pH4.5 herein (see composition in ***Supplementary Information***). The dialysis cells were submerged in a 37 ˚C water bath in a dark room. The buffers flowed by the dialysis cells at a rate of 60 µL/min, or ~3 mL/h. A fraction collector with metal-free, pre-weighed polypropylene tubes was used to collect the dialysates over the course of 7 days. For the first 24 h, two-hour fractions were collected (so, 12 fractions for Day 1); thereafter, the fractions were combined such that there were 6 daily fractions. The sample weight for each tube was recorded. After 7 days, the following additional samples were collected in ultra-clean polypropylene digestion tubes for analysis: the remaining solids in the upper chamber; three rinses with 18 MΩ deionized water; and the dialysis membrane. The tubes were placed in a 90 °C heating block. Ultra-pure nitric acid was added to dissolve the membrane and the $BaSO_4$ nanoparticles. The Ba remaining in the upper cell after 7 days, the Ba left in the dialysis membrane, and the Ba found in each fraction was quantitated via atomic emission spectroscopy (Beckman Spectraspan V, Fullerton, CA; instrument limit of detection, ~10 µg/L).

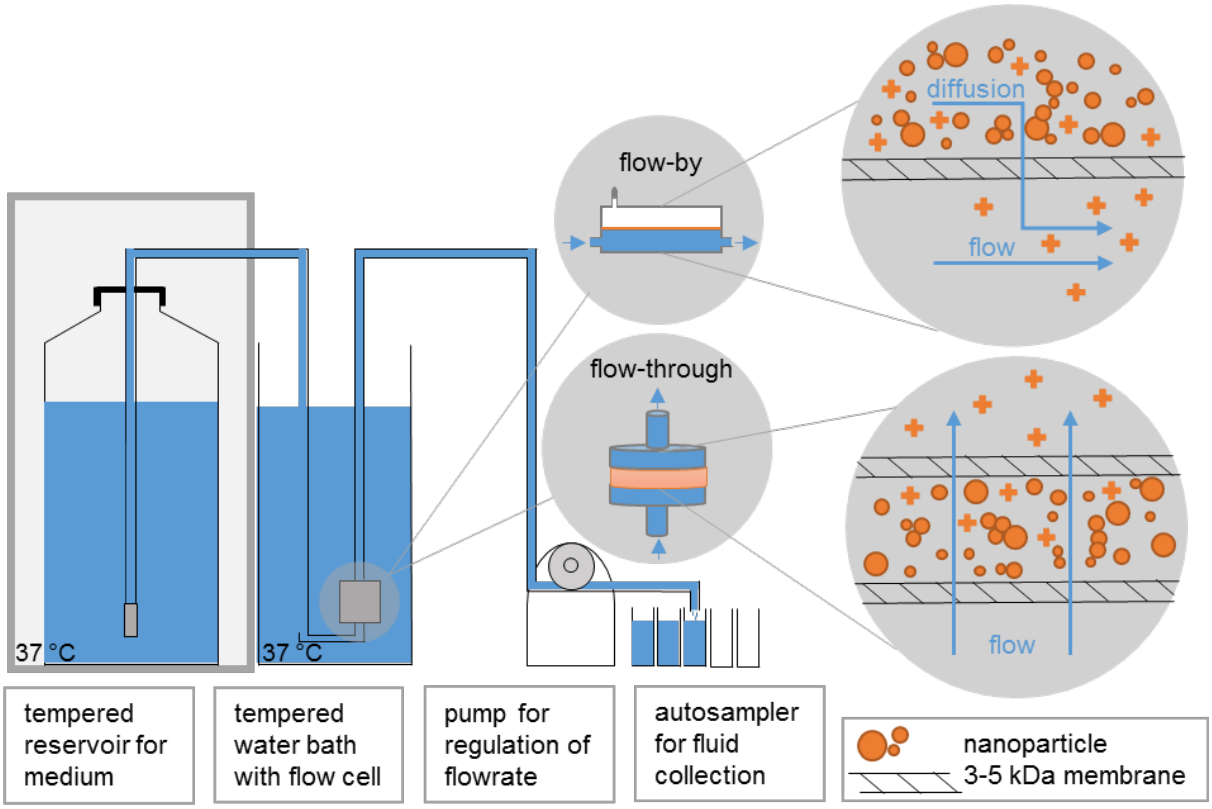

Figure 1 Dissolution method in abiotic flow cells (adapted from [36]). The medium was selected to match the conditions of either the phagolysosomal (pH 4.5) or lung lining fluid (pH 7.4) microenvironment. Particles are in direct contact with the membrane. The choice of the ultrafiltration membrane permeation cutoff is essential; a range 3 kDa to 5 kDa is recommended. This represents a size cut-off of ~1-2 nm (Ren et al., 2006). Smaller cutoffs could induce excess pressure drops and are not recommended. Other options include (recommended): 1) especially for flow-through operation, anti-clogging filters on inlet tubing in the reservoir and elevation of the reservoir by roughly 30 cm, such that hydrostatic pressure compensates for the pressure drop by ultra-high molecular-weight polyethylene (UHMWPE) ultrafiltration membranes. 2) In one implementation, we operated five cells in parallel with a programmable autosampler. Each cell then has its own reservoir inlet tube, peristaltic pump tubing, and sampling.

Flow-through abiotic dissolution and transformation

The flow-through setup (**Figure 1**) was recently described in detail as another implementation of a CFS according to ISO TR 19057 [36,37]. CFS is established as a screening method of the dissolution kinetics of mineral fibers [25,38,39]. Unless otherwise mentioned, an ENM mass of M_0 = 1 mg was weighed onto a membrane (cellulose triacetate, Sartorius Stedim Biotech GmbH, Goettingen, Germany: 47 mm diameter, 5 kDa pore size), topped by another membrane, and enclosed in flow-through cells. The flow through cells were kept upright within a tempered water bath to ensure that emerging air bubbles can leave the system and do not accumulate within the cell. The initial surface area SA is M_0*BET (Table 1). The flow rate (V) was 48 mL/d, but was varied up to 100 mL/d. For the lower flow rate, this corresponds to a ratio, SA/V = 0.02 h/cm. The compositions of simulant fluids vary significantly in literature.[40] With the compositions documented in **Table S1**, the EU pH4.5 medium with a whole range of organic acids, or the simpler PSF medium –previously validated for the purpose of particle dissolution [21]– were employed at 37 ± 0.5 °C. The programmable sampler drew 10 mL eluates once per day from the total 100 mL collected. The Ba concentration in the eluates was determined by ICP optical emission spectrometry (ICP-OES, Agilent 5100). After the experiment, the cells were flushed with deionized water before opening them to rinse the remaining solids off the membrane. The resulting suspension was then pelleted onto a transmission electron microscopy (TEM) grid held at the bottom of a centrifuge vial within 30 min and then dried [36] so that the morphology of the remaining solids could be inspected with a reduction of interference from drying artifacts of PSF salts, which are removed by this preparation. Particle morphology was analyzed by TEM with a Tecnai G2-F20ST or Tecnai Osiris Microscope (FEI Company, Hillsboro, USA) at an acceleration voltage of 200 keV under bright-field conditions. X-ray photoelectron spectroscopy (XPS) was done using a Phi Versa Probe 5000 spectrometer using monochromatic Al Kα radiation.

Derivation of dissolution rates

For both of the flow-cell setups, we multiplied the measured Ba concentration of each eluate by the eluted volume to obtain a mass of dissolved Ba ions per sample and then stoichiometrically adjusted this value to obtain the dissolved mass of $BaSO_4$ at each sampling interval, Δt. We then analyzed the dissolution kinetics in three alternative ways:

- Cumulative rate: The amount of dissolved $BaSO_4$ at each time point $M_{ion}(T)$, is expressed as a fraction of the initial mass loading (M_0 = 100%) and cumulated from all samplings with concentration c_i, flow V_i and sampling interval Δt_i , and includes the stoichiometry of $BaSO_4$:

$$\frac{M_{ion}(T)}{M_0} = \frac{m(BaSO_4)}{m(Ba)*M_0} * \sum_{i=0}^{T} c_i(Ba) * V_i * \Delta t_i \qquad \text{(Eq. 1a)}$$

$$k = \frac{M_{ion}(T)}{M_0}\frac{1}{T*BET} \qquad \text{(Eq. 1b)}$$

  The rate k incorporates the BET value in order to report results with a focus on composition or coating dependence, instead of size dependence. The conventional units of k are ng/cm²/h.[25,41] We typically determine k by the cumulated ions at the end of the test.

- Curve fitting: To verify first-order dissolution kinetics,[41] the cumulative dissolved $BaSO_4$ mass is expressed as an inverse relationship, i.e., decreasing solid retained $BaSO_4$ mass ($M_{ion}(T)–M_0)/M_0$, and plotted against time on a semi-log scale. The dissolution rate – expressed as a fraction per hour – is calculated from the slope of this line and then converted to percent per day using the total system available starting mass. Dissolution rate and half-time ($t'_{1/2}$, 50% dissolved) are inversely related and can be expressed in two alternative metrics (below) as given for first order modeling in ISO 19057:2017 [37,41]. The $BaSO_4$ dissolution half-time allows direct extrapolation and comparison to the *in vivo* dissolution $t_{1/2}$ of inhaled $BaSO_4$, which is derived from the total *in vivo* $t_{1/2}$:

$$b_{diss} = \frac{\ln 2}{t'_{1/2}} \qquad \text{or} \qquad t'_{1/2} = \frac{\ln 2}{b_{diss}} \qquad \text{(Eq. 2a)}$$

$$k_{diss} = \frac{\ln 2}{t_{1/2} * BET} \qquad \text{or} \qquad t_{1/2} = \frac{\ln 2}{k_{diss} * BET} \qquad \text{(Eq. 2b)}$$

- Instantaneous rates: For each sampling interval Δt, the instantaneous dissolution rate k was constructed as:

  $$k(t) = M_{ion}(t) / SA(t) / \Delta t. \qquad \text{(Eq. 3)}$$

  We approximated the instantaneous surface area

  $$SA(t) = BET(t=0) * (M_0 - M_{ion}(t)) \qquad \text{(Eq. 4)}$$

  and, thus, ignored changes of the size distribution and shape (see Discussion). Elsewhere [36] we explore modeling of SA(t) via the assumption of shrinking spheres,[37,41] which does not apply for particles with a tendency to transform, such as $BaSO_4$.

It should be noted that the BET value that is used in Eq. 2b for the determination of $t_{1/2}$ cancels out with BET in Eq. 1b. Accordingly, the two evaluation approaches (fitting vs. cumulated rate) should coincide if the assumption of exponential decay (first order kinetics) is true. Also, the cumulative rate and the instantaneous rate should coincide in the absence of transformation during the test.

Expression of the rate as k_{diss} favors the read-across between nanoform and non-nanoform, because it eliminates the dissimilarity of the specific surface and focuses on modulation of the rate by different coatings or different crystallinities. The expression of the rate as b_{diss} avoids uncertainties regarding changes in particle surface area during the test and indicates a fraction of mass loss per unit time, which can readily be compared to *in vivo* dissolution rates – or to predict them – with the assumption of rapid clearance (no binding) of the dissolved ions.

Evaluation of *in vivo* structural transformations via high-resolution analytical TEM

Rat lung blocks from the 24-months inhalation study at 50 mg/m³ of $BaSO_4$ NM-220 [5] were cut to 50 to 70 nm thick sections and collected on 200 mesh Formvar/carbon coated copper grids. For

ultrastructural and elemental characterization of selected lung sections high resolution scanning transmission microscopy (HRSTEM) was performed using a JEOL 2100F field emission TEM/STEM operated at 200 keV with an analytic pole piece. Tissue sections for HRSTEM were prepared without staining or osmication since OsO_4 nanoparticles form and can bind to select tissue regions, which makes it difficult to optically distinguish those from potentially inhaled $BaSO_4$ nanoparticles or second-generation particles from *in vivo* processing. Images were recorded with a Gatan Ultrascan 4kx 4k CCD camera and data analysis and processing used Gatan Digital Micrograph software (Gatan, Inc.). HRSTEM imaging and Energy-dispersive X-ray spectroscopy (EDS) were performed with a GATAN HAADF detector, Digiscan II, Gatan 2000 Image Filter (GIF), and an Oxford Aztec EDS system (Oxford Instruments, Oxfordshire, United Kingdom) respectively. All HRSTEM images were acquired using an analytical probe with 0.17 nm. A FEI Talos transmission and scanning electron microscope was used for fast EDS mapping with a high degree of sensitivity due to the wrap-around style EDS detector mounted on the objective lens. Maps generally took 1 to 2 min to acquire with a sensitivity great enough to detect elemental concentrations in 4-nm size particles. EDS provides the means to determine the relationship between elemental accumulation and tissue regions, particularly in a situation where dynamic processes may be in play such as *in vivo* processing [9].

Results

Static abiotic solubility

Data on the water solubility of $BaSO_4$ (2.45 ppm Ba ions at 20 °C [42]) cannot explain the *in vivo* observations. Even when solubility was measured in a medium that mimicked the intraphagolysosomal space, $BaSO_4$ was classified as insoluble with less than 0.1 % dissolved (1000 ppm Ba ions) [3]. Here we replicated the static solubility measurements in different media and found 8 mg/L $BaSO_4$ (or 0.08 %, nominal) dissolved in pH 4.5 phagolysosomal simulant fluid (PSF) over 7 days, stagnating at 5 mg/L (or 0.05 %, nominal) after 28 days. We hypothesize it is not appropriate to express the data from a known static system as a rate but indicate nominal rates here to test the hypothesis. One sample of $BaSO_4$

was left to settle in PSF for nearly 2 years in a 200-mL beaker. The resulting ion concentration after nearly 2 years was identical to the concentration after 7 days. The addition of EDTA, to mimic alkaline earth metal-transporting proteins, only minimally increased $BaSO_4$ solubility to 9 mg/L within 28 days (or 0.09 %). This is in contrast to recent investigations on Zn-ENM, for which adjustment of the relevant medium was sufficient to induce dissolution, thus better-matching the lack of *in vivo* biopersistence [20].

We also evaluated the quasi-dynamic dissolution of $BaSO_4$ using dialysis [43]. The ion concentration in the receptor medium remained roughly constant in this system: 1.3 mg/L, 1.2 mg/L, 1.1 mg/L, 1.0 mg/L, and 2.0 mg/L on days 1, 2, 3, 4 and 7, respectively. The cumulative dissolution of 0.07 % over 7 days and an apparent dissolution rate of k = 0.01 ng/cm²/h remained on the same level as the static solubility system, but below *in vivo* rates. This indicates that an equilibrium Ba concentration of about 1 to 2 mg/L in the pH 4.5 PSF medium is the limiting factor preventing further dissolution.

Dynamic abiotic dissolution

Motivated by a correlation between the *in vivo* biopersistence of mineral fibers and their abiotic dynamic dissolution rates, two laboratories independently evaluated the dissolution of $BaSO_4$ NM-220 using similar macrodialysis systems: one flow-by and one flow-through (**Figure 1**). While a flow-by system with the EU pH4.5 medium (composition in **Table S1**) was used at the University of Rochester, a flow-through system with PSF medium (**Table S1**) was used at BASF SE. The initial mass (~1 mg $BaSO_4$) was the same and the flow rates (2-3 mL/h) were similar. Both labs found that $BaSO_4$ NM-220 exhibited a significant dissolution (≥20 % over 7 days) under dynamic conditions (**Figure 2A**). The dissolution rates and half-times for the two setups do not agree quantitatively despite similar initial mass loadings and flow rates. Exponential fits (**Figure 2A**) indicate dissolution $t_{1/2}$ values of 5.9 days (flow-through, pH 4.5 PSF) and 28.9 days (flow-by, EU pH4.5), estimating about 10 % uncertainty due to extrapolation of surface areas for the flow-by data. The different composition of the pH 4.5 media and the different flow geometries are potential reasons for the differing values.

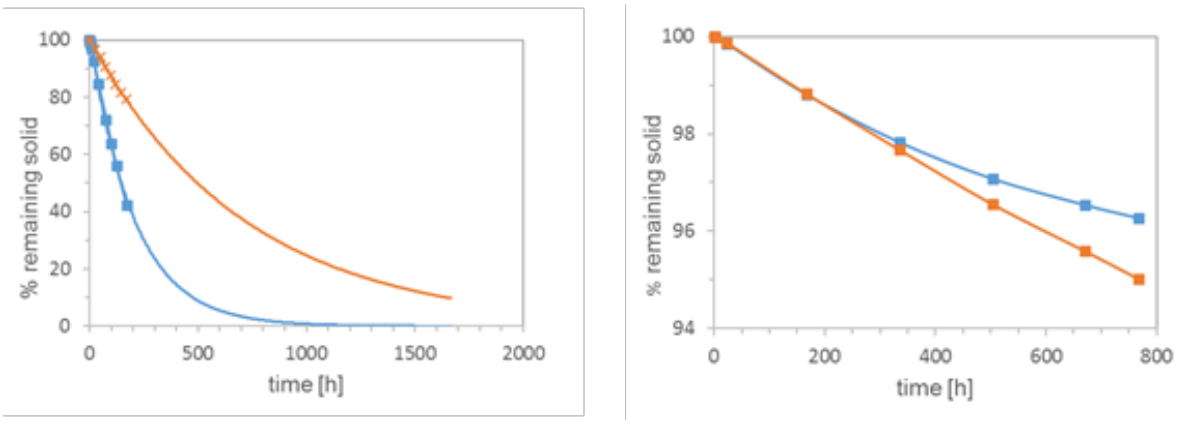

Figure 2 Dissolution kinetics of $BaSO_4$ (starting mass, ~1 mg) in pH 4.5 medium, tested by two dynamic dissolution methods: **A** flow-through (BASF, blue boxes) or flow-by (Rochester, orange crosses) macrodialysis. **B** comparison of both simulant fluids in the flow-through geometry (starting mass, 50 mg): PSF (blue boxes), EU pH4.5 (orange boxes). Note the different ranges of the y-axes.

We replicated the experiment at BASF using EU pH4.5 and the flow-through system, keeping all other parameters unchanged except that the starting mass was increased to 50 mg. The dissolution kinetics in the flow-through setup were identical between the more complex EU pH4.5 and the simpler PSF pH4.5 media over the first few days (**Figure 2B**). After 7 days, the dissolution rate in the PSF medium slowed down slightly as compared to the rates in the EU pH4.5 medium. Although it is possible that the phthalates in the PSF acted as ion scavengers – which would increase the solubility limit – PSF seems to slightly favor re-precipitation, thus reducing the apparent dissolution rate. To confirm this hypothesis, we changed the temperature during flow-through dissolution from 37 °C to 4 °C but started with the same initial mass of 1 mg. The apparent dissolution rate was reduced significantly by a factor of 2.5 (data not shown). Also, dissolution in neutral pH medium at 37 °C demonstrated significantly lower rates compared to media with pH 4.5 (***Figure S1 and S3***), whereas an omission of organic acid and salts resulted in slight acceleration of apparent dissolution by 7 % (data not shown). Thus, temperature, pH, flow geometry, and initial loading can all slightly impact the reproducibility of dissolution tests for partially-biosoluble materials such as $BaSO_4$. In flow-by geometry, the diffusion of ions from the sample compartment through the membrane into the flow (receptor) compartment

could add another rate-limiting step that tends to reduce the apparent dissolution rate as observed from the ion concentrations in the flow compartment.

Both labs observed that the dissolution kinetics depend on the initial mass of $BaSO_4$ (**Table 2**). Specifically, both labs observed that the Ba ion concentration was limited to a maximum of ~1 mg/L in the eluate from flow-through cells and to ~0.3 mg/L in the dialysate from flow-by cells. This limit is better reflected by the integral of the total mass of ions over the entire duration of the dissolution period, M_{ion}/T (**Equation 1a)**, which turns out to be limited to about 60 µg/day in flow-through and about 15 µg/day in flow-by geometry (**Table 2**) at the specific flow rates used here. See also **Figure 2B** and **Figure S2**, demonstrating that higher M_O leads to system saturation.

Table 2 Evaluation of cumulative dissolution of $BaSO_4$ in flow cells with pH 4.5 media using flow-through or flow-by methodology. The half-times $t'_{1/2}$ are obtained from b_{diss} by direct fitting of the decay curve on a semi-log plot using Eq. 2a, whereas the half-times $t_{1/2}$ are derived via conversion of the cumulative rate k by Eq. 2b.

	M_0	M_{ion}/T	$t_{1/2}$	k_{diss}	$t'_{1/2}$	b_{diss}
		[µg/d]	[d]	[ng/cm²/h]	[d]	[%/d]
Flow-through, PSF pH4.5	0.17 mg	17.5	2.6	44.7	1.6	43.3
	1 mg	51.1	5.9	10.3	6.8	10.2
	10 mg	53.6	72.1	0.9	78	0.89
	50 mg	58.0	247	0.2	346	0.2
Flow-by, EU pH4.5	0.08 mg	3.9	5	13.8	5.6	12.4
	0.8 mg	13.7	28.9	3.4	25.7	2.7
	8 mg	14.7	72.2	0.32	53.3	1.3

Although the mass loadings in abiotic dissolution experiments are not likely to mimic realistic *in vivo* exposure conditions, an observed solubility limit may be predictive of saturation-related events that occur *in vivo*. This is discussed further below, but first we rationalize the solubility limit by considering

the ion sources (by particle dissolution) and ion losses (by flow [37], flow cell geometries and reprecipitation).

The maximum observed ion concentration in flow-through geometry is close to the pH 4.5 solubility limit observed in the static and quasi-dynamic geometries but is about an order of magnitude higher than in flow-by geometry. The lower threshold of the flow-by system is attributed to the ion concentration in the local vicinity of the particles reaching the pH 4.5 solubility limit. We interpret the data to suggest that upon reaching the pH 4.5 solubility limit locally, ions reprecipitate before the flow removes them. This phenomenon can indeed be observed in both the flow-through and flow-by systems, i.e., only the measurements at lowest M_0 (0.17 mg or 0.08 mg, respectively) remain below this limit. We also doubled the flow rate to V= 4 mL/h for M_0=10 mg and observed an increase in M_{ion}/T to 102 µg/day, which is roughly twice the observed value at a flow rate of V=2 mL/h (**Table 2**). In summary, the cumulative apparent dissolution rates *k* and b (**Table 2**) scale roughly linearly with the SA/V ratio. Thus, to avoid reaching the solubility limit, either the initial mass can be reduced, or the flow can be increased.

We extensively tested both the reduction of initial mass or the increase of flow independently and in combination and analyzed both cumulative and instantaneous dissolution rates of the identical raw data. If we determine for each sampling interval the instantaneous rates k (in units of ng/cm²/h, **Eq. 3**) and the instantaneous surface area per volume flow SA/V (in units of h/cm, **Eq. 4**), hundreds of instantaneous release rates collapse on a single linear relationship, regardless if SA/V was modulated by initial surface area or by flow rate or by gradual dissolution (**Figure 3**). To ensure that this unusual observation is not an artifact of the experimental parameters, but truly a material-specific phenomenon, we tested another nanomaterial under identical conditions. We chose 10-nm CuO because it is a benchmark material in the draft OECD guideline on nanomaterial solubility and dissolution [22] and in the DF4nanoGrouping framework [44]. Like $BaSO_4$, no redox processes are involved in CuO dissolution, whereas other benchmark materials might differ by oxidative or reductive dissolution mechanisms.[12] If the CuO dissolution process is mediated by the ENM surface, re-

precipitation remains irrelevant, and our calculation is correct, then *k(t)* of CuO should be constant for all *t* until full dissolution. Indeed, the instantaneous dissolution rates *k* of CuO were independent of SA/V across many orders of magnitude (**Figure 3**), contrasting to the $BaSO_4$ NM-220 behavior.

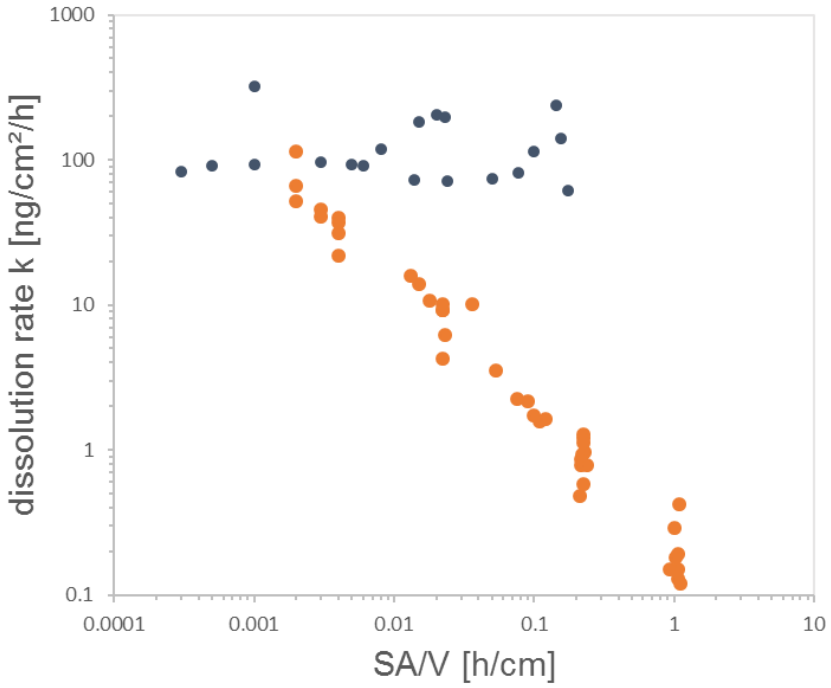

Figure 3 Instantaneous rate evaluation of biodissolution of $BaSO_4$ in flow-through cells with pH 4.5 PSF media. Each cloud of stepwise rates stems from separate experiment of initial mass M_0 and volume flow V. Five experiments for $BaSO_4$ (orange) and two for CuO (black). See **Table 2** for conventional evaluation (cumulative rates) of the same raw data.

Table 2 also highlights that the half-times $t_{1/2}$ obtained by direct fitting on a semi-log plot are in close agreement with the half-times $t'_{1/2}$ derived from conversion of the cumulative dissolution rate via Eq. 2a. Of note, the conversion assumes an exponential shape of the decay curve. Only for the highest initial loadings $M_0 \geq 8$mg, the values disagree significantly, because the saturation processes are reflected by linear (not exponential) kinetics (**Figure S3**).

We also investigated the transformation of the shape and speciation of solids after abiotic testing: We flushed the flow-through cells with water, then opened the cells and rinsed off the remaining solids into a centrifuge vial with a TEM grid at the bottom as described in methodical detail in a recent paper and SI [36]. By centrifugation, all solid >10 nm was spun onto the TEM grid and the supernatant with its buffer salts was discarded. Compared to as-produced $BaSO_4$ NM-220 (**Figure 4A**), there was a shift towards larger particle diameters (**Figure 4B**). Structural rearrangement towards a loss of small radii of curvature are observed (**Figure 4B**), and occasionally, very large spherical structures were observed (**Figure 4D**). Two different transformation processes are possible reasons for this observation. Ostwald ripening, which is generally explained as a minimization of interfacial energy by an overall increase of the radii of curvature mediated by a minimal solubility of ions first described in [45]. Or secondly, competing intermolecular forces at the particle-particle interface inducing a material transport between particles of different sizes, as deduced from the study of perfluorocarbon blood substitutes.[46] Both processes are driven by the reduction of free energy. When comparing the TEM median particle size before and after continuous flow in PSF (**Figure 4C)**, a size shift from 32.2 ± 16 nm to 39.9 ± 16.4 nm was measured (by manual evaluation of approximately 300 particles). In contrast, the "shrinking sphere" model [37] would predict a diameter of 23 nm to match the 60 % mass loss that is quantified as dissolved ions in the same experiment. XPS analysis confirmed that the preferred recrystallization species is $BaSO_4$ (**Figure 5, Figure S4**), in accord with the *in vivo* EDS observations (see next section).

With the present protocol, the flow conditions are highly controlled, but it is not possible to image the same nanoparticle over time. We also explored an alternative approach, where we repeatedly imaged the same ensemble of nanoparticle very far below the solubility limit at pH 4.5, but without controlling flow. The repeat scan shows that the sphericity of the remaining structures increases at the expense of structures with smaller radius of curvature (**Figure S5**), consistent with either of the material transport mechanisms.

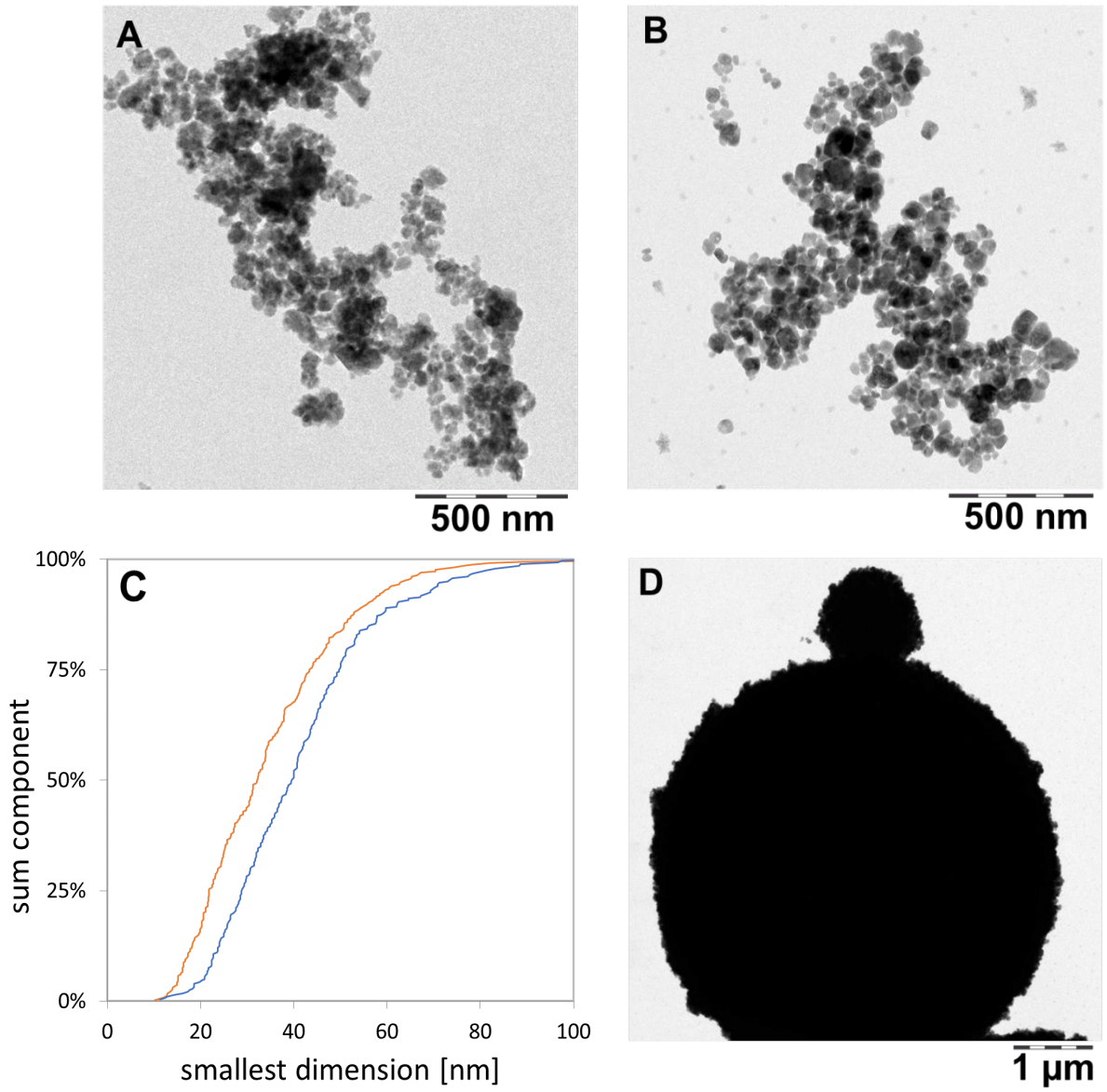

Figure 4 TEM images of $BaSO_4$ transferred from remaining solids onto TEM grids (scale bar corresponds to 500 nm for **A** and **B** and 1 µm for **D**. Panels: **A** as-produced particles; **B** and **D** after 72 hours of treatment in the flow-through cells with PSF. **C** shows the TEM particle size analysis of pristine $BaSO_4$ particles (orange) and $BaSO_4$ particles after treatment in PSF (blue) (N_A=331; N_B=280).

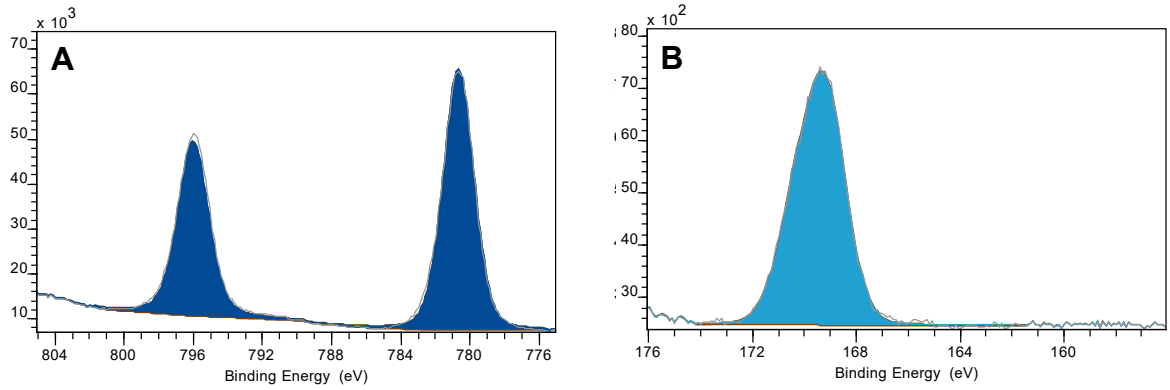

Figure 5 XPS results for $BaSO_4$ after flow-through testing in pH 4.5 PSF for 72 h. **A** photoelectron energy line for Ba (3 days). **B** photoelectron energy line for S (2p). The spectra can be fitted quantitatively with the benchmark chemical shifts of $BaSO_4$. The elemental composition (**Figure S4**) confirms a ratio Ba:S of 1:1.023, all consistent with an identification of the transformation product as $BaSO_4$. Data was acquired and averaged on N=5 measurements.

Bioprocessing of $BaSO_4$ particles in lung tissue: contributions to overall retention kinetics

Long-term inhalation exposures (12-24 months) to $BaSO_4$ NM-220 (**Figure 6A, B**) at a high aerosol concentration (50 mg/m³) resulted in significant accumulation of $BaSO_4$ in lung macrophages (**Figure 6C, D**). The retention of $BaSO_4$ particles in the lung had reached a maximum at ~12 months of exposure. At 12 months of continued inhalation exposure, the retained dose of $BaSO_4$ did not increase further, despite continued exposure. It appears that the continued pulmonary deposition of inhaled $BaSO_4$ was counterbalanced by removal (dissolution of the nanoparticles due to shedding of ions from the particle surfaces and elimination from the lung). The retained Ba in the lung was, thus, at an equilibrium between 12 and 24 months of exposure. The lung macrophages (**Figure 6C**) contained nanoparticles that were identified with high resolution EDS to correspond to $BaSO_4$ (**Figure 6E**). The spacing or relative distance between $BaSO_4$ particles inside the macrophages was rather small, with many particles seeded side-by-side (**Figure 6C-E**). Surprisingly, the particle size distribution of $BaSO_4$ inside macrophages was significantly larger as compared with the parent material (**Figure 6A, B**). This

indicates that Ba and SO_4 ion concentrations inside the macrophage environment that contained many densely packed $BaSO_4$ particles, approached supersaturation conditions following the long-term inhalation exposure at a very high aerosol concentration (50 mg/m^3). This resulted in the transformation and recrystallization of particles inside the lung macrophages. Material transport between particles had also occurred, whereby smaller particles dissolved faster, and the released ions were not removed, but rather deposited onto neighboring particle surfaces, allowing selective particle growth to take place (**Figure 6D, E**). This is the first documentation of an inter-particle material transport mechanism of nanoparticles after uptake *in vivo*. In addition, $BaSO_4$ particles exhibited a greater size range (from sub-nano to micron scale) as compared with that of the starting materials which is in good agreement with observations from the abiotic flow through cells. Transformation of $BaSO_4$ involved a particle size effect and a recrystallization of the particles which was controlled by the saturation and supersaturation conditions in the macrophage microenvironment. The shedding of ions drove not only the in vivo dissolution kinetics, but also controlled the shape, morphology, and size distribution of retained $BaSO_4$ in the lung. This indicates that $BaSO_4$ undergoes transformation mediated by non-equilibrium dissolution (in line with the observed incorporation of Ba in bones within days after intratracheal instillation) and recrystallization, thus modulating the overall biopersistence of the particles. Not all macrophages contain copious amounts of densely packed $BaSO_4$ and it is important to point out that each macrophage represents a unique system where dissolution and supersaturation conditions are subject to the nanoparticle accumulation rate. Only when enough $BaSO_4$ nanoparticles collect inside a macrophage transformation can occur.

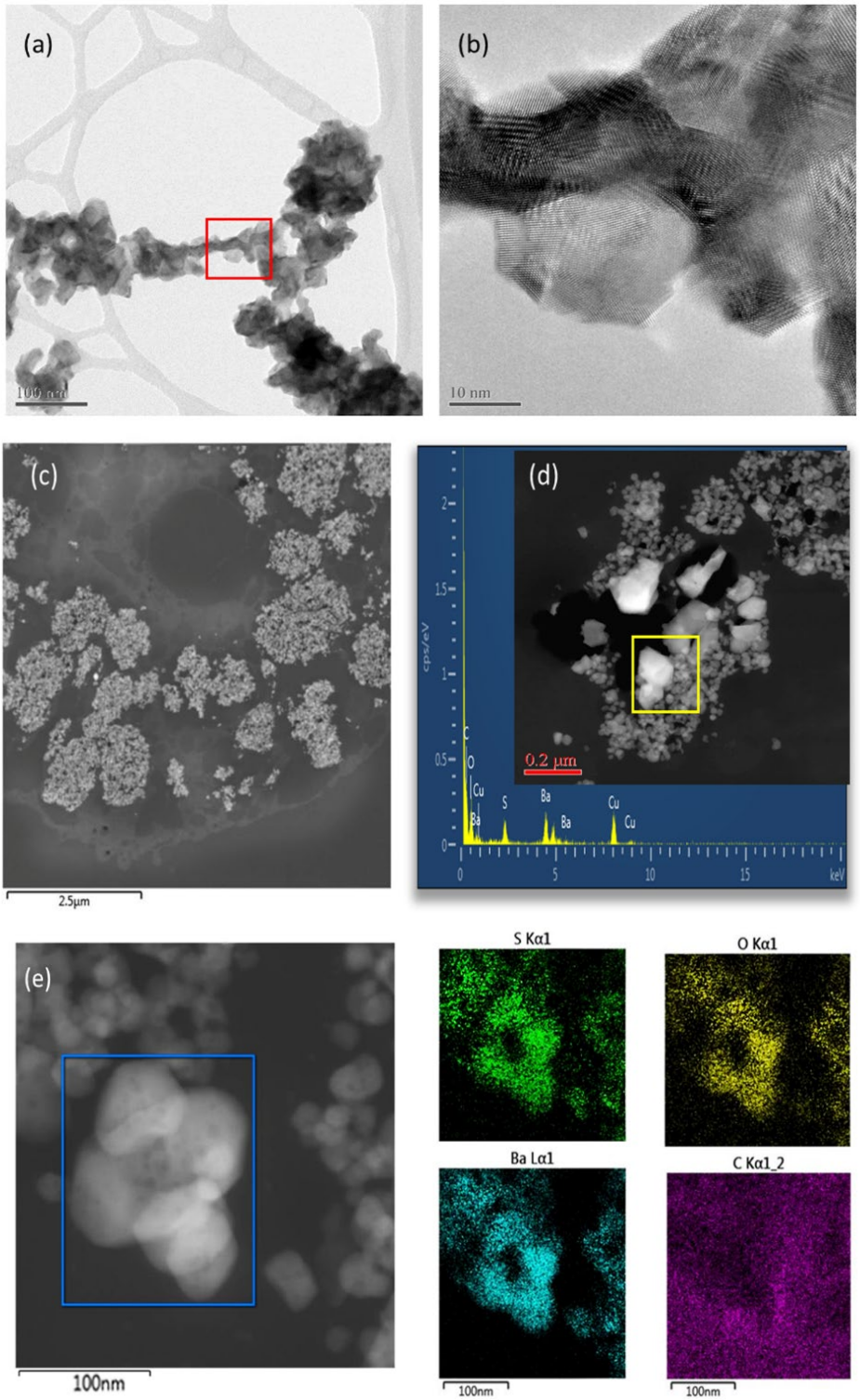

Figure 6 HRTEM/STEM structural characterization of as-produced $BaSO_4$ nanoparticles and in rat lung sections. **(a)** and **(b)** pristine $BaSO_4$ NM-220; **(c)** $BaSO_4$ after 12 months inhalation exposure: accumulation in lung macrophage; **(d)** Transformation of $BaSO_4$ in macrophage showing particle growth with crystaline facets. **(e)** HRSTEM of recrystallized $BaSO_4$ in macrophage with corresponding high-resolution EDS mapping for S, Ba, O and C.

Discussion

We posit that the measurement of dynamic particle dissolution should be an important element of predictive toxicity testing, i.e., the determination of dissolution *rates* in abiotic systems as opposed to static *solubility.* The *solubility* categorizes $BaSO_4$ (including the specific NM-220 grade) as poorly-soluble in water. However, solubility in water does not reflect *in vivo* reality in terms of 1) ongoing dynamic processes and 2) composition and pH of physiological fluids. The *dissolution rates* in physiological media better reflect an important component of *in vivo* particle clearance, considering that both absorptive chemical and physical clearance mechanisms are always working in tandem to affect total particle clearance (see below). Dissolution rates determined in appropriately-designed *abiotic* systems will be useful for grouping and classification of ENMs. From these predictive testing results, we also gain insight into the mechanisms that underlie biosolubility, which may explain experimental findings, e.g., the incorporation of Ba^{2+} in bones (as Ca^{2+} analogue).

Concerning the methodology, a solubility limit of ~100 mg/L has been proposed for testing strategies [30,47] and grouping frameworks [13] to define readily-soluble particles that would quickly lose their particulate nature. A currently developing OECD guideline describes a "screening test" that fulfills the requirements for Tier 1 grouping frameworks [22]. For purpose of initial screening of equilibrium *solubility*, the test could be performed in water, and then in the most relevant medium for exposure-specific testing [20]. For ENMs with solubility limits below 100 mg/L, for hazard assessment of innovative nanomaterials, or for endpoint-specific grouping and read-across between nanoforms, flow-by or flow-through dynamic dissolution (both are continuous flow systems [37]) in relevant media can offer predictivity of *in vivo* dissolution behavior [10], but not necessarily total *in vivo* clearance rates.

In order to best model the contribution of dissolution to *in vivo* clearance, it makes good sense to focus on the intraphagolysosomal environment at pH 4.5 (although dissolution in extracellular fluid (at neutral pH) could also be considered and included in kinetic model equations). Additional information about the impact of different flow rates and starting masses would provide insight regarding saturability, which could be predictive of *in vivo* events. The selected methods for ion analysis should

ideally have a limit of detection of 10 µg/L or below for the target analyte. Methods for morphological analysis of remaining solids require sample preparation, which was developed here based on the NanoDefine D6.3 protocol for TEM analysis, using centrifugal pelleting of remaining solids onto a TEM grid (which inherently is a purification from dissolved species). To assess the extent of transformation, we recommend TEM-based morphological and size distribution analyses (N>>100), with optional confirmation of chemical speciation, e.g., via SAD or XPS or XANES. For materials other than $BaSO_4$, more complex re-speciations must be expected, e.g. Ag sulfidation, Cu oxidation [48,49], CeO_2 re-speciation to $CePO_3$ needles [29]). Reprecipitation in flow-cells has been observed frequently during dissolution testing of stone wool mineral fibers, where especially Si tends to reprecipitate as gel on the surface of the fibers [50-53]. Most interestingly, a faster flow (lower SA/V ratio) is known to suppress gel formation and to increase the apparent stone wool dissolution rate [54]. These reports are analogous to our findings with $BaSO_4$.

Dissolution should be expressed in terms of rate (e.g., k in units of ng/cm²/h or %/day) for which ample literature on dusts exists [10]. This approach challenges the cutoffs for categorization and grouping of ENMs, typically expressed in % dissolved or mg/L concentrations. $BaSO_4$ is clearly "insoluble" in mg/L metrics as determined using static systems but is correctly predicted to dissolve *in vivo* by the dynamic dissolution methods.

The findings from these studies could be used to propose alternative categories for grouping approaches of ENMs. For the rat, lung retention half-times ($t_{1/2}$) for 'poorly-soluble low-toxicity' particles (PSLTs) are ~70 days and, by definition, reflect mechanical, macrophage-mediated clearance, generally following first-order kinetics[10]. Half-time and rate constants are inversely related to each other via **Equation 2**. Using this equation to determine a rate constant for PSLTs yields ~0.01/day or roughly 1% of starting material – as expressed using any metric of choice – per day for the mechanical component of clearance. Knowing that total lung particle clearance reflects the sum of mechanical and dissolution clearance, one can derive groups of dissolution clearance rates such that faster rates would indicate readily- or partially-biosoluble particles. In a previous paper we applied the continuous flow system to 24 different ENMs, and suggested decadic ranges of the dissolution rates between <1

ng/cm²/h (insignificant dissolution – also asbestos falls into this group) and >100 ng/cm²/h (half-times on the order of 1 day) [36]. Expressing dissolution rates in percent per day enables comparisons to and predictions of *in vivo* clearance rates.

The preceding discussion is based on results from studies that were conducted in rats but could be adapted to human hazard characterization via the use of human-specific rate constants or retention half-times. While mechanical clearance rates exhibit species specificity and also be impacted by inflammatory responses, it is predicted that dissolution rates are similar between humans and rodents [10]. The method could be used to enhance the DF4nanoGrouping [13], and to implement the ECHA grouping guidance [55] pending further validation by more varied case studies as proposed elsewhere [36].

With regard specifically to $BaSO_4$ pulmonary clearance and transformation, Konduru and colleagues reported that intratracheally instilled $^{131}BaSO_4$ NM-220 exhibited a lung retention half-time of 9.6 days in rats and that ^{131}Ba was incorporated into the bones, suggesting nanoparticle dissolution and/or extrapulmonary translocation [3]. A subsequent 90-day inhalation study in rats with aerosolized $BaSO_4$ of the same grade (50 mg/m^3, full physicochemical equivalence to NM-220 [4]) showed the gradual accumulation of Ba in lung tissue during exposure followed by steady clearance over a 90-day post-exposure period, with a reported retention half-time of 56 days, indicative of low *in vivo* solubility of $BaSO_4$ affecting its overall lung clearance. A two-year rat inhalation study in rats with $BaSO_4$ NM-220 (50 mg/m^3) confirmed a steady increase of retained Ba in the lung up to one year of exposure, with no further increase during subsequent continued exposure up to two years [5]. The equilibrium lung burden of Ba over the exposure period (12-24 months) is explained by the fact that the daily deposited dose in the lung is equal to the amount being cleared daily, i.e., deposition and clearance rates are in equilibrium. Knowing the $BaSO_4$ aerosol characteristics (mass median aerodynamic diameter, geometric standard deviation, exposure concentration) and exposure duration, the daily deposition rate can be estimated using the MPPD model for rats with body weight-adjusted respiratory parameters, which results in a daily $BaSO_4$ lung clearance rate of 0.0154 % of the daily deposited dose. This is equivalent to a retention half-time of 45 days (**Equation 2a**). Since the lung clearance rate for biosoluble particles is the sum of mechanical and dissolution clearance rates, the difference between

the normal rat clearance rate for PSLT particles (0.01/day) and the observed clearance rate in the equilibrium phase (0.0154/day) is the $BaSO_4$ *in vivo* dissolution clearance rate (0.0054/day; $t_{1/2}$ = 128 d) (**Table 3**). The available data show that, for acute exposures, rapid clearance of $BaSO_4$ occurs and that dissolution contributes significantly to the total clearance. Following subchronic or chronic exposures, total lung clearance is slower, but is nevertheless faster than mechanical clearance alone. Of note is that the predicted dissolution rates and associated half-times for the 90-day and two-year studies are prolonged as compared to acute exposures, suggesting a saturation event. Both the fast, short-term *in vivo* dissolution at a lower 'dose' and the saturation at higher 'doses' were predicted by the abiotic assay (**Table 2**). The bioavailability of ionic Ba could predict secondary organ uptake with the caveat that there could be macromolecule binding events that might limit the clearance of Ba.

Table 3 Pulmonary dissolution rates and associated half-times for $BaSO_4$ derived from acute and repeated rat exposure studies

Exposure duration	Particle type and method of delivery	Total Retention $t_{1/2}$ (d)	b_{tot} (d^{-1})	Dissolution Retention $t_{1/2}$ (d)	b_{diss} (d^{-1})
---- [3]	$^{131}BaSO_4$ NM-220 intratracheal instillation	9.6	7.23 %	11.1	6.23 %
90 days [4]	$BaSO_4$ NM-220 nose-only inhalation	56	1.24 %	289	0.24 %
2 years [5]	$BaSO_4$ NM-220 head-nose inhalation	45*	1.54 %	128	0.54 %

* At steady-state

Depending on the initial loading, flow rate and flow cell geometry, the b_{diss} in the abiotic test ranges from 0.2 % at strong saturation to 43 % well below saturation, and abiotic dissolution half-times range from 350 days to 2 days (**Table 2**). The range of the half-time and rate values includes that which was found in the different *in vivo* studies. One might interpret that the intratracheal instillation study induced no or only mild saturation (locally), whereas the 90-day and two-year inhalation studies induced significant saturation, consistent with the morphological observations (**Figure 6**).

The collective *in vivo* findings and those from the present dissolution studies suggest that Ba ions dissolved from lung-deposited particles – as opposed to the particles themselves – and were

transported throughout the body and incorporated in bone epiphysis.[56-58]. Furthermore, the long-term inhalation study results can be explained by a phenomenon whereby bone tissue – with its limited capacity and varying demand for bivalent cations over time – was saturated,[59] after which the net transport of Ba from lungs to bone decreased and, ultimately, the accumulation of Ba in the lungs increased. Within the (local) environment of the lungs, the ion removal rate depends on many factors, e.g., binding to biomolecules, that may affect the clearance rate.

Whether there is a specific or non-specific transport mechanism of Ba ions from the lung or a key trigger whose signaling results in the reduced removal of Ba from the lung remains to be elucidated. The measurement of Ba blood levels might help to shed light onto these questions. In addition, local clearance mechanisms in the lungs, such as mucociliary clearance and the clearance by alveolar macrophages, might be prolonged. We qualitatively observed significant accumulation of $BaSO_4$ in rat lung macrophages exposed for 12 months or longer to $BaSO_4$. Of note, the acidic pH of the macrophage lysosome is essential to $BaSO_4$ dissolution, which is very significantly reduced at pH 7.4 (**Figure S1**), by ~35 % as compared to pH 4.5. Furthermore, removing the organics from the PSF pH 4.5 medium results in a significant decrease in dissolution (**Figure S3**) and thus points to the ion scavenging effect of organic acids in lysosomal fluids. Taken together, uptake in macrophages and active transport of the ions are most likely steps in the clearance pathway, but dissolution in the neutral lining fluid may also contribute to total *in vivo* clearance.

Since the time-resolved abiotic dissolution shows that saturation conditions are reached, and furthermore crystalline particle growth was observed in vivo as well as in abiotic conditions, the structural transformation process are best described as Ostwald ripening. Once the net transport ceases, accumulation entails supersaturation conditions leading to the Ostwald ripening in macrophages that have accumulated $BaSO_4$ particles in phagolysosomes. Since each macrophage harbors unique concentrations of $BaSO_4$ particles, there are just as many systems (local supersaturation) to be considered. In this concept, the structure formation process is a self-catalyzing phenomenon: once the local ion concentration exceeds the solubility, triggering particle growth, the

specific surface area of the deposited particles decreases, thus slowing dissolution until equilibrium is reached between removal via dissolution and addition by deposition. Further evidence for *in vivo* Ostwald ripening of inhaled $BaSO_4$ particles in lung tissue was recently presented.[60] Families of (nano)forms that share each one substance but differ in sizes, coatings or shapes, have been assessed by the same methodology for dissolution and transformation [36]. The $BaSO_4$ dissolution rate is intermediate in comparison, and materials such as amorphous silica show related reprecipitation phenomena, albeit at slower rate [36].

Although the present study was designed to rationalize the clearance of $BaSO_4$ after inhalation, we note that the same concepts of local supersaturation (reaching the solubility limit of the specific ion in the lung medium) may be relevant to understand biokinetics after any other uptake routes. Accumulation of Ba in the lungs was reported after IV injection: [3,61] Giese 1934 and 1935 found after IV injection of $BaSO_4$ deposition in bone marrow, liver, spleen and lungs. Konduru et al found 20% of the administered dose in lungs at 2 days post IV injection [3]. Ba ions are likely to have precipitated, similar to the observation via HRTEM of newly formed Ce-containing (nano)particles in the liver [43,62]. Huston et al. observed the formation of "refractile masses" after instillation of a Ba containing solution Veriopaque, which was accompanied by inhibited removal of Ba by macrophages.

Ba^{2+} ions elicit systemic toxicity mainly via hypokalemia that is caused by the blocking of rectifying potassium channels in many cell types [63]. Although these effects do not necessarily require cellular uptake, it should be pointed out that Ba^{2+} ions, similar to Sr^{2+} ions, are capable of permeating specific Ca channels as well as non-selective cation channels of the cell membrane [64-66], and some of these channels have been shown to be essential for macrophage function [67-69]. Ba^{2+} ions may also be actively transported against an electrochemical gradient by Ca^{2+} ATPases [70]. Once inside a cell, Ba^{2+} ions may further pass to the different cell organelles such as endoplasmic reticulum, mitochondria, and lysosomes [71]. Thus, Ba^{2+} ions dissolving from $BaSO_4$ nanoparticles may distribute across membranes between subcellular compartments with the net fluxes being determined by electrochemical driving forces: of note, phagolysosomes are acidified by an active transport of H^+ ions carried out by V-ATPases

[69], resulting in a positive potential of approximately 30 mV. This potential may act as an outward driving force for Ba^{2+} ions, while at the same time creating an inward driving force for chloride ions, e.g., via CLC channels [68,69]. Although not yet proven it is tempting to speculate that these processes may be involved in fostering dissolution and/or recrystallization processes of $BaSO_4$ nanoparticles trapped in a macrophage`s phagolysosome.

Conclusion

Our results confirmed the previous findings that prediction of dissolution rates requires the use of relevant biological/physiological fluids rather than water.[20] The methodologies described herein for measuring abiotic dynamic particle dissolution and transformation involve a number of improvements:

- The use of continuous flow, rather than static incubation;
- The integrated assessment of residual solids with respect to transformations of shape, size distribution, and crystallinity by protocols for preparation, analysis and statistical image analysis, using TEM, optionally supported by XPS and EDX.
- The ready comparison, using the same experimental system, to compare to rapidly- and poorly-soluble benchmark particles, for grouping purposes as demonstrated elsewhere;[36]
- Ability to predict *in vivo* dissolution rates (with the acknowledged limitation that dissolved ions could be retained in tissues via binding to other molecules);
- The observation of dependence on initial loading mass could be useful for estimating *in vivo* solubility limits and, thus, provide insight regarding supersaturation that would impact total clearance rates.

Specifically, to $BaSO_4$ we propose that the unusual biokinetics of the long-term, high concentration $BaSO_4$ rat inhalation studies indicate a) the release of Ba ions via *in vivo* dissolution of phagocytosed particles, with transport to and uptake into the bone and b) recrystallization in lungs as additional transformation process that modifies ENM lung retention. The process is a self-catalyzing phenomenon as the specific surface area of the transforming particles decreases, thus slowing down dissolution.

Especially the second year of the two-year inhalation study was, thus, conducted at significant saturation. Control measurements on CuO demonstrated that Ostwald ripening and supersaturation phenomena are not a methodical artifact, but characteristic of the $BaSO_4$ properties, and were reproducible in two labs and different lysosomal simulants. The rates and the transformation and the Ba speciation were verified *in vivo*, with the only limitation that *in vivo* processing resulted in less sphericity and more crystalline facets. The dynamic dissolution results thus qualitatively predicted the *in vivo* $BaSO_4$ dissolution, as well as the concentration-dependent Ostwald ripening process observed within the rat lung.

Declarations

Acknowledgements

We thank Kai Werle for excellent technical support. We thank Philipp Müller who supervised the TEM analyses, and Sabine Hirth who supervised the XPS analyses.

Funding

This work was partially supported by project nanoGRAVUR (BMBF, FKZ 03XP0002B).

Availability of data and materials

The test material $BaSO_4$ NM-220 is available from the OECD sponsorship repository at Fraunhofer Institute, Schmallenberg. The same-grade-later-batch used for the long-term inhalation study is available as JRCNM50001a in the frame of the PATROLS project from the JRC repository, Ispra.

Authors contributions

JGK performed the flow-through testing; UG performed the HRTEM study; RG performed, and AE supervised the flow-by testing; JKJ performed the static solubility and quasi-dynamic abiotic dissolution testing; RL, LMH, GO, MW contributed to the interpretation of results; WW conceived and supervised the project. All authors contributed to the writing of the manuscript.

Ethics approval and consent to participate

All experiments were performed in accordance with relevant guidelines and regulations. The long-term two-year inhalation study with interim sacrificing after 12 months exposure was approved by the local authorizing agency for animal experiments (Landesuntersuchungsamt Koblenz, Germany) as referenced by the approval number G 12-3 028.

Consent for publication

All authors read and approved the final manuscript.

Competing interests

JGK, JKJ, LMH, RL, WW are employees of BASF SE, a company producing nanomaterials.

Bibliography

1 Tran, C. L. *et al.* Inhalation of poorly soluble particles. II. Influence Of particle surface area on inflammation and clearance. *Inhal Toxicol* **12**, 1113-1126 (2000).

2 R. T. Cullen, C. L. T. D. B. J. M. G. D. A. S. A. D. J. K. D. INHALATION OF POORLY SOLUBLE PARTICLES. I. DIFFERENCES IN INFLAMMATORY RESPONSE AND CLEARANCE DURING EXPOSURE. *Inhalation Toxicology* **12**, 1089-1111, doi:10.1080/08958370050166787 (2000).

3 Konduru, N. *et al.* Biokinetics and effects of barium sulfate nanoparticles. *Particle and fibre toxicology* **11**, 55 (2014).

4 Schwotzer, D. *et al.* Effects from a 90-day inhalation toxicity study with cerium oxide and barium sulfate nanoparticles in rats. *Particle and Fibre Toxicology* **14**, 23, doi:10.1186/s12989-017-0204-6 (2017).

5 Ma-Hock, L. *et al.* in *Eurotox 2017* (2017).

6 Kreyling, W. G. Interspecies Comparison of Lung Clearance of "Insoluble" Particles. *Journal of Aerosol Medicine* **3**, S-93-S-110, doi:10.1089/jam.1990.3.Suppl_1.S-93 (1990).

7 Pauluhn, J. Pulmonary Toxicity and Fate of Agglomerated 10 and 40 nm Aluminum Oxyhydroxides following 4-Week Inhalation Exposure of Rats: Toxic Effects are Determined by Agglomerated, not Primary Particle Size. *Toxicological Sciences* **109**, 152-167 (2009).

8 Graham, U. *et al. Calcium co-Localization with in vivo Cerium Phosphate Nanoparticle Formation after Intratracheal Instillation Dosing with CeCl3 or CeO2 NPs*. Vol. 23 (2017).

9 Graham, U. M. *et al.* in *Modelling the Toxicity of Nanoparticles* (eds Lang Tran, Miguel A. Bañares, & Robert Rallo) 71-100 (Springer International Publishing, 2017).

10 Oberdörster, G. & Kuhlbusch, T. A. J. In vivo effects: Methodologies and biokinetics of inhaled nanomaterials. *NanoImpact* **10**, 38-60, doi:https://doi.org/10.1016/j.impact.2017.10.007 (2018).

11 Burden, N. *et al.* The 3Rs as a framework to support a 21st century approach for nanosafety assessment. *Nano Today* **12**, 10-13 (2017).

12 Gray, E. P. *et al.* Biodissolution and cellular response to MoO 3 nanoribbons and a new framework for early hazard screening for 2D materials. *Environmental Science: Nano* (2018).

13 Arts, J. H. E. *et al.* A decision-making framework for the grouping and testing of nanomaterials (DF4nanoGrouping). *Regulatory Toxicology and Pharmacology*, doi:http://dx.doi.org/10.1016/j.yrtph.2015.03.007 (2015).

14 Collier, Z. A. *et al.* Tiered guidance for risk-informed environmental health and safety testing of nanotechnologies. *Journal of Nanoparticle Research* **17**, 155, doi:10.1007/s11051-015-2943-3 (2015).

15 Drew, N. M., Kuempel, E. D., Pei, Y. & Yang, F. A quantitative framework to group nanoscale and microscale particles by hazard potency to derive occupational exposure limits: Proof of concept evaluation. *Regulatory Toxicology and Pharmacology* **89**, 253-267, doi:https://doi.org/10.1016/j.yrtph.2017.08.003 (2017).

16 Godwin, H. *et al.* Nanomaterial Categorization for Assessing Risk Potential To Facilitate Regulatory Decision-Making. *ACS Nano* **9**, 3409-3417, doi:10.1021/acsnano.5b00941 (2015).

17 Kuempel, E., Castranova, V., Geraci, C. & Schulte, P. Development of risk-based nanomaterial groups for occupational exposure control. *J. Nanopart Res* **14**, 1029 (2012).

18 Oomen, A. G. *et al.* Grouping and read-across approaches for risk assessment of nanomaterials. *International journal of environmental research and public health* **12**, 13415-13434 (2015).

19 Oomen, A. G. *et al.* Risk assessment frameworks for nanomaterials: Scope, link to regulations, applicability, and outline for future directions in view of needed increase in efficiency. *NanoImpact* **9**, 1-13, doi:https://doi.org/10.1016/j.impact.2017.09.001 (2018).

20 Avramescu, M.-L., Rasmussen, P. E., Chénier, M. & Gardner, H. D. Influence of pH, particle size and crystal form on dissolution behaviour of engineered nanomaterials. *Environmental Science and Pollution Research*, 1-12, doi:10.1007/s11356-016-7932-2 (2016).

21 Stefaniak, A. B. *et al.* Characterization of phagolysosomal simulant fluid for study of beryllium aerosol particle dissolution. *Toxicology in Vitro* **19**, 123-134, doi:10.1016/j.tiv.2004.08.001 (2005).
22 Rasmussen, K. *et al.* Physico-chemical properties of manufactured nanomaterials - Characterisation and relevant methods. An outlook based on the OECD Testing Programme. *Regulatory Toxicology and Pharmacology* **92**, 8-28, doi:https://doi.org/10.1016/j.yrtph.2017.10.019 (2018).
23 Potter, R. M. & Mattson, S. M. Glass fiber dissolution in a physiological saline solution. *Glastechnische Berichte* **64**, 16-28 (1991).
24 Eastes, W., Potter, R. M. & Hadley, J. G. ESTIMATING IN VITRO GLASS FIBER DISSOLUTION RATE FROM COMPOSITION. *Inhalation Toxicology* **12**, 269-280, doi:10.1080/089583700196149 (2000).
25 IARC, I. A. F. R. O. C. *IARC MONOGRAPHS ON THE EVALUATION OF CARCINOGENIC RISKS TO HUMANS* 1-433 (WORLD HEALTH ORGANIZATION, 2002).
26 Pompa, P. P., Sabella, S. & Cingolani, R. (Google Patents, 2015).
27 Bove, P. *et al.* Dissolution test for risk assessment of nanoparticles: a pilot study. *Nanoscale* **9**, 6315-6326, doi:10.1039/c6nr08131b (2017).
28 Li, R. *et al.* Surface Interactions with Compartmentalized Cellular Phosphates Explain Rare Earth Oxide Nanoparticle Hazard and Provide Opportunities for Safer Design. *ACS Nano* **8**, 1771-1783, doi:10.1021/nn406166n (2014).
29 Graham, U. M. *et al.* Analytical High-resolution Electron Microscopy Reveals Organ-specific Nanoceria Bioprocessing. *Toxicologic Pathology* **46**, 47-61, doi:10.1177/0192623317737254 (2018).
30 Laux, P. *et al.* Biokinetics of nanomaterials: The role of biopersistence. *NanoImpact* **6**, 69-80, doi:https://doi.org/10.1016/j.impact.2017.03.003 (2017).
31 Driessen, M. *et al.* Proteomic analysis of protein carbonylation: a useful tool to unravel nanoparticle toxicity mechanisms. *Particle and Fibre Toxicology* **12**, 36 (2015).
32 Hellack, B. *et al.* Characterization report for all nanoGEM materials. 1-41 (2013). Landsiedel,
33 R., Sauer, U. G., Ma-Hock, L., Schnekenburger, J. & Wiemann, M. Pulmonary toxicity of nanomaterials: a critical comparison of published in vitro assays with in vivo inhalation or instillation studies. *Nanomed* **9**, doi:10.2217/nnm.14.149 (2014).
34 ECHA. How to prepare registration dossiers that cover nanoforms: best practices. doi:10.2823/128306 (2017).
35 Elder, A. *et al.* Translocation of Inhaled Ultrafine Manganese Oxide Particles to the Central Nervous System. *Environmental Health Perspectives* **114**, 1172-1178, doi:10.1289/ehp.9030 (2006).
36 Koltermann-Jülly, J. *et al.* Abiotic dissolution rates of 24 (nano)forms of 6 substances compared to macrophage-assisted dissolution and in vivo pulmonary clearance: Grouping by biodissolution and transformation. *NanoImpact* **12**, 29-41, doi:https://doi.org/10.1016/j.impact.2018.08.005 (2018).
37 Nti. in *Nanotechnologies. Use and application of acellular in vitro tests and methodologies to assess nanomaterial biodurability* (2017).
38 Wohlleben, W. *et al.* Composition, Respirable Fraction and Dissolution Rate of 24 Stone Wool MMVF with their Binder. *Particle and Fibre Toxicology* **14**, 29, doi:10.1186/ s12989-017-0210-8 (2017).
39 Guldberg, M., Christensen, V. R., Krøis, W. & Sebastian, K. Method for determining in-vitro dissolution rates of man-made vitreous fibres. *Glass science and technology* **68**, 181-187 (1995).
40 Kastury, F., Smith, E. & Juhasz, A. L. A critical review of approaches and limitations of inhalation bioavailability and bioaccessibility of metal(loid)s from ambient particulate matter or dust. *Science of The Total Environment* **574**, 1054-1074, doi:https://doi.org/10.1016/j.scitotenv.2016.09.056 (2017).

41 Utembe, W., Potgieter, K., Stefaniak, A. B. & Gulumian, M. Dissolution and biodurability: Important parameters needed for risk assessment of nanomaterials. *Particle and Fibre Toxicology* **12**, 11 (2015).
42 McPherson, P. *Practical Volumetric Analysis*. (Royal Society of Chemistry, 2014).
43 Yokel, R. A., Hancock, M. L., Grulke, E. A., Unrine, J. M. & Graham, U. M. Nanoceria Dissolution and Carboxylic Acid Stabilization in Aqueous Dispersions. *The FASEB Journal* **31**, lb624 (2017).
44 Arts, J. H. E. *et al.* Case studies putting the decision-making framework for the grouping and testing of nanomaterials (DF4nanoGrouping) into practice. *Regulatory Toxicology and Pharmacology* **76**, 234-261, doi:http://dx.doi.org/10.1016/j.yrtph.2015.11.020 (2016). Lifshitz,
45 I. & Slezov, V. Kinetics of diffusive decomposition of supersaturated solid solutions. *Soviet Physics JETP* **35**, 331 (1959).
46 Sommer, A. P., Röhlke, W. & Franke, R. P. Free Energy Reduction by Molecular Interface Crossing: Novel Mechanism for the Transport of Material Across the Interface of Nanoscale Droplets Induced by Competing Intermolecular Forces for Application in Perfluorocarbon Blood Substitutes. *Naturwissenschaften* **86**, 335-339, doi:10.1007/s001140050629 (1999).
47 Committee on Hazardous, S. Announcement on Hazardous Substances 527. *BekGS* **527** (2013).
48 Vencalek, B. E. *et al.* In Situ Measurement of CuO and Cu(OH)2 Nanoparticle Dissolution Rates in Quiescent Freshwater Mesocosms. *Environmental Science & Technology Letters* **3**, 375-380, doi:10.1021/acs.estlett.6b00252 (2016).
49 Kent, R. D. & Vikesland, P. J. Dissolution and Persistence of Copper-Based Nanomaterials in Undersaturated Solutions with Respect to Cupric Solid Phases. *Environmental Science & Technology* **50**, 6772-6781, doi:10.1021/acs.est.5b04719 (2016).
50 Guldberg, M. Method for determining in-vitro dissolution rates of man-made vitreous fibres. *Glass science and technology* **68** (1995).
51 Guldberg, M. *et al.* Measurement of in-vitro fibre dissolution rate at acidic pH. *Annals of Occupational Hygiene* **42**, 233-243 (1998).
52 Guldberg, M., Jensen, S. L., Knudsen, T., Steenberg, T. & Kamstrup, O. High-alumina low-silica HT stone wool fibers: A chemical compositional range with high biosolubility. *Regulatory Toxicology and Pharmacology* **35**, 217-226 (2002).
53 Zoitos, B. K. In vitro measurement of fibre dissolution rate relevant to biopersistence at neutral pH: An interlaboratory round robin. *Inhalation toxicology* **9**, doi:10.1080/089583797198051 (1997).
54 Thelohan, S. & De Meringo, A. In vitro dynamic solubility test: influence of various parameters. *Environmental health perspectives* **102**, 91 (1994).
55 ECHA. Appendix R.6-1 for nanomaterials applicable to the Guidance on QSARs and Grouping of Chemicals. doi:10.2823/884050 (2017).
56 Bligh, P. H. & Taylor, D. M. Comparative studies of the metabolism of strontium and barium in the rat. *The Biochemical journal* **87**, 612-618 (1963).
57 Panahifar, A. *et al.* Three-dimensional labeling of newly formed bone using synchrotron radiation barium K-edge subtraction imaging. *Phys Med Biol* **61**, 5077-5088, doi:10.1088/0031-9155/61/13/5077 (2016).
58 Moore, W. (1964).
59 Misawa, Y. *et al.* Effect of age on alveolar bone turnover adjacent to maxillary molar roots in male rats: A histomorphometric study. *Archives of Oral Biology* **52**, 44-50, doi:10.1016/j.archoralbio.2006.06.012 (2007).
60 Graham, U. *et al.* in *9th International Conference on Nanotoxicology* Vol. P15.37 (Neuss, Germany, 2018).
61 Giese, W. Experimentelle Untersuchungen zur Staublungenfrage. *Beitr. path. Anat* **94**, 35 (1934).
62 Yokel, R. A., Unrine, J. M., Wu, P., Wang, B. & Grulke, E. A. Nanoceria biodistribution and retention in the rat after its intravenous administration are not greatly influenced by dosing

schedule, dose, or particle shape. *Environmental Science: Nano* **1**, 549-560, doi:10.1039/C4EN00035H (2014).
63 Hille, B. *Ion channels of excitable membranes*. Vol. 507 (Sinauer Sunderland, MA, 2001).
64 Mörk, A.-C. *et al.* Effects of particulate and soluble (1–3)-β-glucans on Ca2+ influx in NR8383 alveolar macrophages. *Immunopharmacology* **40**, 77-89 (1998).
65 Campo, B., Surprenant, A. & North, R. A. Sustained depolarization and ADP-ribose activate a common ionic current in rat peritoneal macrophages. *The Journal of Immunology* **170**, 1167-1173 (2003).
66 Dernison, M. *et al.* Growth-dependent modulation of capacitative calcium entry in normal rat kidney fibroblasts. *Cellular signalling* **22**, 1044-1053 (2010).
67 Vaeth, M. *et al.* Ca2+ signaling but not store-operated Ca2+ entry is required for the function of macrophages and dendritic cells. *The Journal of Immunology* **195**, 1202-1217 (2015).
68 Link, T. M. *et al.* TRPV2 has a pivotal role in macrophage particle binding and phagocytosis. *Nature immunology* **11**, 232 (2010).
69 Riazanski, V. *et al.* TRPC6 channel translocation into phagosomal membrane augments phagosomal function. *Proceedings of the National Academy of Sciences* **112**, E6486-E6495 (2015).
70 Ohsumi, Y. & Anraku, Y. Calcium transport driven by a proton motive force in vacuolar membrane vesicles of Saccharomyces cerevisiae. *Journal of Biological Chemistry* **258**, 5614-5617 (1983).
71 Xu, H., Martinoia, E. & Szabo, I. Organellar channels and transporters. *Cell Calcium* **58**, 1-10 (2015).

6.2.1 Authors contributions

Predicting dissolution and transformation of inhaled nanoparticles in the lung using abiotic flow cells: The case of barium sulfate

Johannes G. Keller[1], Uschi Graham[1], **Johanna Koltermann-Jülly**, Robert Gelein, Lan Ma-Hock,
Robert Landsiedel, Martin Wiemann, Günter Oberdörster, Alison Elder, Wendel Wohlleben

[1] *Equal contribution.*

Scientific Reports, 2019, submitted manuscript

Authors contributions

JGK performed the flow-through testing.
UG performed the HRTEM study.
RG performed, and AE supervised the flow-by testing.
JKJ performed the static solubility and quasi-dynamic abiotic dissolution testing.
RL, LMH, GO, MW contributed to the interpretation of results.
WW conceived and supervised the project.
All authors contributed to the writing of the manuscript.

We hereby confirm the accuracy of the above information (all authors).

Keller, Johannes Georg	
Name	*Date, Signature*
Graham, Dr. Uschi	
Name	*Date, Signature*
Koltermann-Jülly, Johanna	
Name	*Date, Signature*
Gelein, Robert	
Name	*Date, Signature*
Ma-Hock, Dr. Lan	
Name	*Date, Signature*
Landsiedel, PD Dr. Robert	
Name	*Date, Signature*
Wiemann, Prof. Dr. Martin	
Name	*Date, Signature*
Oberdörster, Prof. Dr. Günter	
Name	*Date, Signature*
Elder, Prof. Dr. Alison	
Name	*Date, Signature*
Wohlleben, Dr. Wendel	
Name	*Date, Signature*

6.3 Paper 3: „Appearance of alveolar macrophage subpopulations in correlation to histopathological effects in short-term inhalation studies with biopersistent (nano)materials“

The following section contains the publication:

Appearance of alveolar macrophage subpopulations in correlation to histopathological effects in short-term inhalation studies with biopersistent (nano)materials

Johanna Koltermann-Jülly, Lan Ma-Hock, Sibylle Gröters, Robert Landsiedel

Toxicologic Pathology, submitted manuscript

Appearance of alveolar macrophage subpopulations in correlation to histopathological effects in short-term inhalation studies with biopersistent (nano)materials

Johanna Koltermann-Jülly[a, b], Lan Ma-Hock[a], Sibylle Gröters[a], Robert Landsiedel[a, *]

[a]Experimental Toxicology and Ecology, BASF SE, 67056 Ludwigshafen, Germany

[b]Biopharmaceutics and Pharmaceutical Technology, Saarland University, 66123 Saarbrücken, Germany

*corresponding author: Robert Landsiedel, BASF SE, Experimental Toxicology and Ecology, 67056 Ludwigshafen, Germany; robert.landsiedel@basf.com

Abstract

Following inhalation and deposition in the alveolar region at sufficient dose, biopersistent (nano)materials generally provoke pulmonary inflammation. Alveolar macrophages (AMs) are mediators of pulmonary immune responses. According to their disparate functions, both pro-inflammatory M1 and anti-inflammatory M2 macrophages have been described. This study aimed at broadly identifying AM phenotype as M1 or M2 upon short-term inhalation exposure to different (nano)materials followed by a post-exposure period. AM phenotyping was retrospectively performed using immunohistochemistry. M1 ($CD68^+iNOS^+$) and M2 ($CD68^+CD206^+$ and $CD68^+ArgI^+$) macrophages were characterized in formalin-fixed paraffin-embedded lung tissue of rats exposed for 6 h/day on five consecutive days to air (control), 100 mg/m³ nano-TiO_2, 25 mg/m³ nano-CeO_2, 32 mg/m³ multi-walled carbon nanotubes, or 100 mg/m³ micron-sized quartz. During acute inflammation, relative numbers of M1 AM were markedly increased, whereas relative numbers of M2 were generally decreased compared to control. Following an exposure-free period, changes in iNOS or CD206 expression correlated with persistence, regression or progression of the inflammation, suggesting a role of M1/M2 AMs in the pathogenesis of pulmonary inflammation. However, no clear correlation of AM subpopulations with qualitatively distinct histopathological findings caused by different (nano)materials was found. A more detailed understanding of the biokinetics of the (nano)material in the lung and of the processes underlaying morphological changes is needed, to identify early biomarkers for different histopathological outcomes.

1. Introduction

Nanomaterials are widely used in industrial applications. During the production and processing of nanomaterials in the workplace, particulate matter might be released to the air[1,2]. Thus, inhalation is a major route of occupational exposure to nanomaterials. *In vivo* inhalation studies in laboratory animals suggest a potential hazard of biopersistent nanomaterials to the lungs, commonly initiated by a pulmonary inflammatory response[3-6].

Early human epidemiological data and rat inhalation studies showed that different poorly-soluble dusts at sufficient dose caused pulmonary inflammation upon inhalation exposure[7-9], although these materials were of very low inherent toxicity in oral and dermal studies. More recent inhalation toxicity studies in rats showed distinct differences in morphological changes of lungs caused by different poorly-soluble nanomaterials[3,5,10-14]. The inflammatory potency as well as the quality of the inflammation of these biopersistent particles differ largely from each other.

For the present examinations, nano-TiO_2, nano-CeO_2, multi-walled carbon nanotubes (mwCNT), and micron-sized quartz were chosen as model substances because data from short-term as well as long-term rat inhalation toxicity studies are available for all four materials[3-5,15]. These substances are considered poorly-soluble and highly biopersistent. Quartz and mwCNT are known to exhibit specific toxicity due to their surface reactivity or shape, respectively. In the past, TiO_2 and CeO_2 were considered as "poorly-soluble particles with low inherent toxicity", however, it was shown that both TiO_2 and CeO_2 nanoparticles provoke distinct pulmonary toxicity in rat lungs upon inhalation exposure. In a 90-day inhalation study[16] TiO_2 caused only minimal to mild lesions comprising particle-laden macrophage accumulation, aggregations in sub-pleural region and in centriacinar region at an aerosol concentration of 2 mg/m³. These lesions were associated with minimal hypertrophy and hyperplasia of alveolar epithelial type II cells. At 10 mg/m³ more severe epithelial proliferative changes were observed. Most of these lesions regressed post-exposure (13-52 weeks). In comparison, sub-acute (28 days) and sub-chronic (90 days) inhalation exposure to CeO_2 elicited pulmonary inflammation at very low dust aerosol concentrations (down to 0.1 mg/m³). The CeO_2 induced inflammatory reaction persisted during a post-exposure period of 13 weeks and progressed during this time to granulomatous inflammation[12,17]. The initial pulmonary inflammation was characterized by an increased number of AMs loaded with amber-colored small particles, diagnosed as histiocytosis, alveolar – with particles. Whereas the granulomatous inflammation was characterized by septal/interstitial conglomerates of particle-laden macrophages intermingled with mixed inflammatory cells (lymphocytes, plasma cells). Also, biopersistent nanomaterials with high aspect ratio, such as mwCNT, showed high inflammogenic potential following inhalation exposure[14]. Sub-chronic exposure to 0.1, 0.5, or 2.5 mg/m³ mwCNT caused dose-dependently initial granulomatous inflammation, characterized by conglomerated

macrophages, lymphocytes and plasma cells, even at the lowest aerosol concentration tested. The inflammation was composed of AMs and polymorphonuclear neutrophils and was located in the centriacinar region. In addition, intraseptal granulomas were observed[14]. With prolonged exposure duration (up to two years in rats), long-term effects caused by nanomaterials were observed to persist or progress to fibrosis or possibly lung tumor formation[3-5,15].

Compared to sub-chronic inhalation studies, short-term inhalation studies (STIS) (five-day exposure) provide important information on early key elements of pulmonary inflammation caused by nanomaterials and consistent prediction of respiratory tract toxicity. Combining information from quantitative analysis of bronchoalveolar lavage fluid (BALF) with histopathological findings and with information on the location, persistence, regression or progression of effects, STIS are well suitable for the hazard assessment of nanomaterials[6,18,19]. Archived formalin-fixed paraffin-embedded (FFPE) lung tissue of formerly performed STIS were chosen for the present examinations. Rats were inhalation exposed to 100 mg/m³ nano-TiO_2, 25 mg/m³ nano-CeO_2, 32 mg/m³ mwCNT or 100 mg/m³ micron-sized quartz. The studies were published previously[10,13,14]. Main findings are summarized in table 1. In brief, the inhalation exposure to 100 mg/m³ TiO_2 caused pulmonary inflammation composed of minimal to moderate diffuse, alveolar histiocytosis and minimal multifocal infiltration with neutrophils. Importantly, the inflammation declined 14 days after the end of exposure[13]. Exposure to 25 mg/m³ CeO_2 resulted in pulmonary inflammation composed of minimal to slight alveolar histiocytosis. Here, inflammation persisted following a 21-day post exposure period. Short-term inhalation exposure to 32 mg/m³ mwCNT lead to granulomatous inflammation in lungs of exposed animals. Histopathological findings were not reversible and granulomatous inflammation persisted during a 21-day post-exposure period[14]. In comparison, 100 mg/m³ quartz lead to a very strong inflammatory response with minimal to moderate diffuse, alveolar histiocytosis in lungs of exposed animals immediately following 5-day exposure. 14 days post-exposure, increases of inflammatory parameters were not reversible, on the contrary, histological findings of a diffuse inflammatory response, composed of AMs, neutrophils and cell debris, increased in severity[13].

Obviously, AMs have a crucial role in pulmonary clearance as well as in orchestrating pulmonary immune responses[20]. Data published during the past three decades suggest that these various activities are mediated by distinct subpopulations of macrophages, which are induced by signals they encounter in their local tissue microenvironment[21-35]. In a rather simplistic view, these subpopulations can be divided into two major distinct macrophage phenotypes, which have been categorized broadly as pro-inflammatory/ cytotoxic M1 macrophages and anti-inflammatory/ wound repair M2 macrophages[36-38]. Increasing evidence suggests that nanomaterials are capable of activating macrophages to the M1 phenotype, leading to the expression of pro-inflammatory mediators and

Table 1 Short-term inhalation studies (STIS) in rats. Summary of substance characterization, study design, and main findings of TiO_2 and quartz STIS, CeO_2 STIS, and mwCNT STIS.

	TiO_2	**CeO_2**	**mwCNT**	**quartz**
Producer	Evonik (former Degussa)	Umicore	Nanocyl S.A.	Dörentrup Quarz GmbH
Primary particle size, descriptions	20 - 50 nm, globular, 30% rutile, 70% anatase	40 nm, roughly globular, cerianite cubic, NM-212	average diameter 10 nm, length 0.1 to 10 µm	100 to 7000 nm, platelets, DQ12
Pore sizes (Hg porosimetry)	40 nm	25 nm, 7000 nm		500 nm, 30000 nm
BET surface area	51.1 m^2/g	27 m^2/g	250-300 m^2/g	5.9 m^2/g
Purity	> 99.5%	> 99%	90% C, 10% metal oxide	
Solubility in water and DMEM/FCS	Ti < 0.1 ppm	Ce < 0.001%	n.d.	Si 41 ppm
Study design	6 h/d, 5d exposure, two weeks post-exposure	6 h/d, 5d exposure, three weeks post-exposure	6 h/d, 5d exposure, three weeks post-exposure	6 h/d, 5d exposure, two weeks post-exposure
Necropsy time point	directly after the last exposure, and two weeks thereafter	directly after the last exposure, and three weeks thereafter	3 days after the last exposure, and three weeks thereafter	directly after the last exposure, and two weeks thereafter
Exposure aerosol concentration	100 mg/m^3	25 mg/m^3	32 mg/m^3	100 mg/m^3
Lung weight shortly after exposure	absolute: + 33% relative: + 35%	no lung weight change	absolute: + 17% relative: + 19%	absolute: + 36% relative: + 45%
Histological findings shortly after exposure	histiocytosis, diffuse pigment loaded macrophages infiltration granulocytic (multi)focal hyperplasia/hypertrophy, bronchiolar	histocytosis with particles insinde of histiocytes	granulomatous inflammation, granulocytic infiltration	histiocytosis, diffuse infiltration granulocytic (multi)focal infiltration, lymphoid (multi)focal
BALF analysis shortly after exposure (x-fold increase compared to control)	increased protein concentration (3x), increased activities of LDH (4x), GGT (3x), ALP (2x), and NAG (1.4x), increased total cell count (5x), increased counts of neutrophils (1882x) and lymphocytes (36x)	increased protein concentration (5x), increased activities of LDH (5x), GGT (6x), ALP (4x) and NAG (2x), increased total cell count (5x), increased counts of neutrophils (330x) and lymphocytes (42x)	increased protein concentration (6x), increased activities of LDH (5x), GGT (6x), ALP (4x) and NAG (3x), increased total cell count (8x), increased neutrophils (222x)	increased protein concentration (7x), increased activities of LDH (15x), GGT (4x), ALP (4x) and NAG (3x), increased total cell count (17x), increased counts of neutrophils (6101x) and lymphocytes (55x)
Lung weight after post-exposure period	no lung weight change	no lung weight change	absolute: + 16% relative: + 10%	absolute: + 45% relative: + 45%

Table 1 (continued) Short-term inhalation studies (STIS) in rats. Summary of substance characterization, study design, and main findings of TiO_2 and quartz STIS, CeO_2 STIS, and mwCNT STIS.

	TiO_2	**CeO_2**	**mwCNT**	**quartz**
Histological findings after post-exposure period	histiocytosis (multi)focal pigment loaded macrophages	histiocytosis with particles in histiocytes	granulomatous inflammation	inflammation, diffuse
BALF analysis after post-exposure period (x-fold increase compared to control)	total cell count (2x), increased neutrophils (62x)	minimally increased neutrophils (7x), slightly increased LDH (2x), GGT (2x) and ALP (2x)	increased protein concentration (2x), increased activities of LDH (4x), GGT (3x), ALP (2x), and NAG (2x), increased total cell count (6x), increased neutrophils (572x) and lymphocytes (11x)	increased protein concentration (9x), increased activities of LDH (21x), GGT (8x), ALP (4x), and NAG (6x), increased total cell count (37x), increased counts of neutrophils (5228x) and lymphocytes (143x)
Reference	13	10	14	13

recruitment of inflammatory cells. Ultimately nanomaterials may have an impact on the M1/M2 balance, which might change immune defense properties[39,40]. Furthermore, over-activation, characterized by prolonged or excessive release of mediators, of M1 and/or M2 macrophages can contribute to tissue injury and disease progression, such as the development of fibrosis[20,41].

The present study is a retrospective investigation and the histological specimens examined were derived from available FFPE lungs of the studies mentioned above[10,13,14]. Since AMs represent the immediate, immunocompetent main contact with particulate matter in the alveolar region, the main focus was on the possibility and feasibility to characterize the different phenotype (M1 or M2) of AMs in existing FFPE lung tissue, which is comparable to material coming from toxicity studies for regulatory purposes, and to elucidate whether AMs subsets can be correlated to the qualitatively different histopathological findings of different (nano)materials. We hypothesize that initial macrophage polarization is dependent on intrinsic material properties and affects the different morphological changes observed. The available, FFPE specimen did not allow for further detailed mechanistic investigations or high throughput quantification as qRT-PCR or flow cytometry of not-paraffinized tissue would have allowed, respectively. However, immunohistochemistry allowed specific assessment of polarized AMs in the alveolar lumen *in situ*, without the need for sophisticated immunophenotyping of pulmonary immune cells. In addition, it was repeatedly described that bronchoalveolar lavage techniques are not capable of detaching sessile macrophages out of the lungs[42,43]. Furthermore, using an immunohistochemical approach restricted the current investigations to a simplistic classification of macrophages exhibiting merely a pro-inflammatory M1 or anti-inflammatory M2 phenotype. Future studies, using for instance flow cytometry, could identify in more detail macrophages that share characteristics of different shades of activation.

As STIS are commonly used to identify hazard and inflammogenic potency of inhaled nanomaterials[18,19] and proved to be useful in prioritizing[6,44] and grouping nanomaterials[45], this retrospective study was performed to examine the appearance of AM subpopulations in lung tissue upon short-term exposure to poorly-soluble (nano)materials and aimed at identifying a potential correlation of early AM polarization with histopathological outcome. Using an immunohistochemical approach, we identified polarized AMs, which accumulated in lung tissue following inhalation exposure to (nano)materials. The expression of general and specific macrophage markers was detected by double immunolabelling. In addition, we quantitatively analyzed the macrophage subpopulations subsequently to the termination of exposure and following an exposure-free period.

2. Materials and Methods

2.1 Test substances

TiO_2 P25 (CAS No. 13463-67-7) was commercially obtained from the producer (Degussa AG, Frankfurt am Main, Germany) and described in detail in[13]. Shortly, nano-TiO_2 was specified with a purity of >99.5% and consisted of anatase as well as rutile forms (70%/30%), without surface coating. The primary particle size was in the size range of 20–30 nm (globular shape) and the BET-specific surface area (determined with the Brunauer Emmet Teller (BET) method) amounted to 48.6 m^2/g. CeO_2 NM-212 was received from the repository of the Organization for Economic Co-operation and Development (OECD) sponsorship program for the testing of manufactured nanomaterials and was extensively characterized in[10]. In brief, CeO_2 NM-212 had an average primary particle size of 40 nm and a BET-specific surface area of 27 m^2/g with an irregular, but globular primary particle shape. MwCNT were provided by Nanocyl S.A. (Sambreville, Belgium) under the product name Nanocyl NC 7000[14]. The purity was 90 % carbon and 10 % metal oxides. According to the manufacturer, the tubes had diameters of 5–15 nm and length of 0.1–10 µm, with a BET-specific surface area of 250–300 m^2/g. Quartz DQ12 was commercially acquired from the producer (Dörentrup Quarz GmbH, Westfalen, Germany) as depicted in[13]. Briefly, quartz possessed a median particle size of 315 nm in ethanol and a BET-specific surface area of 5.9 m^2/g. For more detailed information on material characterization please refer to[46].

2.2 Short-term inhalation studies

Short-term inhalation studies were performed as previously described[6,18,19]. In brief, Wistar rats were inhalation-exposed for six hours per day on five consecutive days to 100 mg/m^3 TiO_2, 25 mg/m^3 CeO_2 NM-212, 32 mg/m^3 mwCNT, or 100 mg/m^3 quartz aerosols. Concurrent control groups were exposed to conditioned air only. Please note that three independent studies were performed. One study for CeO_2 exposure (female rats, five animals per group), a second one for mwCNT exposure (male rats, three animals per group) and a third one for TiO_2 or quartz exposure (male rats, six animals per group). Animals were sacrificed immediately following the last exposure in the CeO_2 and the TiO_2 and quartz studies. In the mwCNT study, animals were sacrificed three days after the last exposure. Additional post-exposure groups were sacrificed after an exposure-free period of 14 days (in case of TiO_2 and quartz) or 21 days (in case of mwCNT). Further, selected tissues, i.e. mesenteric lymph nodes, liver, and spleen, were collected as positive control tissues for immunohistochemistry from untreated animals. Tissue selection was based on the expression patterns of the proteins of interest known from literature. Tissues were collected immediately following sacrifice, lungs were inflated with 10% neutral

buffered formalin (NBF) and all organs were placed in NBF at room temperature. Fixation was followed by standard histotechnical processing and paraffin embedding (Leica ASP300 S, Leica Biosystems). Subsequently, tissues were sectioned (2-3 µm, Microm HM 355S, Thermo Scientific), mounted onto slides and hematoxylin-eosin (HE) stained for standard diagnostic evaluation by a well-experienced and board-certified veterinary pathologist. Histopathological analyses were performed in a blinded manner and according to the International Harmonization of Nomenclature and Diagnostic Criteria (INHAND)[47]. For further details please refer to[13,14,17].

2.3 Immunohistochemistry

For immunohistochemical investigations, tissue sections of the left lung lobe (lobus pulmo sinister), mesenteric lymph nodes, liver, and spleen were mounted onto silane-coated slides (Q Path adhesive slide, Q Path). From each left lung lobe several sections were prepared. One was used for HE routine staining in the original study (see above). And three for iNOS-CD68, ArgI-CD68 or CD206-CD68 double immunostaining, and three more as negative control for each immunostaining for the present retrospective study. The sections for immunohistochemistry were prepared right before staining.

Mesenteric lymph node as well as liver and spleen tissue served as positive control tissue for CD68 immunostaining and liver tissue served also as positive control tissue for iNOS (Kupffer cells), ArgI (hepatocytes) or CD206 (liver sinusoidal endothelial cells) staining[48-54].

First, tissue sections were deparaffinized and rehydrated, followed by heat-mediated antigen retrieval and quenching of endogenous peroxidase activity using 6% hydrogen peroxide. Subsequently, slides were subjected to immunohistochemical staining. Primary polyclonal rabbit anti iNOS (1:100, ab15323, abcam), polyclonal rabbit anti ArgI (1:600, LS-B4660, LifeSpan BioSciences), polyclonal rabbit anti CD206 (1:5000, ab64693, abcam) antibody, or serum/IgG negative control (universal negative control serum, Biocare Medical) were applied. As secondary antibody for the first staining anti rabbit conjugated to horse radish peroxidase (HRP) (CytoChem-Plus HRP Polymer Kit, Zytomed Systems) was used according to the manufacturer. As first chromogen served 3,3'-Diaminobenzidine (DAB) (Zytomed Systems). Subsequently, the same slides were incubated again with a primary antibody, monoclonal mouse anti CD68 (1:300, MCA341, abd serotec), or serum/IgG negative control. Afterwards, biotinylated anti mouse immunoglobulins were applied followed by streptavidin linked to alkaline phosphatase (AP) incubation (link label IHC detection system, BioGenex) according to the manufacturer. As second chromogen served Permanent AP Red (Zytomed Systems).

2.4 Quantitative immunohistochemistry

Slides were digitalized using a slide scanner (NanoZoomer 2.0HT, Hamamatsu) and ndp.scan software (NanoZoomer Digital Pathology v2.5, Hamamatsu). Evaluation of scanned left lung tissue was performed with ndp.view software (NanoZoomer Digital Pathology v2.5, Hamamatsu).

Each left lung was assessed for four immunohistochemical markers (CD68 (macrophage marker), iNOS (M1), CD206 (M2), ArgI (M2)), applying three double-immunolabeling protocols (CD68-iNOS, CD68-ArgI or CD68-CD206). Hence, each lung was analyzed three times (one slide for each double-immunostaining). Positively stained macrophages were identified by a red reaction product covering the cytoplasm in case of CD68 immunolabeling, eventually accompanied by a brown reaction product covering the cytoplasm for iNOS, ArgI or CD206 immunolabeling. Only cells located in the alveolar region and showing typical AM morphology regarding size and shape were included in the analysis. Apoptotic or necrotic cells exhibiting red and/or brown reaction product were excluded from quantification. The number of macrophage cells in lung tissue per high power field (HPF) differed between the control groups and the treatment groups, the latter being diagnosed with diffuse histiocytosis. Thus, the total lung tissue area analyzed differed between the different exposure groups. Overall, a total of 100 $CD68^+$ cells per lung section, scattered throughout the tissue, were counted manually. Considering the objectives of this paper, macrophages present at sites of inflammation were preferentially assessed. Counting was truncated once the minimum number of 100 AMs was reached. Out of those 100 $CD68^+$ cells, double-stained AMs were counted. Then, for each lung section the relationship of single-/and double labeled AM was calculated. As the control animals revealed a lower number of AMs per HPF, more HPFs had to be evaluated in controls reaching the number of 100 $CD68^+$ AMs.

2.5 Statistical analysis

Group sizes varied from 3 animals per group in the mwCNT study to 5 animals per group in the CeO_2 study, and 6 animals per group in the TiO_2 and quartz study. Percentages of M1 or M2 marker double-positive AMs were calculated from counted $CD68^+$ AMs. Then, data were evaluated using arcsine transformation. The arcsine transformation is indicated when dealing with percentages. It pulls the values close to 0 and 100 apart while compressing the mean values. This enables a more powerful evaluation of substantial changes e.g. from 4% to 8% compared to changes from 50% to 54%. Each dose group was compared to the concurrent control group of the respective study. Because of differences in study design, the dose groups were not compared to each other. Therefore, an unpaired t-test was performed (dose group vs. concurrent control). In lungs of control animals baseline

expression of iNOS is approximately 0%. Thus, a one-sided t-test for iNOS data was chosen. Baseline expression of CD206 and ArgI is more variable and both, increase and decrease of CD206 or ArgI expression was assumed. Here, a two-sided t-test was performed[55]. $p < 0.05$ was considered significant. Accordingly, labeling * for $p \leq 0.05$ or ** for $p \leq 0.01$ was applied. Data are presented as mean ± SD.

3. Results

3.1 Immunohistochemistry of histological sections of rat lungs exposed to different (nano)materials

In the lungs of control animals, small, spindle-shaped $CD68^+$ AMs were found sparsely scattered throughout the tissue. In some animals, occasionally, single macrophage-like cells were found unstained. This is consistent with previous findings, which showed a high and specific CD68 expression in the vast majority of mature, resident AMs[56]. CD68 immunostaining was restricted to the cytoplasm of macrophage cells, without any background staining. iNOS immunolabeling in lung tissue was found cytoplasmatically in $CD68^+$ AMs of treated but not of control animals. Further, untreated animals showed a high abundance of $CD68^+CD206^+$ macrophages, whereby specific immunostaining was discernible in the cytoplasm. Positive signal of ArgI was observed in the nuclei of bronchial and alveolar epithelial cells, as well as in the nuclei of the cells of the vasculature. Nuclear ArgI signal was also found in AMs, therefore $ArgI^+$ staining was defined for quantification as brown reaction product in the cytoplasm of $CD68^+$ cells.

Following five-day exposure to 100 mg/m³ TiO_2 a large proportion of $CD68^+$ AMs was fully loaded with grey, globular material, presumably TiO_2 agglomerates. In addition, CD68 staining was accompanied by cytoplasmic iNOS, ArgI or CD206 immunolabeling (Fig. 1, second row). In the 25 mg/m³ CeO_2 treatment group particulate matter in the cytoplasm of $CD68^+$ AMs was noted, which was accompanied by an increase in cellular size and a more globular cell shape. Additionally, particulate matter and cell debris were found in the alveolar lumen. Immunohistochemical M1 and M2 specific double-staining was restricted to the cytoplasm (Fig. 1, third row). Subsequently to the five-day exposure to 32 mg/m³ mwCNT $CD68^+$ AMs were laden with black fibrous structures. Cell debris as well as intact $CD68^+iNOS^+$, $CD68^+ArgI^+$ or $CD68^+CD206^+$ cells could be observed (Fig. 1, fourth row). In comparison, exposure of rats to 100 mg/m³ quartz resulted in considerable amount of cell debris and necrotic cells in the alveolar lumen, which were stained with red reaction product (Fig. 1, bottom row).

At the end of a 14-day post-exposure period the distribution of M1 specific immunostaining of cells changed. Only AMs which obviously internalized grey TiO_2 particles were $CD68^+$ and $iNOS^+$. AMs not obviously loaded with particulate matter were $CD68^+$ only. For the M2 specific double- immunolabeling

---

Fig. 1 Micrographs of left lung sections of animals exposed to different (nano)materials for 5 days. Effects on iNOS (M1), ArgI (M2) and CD206 (M2) expression shortly after the last exposure were visualized by immunohistochemistry. Binding of antibodies was visualized using a red chromogen for the AM marker CD68 and a brown chromogen for the M1 (iNOS) and M2 (ArgI and CD206) markers. Arrows indicate AMs in insets. Scale bars in insets are 10 µm one scale line. Representative sections from each treatment group are shown. Controls were exposed to air only.

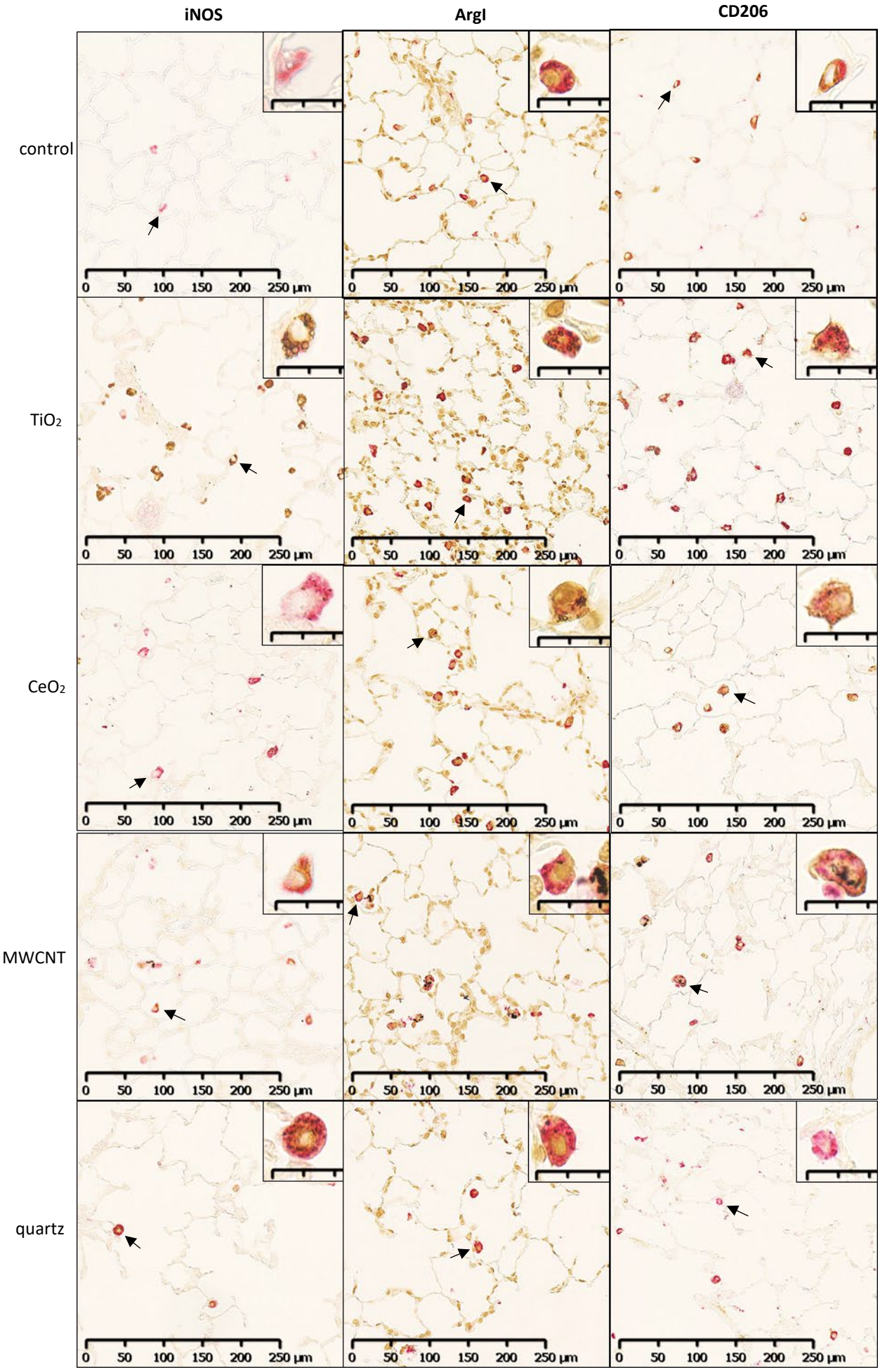
iNOS
Arg1
CD206
control
TiO2
CeO2
MWCNT
quartz
0 50 100 150 200 250 µm

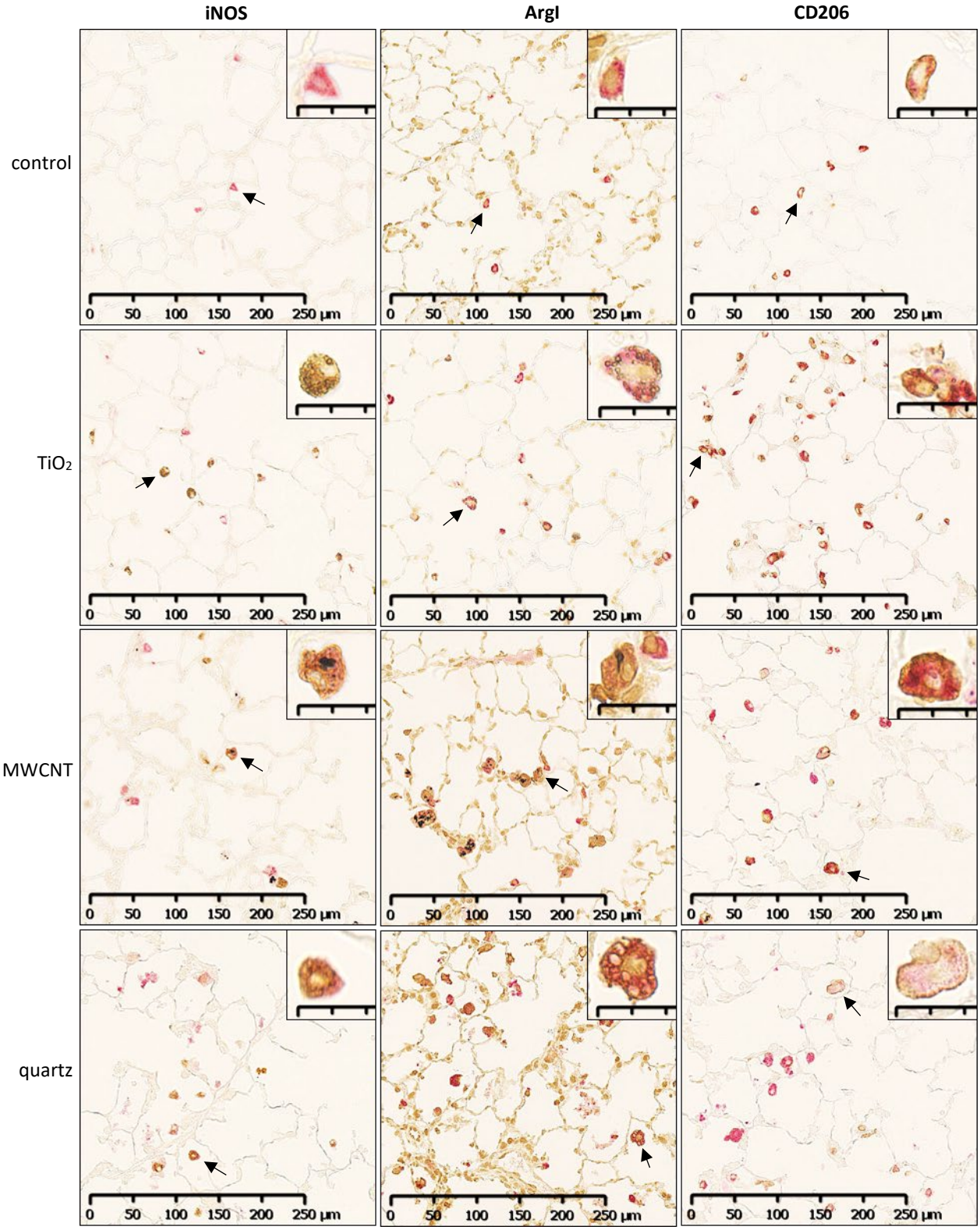

Fig. 2 Micrographs of left lung sections of animals exposed to different (nano)materials following an exposure-free period (14 days in case of TiO_2 and quartz, 21 days in case of mwCNT). Effects on iNOS (M1), ArgI (M2) and CD206 (M2) expression were visualized by immunohistochemistry. Binding of antibodies was visualized using a red chromogen for the AM marker CD68 and a brown chromogen for the M1 (iNOS) and M2 (ArgI and CD206) markers. Arrows indicate AMs in insets. Scale bars in insets are 10 µm one scale line. Representative sections from each treatment group are shown. Controls were exposed to air only.

of AMs such a separation was not noticeable. Here, $CD68^+ArgI^+$ or $CD68^+CD206^+$ immunostaining of AMs was not obviously associated with the cellular content (Fig. 2, second row). 21 days post inhalation exposure to 32 mg/m³ mwCNT and in contrast to the TiO_2 exposure group, the M1 specific immunolabeling of AMs did not show an apparent association with the staining and the cellular content. Interestingly, the intracellular localization of the CD206 immunostaining translocated in a few cells from the cytoplasm to the cell membrane (Fig. 2, third row). In rats treated with 100 mg/m³ quartz the 14-day post-exposure period resulted in AMs that were increased in size, more globular in shape and more vacuolated. The pronounced accumulation of cell debris found in the alveolar space, which was stained with red reaction product, was very prominent. Notably, the staining pattern of CD206 changed. So far, CD206 labeling was found cytoplasmatically, here, the immunolabeling was concentrated at the cellular surface for most of the cells, similar but more pronounced than in the mwCNT group (Fig. 2, bottom row).

3.2 Quantitative evaluation of the phenotype of immunolabeled AMs

To more objectively characterize the occurrence of polarized AMs, we quantified immunohistochemically labeled AMs positive for the general AM marker CD68 and M1 (iNOS) or M2 (CD206 and ArgI) macrophage markers in lungs of (nano)material exposed animals. In all concurrent control groups following five-day exposure, the baseline expression of the M1 marker iNOS was low, i.e. between 0 and 2% of counted cells. The exposure to TiO_2, however, increased the expression of iNOS in AMs to 79%. In contrast, CeO_2 exposure lead to a small but significant increase in iNOS expression to 8%. In animals exposed to mwCNT, iNOS expression levels were significantly elevated to 42%. And quartz caused a significant increase up to 45% (Table 2). Further, we evaluated the expression of M2 macrophage markers after the five-day exposure period. The percentages of $CD68^+CD206^+$ macrophages generally decreased following exposure to nanomaterials or quartz. A reduction of CD206 frequency was observed in TiO_2 treated animals (65%) compared to control animals (77%), however, not significant. A slight but significant decrease was observed in CeO_2 (control: 93%, CeO_2: 83%) and mwCNT (control: 90%, mwCNT: 72%) exposed animals. And a marked decrease was observed following exposure to quartz (control: 77%, quartz: 56%) (Table 2). Quantitative analysis of ArgI expression revealed variable values of the control groups of the three different inhalation-studies (Table 2 and 3). One possible explanation is that the animals of the TiO_2 and quartz study were subjected to surgery (implantation of BrdU-minipumps). This might have affected the immunological state of the animals. Compared to the concurrent control group of the TiO_2 and quartz study, ArgI expression in TiO_2 exposed animals was not altered (control: 48%, TiO2: 55%), whereas it significantly decreased in quartz exposed animals to 26%. CeO_2 exposure lead to a significant increase in the

percentage of ArgI$^+$ cells (33%) compared to the control (17%). The exposure to mwCNT, however, did not alter the expression of ArgI in treated (22%) compared to control (22%) animals (Table 2).

After an exposure-free period of 14 days the percentage of iNOS positive cells in animals exposed to TiO_2 remained elevated at 73.4% but decreased compared to values one day post-exposure. Similarly, the increased iNOS expression values in animals exposed to mwCNT did not change following a post-exposure period of 21 days (45%). In contrast, animals exposed to quartz exhibited even higher percentage of iNOS$^+$ positive cells, significantly increased to 59% compared to the control and the five-day exposure group (Table 3). Further, CD206 expression in the TiO_2 exposure group recovered to 81% (control: 82%), whereas it remained significantly decreased in mwCNT (79%, control: 94%) and quartz (67%, control: 82%) exposure groups (Table 3). The careful evaluation of the ArgI expression levels of the post-exposure groups revealed a general increase. In TiO_2 treated animals ArgI expression remained elevated at 47% compared 37% of the concurrent controls. For the mwCNT and quartz treated groups a progressive increase in ArgI expression levels to 39% and 41% could be observed 14 and 21 days post exposure, respectively (Table 3).

Table 2 Percentages of CD68 and M1 (iNOS) or M2 (CD206 or ArgI) marker double-positive alveolar macrophages (AMs) of animals sacrificed after 5-day exposure to 100 mg/m³ TiO_2 (n=6), 100 mg/m³ quartz (n=6), 25 mg/m³ CeO_2 (n=5), or 32 mg/m³ mwCNT (n=3). Each animal was assessed for all three markers, i.e. three lung sections with one double-immunostaining each. In each lung section the marker-expression of one hundred AMs was assessed. Because mixed phenotype macrophages co-exist with M1 and M2 macrophages the overall percentage of cells per lung might exceed one hundred percent.

	M1 or M2 marker expressing AMs [%] ± SD			
	iNOS (M1)	**CD206** (M2)	**ArgI** (M2)	Lung burden [mg/lung]
control[a]	1.5 ± 0.8	77.2 ± 4.8	47.7 ± 5.4	
TiO_2	79.3 ± 9.6**	65.2 ± 15.5	55.1 ± 6.8	2.02[c]
quartz	44.9 ± 5.1**	55.5 ± 8.8**	26.0 ± 6.0**	2.19[c]
control[b]	0.7 ± 0.2	91.5 ± 2.2	19.5 ± 5.5	
CeO_2	8.0 ± 1.9**	83.2 ± 3.6**	33.0 ± 5.3**	0.53[c]
mwCNT	42.0 ± 1.7**	71.7 ± 4.2**	21.7 ± 0.9	n.m.[d]

SD standard deviation

[a] control group of TiO_2 and quartz study

[b] mean of control groups of CeO_2 and mwCNT studies

[c] pulmonary particle clearance was retarded/ reached overload

[d] n.m. lung burden was not measured

* $p \leq 0.05$ treated vs. control group

** $p \leq 0.01$ treated vs. control group

Table 3 Percentages of CD68 and M1 (iNOS) or M2 (CD206 or ArgI) marker double-positive alveolar macrophages (AMs) of animals sacrificed 14 (TiO_2, quartz) or 21 (mwCNT) days post exposure. Animals were exposed for 5 days to 100 mg/m³ TiO_2 (n=6), 100 mg/m³ quartz (n=6), or 32 mg/m³ mwCNT (n=3). Each animal was assessed for all three markers, i.e. three lung sections with one double-immunostaining each. In each lung section the marker-expression of one hundred AMs was assessed. Because mixed phenotype macrophages co-exist with M1 and M2 macrophages the overall percentage of cells per lung might exceed one hundred percent.

	M1 or M2 marker expressing AMs [%] ± SD			
	iNOS (M1)	**CD206** (M2)	**ArgI** (M2)	Lung burden [mg/lung]
control[a]	2.0 ± 2.5	82.0 ± 6.4	37.0 ± 2.3	
TiO_2	73.4 ± 8.3**	80.7 ± 4.2	47.2 ± 7.7*	1.55[c]
quartz	59.1 ± 10.6**	66.7 ± 6.4**	41.0 ± 5.1	1.76[c]
control[b]	2.0 ± 0.8	93.7 ± 2.5	24.2 ± 7.6	
mwCNT	44.7 ± 4.9**	78.5 ± 0.5*	38.8 ± 2.0	n.m.[d]

SD standard deviation

[a] control group of TiO_2 and quartz study

[b] control group of mwCNT study

[c] pulmonary particle clearance was retarded/ reached overload

[d] n.m. lung burden was not measured

* $p \leq 0.05$ treated vs. control group

** $p \leq 0.01$ treated vs. control group

4. Discussion

The present investigation was conducted to assess whether possible differences in early alveolar macrophage (AM) polarization upon short-term (5 days) inhalation exposure correlates with variable histopathological findings of poorly-soluble (nano)materials, especially regarding the possible onset of granulomatous inflammation. Using an immunohistochemical approach, we identified AM subpopulations, which appeared in lung tissue following exposure to poorly-soluble (nano)materials. Further, we quantitatively analyzed the initial macrophage polarization shortly after five-day exposure and the polarization state seen after 14 or 21 days post-exposure. TiO_2, CeO_2, mwCNT and quartz served as model substances, representing thoroughly-studied materials with high biopersistence and qualitatively different histopathological effects (Tables 1 and 4). However, the available, paraffinized specimen did not allow for detailed mechanistic investigations. For more information on cytokine expression please refer to the BALF analysis of the respective study publication. Measured lung burdens are summarized in table 4. Similarly, assessing biokinetics was not the motivation of the current study, therefore please refer to the respective publications. Furthermore, there is an emerging concept that AMs and interstitial macrophages within rodent lungs are differentially recruited[57] following exposure to particles[58] and that they differ in their cytokine secretion profiles[57,59]. Investigations in macaques[60] revealed that both cell types, AMs as well as interstitial macrophages, are $CD68^+$. Thus, differentiation between resident AMs and recruited interstitial macrophages in the alveolar lumen is not possible with the current study design. However, this was not the focus of the present study.

4.1 Immunohistochemical method for labeling AMs in lung sections using macrophage markers

Our immunohistochemical observations of the expression of CD68, iNOS, ArgI and CD206 are in line with previous studies. CD68, often handled as the ‚pan' macrophage marker, was discussed not to be a suitable marker for macrophages in general, but rather a marker indicative of phagocytosis[61,62]. However, we found high expression of CD68 in AMs and only rarely single cells with macrophage like appearance throughout all study groups not labelled for CD68, resembling the findings of Zaynagetdinov et al.[56]. Therefore, we considered immunolabeling of cells with anti-CD68 antibody as a suitable tool to identify AMs.

iNOS serves commonly as marker of pro-inflammatory macrophages (M1)[37]. It becomes early induced in the frame of a pro-inflammatory immune response; nitric oxide (NO) production by iNOS is important for e.g. microbial killing[63]. Like other investigations, we observed no expression of iNOS in

Table 4 Summary of the test results obtained in the present study for alveolar macrophage polarization (%) and obtained in published inhalation studies, which measured lung burden and examined histological lung sections after short-term or sub-chronic exposure to different (nano)materials.

(Nano-) material	This study			Published data				
	M1 (iNOS) M2 (CD206)		Observations following post-exposure period	Lung burden (5-day exposure) [mg/lung]	Short-term effects (5-day expoure)	Post-exposure observations	additional effects observed in sub-chronic studies (90-day exposure)	References
	5-day exposure	Post-exposure						
TiO_2	79% 65%	73% 81%	Decrease M1 Increase M2	2 mg at study day 5 1.55 mg at study day 19 **overload**	Neutrophilic inflammation Histiocytosis	Regression of inflammation	+ epithelial hyperplasia/ hypertrophy	Bermudez et al., 2004; van Ravenzwaay et al., 2009
CeO_2	8% 83%			0.53 mg at study day 5 0.4 mg at study day 25 **overload**	Inflammation Histiocytosis	Persistence of inflammation	+ granulomatous inflammation + interstitial fibrosis + bronchiolo-alveolar hyperplasia	Keller et al., 2014; Schwotzer et al., 2017
mwCNT	42% 72%	45% 79%	No change M1 Increase M2	lung burden was not measured	Granulomatous inflammation Histiocytosis	Progression of inflammation	+ lipoproteinosis	Ma-Hock et al., 2009b; Pauluhn, 2010; Kasai et al., 2016
Quartz	45% 56%	59% 67%	Increase M1 Increase M2	2.2 mg at study day 5 1.76 mg at study day 19 **overload**	Neutrophilic inflammation Histiocytosis	Progression of inflammation	+ granuloma + cellular debris + lipoproteinosis + interstitial fibrosis	Reuzel et al., 1991; Johnston et al., 2000; van Ravenzwaay et al., 2009

control animals but strong iNOS induction in AMs of treated animals[64,65]. Thus, we found iNOS a specific and suitable immunohistochemical marker for the identification of M1 macrophages.

Further, and in accordance with previous observations[48,66], we detected the enzyme ArgI (M2 marker), which was initially described as a cytoplasmic enzyme[67], in the cytoplasm and nuclei of AMs, and within the nuclei of other cell types of histological lung sections. Available data demonstrate a colocalization of arginase with heterochromatin, suggesting an important role for arginase, or its family, in nuclear events related to cell cycle progression[68]. In addition, ArgI immunohistochemical labeling was previously observed in rat bronchial and alveolar epithelial cells[69] and it was shown that ArgI plays an important role in physiological blood vessel function when expressed in endothelial and smooth muscle cells[70,71]. Considering the available data, our observations in the present study are in accordance with previously published results and thus, the use of ArgI immunolabeling for M2 identification using the current staining protocol seemed well justified.

As reported earlier, the mannose receptor CD206 is highly expressed by AMs under homeostatic conditions[24,56]. In addition, it was early recognized as an important marker for alternative activation of macrophages (M2)[72]. Accordingly, we found specific and abundant immunolabeling for CD206 of AMs of control animals and used CD206 as a marker for M2 macrophage identification. The combination of cell membrane and cytoplasmic immunostaining derives from the fact that CD206 continuously recycles between the surface membrane of macrophages and intracellular phagolysosomal compartments. Under homeostatic conditions up to 70% of CD206 receptors can be localized intracellularly[73,74]. Therefore, cytoplasmic occurrence is repeatedly seen in immunohistochemical investigations[62,65].

4.2 AM polarization correlates with histopathological findings and the post exposure pro- or regression

As reported previously, five-day inhalation exposure to the for example used in this study examined (nano)materials caused pulmonary inflammation which was diagnosed by light microscopic examination of HE stained slides and changes of respective BALF parameters[13,14,17]. Histological findings were consistent with the original publications (Table 1). In accordance with the ongoing inflammatory process, our examination using immunohistochemistry revealed relative increase of the expression of the M1 marker iNOS in $CD68^+$ AMs, which was accompanied by a decrease of the M2 marker CD206. This is consistent with the pro-inflammatory characteristics of M1 and anti-inflammatory characteristics of M2 macrophages. The most significant relative increase of M1 macrophages was observed in TiO_2-exposed animals, while the decrease of M2 macrophages was most prominent in quartz-exposed animals.

Although TiO_2 (nano)particles were described as poorly-soluble and of low toxicity, several studies suggested that TiO_2 might induce cellular oxidative stress, affecting intracellular redox signaling, and ultimately leading to the expression of pro-inflammatory mediators, including pro-inflammatory enzymes such as iNOS[75-77]. Noteworthy, CeO_2 elicited pulmonary inflammation similar to the other materials investigated but iNOS expression levels were only slightly increased compared to the others. Notably, inflammation caused by 25 mg/m³ CeO_2 dust aerosol concentration, progressed to a granulomatous inflammation following 28-days exposure plus 34 days post-exposure[17]. Given the fact that CeO_2 induced inflammatory changes that included granulomatous inflammation following a post-exposure period, more detailed investigations might unravel possible differences in the initiation and progression of effects.

Following an exposure-free period, light microscopic examination of HE stained lung sections and BALF analysis of the original publications, revealed that biological effects elicited by the investigated (nano)materials changed differently over time (regression, persistency or progression of effects induced by TiO_2, mwCNT or quartz, respectively)[13,14,17]. Correspondingly, differences were seen in temporal patterns of AMs depending on the nanomaterial. In general, our quantitative analysis revealed, that the occurrence of M1 and M2 macrophages correlated with the persistence, progression, or regression of pulmonary inflammation. $CD68^+iNOS^+$ M1 macrophage percentages decreased, whereas $CD68^+CD206^+$ M2 macrophage percentages recovered in case of resolution of inflammation. This statement is based on the observations made for TiO_2, where a decline of inflammatory parameters in BALF and a disappearance of granulocytic infiltration in lung tissue indicated a regression of the inflammatory response. It remains to be elucidated whether this applies also to other materials showing transient inflammatory responses in rat lungs. In case of persistent pulmonary inflammation, increased $CD68^+iNOS^+$ (M1) as well as decreased $CD68^+CD206^+$ (M2) cell numbers did not substantially change over time, although exposure was terminated. This was observed for animals exposed to 32 mg/m³ mwCNT, where granulomatous inflammation persisted 21 days post-exposure. Furthermore, progressive inflammation was correlated with additional relative increase of M1 macrophages after an exposure free period. For example, quartz histopathological findings increased in severity during the post-exposure period, which was paralleled with a significant relative increase of $CD68^+iNOS^+$ AMs when compared to the control and the exposure group analyzed immediately following the last exposure.

As it was recognized that surface reactivity is a major component of (nano)material toxicity[78,79], the increase of $CD68^+iNOS^+$ cell numbers might arise from signals of different origin. On one hand AMs could have been polarized to the M1 phenotype by the engulfed material itself. Depending on the physicochemical properties of (nano)materials, the uptake mechanisms by which macrophages internalize the foreign material can substantially differ, which already influences the intracellular

signaling cascades to be initiated[77,80-82]. In addition, the surface reactivity of (nano)materials may disturb intracellular homeostasis and ultimately effect gene expression[78,83]. On the other, AMs could have been polarized to the M1 phenotype due to extracellular, pro-inflammatory signals they encountered in the pulmonary microenvironment, for example released by wounded epithelial cells. Interestingly, only in TiO_2-exposed animals of the post-exposure group, iNOS expression was restricted to AMs harboring grey, globular material, assumed to be TiO_2 agglomerates. $CD68^+$ AMs not obviously laden with particulate matter, did not show $iNOS^+$ immunolabelling in the post-exposure group. One explanation for this might be, as speculated above, that TiO_2 particles themselves induced intracellular signaling, which gave rise to iNOS expression, either through binding to respective effector proteins or through their surface reactivity, which might have disturbed chemical cell homeostasis. Another explanation is that the local pulmonary microenvironment changed during the post-exposure period from a pro- to an anti-inflammatory one. Monocytes, which entered the lung at a late timepoint, where engulfment of TiO_2 particles from the alveolar surface was already accomplished and resolution of inflammation was already ongoing, did not encounter M1 inducing signals.

Similarly, the decrease of $CD68^+CD206^+$ M2 macrophages observed in the present study might be the result of different mechanisms. As the pulmonary microenvironment, which is usually immunosuppressive[84-86], was altered to a pro-inflammatory microenvironment subsequent to (nano)material exposure, M1 mediators were upregulated and M2 mediators were downregulated. But also, cell death of M2 macrophages, which were initially present in high amounts in the lungs, due to cytotoxic properties of the inhaled materials, might have led to the decrease of $CD68^+CD206^+$ cell numbers. For CeO_2, free granular material was described in alveoli of exposed animals, most probably cell debris of destroyed AMs, indicating it's cytotoxic potential[17]. In addition, we observed a change in localization of the immunolabelling of $CD68^+CD206^+$ AMs for two post-exposure groups. Intracellular localization of CD206 changed from a diffuse (cell membrane and cytoplasm) to a cell membrane restricted manner, to some extend in the mwCNT post-exposure group (Fig. 3, third row) and to a greater extend in the quartz post-exposure group (Fig. 3, bottom row). The reason for and relevance of this observation is unclear. However, the importance of intact intracellular trafficking of the phagocytic receptor CD206 becomes particularly apparent when considering its role in the resolution of inflammation[22,87,88].

In addition to CD206, ArgI is a well-known and important marker for M2 polarization of macrophages[27,89]. Several studies point to the crucial role of the arginine metabolism in immune responses and the herewith associated regulation of iNOS and ArgI expression[90-93]. Because M2 macrophages exert a wide spectrum of immunological functions, which led to subdividing them into different subtypes[94], we chose two markers for M2 identification, each indicative for the different processes macrophages are involved in. In the present study, ArgI expression was found to be variable

between the control groups of the three different inhalation-studies. One possible explanation is that the animals of the TiO_2 and quartz study were subjected to surgery. For the purpose of assessing the proliferation rate of bronchial cells, small BrdU-containing minipumps were implanted beneath the skin of the experimental animals on the second day of exposure. The implantation of the BrdU-minipumps might have affected the immunological state of the animals. Thus, careful data analysis should be conducted, and values of treatment groups should be compared to the concurrent control group of the respective study only. When comparing the ArgI values of the treatment groups with the respective concurrent control group, $CD68^+ArgI^+$ macrophages were significantly upregulated in CeO_2 exposed animals and significantly downregulated in the quartz exposure group. This observation might trigger speculations, considering that ArgI is suspected to be involved in granuloma formation and healing processes[91,95,96], and CeO_2 causes granulomatous inflammation and quartz progressive inflammation and tissue destruction. However, although granulomatous inflammation was also observed in mwCNT exposed animals, ArgI expression was not changed. Nevertheless, we consider our data as valid because several studies reported contradictory results on the role of ArgI in tissue repair processes, fibrosis, and granuloma formation[90-92,97-99]. Thus, the exact role of ArgI in pulmonary inflammation and fibrosis is still not fully resolved.

An increasing body of data demonstrates that nanomaterials differentially influence macrophage polarization. TiO_2 as well as quartz particles were repeatedly found to differently influence M1 and M2 specific protein expression[39,77,83,100-102]. Further, there is first evidence that CeO_2 and mwCNT might affect macrophage polarization as well[99,103-107]. However, several aspects should be considered when investigating macrophage polarization and biological effects of inhaled nanomaterials *in vivo*. Obviously, the dose is a central element in eliciting toxicity, in addition, duration of exposure but also dose rate should be considered. All these factors will differently influence the spatio-temporal dynamics of M1 and M2 polarization. For instance, Kumar et al. found a dose-dependent shift in macrophage polarization[101]. Others found a time-dependent, sequential switch in the appearance of macrophage subpopulations[65,99,104,108]. Interestingly, first evidence points out that the crucial balance of M1 and M2 immune reactions is not necessarily sequential but there are various pathways, which are early stimulated at the same time, and which seem to be independent from each other; each leading to a different aspect of the observed pathophysiology[109-111]. Unraveling these pathways will add to our understanding of the pathogenesis of morphological changes observed, the exact contribution of AMs, and might identify powerful, specific biomarkers, which potentially allow for the prediction of long-term outcome following nanomaterial exposure[77,112,113].

In conclusion, the overall appearance of pro-inflammatory M1 and anti-inflammatory M2 macrophages correlated with histopathological findings indicative for pulmonary inflammation upon

short-term (5 days) inhalation exposure at the end of the exposure as well as after a post-exposure period (14 or 21 days). Initial pulmonary inflammation correlated with a strong upregulation of M1 and a downregulation of M2 AMs, and sequential changes in macrophage polarization correlated with changes in histopathological findings post-exposure. However, AM polarization was not indicative for the different quality of histopathological findings observed with different (nano)materials at later timepoints in longer-term studies. Between the four investigated (nano)materials no substantially different expression pattern of M1 or M2 AMs at an early timepoint (5 day exposure) or 14/21 days post-exposure was seen, that could explain the different histopathological patterns (especially granulomatous inflammation) observed at later timepoints in longer-term studies.

A distinct induction of AM polarization might indicate different underlying initiating events, which in turn might explain the various histopathological outcomes after long-term exposure to different inhaled (nano)materials. Unraveling the underlying pathways might identify biomarkers, which could allow for the prediction of the quality of histopathological outcome following long-term exposure. For this, a more in-depth understanding of the underlying processes of nanomaterial-induced histopathological changes and the role of AMs in the pathophysiology is needed. Investigations on biokinetics and cytokine mediated signaling will add to this understanding. Additional or more specific early markers of long-term inhalation outcomes will promote further development of scientifically sound adverse outcome pathways for inhalation hazard of biopersistent particulate matter.

Acknowledgements

We gratefully thank Claus-Michael Lehr for helpful discussion.
We particularly thank Thomas Tatarewicz and Hans-Robert Hofmann for excellent laboratory support on IHC. We gratefully thank Heike Marxfeld for valuable discussion on IHC.

Conflict of interest

JKJ, LMH, SG and RL are employees of BASF SE, a company producing nanomaterials.

References

Supplemental tables and figures can be found at http://tpx.sagepub.com/supplemental.

1. Kuhlbusch TA, Asbach C, Fissan H, Gohler D, Stintz M. Nanoparticle exposure at nanotechnology workplaces: a review. *Part Fibre Toxicol.* 2011;8:22.
2. Kuhlbusch TAJ, Wijnhoven SWP, Haase A. Nanomaterial exposures for worker, consumer and the general public. *NanoImpact.* 2018;10:11-25.
3. Heinrich U, Fuhst R, Rittinghausen S, et al. Chronic inhalation exposure of wistar rats and two different strains of mice to diesel engine exhaust, carbon black, and titanium dioxide. *Inhal Toxicol.* 1995;7:533-556.
4. Muhle H, Kittel B, Ernst H, Mohr U, Mermelstein R. Neoplastic lung lesions in rat after chronic exposure to crystalline silica. *Scand J Work Environ Health.* 1995;21 Suppl 2:27-29.
5. Kasai T, Umeda Y, Ohnishi M, et al. Lung carcinogenicity of inhaled multi-walled carbon nanotube in rats. *Part Fibre Toxicol.* 2016;13(1):53.
6. Landsiedel R, Ma-Hock L, Hofmann T, et al. Application of short-term inhalation studies to assess the inhalation toxicity of nanomaterials. *Part Fibre Toxicol.* 2014;11:16.
7. Pepelko WE, Mattox JK, Yang YY, Moore W, Jr. Pulmonary function and pathology in cats exposed 28 days to diesel exhaust. *J Environ Pathol Toxicol.* 1980;4(2-3):449-457.
8. Green FH, Boyd RL, Danner-Rabovsky J, et al. Inhalation studies of diesel exhaust and coal dust in rats. *Scand J Work Environ Health.* 1983;9(2 Spec No):181-188.
9. Lee KP, Henry NW, 3rd, Trochimowicz HJ, Reinhardt CF. Pulmonary response to impaired lung clearance in rats following excessive TiO2 dust deposition. *Environ Res.* 1986;41(1):144-167.
10. Keller J, Wohlleben W, Ma-Hock L, et al. Time course of lung retention and toxicity of inhaled particles: short-term exposure to nano-Ceria. *Arch Toxicol.* 2014;88(11):2033-2059.
11. Konduru N, Keller J, Ma-Hock L, et al. Biokinetics and effects of barium sulfate nanoparticles. *Part Fibre Toxicol.* 2014;11:55.
12. Schwotzer D, Ernst H, Schaudien D, et al. Effects from a 90-day inhalation toxicity study with cerium oxide and barium sulfate nanoparticles in rats. *Part Fibre Toxicol.* 2017;14(1):23.
13. van Ravenzwaay B, Landsiedel R, Fabian E, Burkhardt S, Strauss V, Ma-Hock L. Comparing fate and effects of three particles of different surface properties: nano-TiO2, pigmentary TiO2 and quartz. *Toxicol Lett.* 2009;186(3):152-159.
14. Ma-Hock L, Treumann S, Strauss V, et al. Inhalation toxicity of multiwall carbon nanotubes in rats exposed for 3 months. *Toxicol Sci.* 2009;112(2):468-481.
15. Ma-Hock L, Gröters S, Strauss V, et al. Long-term inhalation study with CeO2- and BaSO4 nanomaterials – study design, in-life findings, and lung burden. Eurotox 2017; 2017.
16. Bermudez E, Mangum JB, Wong BA, et al. Pulmonary responses of mice, rats, and hamsters to subchronic inhalation of ultrafine titanium dioxide particles. *Toxicol Sci.* 2004;77(2):347-357.
17. Keller J, Wohlleben W, Ma-Hock L, et al. Time course of lung retention and toxicity of inhaled particles: Short-term exposure to nano-Ceria. *Archives of Toxicology.* 2014;88(11):2033-2059.
18. Ma-Hock L, Burkhardt S, Strauss V, et al. Development of a short-term inhalation test in the rat using nano-titanium dioxide as a model substance. *Inhal Toxicol.* 2009;21(2):102-118.
19. Klein CL, Wiench K, Wiemann M, Ma-Hock L, van Ravenzwaay B, Landsiedel R. Hazard identification of inhaled nanomaterials: making use of short-term inhalation studies. *Arch Toxicol.* 2012;86(7):1137-1151.
20. Mills CD, Lenz LL, Ley K. Macrophages at the fork in the road to health or disease. *Front Immunol.* 2015;6:59.
21. Porcheray F, Viaud S, Rimaniol AC, et al. Macrophage activation switching: an asset for the resolution of inflammation. *Clin Exp Immunol.* 2005;142(3):481-489.
22. Kambara K, Ohashi W, Tomita K, et al. In vivo depletion of CD206+ M2 macrophages exaggerates lung injury in endotoxemic mice. *Am J Pathol.* 2015;185(1):162-171.

23. Lu HL, Huang XY, Luo YF, Tan WP, Chen PF, Guo YB. Activation of M1 macrophages plays a critical role in the initiation of acute lung injury. *Bioscience reports.* 2018;38(2).
24. Misharin AV, Morales-Nebreda L, Mutlu GM, Budinger GR, Perlman H. Flow cytometric analysis of macrophages and dendritic cell subsets in the mouse lung. *Am J Respir Cell Mol Biol.* 2013;49(4):503-510.
25. Duffield JS, Forbes SJ, Constandinou CM, et al. Selective depletion of macrophages reveals distinct, opposing roles during liver injury and repair. *J Clin Invest.* 2005;115(1):56-65.
26. Buttner C, Skupin A, Reimann T, et al. Local production of interleukin-4 during radiation-induced pneumonitis and pulmonary fibrosis in rats: macrophages as a prominent source of interleukin-4. *Am J Respir Cell Mol Biol.* 1997;17(3):315-325.
27. Misson P, van den Brule S, Barbarin V, Lison D, Huaux F. Markers of macrophage differentiation in experimental silicosis. *J Leukoc Biol.* 2004;76(5):926-932.
28. Hancock A, Armstrong L, Gama R, Millar A. Production of interleukin 13 by alveolar macrophages from normal and fibrotic lung. *Am J Respir Cell Mol Biol.* 1998;18(1):60-65.
29. Edwards JP, Zhang X, Frauwirth KA, Mosser DM. Biochemical and functional characterization of three activated macrophage populations. *J Leukoc Biol.* 2006;80(6):1298-1307.
30. Perkins RC, Scheule RK, Hamilton R, Gomes G, Freidman G, Holian A. Human alveolar macrophage cytokine release in response to in vitro and in vivo asbestos exposure. *Experimental lung research.* 1993;19(1):55-65.
31. Sindrilaru A, Peters T, Wieschalka S, et al. An unrestrained proinflammatory M1 macrophage population induced by iron impairs wound healing in humans and mice. *J Clin Invest.* 2011;121(3):985-997.
32. de Waal Malefyt R, Figdor CG, Huijbens R, et al. Effects of IL-13 on phenotype, cytokine production, and cytotoxic function of human monocytes. Comparison with IL-4 and modulation by IFN-gamma or IL-10. *J Immunol.* 1993;151(11):6370-6381.
33. Anthony RM, Urban JF, Jr., Alem F, et al. Memory T(H)2 cells induce alternatively activated macrophages to mediate protection against nematode parasites. *Nat Med.* 2006;12(8):955-960.
34. Laskin DL, Malaviya R, Laskin JD. Role of Macrophages in Acute Lung Injury and Chronic Fibrosis Induced by Pulmonary Toxicants. *Toxicol Sci.* 2019;168(2):287-301.
35. Murray PJ, Wynn TA. Protective and pathogenic functions of macrophage subsets. *Nat Rev Immunol.* 2011;11(11):723-737.
36. Mills CD. M1 and M2 Macrophages: Oracles of Health and Disease. *Critical reviews in immunology.* 2012;32(6):463-488.
37. Martinez FO, Gordon S. The M1 and M2 paradigm of macrophage activation: time for reassessment. *F1000prime reports.* 2014;6(March):13-13.
38. Gordon S, Plüddemann A, Martinez Estrada F. Macrophage heterogeneity in tissues: Phenotypic diversity and functions. *Immunological Reviews.* 2014;262(1):36-55.
39. Chang X, Fu Y, Zhang Y, Tang M, Wang B. Effects of Th1 and Th2 cells balance in pulmonary injury induced by nano titanium dioxide. *Environ Toxicol Pharmacol.* 2014;37(1):275-283.
40. Miao X, Leng X, Zhang Q. The Current State of Nanoparticle-Induced Macrophage Polarization and Reprogramming Research. *Int J Mol Sci.* 2017;18(2).
41. Laskin DL. Macrophages and inflammatory mediators in chemical toxicity: a battle of forces. *Chem Res Toxicol.* 2009;22(8):1376-1385.
42. Henderson RF. Use of bronchoalveolar lavage to detect respiratory tract toxicity of inhaled material. *Experimental and Toxicologic Pathology.* 2005;57:155-159.
43. Porter DW, Ye J, Ma J, et al. Time course of pulmonary response of rats to inhalation of crystalline silica: NF-kappa B activation, inflammation, cytokine production, and damage. *Inhalation Toxicology.* 2002;14(4):349-367.
44. Landsiedel R, Wiench K, Wohlleben W. Geeignete Methoden zur Prüfung der Sicherheit von Nanomaterialien. *Chemie Ingenieur Technik.* 2008; 80(11):1641-1651.
45. Arts JH, Hadi M, Irfan MA, et al. A decision-making framework for the grouping and testing of nanomaterials (DF4nanoGrouping). *Regul Toxicol Pharmacol.* 2015;71(2 Suppl):S1-27.

46. Wohlleben W, Ma-Hock L, Boyko V, et al. *Nanospecific Guidance in REACH: A Comparative Physical-Chemical Characterization of 15 Materials with Methodical Correlations.* Vol 42013.
47. Renne R, Brix A, Harkema J, et al. Proliferative and Nonproliferative Lesions of the Rat and Mouse Respiratory Tract. *Toxicologic Pathology.* 2009;37(7_suppl):5S-73S.
48. Hochstedler CM, Leidinger MR, Maher-Sturm MT, Gibson-Corley KN, Meyerholz DK. Immunohistochemical detection of arginase-I expression in formalin-fixed lung and other tissues. *J Histotechnol.* 2013;36(4):128-134.
49. Holness CL, Simmons DL. Molecular cloning of CD68, a human macrophage marker related to lysosomal glycoproteins. *Blood.* 1993;81(6):1607-1613.
50. Badylak SF, Valentin JE, Ravindra AK, McCabe GP, Stewart-Akers AM. Macrophage phenotype as a determinant of biologic scaffold remodeling. *Tissue Eng Part A.* 2008;14(11):1835-1842.
51. Seki S, Ikarashi M, Kinoshita M, Nakashima M, Nakashima H. New Findings about Liver Kupffer Cells / Macrophages , B Cells and their Functions. *Journal of Hepatitis Research.* 2014;1(1):11-13.
52. Damoiseaux JG, Dopp EA, Calame W, Chao D, MacPherson GG, Dijkstra CD. Rat macrophage lysosomal membrane antigen recognized by monoclonal antibody ED1. *Immunology.* 1994;83(1):140-147.
53. Dijkstra CD, Döpp EA, Joling P, Kraal G. The heterogeneity of mononuclear phagocytes in lymphoid organs: distinct macrophage subpopulations in the rat recognized by monoclonal antibodies ED1, ED2 and ED3. *Immunology.* 1985;54(3):589-599.
54. Malovic I, Sorensen KK, Elvevold KH, et al. The mannose receptor on murine liver sinusoidal endothelial cells is the main denatured collagen clearance receptor. *Hepatology.* 2007;45(6):1454-1461.
55. Snedecor GW, Cochran WG. *Statistical Methods.* Eight edition ed. Ames, Iowa: Iowa State University Press; 1989.
56. Zaynagetdinov R, Sherrill TP, Kendall PL, et al. Identification of myeloid cell subsets in murine lungs using flow cytometry. *American Journal of Respiratory Cell and Molecular Biology.* 2013;49(2):180-189.
57. Sabatel C, Radermecker C, Fievez L, et al. Exposure to Bacterial CpG DNA Protects from Airway Allergic Inflammation by Expanding Regulatory Lung Interstitial Macrophages. *Immunity.* 2017;46(3):457-473.
58. Huaux F, De Gussem V, Lebrun A, et al. New interplay between interstitial and alveolar macrophages explains pulmonary alveolar proteinosis (PAP) induced by indium tin oxide particles. *Archives of Toxicology.* 2018;92(4):1349-1361.
59. Pugliese SC, Kumar S, Janssen WJ, et al. A Time- and Compartment-Specific Activation of Lung Macrophages in Hypoxic Pulmonary Hypertension. *The Journal of Immunology.* 2017;198(12):4802-4812.
60. Cai Y, Sugimoto C, Arainga M, Alvarez X, Didier ES, Kuroda MJ. In vivo characterization of alveolar and interstitial lung macrophages in rhesus macaques: implications for understanding lung disease in humans. *Journal of immunology (Baltimore, Md : 1950).* 2014;192(6):2821-2829.
61. Kunisch E, Fuhrmann R, Roth A, Winter R, Lungershausen W, Kinne RW. Macrophage specificity of three anti-CD68 monoclonal antibodies (KP1, EBM11, and PGM1) widely used for immunohistochemistry and flow cytometry. *Annals of the rheumatic diseases.* 2004;63(7):774-784.
62. Palmer JA, Abberton KM, Mitchell GM, Morrison WA. Macrophage phenotype in response to implanted synthetic scaffolds: an immunohistochemical study in the rat. *Cells Tissues Organs.* 2014;199(2-3):169-183.
63. MacMicking JD, Nathan C, Hom G, et al. Altered responses to bacterial infection and endotoxic shock in mice lacking inducible nitric oxide synthase. *Cell.* 1995;81(4):641-650.
64. Goldman D, Cho Y, Zhao M, Casadevall A, Lee SC. Expression of inducible nitric oxide synthase in rat pulmonary Cryptococcus neoformans granulomas. *Am J Pathol.* 1996;148(4):1275-1282.

65. Venosa A, Malaviya R, Choi H, Gow AJ, Laskin JD, Laskin DL. Characterization of Distinct Macrophage Subpopulations during Nitrogen Mustard-Induced Lung Injury and Fibrosis. *Am J Respir Cell Mol Biol.* 2016;54(3):436-446.
66. Que LG, Kantrow SP, Jenkinson CP, Piantadosi CA, Huang YC. Induction of arginase isoforms in the lung during hyperoxia. *Am J Physiol.* 1998;275(1 Pt 1):L96-102.
67. Skrzypek-Osiecka I, Rahden-Staron I, Porembska Z. Subcellular localization of arginase in rat liver. *Acta Biochim Pol.* 1980;27(3-4):203-212.
68. Hara M, Igarashi J, Yamashita K, et al. Proteins recognized by antibodies against isolated cytological heterochromatin from rat liver cells change their localization between cell species and between stages of mitosis (interphase vs metaphase). 1999;31(5):505-513.
69. Choi S, Park C, Ahn M, Lee JH, Shin T. Immunohistochemical study of arginase 1 and 2 in various tissues of rats. *Acta Histochemica.* 2012;114(5):487-494.
70. Lewis C, Zhu W, Pavkov ML, Kinney CM, Dicorleto PE, Kashyap VS. Arginase blockade lessens endothelial dysfunction after thrombosis. *J Vasc Surg.* 2008;48(2):441-446.
71. Morris SM, Jr. Recent advances in arginine metabolism: roles and regulation of the arginases. *Br J Pharmacol.* 2009;157(6):922-930.
72. Stein M, Keshav S, Harris N, Gordon S. Interleukin 4 potently enhances murine macrophage mannose receptor activity: a marker of alternative immunologic macrophage activation. *J Exp Med.* 1992;176(1):287-292.
73. Gazi U, Martinez-Pomares L. Influence of the mannose receptor in host immune responses. *Immunobiology.* 2009;214(7):554-561.
74. Schweizer A, Stahl PD, Rohrer J. A di-aromatic motif in the cytosolic tail of the mannose receptor mediates endosomal sorting. *J Biol Chem.* 2000;275(38):29694-29700.
75. Singh S, Shi T, Duffin R, et al. Endocytosis, oxidative stress and IL-8 expression in human lung epithelial cells upon treatment with fine and ultrafine TiO2: role of the specific surface area and of surface methylation of the particles. *Toxicol Appl Pharmacol.* 2007;222(2):141-151.
76. Horie M, Nishio K, Fujita K, et al. Cellular responses by stable and uniform ultrafine titanium dioxide particles in culture-medium dispersions when secondary particle size was 100 nm or less. *Toxicol In Vitro.* 2010;24(6):1629-1638.
77. Scherbart AM, Langer J, Bushmelev A, et al. Contrasting macrophage activation by fine and ultrafine titanium dioxide particles is associated with different uptake mechanisms. *Particle and Fibre Toxicology.* 2011;8(1):31-31.
78. Nel A, Xia T, Madler L, Li N. Toxic potential of materials at the nanolevel. *Science.* 2006;311(5761):622-627.
79. Nel A, Xia T, Meng H, et al. Nanomaterial toxicity testing in the 21st century: use of a predictive toxicological approach and high-throughput screening. *Acc Chem Res.* 2013;46(3):607-621.
80. Beningo KA, Wang YL. Fc-receptor-mediated phagocytosis is regulated by mechanical properties of the target. *J Cell Sci.* 2002;115(Pt 4):849-856.
81. Champion JA, Walker A, Mitragotri S. Role of particle size in phagocytosis of polymeric microspheres. *Pharm Res.* 2008;25(8):1815-1821.
82. Doshi N, Mitragotri S. Macrophages recognize size and shape of their targets. *PLoS One.* 2010;5(4):e10051.
83. Lucarelli M, Gatti AM, Savarino G, et al. Innate defence functions of macrophages can be biased by nano-sized ceramic and metallic particles. *European Cytokine Network.* 2004;15(4):339-346.
84. Janssen WJ, McPhillips KA, Dickinson MG, et al. Surfactant proteins A and D suppress alveolar macrophage phagocytosis via interaction with SIRP alpha. *Am J Respir Crit Care Med.* 2008;178(2):158-167.
85. Mayer AK, Dalpke AH. Regulation of local immunity by airway epithelial cells. *Archivum Immunologiae et Therapiae Experimentalis.* 2007;55(6):353.

86. Snelgrove RJ, Goulding J, Didierlaurent AM, et al. A critical function for CD200 in lung immune homeostasis and the severity of influenza infection. *Nat Immunol.* 2008;9(9):1074-1083.
87. Lee SJ, Evers S, Roeder D, et al. Mannose receptor-mediated regulation of serum glycoprotein homeostasis. *Science.* 2002;295(5561):1898-1901.
88. Martinez-Pomares L. The mannose receptor. *J Leukoc Biol.* 2012;92(6):1177-1186.
89. Briken V, Mosser DM. Editorial: switching on arginase in M2 macrophages. *J Leukoc Biol.* 2011;90(5):839-841.
90. Setoguchi K, Takeya M, Akaike T, et al. Expression of inducible nitric oxide synthase and its involvement in pulmonary granulomatous inflammation in rats. *Am J Pathol.* 1996;149(6):2005-2022.
91. Hesse M, Modolell M, La Flamme AC, et al. Differential regulation of nitric oxide synthase-2 and arginase-1 by type 1/type 2 cytokines in vivo: granulomatous pathology is shaped by the pattern of L-arginine metabolism. *J Immunol.* 2001;167(11):6533-6544.
92. Pesce JT, Ramalingam TR, Mentink-Kane MM, et al. Arginase-1-expressing macrophages suppress Th2 cytokine-driven inflammation and fibrosis. *PLoS Pathog.* 2009;5(4):e1000371.
93. Mills CD. Macrophage arginine metabolism to ornithine/urea or nitric oxide/citrulline: a life or death issue. *Crit Rev Immunol.* 2001;21(5):399-425.
94. Gordon S, Martinez FO. Alternative activation of macrophages: mechanism and functions. *Immunity.* 2010;32(5):593-604.
95. Mattila JT, Ojo OO, Kepka-Lenhart D, et al. Microenvironments in tuberculous granulomas are delineated by distinct populations of macrophage subsets and expression of nitric oxide synthase and arginase isoforms. *J Immunol.* 2013;191(2):773-784.
96. Duque-Correa MA, Kuhl AA, Rodriguez PC, et al. Macrophage arginase-1 controls bacterial growth and pathology in hypoxic tuberculosis granulomas. *Proc Natl Acad Sci U S A.* 2014;111(38):E4024-4032.
97. Wangoo A, Sparer T, Brown IN, et al. Contribution of Th1 and Th2 cells to protection and pathology in experimental models of granulomatous lung disease. *J Immunol.* 2001;166(5):3432-3439.
98. Poljakovic M, Porter DW, Millecchia L, et al. Cell- and isoform-specific increases in arginase expression in acute silica-induced pulmonary inflammation. *J Toxicol Environ Health A.* 2007;70(2):118-127.
99. Dong J, Ma Q. Macrophage polarization and activation at the interface of multi-walled carbon nanotube-induced pulmonary inflammation and fibrosis. *Nanotoxicology.* 2018;12(2):153-168.
100. Blackford JA, Jr., Antonini JM, Castranova V, Dey RD. Intratracheal instillation of silica up-regulates inducible nitric oxide synthase gene expression and increases nitric oxide production in alveolar macrophages and neutrophils. *Am J Respir Cell Mol Biol.* 1994;11(4):426-431.
101. Kumar S, Meena R, Paulraj R. Role of Macrophage (M1 and M2) in Titanium-Dioxide Nanoparticle-Induced Oxidative Stress and Inflammatory Response in Rat. *Appl Biochem Biotechnol.* 2016;180(7):1257-1275.
102. Rao KM, Porter DW, Meighan T, Castranova V. The sources of inflammatory mediators in the lung after silica exposure. *Environ Health Perspect.* 2004;112(17):1679-1686.
103. Li K, Shen Q, Xie Y, You M, Huang L, Zheng X. Incorporation of cerium oxide into hydroxyapatite coating regulates osteogenic activity of mesenchymal stem cell and macrophage polarization. *J Biomater Appl.* 2017;31(7):1062-1076.
104. Ma, Zhao, Mercer, et al. Cerium oxide nanoparticle-induced pulmonary inflammation and alveolar macrophage functional change in rats. *Nanotoxicology.* 2011;5(3):312-325.
105. Barna BP, Huizar I, Malur A, et al. Carbon nanotube-induced pulmonary granulomatous disease: Twist1 and alveolar macrophage M1 activation. *Int J Mol Sci.* 2013;14(12):23858-23871.

106. Meng J, Li X, Wang C, Guo H, Liu J, Xu H. Carbon nanotubes activate macrophages into a M1/M2 mixed status: recruiting naive macrophages and supporting angiogenesis. *ACS Appl Mater Interfaces.* 2015;7(5):3180-3188.
107. Rydman EM, Ilves M, Koivisto AJ, et al. Inhalation of rod-like carbon nanotubes causes unconventional allergic airway inflammation. *Part Fibre Toxicol.* 2014;11:48.
108. Xiang GA, Zhang YD, Su CC, et al. Dynamic changes of mononuclear phagocytes in circulating, pulmonary alveolar and interstitial compartments in a mouse model of experimental silicosis. *Inhal Toxicol.* 2016;28(9):393-402.
109. Nikota J, Banville A, Goodwin LR, et al. Stat-6 signaling pathway and not Interleukin-1 mediates multi-walled carbon nanotube-induced lung fibrosis in mice: insights from an adverse outcome pathway framework. *Part Fibre Toxicol.* 2017;14(1):37.
110. Re SL, Giordano G, Yakoub Y, et al. Uncoupling between inflammatory and fibrotic responses to silica: evidence from MyD88 knockout mice. *PLoS One.* 2014;9(7):e99383.
111. Fritsch-Decker S, Marquardt C, Stoeger T, Diabate S, Weiss C. Revisiting the stress paradigm for silica nanoparticles: decoupling of the anti-oxidative defense, pro-inflammatory response and cytotoxicity. *Arch Toxicol.* 2018;92(7):2163-2174.
112. Ji Z, Wang X, Zhang H, et al. Designed synthesis of CeO2 nanorods and nanowires for studying toxicological effects of high aspect ratio nanomaterials. *ACS Nano.* 2012;6(6):5366-5380.
113. Duke KS, Taylor-Just AJ, Ihrie MD, et al. STAT1-dependent and -independent pulmonary allergic and fibrogenic responses in mice after exposure to tangled versus rod-like multi-walled carbon nanotubes. *Part Fibre Toxicol.* 2017;14(1):26.

6.3.1 Author contribution

Appearance of alveolar macrophage subpopulations in correlation to histopathological effects in short-term inhalation studies with biopersistent (nano)materials

Johanna Koltermann-Jülly, Lan Ma-Hock, Sibylle Gröters, Robert Landsiedel

Toxicologic Pathology, 2019, submitted manuscript

Authors contributions

JKJ performed immunohistochemistry and data analysis.
JKJ, LMH did the interpretation of results.
RL, SG, LMH conceived and supervised the project and contributed to the discussion of results.
All authors contributed to the writing of the manuscript.

We hereby confirm the accuracy of the above information (all authors).

Koltermann-Jülly, Johanna	
Name	*Date, Signature*
Ma-Hock, Dr. Lan	
Name	*Date, Signature*
Gröters, Dr. Sibylle	
Name	*Date, Signature*
Landsiedel, PD Dr. Robert	
Name	*Date, Signature*

7. List of publications, oral and poster presentations

7.1 Peer-reviewed publications

1. Abiotic dissolution rates of 24 (nano)forms of 6 substances compared to macrophage-assisted dissolution and in vivo pulmonary clearance: Grouping by biodissolution and transformation
   Johanna Koltermann-Jülly[1], Johannes G. Keller[1], Antje Vennemann, Kai Werle, Philipp Müller, Lan Ma-Hock, Robert Landsiedel, Martin Wiemann, Wendel Wohlleben
   [1]equal contribution
   NanoImpact https://doi.org/10.1016/j.impact.2018.08.005

2. Predicting dissolution and transformation of inhaled nanoparticles in the lung using abiotic flow cells: The case of barium sulfate
   Johannes G. Keller[1], Uschi Graham[1], **Johanna Koltermann-Jülly**, Robert Gelein, Lan Ma-Hock, Robert Landsiedel, Martin Wiemann, Günter Oberdörster, Alison Elder, Wendel Wohlleben
   [1]equal contribution
   Scientific Reports, submitted

3. Appearance of alveolar macrophage subpopulations in correlation to histopathological effects in short-term inhalation studies with biopersistent (nano)materials
   Johanna Koltermann-Jülly, Lan Ma-Hock, Sibylle Gröters, Robert Landsiedel
   Toxicologic Pathology, submitted

7.2 Presentations at international conferences

Oral presentation

1. Bridging the disciplines - Nanoforum for Young Scientists, 2017, Mainz, Germany
   'Simulating the lung-clearance of barium sulfate NPs by dissolution'
   Winner of the Young speaker award

Poster presentations

1. 12th International Conference and Workshop on Biological Barriers, 2018, Saarbrücken, Germany
   'Nanoparticle-induced Alveolar Macrophage Polarization *in vivo*'
   Koltermann-Jülly J., Marxfeld H., Ma-Hock L., Lehr C.-M., Gröters S., Landsiedel R.

2. 2nd German Pharm-Tox Summit (DGPT annual meeting), 2017, Heidelberg, Germany
   'Simulating the dissolution process of barium sulfate nanoparticles in the lung'
   Koltermann-Jülly J., Wohlleben W., Wiemann M., Vennemann A., Ma-Hock L., Keller J., Gröters S., Lehr C.M., van Ravenzwaay B., Landsiedel R.

3. 11th International Conference and Workshop on Biological Barriers, 2016, Saarbrücken, Germany
   'Investigations on the dissolution of barium sulfate nanoparticles in phagolysosomal simulant fluid'
   Koltermannn-Jülly J., Ma-Hock L., Gröters S., Wohlleben W., Fabian E., Landsiedel R. and Lehr C.M.

Acknowledgements

Danke an Prof. Dr. Claus-Michael Lehr der sofort bereit war die Betreuung meiner Doktorarbeit zu übernehmen. Trotz der räumlichen Distanz war es nie distanziert, wenn ich in Saarbrücken war. Danke für die uneingeschränkte Unterstützung, hilfreichen Ratschläge und positive, motivierende Einflussnahme auf mein Promotionsprojekt.

Danke an Prof. Dr. Rolf W. Hartmann, der mich und mein Promotionsprojekt als wissenschaftlicher Begleiter betreute.

Danke an mein Prüfungskomitee, welches von Prof. Dr. Martin Schneider und Dr. Jessica Hoppstädter bereichert wurde.

Danke Robert Landsiedel

Dass Sie mich von der Straße geholt haben.

Dass Sie mir das alles bis zum Schluss zuge*mut*et haben.

Dass Sie mich immer haben machen lassen.

Dass Sie immer hinter mir standen.

Und wenn es sein musste sich vor mich gestellt haben.

Danke Lan Ma-Hock

Dass Du in jeglicher Hinsicht eine Bereicherung für mein Leben warst und bist.

Sowohl naturwissenschaftlich als auch privat und menschlich.

Ich habe von kaum einem Menschen so viel gelernt wie von Dir.

Danke, für die vielen Stunden in denen wir zusammen so viele verschiedene Gedanken sortiert haben.

Danke Sibylle Gröters

Dass ich bei Dir immer eine offene Tür und Zuspruch fand.

Dass du so viel relativiert, und damit immer alles wieder in Ordnung gebracht hast. Du hast es immer wieder geschafft meine Bedenken in Ruhe, Ordnung und Motivation zu verwandeln.

Danke an das ganze Labor der Inhalationstoxikologie.

Besonders an

Elke Wittmer

Detlef Wels

Sarah Koppenhagen

Manuel Rissel

Annette Knecht

Dass ich mich vom ersten Tag an bei euch heimisch und aufgehoben gefühlt habe.

Dass ihr euch IMMER Zeit für mich genommen habt, egal wie stressig es gerade war.

Dass ihr auch die außergewöhnlichsten Ideen mit mir mitgemacht habt.

Dass ihr mich durchgefüttert habt.

Danke Thomas Tatarewicz und Hans-Robert Hofmann

„Wie war das nochmal mit der Negativkontrolle???“

Danke, dass ihr zu jeder Zeit und zu jeder Angelegenheit Anlaufstelle und Zuflucht für mich wart.

Für jedes (Aus-)Lachen, für jedes gemeinsame Essen, für die Aufrichtigkeit.

Für eure Freundschaft.

Danke an Heike Marxfeld. Für deine immer offene Tür und besonders für dein immer offenes Ohr bezüglich (immunohistochemischer) Fragen, seien sie auch noch so ungewöhnlich oder verzweifelt.

Danke and das Labor der Biokinetik und an das gesamte Team der Pathologie, das Sektionsteam, das Team der Histopathologie und das Team der klinischen Chemie. Eure stetige, wertvolle, bedingungslose und in höchstem Maße qualifizierte Unterstützung kann mit keiner Schokolade und mit keinem Kuchen der Welt genug aufgewogen werden.

Danke an Johannes Keller, Dr. Uschi Graham, Prof. Dr. Günter Oberdörster, Prof. Dr. Alison Elder und ganz besonders an Wendel Wohlleben. Für die produktive, effektive und effiziente Zusammenarbeit. Ich habe unsere gemeinsamen Telefonkonferenzen immer sehr genossen und kam oft aus dem Staunen nicht mehr heraus.

Danke an Martin Wiemann und Antje Vennemann, von denen ich sehr viel augenöffnendes lernen durfte; und mit denen die Zusammenarbeit großen Spaß gemacht hat. Ich war immer sehr gerne zu Besuch am IBE in Münster.

Nina – Danke, dass du unser Café UT mit deinem Zauber erfüllt hast. Deine Menschlichkeit. Dein Lachen. Deine Herzenswärme. Du hast die Gabe mit deiner Art einen ganzen Tag zu erhellen.
Ich bin unbeschreiblich glücklich darüber die meiste Zeit meiner Doktorandenzeit mit Qiqi und dir im Café UT gelacht, gesnackt, gestopft, gesungen, getanzt und gebastelt zu haben. Wenn dein Taxi-Unternehmen läuft musst du meinen „Macker“ und mich unbedingt mal mit deiner „Karre“ abholen.

Danke an Saskia Sperber, Jana Keller, Caroline Gomes und Daniel Urbisch. Danke für die vielen zusammen gelaufenen Kilometer, für jedes gemeinsame Essen und für die schönen Spaziergänge. Durch euch durfte ich erfahren was ‚geteiltes Leid, ist halbes Leid' wirklich bedeutet.

Danke an meine Kolleginnen und Kollegen aus der regulatorischen Toxikologie. Euer uneingeschränkter Rückhalt gab mir stets Kraft.

Danke Benjamin Spielmann

Dass du so sehr mit mir mitgelitten hast.

Dass du immer und immer wieder tröstende Worte gefunden hast.

Dass du immer da warst.

Danke Franz Berger

Dass du unter widrigen Umständen, dir selbst zu Lasten, so lange so viel von mir weggestemmt hast. Auch wenn es bedeutete, dass du dich zwei-, drei- und vierteilen musstest.

Danke, dass du mir das solideste Fundament gebaut hast, das man einer angehenden Toxikologin bauen kann.

Danke meiner wundervollen Familie und wunderbaren Schwiegerfamilie und meinen phantastischen Freunden, besonders meinen Eltern, meiner fabelhaften Schwester Karin und meinem Lieblingsmenschen Sabrina, die alle so geduldig mit mir waren, mich immer wieder aufgefangen haben, so oft auf mich verzichtet haben, und nie den Glauben an mich verloren haben.

Ohne jeden einzelnen von euch wäre das ganze niemals möglich geworden; ich hätte es nicht geschafft.

Danke Patrick

Für die Verpflegung und Umsorgung.

Für all die Badewannen voller Tränen die du getrocknet hast.

Für all das Lachen, welches du in den unmöglichsten Situationen stets bewirkst.

Für deine unendliche Geduld, für deine unermessliche Stärke, für deinen nie aufhörenden Rückhalt.

Für deine Liebe

Jeden Tag

Jeden Tag mehr